NORTHWESTERN UNIVERSITY

Syntheses of Platinum Catalysts on Strontium Titanate Nanocuboids for Selective Polyolefin Hydrogenolysis

A DISSERTATION

SUBMITTED TO THE GRADUATE SCHOOL
IN PARTIAL FULFILLMENT OF THE REQUIREMENTS

for the degree

DOCTOR OF PHILOSOPHY

Field of Chemistry

By

Ian Lukasz Peczak

EVANSTON, ILLINOIS

June 2023

ABSTRACT

Single-use plastic waste pollution will cause significant harm to the environment if left unaddressed. One possible mitigation strategy is to develop processes, e.g. catalytic hydrogenolysis, that can convert (i.e. upcycle) waste plastics into value-added products capable of participating in a circular economy. Platinum (Pt) catalysts on strontium titanate nanocuboid supports (STO; Pt/STO) are attractive hydrogenolysis catalysts because of properties such as cube-on-cube epitaxy between Pt and STO, which contribute to superior catalytic performance. However, for Pt/STO to commercially upcycle discarded polyolefins, tunable and scalable Pt/STO syntheses that do not harm catalytic performance must be designed.

As part of a broad upcycling study, Pt/STO catalysts were synthesized by scalable methods and used to hydrogenolyze research-grade polyethylene into uniform, straight-chain lubricant products (M_n = 490 Da, Đ = 1.03). Microwave- and convection-based STO nanocuboid syntheses were developed to control support particle size and morphology, and highly cuboidal STO nanoparticles were obtained with average sizes from 20 to 80 nm and low size variance between the particles in each batch. One synthesis produced 20 g STO under relatively mild conditions (16 h, 200 °C) and replaced $TiCl_4$ (l) with titanium (IV) bisammonium lactato dihydroxide, a water-stable Ti^{4+} complex.

Pt nanoparticles were deposited on STO using surface organometallic chemistry (SOMC) and strong electrostatic adsorption (SEA). For both techniques, sequential cycles of deposition and reduction were used to increase Pt loading on the support surface. For SOMC-derived Pt/STO, average loading increased up to 1.5 % Pt by weight, and average Pt particle size increased to about 1.5 nm. For SEA-derived Pt/STO, average loading increased to 0.65 % Pt by weight, and average Pt particle size increased to about 2.8 nm. SOMC-derived Pt/STO converted isotactic polypropylene (starting M_n = 6000 Da) into low-dispersity products (Đ = 1.1 for each sample) with average molecular weights centered between $200 < M_n < 300$ Da. Increasing the scale of Pt/STO synthesis did not adversely affect upcycling product distributions when said catalysts were used for hydrogenolysis. Consistent with experimental

observations, preliminary models of polymer adsorption on Pt/STO via a united-atom representation suggest that long chains adsorb preferentially on Pt.

_____

Professor Kenneth R. Poeppelmeier
Dissertation Advisor

ACKNOWLEDGMENTS

A Ph.D. truly takes a village, and I'm grateful to all those who supported me in my journey to complete this degree. First and foremost, I'd like to thank my advisor, Professor Ken Poeppelmeier, for five wonderful years of mentorship. I learned more than I could have imagined about inorganic chemistry, science, and hard work in general. I owe my ability to be an effective problem solver and scientist to your guidance, and will always fondly remember the time I spent in your group. I thank Dr. Massimiliano Delferro for helping with my research projects and acting as my informal advisor. Max, working with you taught me a lot, and your help was instrumental in keeping my projects moving forward when things were otherwise chaotic and uncertain. Also, you're an incredible skier. I thank Prof.'s Notestein, Kanatzidis, and Stair for serving on my qualifying exam committee, and Prof.'s Notestein and Kanatzidis for also serving on my thesis committee. I thank the Department of Energy and the Institute for the Cooperative Upcycling of Polymers (iCOUP) for funding my graduate research.

Thank you to Dr. Robert Kennedy for everything you've done to teach me science and manage the details of experimentation. Were you to go into academia, you'd be an exceptional professor, and I'm grateful to have worked so closely with you throughout my time here at Northwestern. There are many other students and postdocs who helped me complete the work contained in this Dissertation. To name a few who helped above and beyond expectations: Ryan Hackler, Justin Hancock, Gokhan Celik, Magali Ferrandon, Michael Yeung, Ella Wang, Patrick Ding, Kendall Kamp, Steven Flynn, Alon Chapotevsky, Ryan Paull, Zach Mansley, Emily Greenstein, among others. I thank Max Meirow and Prof. Erik Luijten for our continued modeling collaboration.

I'd like to thank my family, who has supported me every step of the way and driven my passion for science. Thanks for always looking out for me. Above and beyond all others though, thank you Cari for being the most amazing person I've ever met. You're my best friend, and I love you so beyond much. I'm so indescribably excited to start our next chapter together in Denver.

ABBREVIATIONS

ALD: atomic layer deposition.

BET: Brunauer–Emmett–Teller

BF: Bright field

BTO: Barium titanate

CFR: Continuous flow reactor

CH: Convection Hydrothermal Heating

DRIFTS: diffuse reflectance infrared Fourier transform spectroscopy.

HAADF: high angle annular dark field.

HDPE: High-density polyethylene

HREM: high resolution electron microscopy. ICP: inductively coupled plasma.

ICP-OES: inductively coupled plasma optical emission Spectroscopy.

LDPE: Low-density polyethylene

LLDPE: Linear low-density polyethylene

MAH: Microwave-Assisted Hydrothermal Heating

MDPE: Mid-density polyethylene

NC: Nanocuboid

PE: Polyethylene

PP: Polypropylene

PTA: Platinum (IV) tetraamine nitrate

PXRD: powder x-ray diffraction

RT13: ($\sqrt{13} \times \sqrt{13}$) R 33.7°.

SEA: Strong electrostatic adsorption

SCO: Strontium Carbonate

SOMC: surface organometallic chemistry

$Sr(OAc)_2$: strontium acetate

STEM: scanning transmission electron microscopy

STO: $SrTiO_3$

TEM: transmission electron microscopy

TiBALD: titanium (IV) bisammonium lactato dihydroxide

$Ti(OEt)_4$: titanium ethoxide

$Ti(OBu)_4$: titanium butoxide

$Ti(O^tBu)_4$: titanium tetrabutoxide.

$Ti(O^iPr)_4$: titanium isopropoxide

$Ti(OPr)_4$: titanium propoxide

$TiCl_4$: titanium tetrachloride.

XPS: X-ray photoelectron spectroscopy

XRD: X-ray diffraction.

DEDICATION

I dedicate this Dissertation to my parents, Dorota and Pawel. You two are the purest embodiment of American Dream - immigrants from distant shores who left everything behind in search of opportunity in these United States. You sacrificed comfort and security to ensure that my sisters and I could live happy and fulfilling lives. All three of us have taken that to heart, and I hope this Dissertation demonstrates my commitment to honoring those sacrifices and proving they were not in vain. I love you both dearly, and I’m incredibly proud to be your son. Thank you for everything.

TABLE OF CONTENTS

LIST OF TABLES, ILLUSTRATIONS, FIGURES, AND GRAPHS

CHAPTER 1

Introduction

This Chapter was adapted with permission from "I.L. Peczak, R. M. Kennedy, R. A. Hackler, B. Lee, M. Meirow, E. Luijten, M. Delferro, K. R. Poeppelmeier. 'Treasuring Trash: Pt/$SrTiO_3$ Catalysts Process Plastic Waste into High-Value Materials' *Matter*, **2023**, *Submitted*."

1.1 ABSTRACT

Single-use plastics are ubiquitous throughout modern society because they have properties that make them desirable in a wide variety of applications, including low cost of production, high thermal and chemical stability, and tunable mechanical properties. Several of the recycling methods currently used to process single-use plastic waste, such as mechanical recycling and pyrolysis, do not selectively process plastic materials into uniform products, as would be advantageous for repurposing these materials in pursuit of a circular economy. Catalytic hydrogenolysis, whereby carbon–carbon bonds in polymers are broken over a supported catalyst in presence of H_2, is a promising approach to converting plastics into value-added products that can be sold commercially. In this Account, we present some recent advances in polyolefin hydrogenolysis from Argonne National Laboratory and Northwestern University, with a focus on Pt nanoparticles on $SrTiO_3$ nanocuboid supports (Pt/$SrTiO_3$; Pt/STO). Current developments in this field, general challenges, and future directions are discussed.

1.2 INTRODUCTION

1.2.1 Plastic Waste and Current Approaches to End-of-Life Management: Origin, Uses, and Environmental Impact of Plastics

Plastics were first developed in the late 19th century to replace scarce natural materials such as wood and ivory. Beginning with the synthesis of Bakelite in 1907, interest and investment in the development of various fully synthetic plastic materials grew significantly in the early 20th century.[1] With the onset of World War II, plastic production was prioritized because it allowed Western powers to meet material

demands for a wide range of military applications without overusing natural resources. In peacetime, the abundance of material feedstocks and existence of well-established commercial processes facilitated the repurposing of plastics for use in domestic and commercial applications.[2] Since then, plastic production has continuously increased to meet growing consumer needs in areas as wide-ranging as packaging, medical devices, piping, food and beverage containers, and electronics, among others. This demand has recently intensified because of both the COVID-19 pandemic, during which large portions of the global population opted for single-use products in lieu of reusable alternatives, and a general increase in the global standard of living, which has driven consumption of both non-necessity and specialty goods.[2]

While the rate of plastic recycling varies widely by material type, geographic location, and product identity, recycling rates are generally low, ranging from around 20% for polyethylene terephthalate (PET, Society of the Plastics Industry (SPI) Code 1) to near 0% for plastics such as polyvinyl chloride (PVC, SPI Code 3). Globally, overall plastic recycling rates are also low, ranging from around 20% in Europe, to 15% in Asia, and 5–10% in the United States, creating a pollution crisis that will significantly harm both the environment and human health if left unaddressed.[3] Of the 300–400 million annual tons of plastic produced globally, up to 80% are discarded without further processing.[3] These discarded materials often end up in landfills, rivers, or oceans where they leach chemicals such as phthalates into soil and ground water.[4] When present in waterways, single-use plastics can both potentially harm local wildlife and habitats and decompose into microplastics, which may eventually end up in food designated for human consumption.[3,5,6] Beyond creating an environmental hazard, discarded plastics are a major source of untapped chemical energy. By some estimates, the energetic value stored in discarded plastics annually worldwide is equivalent to around 3.5 billion barrels of oil ($175 billion at $50 / barrel).[7]

A critical barrier to the effective processing of plastics is that modern economic arrangements link plastic producers, consumers, and post-use processors in a linear fashion (**Figure 1.1**).[8,9]

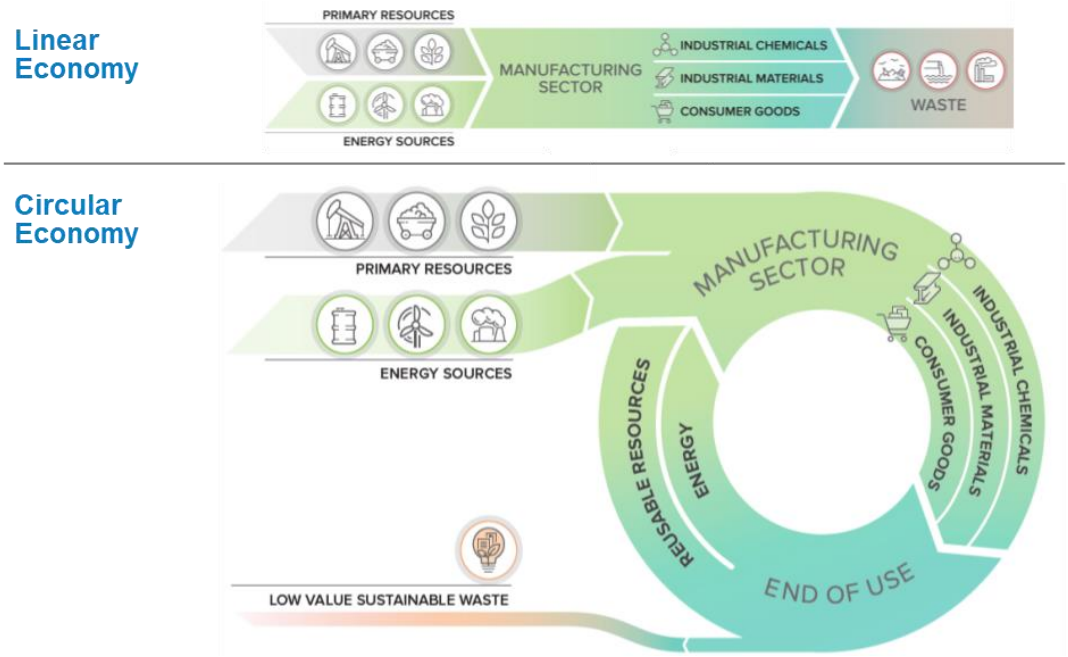

Figure 1.1. Graphical Depictions of Chemical Resource Processing in Linear (Top) and Circular Economies (Bottom). In a linear economy, primary and energy resources are processed in the manufacturing sector to create a variety of industrial chemicals, materials, and consumer goods. These materials are then discarded as waste with limited recovery. In a circular economy, aside from some low-value sustainable waste, resources are repurposed after use into energy and reusable resources, which are returned to the manufacturer for adaptation into new materials and goods. Designed by Argonne National Laboratory.[10]

Fossil fuels and other petrochemical resources are extracted, refined, and distributed to manufacturers, which process these resources into a variety of industrial chemicals, materials, and consumer goods. The low cost of fossil fuels and the excellent properties of synthetic polymers made from virgin materials cement this arrangement and complicate efforts to repurpose plastic waste for commercial use. One effective way to combat this will be to establish profitable and scalable avenues for processing plastics into higher-value commodities. Such an economic arrangement is termed a circular economy and is the

cornerstone of a sustainable future, but will require significant changes to the status quo from companies and governments alike (**Figure 1.1**).[11]

Importantly, the inherent nature of a circular economy will create significant economic opportunities for the repurposing of waste plastics into petroleum-derived materials and goods (**Figure 1.2**). As an example, waxes, lubricants, and surfactants are commercial products that are structurally analogous to chemically recycled plastic materials. These products command significant markets, ranging from $9.8 billion in worldwide annual sales for waxes to $125.8 billion for global lubricant sales. Profit margins for these materials range from ~$1500 per ton on the low end for wax materials, to around $4000 per ton for higher-value surfactants. Thus, there is a potentially huge economic upside in creating these high-value materials from low-value plastic waste. To that effect, novel techniques must be developed to reliably repurpose spent plastics into value-added products. Such techniques, termed “upcycling” in 1999 by Gunter Paul,[12] can take the form of polymer-to-polymer conversions, polymer-to-monomer conversions, or conversions to a product completely independent of the starting material. Over the last five years, a variety of such processes have been developed to selectively convert plastic waste.

It is important to understand how these techniques compare to current methods of waste plastic recycling, and why said methods have not been able to create hydrocarbon products suitable for commoditization.

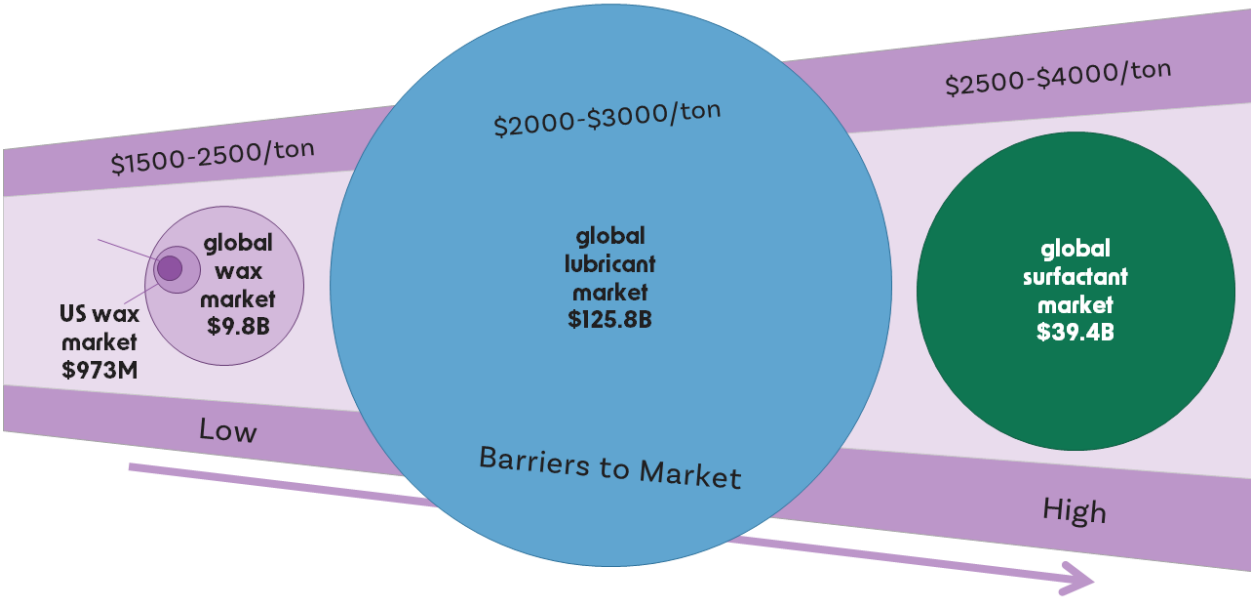

Figure 1.2. Profit Margins, Market Sizes, and Relative Barriers to Market for the Global Wax, Lubricant, and Surfactant Industries. Profit margins in these industries range from around $1500–2500 per ton on the low end (waxes) to around $4000 per ton on the higher end (surfactants). The global wax industry has the smallest market share at around $10 billion annual sales, while the global surfactant and lubricant markets have corresponding sizes of around $40 billion and $126 billion, respectively. Barriers to market (e.g., product purity specifications, regulations, etc.) are lowest for waxes and highest for surfactants. Reproduced with permission from Aeternal Upcycling, Inc.

1.3 RECYCLING METHODS

1.3.1 Mechanical Recycling

Currently, most plastics that do not end up in landfills are recycled through mechanical processes.[4] Mechanical recycling is an umbrella term that refers to both *primary mechanical recycling*, whereby uncontaminated materials are repurposed for their original use, and *secondary mechanical recycling*,

through which the physical form of a plastic is manipulated to generate a new product distinct from the starting polymer.[4]

Primary mechanical recycling repurposes uncontaminated materials without changing their properties, extending the lifetime of an individual product while minimizing damage to material structure. However, very few plastics can be recycled in such fashion because the criteria required for primary mechanical recycling (e.g., known origin, no contamination) are highly stringent and do not apply widely. Secondary mechanical recycling, on the other hand, relies on methods such as grinding, pelletizing, washing, and drying, etc. to form a manipulable polymer material that can be physically engineered into another product.[13,14] First, the starting polymer is cleaned and physically reconfigured to afford a homogeneous plastic mass suitable for further processing. This processing into final products is often done via extrusion because it is cheap, solvent-free, and easily scalable across a variety of polymer types. Heat and rotating screws are used to induce thermal softening and plasticization, after which the polymer melt is fed into a fixed extruder and molded into a desired shape.

Mechanical recycling is largely suitable for processing thermoplastics, such as high-density polyethylene (HDPE, SPI Code 2) and polypropylene (PP, SPI Code 5), which make up most industrial plastics. These materials consist of independent (i.e., not cross-linked) long and short chains, and therefore can undergo multiple heating and cooling cycles as required for physical molding.[15] Thermosets, found in materials such as polyurethane foam or in vulcanized rubber, are another important class of plastics consisting of highly cross-linked three-dimensional structures that do not soften or otherwise change their properties when subjected to heating or cooling. This feature has made thermosets critical in applications that require structural soundness at high temperatures. However, these same properties preclude thermosets from being processed by mechanical recycling. While a variety of potential recycling techniques, such as microbial degradation and microwave irradiation, are currently being investigated for their ability to break down thermosets, a state-of-the-art technique has yet to be established.[15,16]

Materials that are recycled through secondary mechanical recycling are prone to degradation because of radical formation along the polymer chain, which causes β-scissions that degrade the plastic material.[17,18]

This is accelerated by contamination in the starting feedstock and by the presence of pigments or additives, which are found in a wide variety of consumer goods. The scissions that lead to mechanical degradation are often exacerbated by both mechanical shearing and incompatibility between multiple types of polymers in polymer melts, which leads to fracturing in the final extrudate. While these degradation processes are specific to each polymer type, chain length reductions and loss of mechanical properties of the starting polymer are consistently observed.[19] As a result, mechanical recycling permits only a limited number of reprocessing cycles and largely outputs materials of lower value (termed *downcycling*). Thus, for plastic recycling to play a meaningful role in a future circular economy, chemical techniques will need to be developed that can process a wide range of plastics into *value-added* products consistently over many material lifecycles.

1.3.2 Pyrolysis

One non-mechanical method for processing plastics is pyrolysis, whereby plastic materials are heated in a reduced oxygen environment at temperatures between 400 ^{o}C and 800 ^{o}C. Pyrolysis can be both thermally and catalytically driven and can convert a wide range of polymers into alkanes, alkenes, alkynes, and aromatics. The products of such processes are often liquids with physical properties comparable to diesel oil. As a result of the similarities, many pyrolysis processes are currently positioned to eventually compete with virgin petrochemicals for the market share of fuels used in transportation and heating.[20,21]

Several pyrolysis processes are being conducted at the pilot scale and the method is generally moving beyond proof-of-concept towards further commercialization.[22,23] However, challenges still exist. If catalysts are used in pyrolysis, those that are active for cracking are also susceptible to fast deactivation and coking.[24] Moreover, the economics of pyrolysis products fluctuates significantly. Because pyrolysis products compete with virgin petrochemical products, their economic viability is tied to the price of crude oil, incentivizing manufacturers to target niche markets where sustainability is quantified and valued through metrics such as carbon credits. Importantly, pyrolysis processes are not typically selective and yield broad product distributions with gas and char byproducts.[7] Therefore, pyrolysis processes need to

be coupled with extensive separation of the final product mass, which further strains the ability of pyrolysis to create value-added products as part of a circular economy.

1.3.4 Solvent-Based Purification of Plastic Waste

Solvent-based purification (SBP) of polymers has also been explored as a closed-loop recycling method to either recover a desired polymer in whole or to produce polymer components suitable for re-polymerization. Extraction of polymers from mixtures by leveraging differences in solubility is well established[25] and has recently been studied for the recycling of PET, polylactic acid, and PVC.[26] Moreover, some reports exist demonstrating how solvent-based purification can be used to isolate polyolefin materials from waste plastics. It was shown that xylene at 85 ^{o}C can dissolve LDPE without dissolving PP. From this mixture, PP was filtered out and PE was then precipitated out with a propanol antisolvent (99% recovery, 3 kg scale).[27] Additionally, a dissolution/reprecipitation method can be used to recover LDPE, HDPE, and PP from various toluene, hexane, and/or xylene solutions.[28] Importantly, SBP requires large amounts of organic solvent, the production of which may be energy intensive and environmentally harmful.[28] Additionally, SBP is not effective at processing multi-layer plastics, but can only isolate the components of physical polymer mixtures. As a result, it currently competes with existing separation technologies such as infrared sorting, where it is not cost competitive.[26] Nevertheless, several commercial initiatives are underway to execute this technology at scale. The PureCycle process developed by Proctor and Gamble, for example, uses solvent dissolution to recover polypropylene materials.[29] Comparable technologies, such as APK AG's Newcycling® process and Fraunhofer's CreaSolv® process, are also being developed to target multi-layer plastics.[29]

1.3.5 Catalytic Hydrogenolysis of C–C bonds

Catalytic hydrogenolysis is a technique in which carbon–carbon and carbon–hetero atom bonds[30] in organic molecules are selectively cleaved by a supported metal catalyst in an abundance of H_2.[7,31] The mechanism of this process over Pt, Rh, and Ir nanoparticle catalysts for C_2–C_{10} alkanes has been studied in depth (**Figure 1.3**).[32,33,34] It has been proposed that *n*-alkane hydrogenolysis rates and bond cleavage selectivity can be described via a series of elementary steps, one of which is the rate-limiting cleavage of a carbon–carbon bond. While this carbon–carbon bond cleavage has a large enthalpic cost, the formation of gaseous H_2 produces an entropy increase that drives the reaction.[32] Increasing *n*-alkane length significantly increases the rate of hydrogenolysis,[32] likely because longer chains retain a much larger fraction of their entropy upon adsorption to the catalyst surface. Moreover, it was observed that for the hydrogenolysis of molecules containing primary and/or secondary carbons, carbon–carbon bond cleavage proceeds through α,β-bound intermediates that adsorb at two sites on the catalyst surface.[34] For a given intermediate, this results in the formation of three H_2 molecules, which ultimately may inhibit hydrogenolysis because H_2 competitively adsorbs at sites that may otherwise be occupied by alkanes.[34] Branched molecules, however, cannot form these intermediates and must form other species by C–H activation at nearby primary carbon atoms (e.g., α,γ- and α,δ-bound transition states), increasing the entropy and enthalpy of activation and generating more H_2 relative to α,β-bound intermediates.[32–34]

Finally, catalyst particle size also appears to impacts hydrogenolysis rates. This phenomenon is likely exacerbated by particle sintering on the support surface, which is well-established for metal nanoparticles under harsh conditions such as those employed in hydrogenolysis.[35]

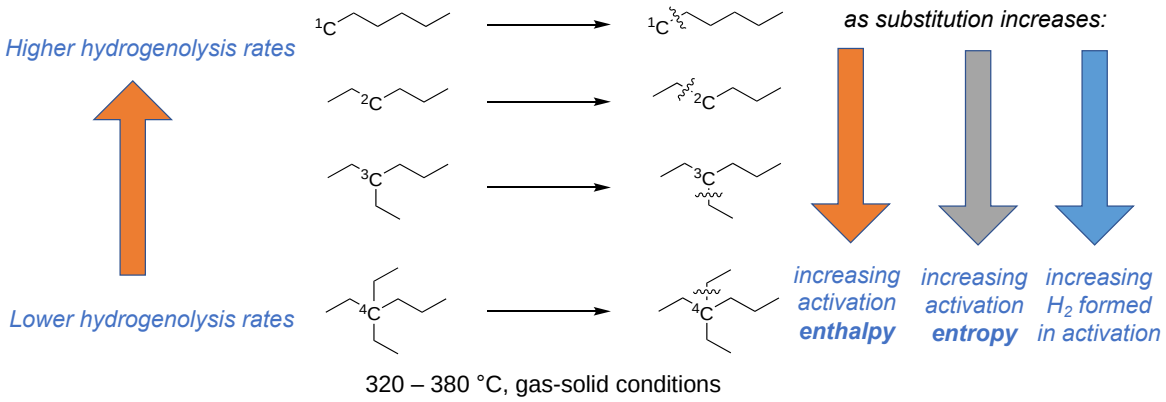

Figure 1.3. Impact of Molecular Branching on Alkane Hydrogenolysis Rates. As the degree of substitution in alkanes increases, hydrogenolysis rates become lower. This increase in substitution is associated with increases in activation enthalpy and entropy, as well as increases in H_2 formed in molecular activation based on proposed elementary steps. Created based on data reported in Refs.[32–34]

In the development of catalytic upcycling methods for use in a circular economy it will be important to translate the knowledge gained about small molecule hydrogenolysis to equivalent processes for macromolecules. Some examples of such conversions (e.g., **Figure 1.4**) have already been reported for polyolefin molecules (polyethylene and polypropylene), which bear many structural similarities to alkanes. These hydrogenolysis reactions have been conducted in solvent-free conditions to prevent spurious side reactions between the hydrogenolysis catalyst and solvent molecules. The solvent-free polymer melt is processed in an abundance of H_2 (20–200 psi) at moderate temperatures (up to 300 °C) over a Pt or Ru catalyst supported on a metal oxide (e.g., TiO_2,[36] SiO_2,[36–38] Al_2O_3,[7,36] tungstated zirconia,[39,40] perovskites,[7,41,42] zeolites[38])[31] or amorphous carbon.[43,44] The products of these reactions are typically liquids and waxes with straight-chain, alkane-like conformations, with backbones that typically number 10–100 carbon atoms (**Figure 1.4, Table 1.1**).

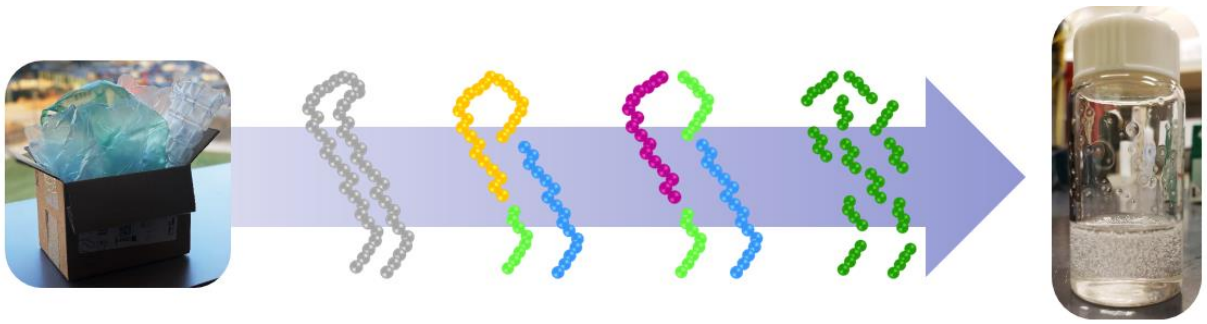

Figure 1.4. Progression of Hydrogenolysis Reaction from Starting Polymer to Final Liquid Product. Polyolefin hydrogenolysis will require cleavage of bonds in polymeric structures (e.g., those found in waste plastics such as packaging) to afford shorter chain liquid products. These processes are similar to those studied in Refs.[32–34]

Table 1.1. Select Summary of Supported Catalysts Recently Tested for Polyolefin Hydrogenolysis, Associated Reaction Conditions, and Final Reaction Products. For each report, the catalyst, support, hydrogenolyzed polymer, reaction conditions (time, temperature, loading by weight), yield to liquid products, and corresponding references are presented below.

Catalyst	Support	Polymer(s)	Temp. (°C)	Time (h)	Loading (%)	Yield (%)	Ref.(s)
Ru	Carbon	PE, PP	200, 225	16	5	> 45	[43,44]
Ru	TiO_2	PP	250	16	5.9	> 66	[36]
Ru	CeO_2	PP	250	16	4.8	6.8	[36]
Ru	CeO_2	PE	200	5	5	77	[45]
Ru	SiO_2	PP	250	16	4.9	23.6	[36]
Ru	Al_2O_3	PP	250	8	5.1	44.7	[36]
Ru	BEA	PE	200	16	5.0	> 50	[38]
Ru	FAU	PE	200	16	5.0	> 40	[38]
Pt	$SrTiO_3$	PE & PP	300	24–96	0.5–10	> 80	[7,41,42,46]
Pt	Al_2O_3	PE	300	18	1	0	[7]
Pt	WO_x/ZrO_2	PE	300	24	0.5	60	[39]
Ni	SiO_2	PE	300	2	15	65	[37]
Co	ZSM-5	PE & PP	250	20	5	< 5	[47]
Zr	AlS	PE & PP	200	0.8	15	> 99	[48]
Zr	$mSiO_2$	PE	300	20	4.7	86	[49]
Ta-H	SO_4/Al_2O_3	PE	150	15	3	< 30	[50]

In polymer hydrogenolysis, ruthenium catalysts are often selected because they appear to be more active than Pt, and often yield final product distributions centered at lower molecular weights. For example, a Ru/C catalyst converted polypropylene (PP) to an alkane product distribution centered between C_5 and C_{32}, with the average product size of a sample depending largely on reaction parameters.[26] The higher activity of Ru catalysts for hydrogenolysis increases terminal C–C bond cleavage, leading to methane formation and hindering production of value-added liquid products.[44,45] However, some Ru-supported catalysts do not exhibit this behavior. For example, Ru/TiO_2 catalysts were found to convert polypropylene samples into oils with carbon centers between C_{50} and C_{70}, while catalysts such as Ru/SiO_2 and Ru/CeO_2 produced predominantly C_1–C_6 alkanes (yields of 65.3% and 97.8%, respectively).[36] Ru/Al_2O_3 produced a lower relative amount of C_1–C_6 alkanes, although this is likely due to lower activity of the catalyst for hydrogenolysis. While the different rates of methane formation may be attributable to features such as support effects and ruthenium particle size, they are overall not well understood.[36,38,43,44]

Platinum catalysts are used for hydrogenolysis because they appear to be more selective than comparable ruthenium-supported catalysts. Indeed, Pt catalysts such as $Pt/SrTiO_3$ have hydrogenolyzed a variety of polyethylene (PE) and PP samples of varying molecular weights (3,000 Da < M_n < 160,000 Da) to liquid and wax products with very low dispersities ($Đ$ = 1.1 for almost all samples). The average sizes of the final product range from around C_{20} for polypropylene samples with starting molecular weights around 4000 Da to C_{70} averages for high-density polyethylene samples with starting molecular weights around 35,000 Da.[7,41,42,46]

To improve the underlying economics of hydrogenolysis, it may be desirable to use earth-abundant metals such as nickel in place of more expensive noble metals such as Pt or Ru. Recently, Ni supported on SiO_2 has been identified as a potential upcycling catalyst. Ni/SiO_2 performed comparably to some Ru- and Pt-supported catalysts, upcycling low-density polyethylene to *n*-alkanes (C_6–C_{35}) at typical hydrogenolysis conditions (300 ^oC, 30 bar H_2) with a liquid yield of 65 wt%.[37] However, further investigation into this and analogous supported nickel catalysts is required to determine which plastics can be hydrogenolyzed and what range of final products can be obtained. Beyond nickel, other earth-abundant metal catalysts such as cobalt and zirconia have also been explored for waste plastic

hydrogenolysis. For example, a cobalt catalyst supported on the zeolite ZSM-5 was reported to hydrogenolyze both polyethylene and polypropylene to propane with 80% selectivity by weight at 523 K and 40 bar H_2 after 20 hours.[47] By contrast, bulk cobalt and cobalt nanoparticles are highly selective for methane production in the same reaction (> 95% by weight). This difference can be attributed to the stabilization of Co on the zeolite support, which prevents further reduction to the metallic species that appears to favor methane formation.[47]

Amorphous zirconia nanoparticles between platelets of mesoporous silica also selectively upcycle polyethylene (M_n = 20,000 Da) into products with a narrow distribution centered around C_{18}.[49] Zirconia in other forms, such as a supported organometallic zirconium catalyst on highly Brønsted acidic sulfated alumina, also converted linear and branched polyolefins to hydrocarbons centered between C_{12} and C_{18} depending on reaction conditions and polymer identity.[48] Finally, tantalum has also been studied as a hydrogenolysis catalyst. A cationic tantalum hydride compound supported on sulfated aluminum oxide converted HDPE waste to C_1–C_{28} alkane products under hydrogenolysis conditions, while also producing a high molecular weight fraction (M_w = 6.2 kDa, $Đ$ = 2.3) and C_{13}-C_{32} alkane products under metathesis conditions.[50]

1.3.6 Choosing Supports for Hydrogenolysis

Beyond choice of catalyst, there are several properties of catalyst supports, such as stability and morphology, that can influence catalyst performance in polyolefin hydrogenolysis. One such property is the presence of metal acid sites on the support surface, which promote hydrocracking activity and can help suppress the formation of light gases and other products derived from terminal C–C cleavage. For example, Ru catalysts supported on acidic supports, such as the zeolites FAU (faujasite framework, Si/Al 2.55) and BEA (beta framework, Si/Al 12.5), can promote the formation of liquid alkanes because of selectivity towards non-terminal C–C bond cracking.[38] Additionally, Pt supported on WO_x/ZrO_2 was studied for PE hydrogenolysis at 250 ^oC and 30 bar H_2 and found that the metal–acid balance on the support surface significantly influenced the final hydrogenolysis products.[39,51] In theory, such an approach

can be used to exert fine control over the hydrogenolysis of various polymers into target products. Similar phenomena have also been observed for γ-Al_2O_3 supports. For example, a physical mixture of SnPt/γ-Al_2O_3 and Re_2O_7/γ-Al_2O_3 was active for the tandem dehydrogenation and olefin cross metathesis of polyethylene. [52]

Hydrogenolysis catalyst supports can also be selected for their reusability and impact on overall activity without promoting tandem processes. The previously mentioned Ru/C system, which hydrogenolyzes polyethylene samples ($M_w \approx 4000$ Da) into liquid alkanes with yields up to 45% by mass, is an example of this.[44] In addition to its widespread commercial availability and relatively low cost, an attractive feature of the Ru/C catalyst is its stability under a flow of *n*-dodecane, which would be desirable in a commercial process based on this reaction. For these reasons, Ru supported on CeO_2 is also an effective and reusable catalyst for polyolefin hydrogenolysis.[45] Ru/CeO_2 has higher activity and selectivity than other supported-Ru catalysts, likely because CeO_2 is a basic metal oxide with comparatively strong Lewis base sites. These sites can strongly interact with metal particles, which may lead to the formation of relatively smaller Ru nanoparticles on the support surface.[45] The CeO_2-supported Ru catalyst was also found to be reusable for five catalytic runs.

1.4 Pt/STO AS A HYDROGENOLYSIS CATALYST

Catalyst supports can also be selected for their well-defined morphologies. Strontium titanate ($SrTiO_3$ / STO) is such a catalyst and has an established track record of use across a variety of catalytic reaction spaces because it is highly ordered, crystalline, and has well-defined particle morphologies.[7,45,53,54,55] In 2019, a study was published detailing how Pt nanoparticles supported on $SrTiO_3$ nanocuboids (Pt/$SrTiO_3$; Pt/STO) selectively transform polyethylene materials into value-added products in solvent-free conditions at 300 °C under 170 psi H_2 (**Table 1.2**).[7] The materials tested included a variety of pre-consumer high-density polyethylene (HDPE) samples ($8 < M_n < 158$ kDa) as well as a commercially sourced, single-use plastic bag ($M_n = 31$ kDa), and the final products had average molecular weights centered at C_{70} with narrow dispersity ($Đ = 1.06$). Small amounts of gaseous hydrocarbons (C_1–C_8) were produced and no

coke formation was observed. By contrast, commercially available Pt/Al_2O_3 gave products with broad ranges in molecular weight and substantial formation of both light gases and C_1–C_8 alkanes. In this work, it was observed that the final M_n of the upcycled product was inversely proportional to conversion and influenced by Pt particle size, with smaller particles appearing to generally be more active for hydrogenolysis. Solid-state nuclear magnetic resonance spectroscopy and density functional theory (DFT) calculations demonstrated that polyethylene adsorption is more favorable on Pt sites than on the STO support, which likely contributes to catalyst selectivity.[7]

Table 1.2. Number-Averaged (M_n) and Weight-Averaged (M_w) Molecular Weights, and Dispersities of Initial and Final Polyethylene Products Hydrogenolyzed by a $Pt/SrTiO_3$ Catalyst Synthesized with Five Cycles of Atomic Layer Deposition. Reproduced from Ref. [7]

Material	M_n (Da)	M_w (Da)	$Đ$
Initial	8150	22,150	2.7
Final	590	625	1.1
Initial	15,400	17,200	1.1
Final	660	700	1.1
Initial	64,300	70,400	1.1
Final	800	920	1.2
Initial	158,000	420,000	2.7
Final	820	960	1.2
Plastic bag	33,000	115,150	3.5
Final	990	1130	1.3

Several features of the Pt/STO catalyst make it an attractive option for polyolefin upcycling. First, owing to a close lattice match between FCC Pt and the {100} facet of STO, Pt nanoparticles exhibit a cube-on-cube epitaxy with STO nanocuboids, which provides stabilization against sintering under the harsh conditions required for catalytic hydrogenolysis.

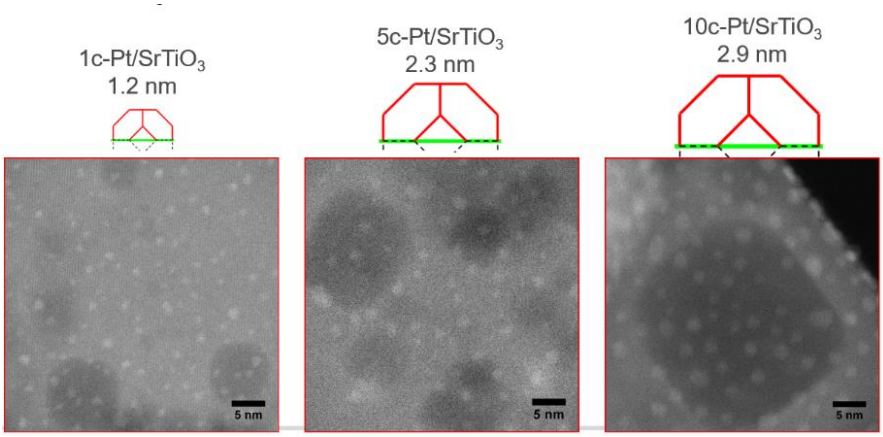

Figure 1.5. Images and Pt Particle Size Measurements of Pt/STO Catalysts Synthesized Through 1, 5, and 10 Cycles of Atomic Layer Deposition (ALD). Pt loading on the STO surface generally increases with additional cycles of ALD, and Pt particle sizes range from 1.2 nm on average after 1 cycle to 2.9 nm on average after 10 cycles. Adapted from Ref. [7].

Because of cube-on-cube epitaxy, Pt nanoparticles adopt well-understood Winterbottom constructions on the STO surface, with a measurable ratio of corners, edges, and facets for a range of particle sizes (**Figure 1.5**). Moreover, this stabilization ensures that there is minimal change to the Pt particle properties after catalytic use (**Figure 1.6**). It has been shown that Pt/STO catalysts can be used consecutively for polyolefin upcycling for at least five hydrogenolysis runs and likely longer with minimal change to product properties and without any reactivation steps.[41] Additionally, epitaxial stabilization makes reactivation of the catalyst more straightforward, because high temperatures can be used to remove carbonaceous buildup without immediate changes to the physical properties of the Pt catalyst. These features, among others, have driven further investigation into (1) the synthesis of the STO nanocuboid support; (2) the deposition method for decorating Pt onto the STO surface; and (3) scale-up of both the support synthesis and deposition method. Moreover, the potential industrial viability of the Pt/STO catalyst has stimulated tribological studies to determine if the products of Pt/STO hydrogenolysis are indeed commercially viable.[56]

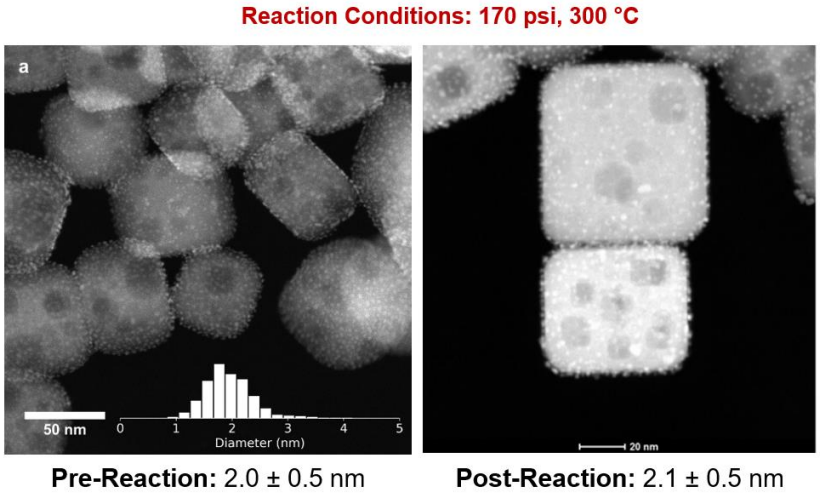

Figure 1.6. Images of STO before and after hydrogenolysis reaction under 170 psi H_2 at 300 ºC. Pt particle size was generally equivalent before (2.0 +/– 0.5 nm) and after (2.1 +/– 0.5 nm) hydrogenolysis, suggesting that minimal sintering occurred during reaction.

1.4.1 Effect of Polymer Structure on Hydrogenolysis

After testing of Pt/STO catalysts for high-density PE hydrogenolysis, additional investigations were conducted to determine how variation in polymer feedstock affects the final product distribution.[46] Pre-consumer polyethylenes (Dow Chemical Company, Engage 8100 (M_n = 50,950, Đ = 2.1), Engage 8200 (M_n = 33,950, $Đ$ = 2.2), Affinity 1875 (M_n = 7,600, $Đ$ = 2.4)) of varying macrostructures (i.e., molecular weight and branch density) as well as polypropylenes of varying macrostructure and tacticity (i.e., microstructure) were converted into lower molecular-weight liquid products and analyzed by gel permeation chromatography (GPC). For polyethylene samples, the initial molecular weight of polyethylene was found to moderately affect the yield of liquid and wax products relative to the total starting mass of polymer, with final values ranging from 55 wt% for starting polymers with $M_n \approx$ 7600 Da to up to 67 wt% for polymers with starting $M_n \approx$ 50,960 Da. However, the final liquid products themselves

appear generally equivalent in molecular weight (M_n ≈ 550 Da), polydispersity ($Đ$ ≈ 1.4), and structure (degree of branching per 1000 carbons), regardless of starting average molecular weight.

When isotactic, atactic, and syndiotactic polypropylene samples were hydrogenolyzed with a Pt/STO catalyst, the final products had average molecular weights centered at C_{18} ($Đ$ ≈ 1.4), C_{64} ($Đ$ ≈ 1.0), and C_{54} ($Đ$ ≈ 1.0), respectively. These differences are likely due to variations in methyl group stereochemistry on each starting polypropylene sample. The arrangement of these groups dictates the shape and structure of the polymer melt, which in turn affects how the hydrocarbon chain interacts with the catalyst surface and impacts how many carbon–carbon bond scissions occur during reaction.

Interestingly, when a mixture of both LDPE and PP was hydrogenolyzed by Pt/STO, the resulting product had no characteristics uniquely attributable to either starting polymer (**Figure 1.7**). This suggests that for some plastic feedstocks, extensive separation of raw materials is not necessary prior to conversion by Pt/STO, removing an obstacle towards future commercialization. This stands in contrast to other processes, such as pyrolysis, which may require extensive separation prior to treatment to ensure that harmful byproducts are not formed during the recycling process.

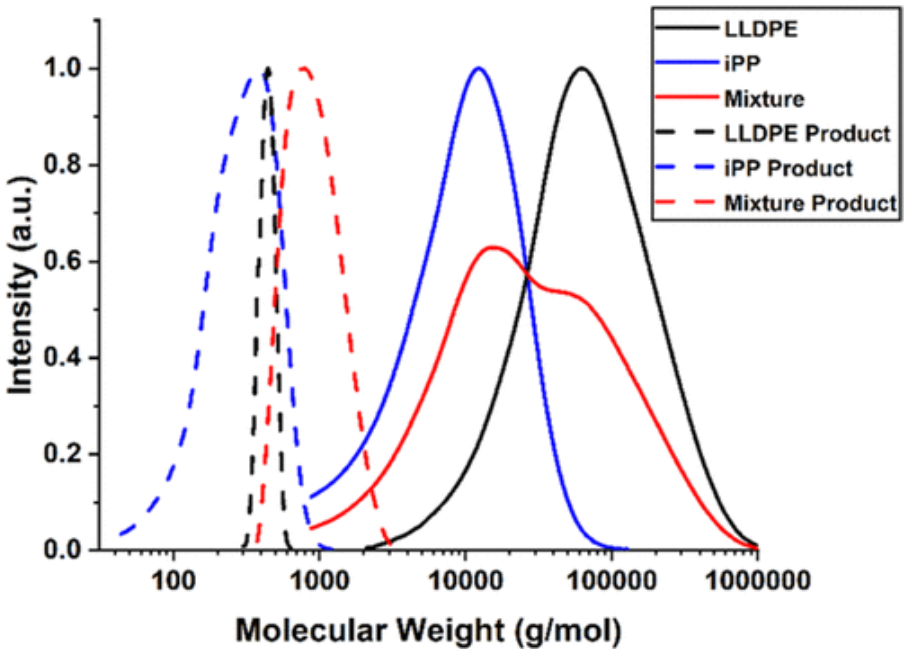

Figure 1.7. Molecular Weight Distributions of Starting LLDPE, iPP Polymers, and an LLDPE-iPP Mixture along with Upcycling Products for Hydrogenolysis of Both Pure Starting Polymers and Their Mixture. The average size of the hydrogenolysis products from the iPP and LLDPE mixture is noticeably larger than that for each individual component. It is possible that dynamics and viscosity of the mixed system slow the overall rate of hydrogenolysis. Reproduced from Ref. [46]

1.4.2 Tribological Applications for Select Upcycling Products

One potentially attractive application of hydrocarbon oils derived from polyolefins is as a component in automotive lubricants. Lubricants are comprised of base oils, which are responsible for most of their friction-reducing properties, as well as additives that both extend material stability and longevity and fine-tune properties for optimal lubricant performance in a desired application.[57] Currently, most lubricants are petroleum-based distillates, and the base oils that comprise these lubricants are classified into four groups. Group I base oils are the cheapest available: they are solvent-refined, which is less expensive than other processing methods, have higher sulfur content, a lower percentage of saturates, and a viscosity-index range from 80 to 120. Group II base oils, which are derived from hydrocracking, are more

expensive, but have the same viscosity-index range as Group I. However, because of the different processing method, they have a higher percentage of saturates (> 90%) and a lower sulfur content. Group III base oils, the most expensive naturally derived base oils, have properties generally equivalent to those of Group II oils, but have a higher viscosity-index range (> 120). Finally, Group IV base oils are fully synthetic oils comprised of poly-α-olefins (PAOs), obtained via selective oligomerization of long-chain α-olefins. They have wide-ranging properties but are primarily desired in applications with extreme cold or heat. All other base oils are classified as Group V base oils.

In a tribological study, a variety of synthetic PAO molecules and Pt/STO-derived hydrogenolysis products (starting materials: HDPE with $M_w \approx 35$ kDa and $M_n \approx 7.7$ kDa; LLDPE; commercially sourced bubble wrap) were subjected to ball-on-disk tribological testing, and lubricating ability as a function of wear-scar volume and coefficient of friction were measured.[56] It was found that a blend of PAO10 and liquid products derived from waste plastics in an 80:20 ratio most significantly reduced friction between contacting metal surfaces (**Figure 1.8**). This may be because larger PAO10 molecules are pushed out from the mixture at the contact point, creating a concentration gradient and diffusion of upcycled liquids to the bulk mixture. This phenomenon enhances fluidity and reduces friction. Importantly, these results demonstrate that lubricants derived from waste plastics can be readily incorporated into existing lubricant packages, and thus initiatives to sustainably synthesize various commercial products can be accomplished while leveraging existing industrial infrastructure.

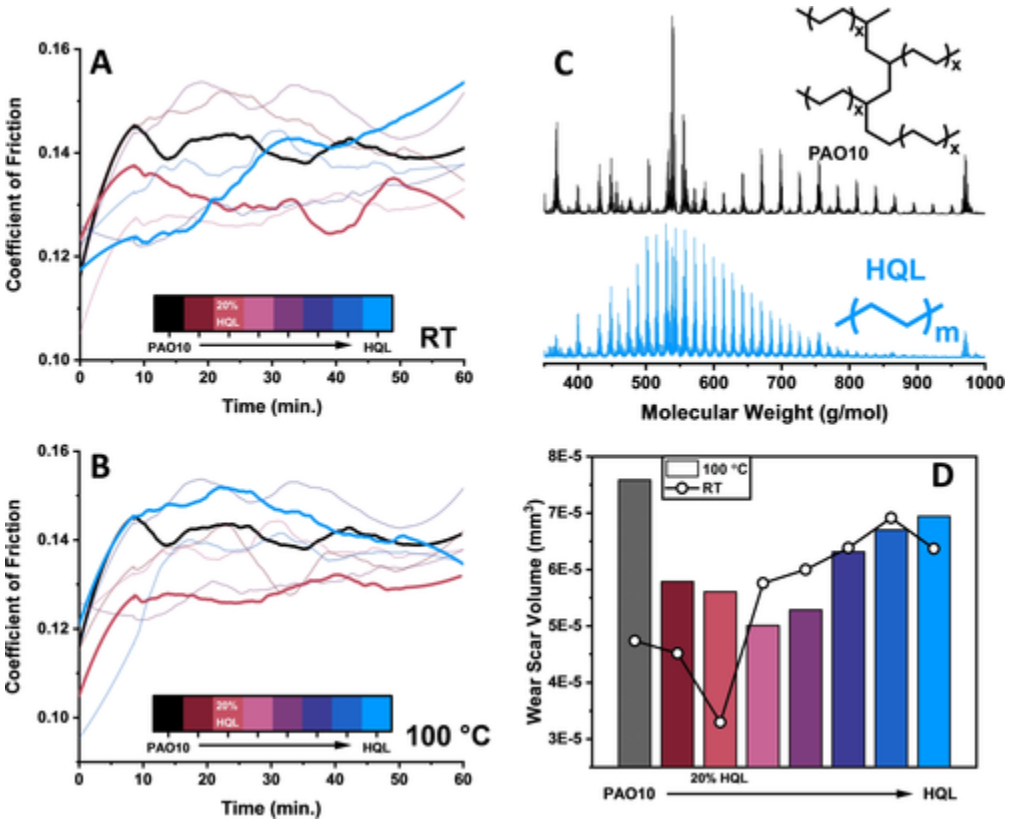

Figure 1.8. Tribological Testing Results for Mixtures of Commercial Lubricants and Plastic-Derived Lubricant Products. Coefficient of friction plots were tested for various mixtures of plastic-derived lubricants and commercial lubricants at room temperature (A) and 100 °C (B). The molecular weight distributions of PAO10 and plastic-derived lubricants were determined by MALDI mass-spectrometry (C). Wear scar volume was measured for these mixtures, and it was found that mixtures of commercial lubricants and plastic-derived lubricants were most effective at reducing wear scar at room temperature and 100 °C (D). Reproduced from Ref. [56]

1.4.3 Techno-economic Analysis and Lifecycle Assessment for Lubricant Production

To effectively participate in a circular economy, technologies such as catalytic hydrogenolysis will need to comply with emissions targets established by local, national, and global guidelines.[11,58] Some of these targets will require extensive decarbonization and have not yet been implemented widely. For example,

as part of broad efforts to reduce greenhouse gas emissions globally by 2050, companies with operations in the United States may soon be required to address Scope 3 emissions, i.e., emissions for greenhouse-gas outputs that are not directly associated with assets possessed by an organization but are still part of the organization's value chain. Although legislation at the U.S. federal level, such as the "Inflation Reduction Act," will aid this through tax credits and other incentives for climate technology development, technologies such as upcycling must be designed with both economic viability and sustainability in mind.[11] Thus, to assess the economic viability of Pt/STO polyolefin upcycling, a preliminary industrial process was modeled and a techno-economic analysis was conducted (**Figure 1.9**).[59] Based on this conceptual design, a lifecycle assessment was conducted to predict hypothetical emissions associated with the conversion of a variety of waste polyolefins, i.e., HDPE, LDPE, LLDPE, and PP, to lubricant products. In this process, plastic waste is first processed and pelletized before being fed into a slurry-type batch reactor preloaded with the catalyst. The reactor is then pressurized to 170 psi H_2 and heated to 300 ^oC, at which point the reaction is executed. After 24 hours, light gases and unreacted hydrogen are vented and fed to a boiler for combustion, thereby generating heating for further iterations of this process.

To extract the product and reset the reactor for future use, the liquid lubricant is pumped out of the reactor before being collected and stored. The catalyst is washed with hexane and transferred back to the reactor for another cycle, and the effluent hexane mixture is distilled to recover pure hexane and potentially recover discarded catalyst material or lubricant product. Based on this hypothetical process and established market pricing for petroleum-derived lubricant products (~$9 per gallon),[56] the profit margin on the sale of these materials can reach $5 per gallon, or around $1500 per metric ton.[56] These profits would be greater than those currently gained from the sale of pyrolysis oils and pyrolysis-derived fuels, which are around $500 and $1000 per metric ton, respectively, and are comparable to current profit margins for the sale of lubricant materials, at around $2000 per metric ton. Moreover, a preliminary lifecycle analysis of this product shows that on-site greenhouse gas emissions would total 0.7 g CO_2 per MJ, compared to 11.5 g CO_2 per MJ for petroleum-derived lubricants.

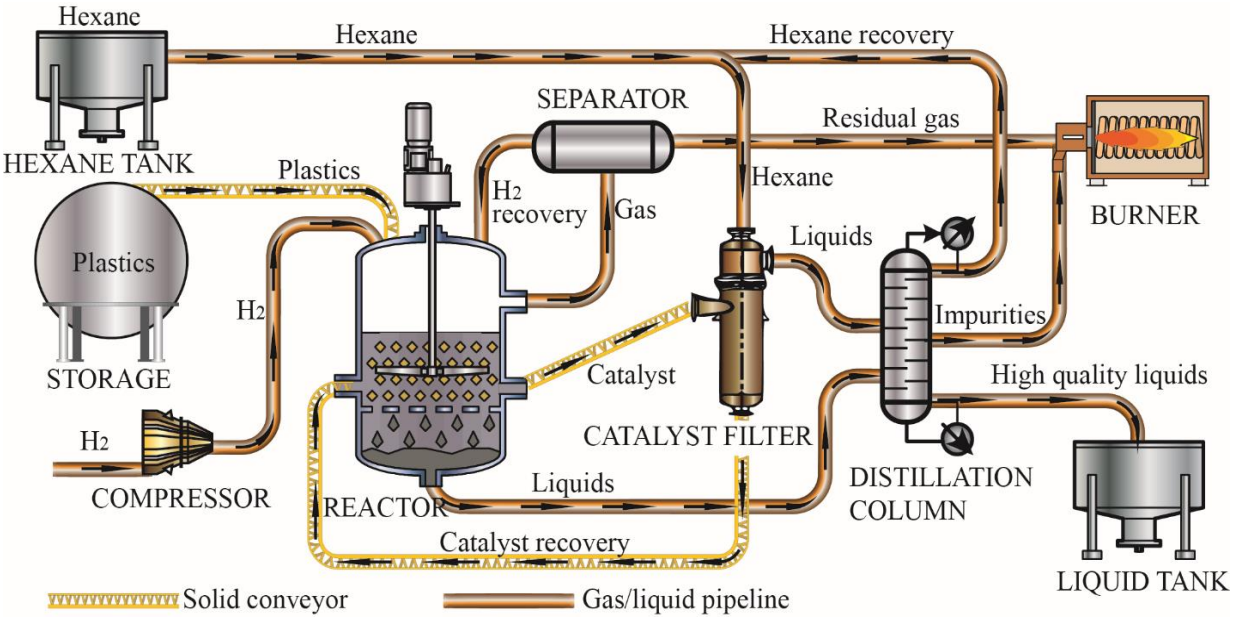

Figure 1.9. Hypothetical Pilot Plant for Waste Plastic Conversion to Lubricant Products. This model plant was used as the basis for a techno-economic analysis and lifecycle assessment of a hypothetical upcycling process based around the Pt/STO catalyst system.[56,59] Based on this model, waste-derived lubricants can be produced and sold at around $9 per gallon. This process would result in greenhouse gas emissions of 0.7 g CO_2 per MJ, compared to 11.5 g CO_2 per MJ for petroleum-derived lubricants.

1.4.4. Pt/$SrTiO_3$ Catalyst Synthesis & Scale-Up

The proven ability of Pt/STO to upcycle a variety of pre- and post-consumer polyolefins to value-added products has incentivized further study of this catalyst, the support, and their interactions, with a focus on both the mechanism behind polyolefin hydrogenolysis and catalyst optimization for specific uses.[7,46,56]

Pt nanoparticle catalysts have typically been deposited onto STO nanocuboid supports using atomic layer deposition (ALD), a gaseous technique in which volatile precursors are introduced onto a support surface in a controlled fashion (**Figure 1.10**).[54,60–62] Some initial studies of this technique focused on understanding the ALD deposition mechanism of Pt onto STO. Initial deposition of Pt precursor onto the STO surface begins when $MeCpPtMe_3$ chemisorbs onto surface hydroxyl groups and releases methane through ligand exchange to form a bound $MeCpPtMe_2$ species. The resulting structure is likely a mixture of monopodal and bipodal species, depending on whether one or two CH_4 ligands are released. Treatment of this material in an oxidizing environment results in the formation of PtO particles on the support surface.[60,63] In the subsequent ALD cycle, fresh $MeCpPtMe_3$ precursor can adsorb either on remaining support hydroxyl groups or on now available PtO species. It was proposed that $MeCpPtMe_3$ preferentially binds to hydroxyl groups and once these are all occupied one molecule of $MeCpPtMe_3$ reacts with one PtO molecule to form metallic Pt. Further treatment in an oxidizing environment causes Pt particle coalescence, decreasing dispersion and increasing average particle size.[63] Owing to their lower surface area, STO nanocuboid support surfaces appear to saturate after less exposure to $MeCpPtMe_3$ than required for supports such as γ-Al_2O_3 or TiO_2, driving formation of metallic Pt and resulting in higher loading and more particle growth. Thus, successive cycles of deposition and reduction can be employed to increase average Pt particle size, which may impact the final products of polyolefin hydrogenolysis.[7,41] Through such synthesis techniques, Pt/STO catalysts can be rationally designed to target clear ratios of Pt particle edges, corners, and facets, as well as Pt particle dispersion on the support surface, which in turn can select for desired hydrogenolysis products.

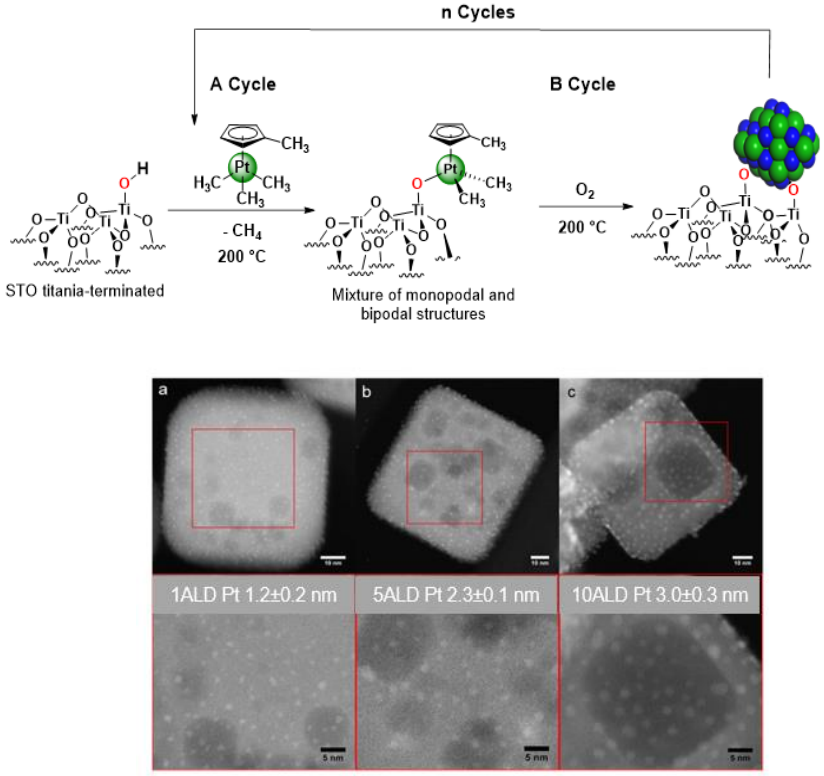

Figure 1.10. Representation of Pt/STO Synthesis by Atomic Layer Deposition (ALD). In ALD, a cycle (A) is first employed to decorate the STO surface with a $MePtCpMe_3$ precursor, after which a cycle (B) is employed to anneal away the ligands and afford bare Pt nanoparticles on the STO surface. This has been employed for up to 10 cycles to synthesize Pt/STO samples with Pt nanoparticles that range from ~1.2 nm to ~3.0 nm. Importantly, the physical properties of the installed catalyst can be controlled by controlling the number of ALD cycles. Adapted from Ref.[7]

In general, ALD is desirable for use in deposition processes because it is self-limiting, unlike analogous vapor-phase processes such as chemical vapor deposition. Each precursor reacts with a specific surface site before another precursor is introduced, meaning that uncontrolled deposition is unlikely. Based on these principles, sequential cycles of deposition and reduction can be used to control the amount of catalyst that is deposited onto the support surface. Within a particular cycle of deposition and reduction, global parameters such as reaction temperature, feed rate, and precursor reactivity can be used to control the amount of catalyst introduced as well. By carefully tuning such parameters, a variety of ALD processes have been developed to target the synthesis of materials for specific applications. Many of these materials contain 1–10 nm nanoparticles of metals such as Pt, Ru, Ni, and Pd, as well as various bimetallic combinations of noble metals and late transition metals, onto various supports.

In addition to mechanistic investigation, initial studies of ALD-derived Pt/STO targeted controlled growth of Pt nanoparticles from a $MePtCpMe_3$ precursor, with the goal of measuring their size, dispersion, and chemical state.[60,63] X-ray scattering and X-ray absorption spectroscopy were found to show a progression towards metallic platinum and an increase in nanoparticle size and spacing with successive ALD cycles.[60] It was observed that for five cycles of deposition and reduction, Pt loading increased by 2.1 % by mass for each cycle, and that the final average particle size after five cycles was 2.5 nm.[60] These catalysts were utilized for propane oxidation and differences in particle size were found to affect final conversion to product.[64]

Despite these advantages, ALD is expensive and requires specialized instrumentation, and so significant capital investments must be made to output material beyond the gram scale. Although there are commercial examples of ALD processes,[65] such investments are not readily feasible for all applications. For this reason, various solution-phase deposition techniques have been pursued as alternative methods of Pt/STO synthesis. Surface-organometallic chemistry (SOMC) has been proposed as a solution-phase deposition technique that can retain the benefits of atomic layer deposition.[41] In this process, an organometallic catalyst precursor, such as $Pt(acac)_2$ or $MePtCpMe_3$, is chemisorbed onto a support

surface in solution. Next, annealing in an oxidizing or reducing environment yields a bare catalyst metal. SOMC techniques have been used to synthesize highly dispersed, single-atom catalysts designed to mimic organometallic catalysis in heterogeneous form. These catalysts, typically early transition metals on common supports such as titania, alumina, and silica, have been used for metatheses, polymerizations, and dry reforming of methane, among others.[66]

Pt/STO catalysts were synthesized on a gram scale by depositing a $Pt(acac)_2$ precursor in toluene at 80 °C and treating the ligated sample under H_2 (**Figure 1.11**).[41] This approach was tested for three successive cycles of deposition and reduction to synthesize Pt nanoparticles with average sizes of 1.2–1.8 nm depending on the conditions employed. One such catalyst was used to upcycle isotactic polypropylene (starting M_n = 5000 Da) into liquid products with average M_n of 270 Da and $Đ$ = 1.1, with comparable performance observed across five consecutive hydrogenolysis runs. This suggests that Pt/STO catalysts can be scaled in a solution-phase process while retaining the desirable performance observed in ALD-derived catalysts.

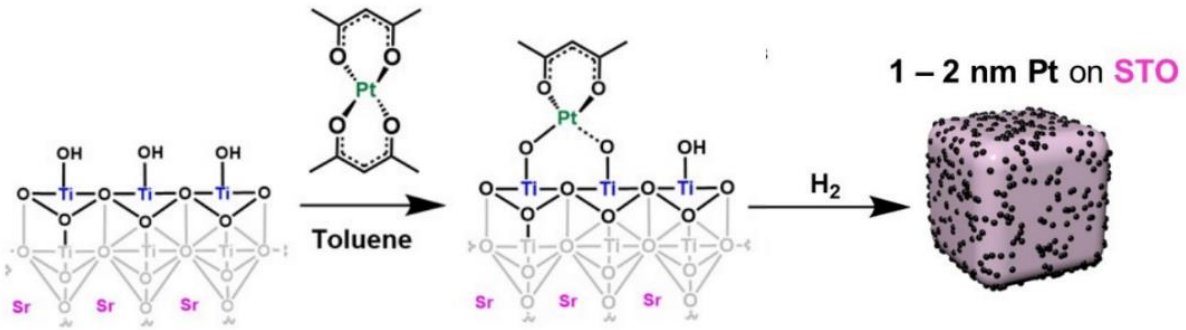

Figure 1.11. Schematic of SOMC-Derived Pt/STO Synthesis Using a $Pt(acac)_2$ Precursor. In toluene at 80 °C, $Pt(acac)_2$ was chemisorbed onto the surface of STO nanocuboid supports. The resulting structure was treated in a reducing environment to afford bare 1–2 nm Pt nanoparticles on the STO nanocuboid surface. Adapted from Ref.[41]

In developing supported nanoparticle catalysts, it may also be desirable to explore deposition techniques that are not based on covalent bonding, unlike ALD and SOMC. One strategy is incipient wetness, in which a support is loaded into a solution of an active metal precursor, and after deposition the ligated material is dried and calcined to remove the volatile components of the catalyst.[67] The simplicity of the incipient wetness method has led to its widespread use in chemical industry.[68] However, it is often difficult to control catalyst deposition, and the physical properties of deposited catalyst can vary widely from particle to particle. Some deposition methods may be able to retain both the simplicity of processes such as incipient wetness and the precision of methods such as ALD and SOMC. One candidate is strong electrostatic adsorption (SEA), a deposition method that takes advantage of the charge-dependent nature of a metal oxide support surface. By controlling solution pH, surface hydroxyl groups can be deprotonated or protonated, thereby generating charged species that electrostatically bind to an ionic catalyst precursor (e.g., $Pt(NH_3)_4^{2+}$). Subsequent treatment in a reducing environment yields bare nanoparticles on the support surface.[68,69] This method has been utilized in a proof-of-concept synthesis of 0.3 g, SEA-derived Pt/STO to afford 1.7 nm Pt nanoparticles on the STO surface.[42] Upcycling of HDPE with this material (M_n ≈ 35 kDa) affords a linear wax final product (M_n ≈ 2400 Da, $Đ$ ≈ 1.1).

1.4.5. Recent Advances in STO Support Synthesis

Independent of the demonstrated performance of Pt/STO in catalytic hydrogenolysis, the STO support itself has several properties that generally make it desirable for use in catalysis. STO, a highly ordered crystalline material with the perovskite structure, consists of alternating layers of SrO and TiO_2 stacked along the [100] direction. Its high refractive index and melting point make it resistant to transformations under catalytic conditions. At the nanoscale, STO particles often adopt morphologies with well-defined faceting, such as nanocuboids or nanododecahedra.[42,70,71] These facets have well-known surface reconstructions.[72–77] For nanocuboids, which have the Wulff shape and are terminated with the {100} facet, the $\sqrt{13} \times \sqrt{13}$ R 33.7° surface reconstruction is the most stable reconstruction in an aqueous

medium.[78] This faceting leads to clear dispersion of catalyst on the support surface, making Pt/STO an attractive model system for fundamental catalytic studies.[53,71,78,79]

Furthermore, the {100} facet of STO exhibits a lattice match with FCC Pt, which results in cube-on-cube epitaxy and stabilizes Pt on the STO surface, preventing sintering of catalyst particles during hydrogenolysis.[7,41] Previously, this cube-on-cube epitaxy has been observed in pristine Pt/STO samples and for samples studied during propane oxidation, where Pt/STO remains in well-defined Winterbottom constructions before and after reaction.[54,60,62] It has been reported that Pt/STO catalysts also resist sintering for polypropylene and polyethylene hydrogenolysis for at least five consecutive catalytic runs.[41,46]

The STO surface can be modified by altering global synthetic parameters or by using post-synthesis treatments to selectively expose either SrO or TiO_2 layers at the STO surface.[80] This affects the relative proportion of both acidic and basic sites, which can influence the final products of catalysis. This effect has been studied for STO nanocuboids of various morphologies and truncations.[81–84] For ethanol dehydrogenation and the oxidative coupling of methane,[81,83] it was found that the relative proportion of available acidic or basic sites affects conversion more than the faceting available for adsorption of catalyst or reactant material. Thus, synthetic methods can play a powerful role in tuning support properties and provide another handle by which to optimize reactions.[81–84]

STO synthesis has been closely studied over the last 30 years and numerous methodologies have been developed to synthesize a wide suite of particles with various shapes and facets.[85–88] Many syntheses utilize solid state conversion of Sr- and Ti-containing reagents (e.g., $SrCO_3$ and TiO_2) in air at temperatures between 600 ^oC and 1000 ^oC for 4 to 10 days. While straightforward, such processes require significant energetic input and often produce samples with wide variation in particle size and morphology unsuitable for catalysis.[85,86]

Many reported STO syntheses are conducted using a hydrothermal or solvothermal method, in which solution-phase Sr and Ti precursors are heated in a basic aqueous medium in a fixed volume to produce the final STO product. Such methods require milder conditions than solid-state processes, and often

afford more control over product morphology and size. For example, hydrothermal techniques were shown to be superior over molten-salt and solid-state methods in synthesizing STO nanocuboids with well-defined cuboidal morphologies and uniform average particle size.[89] Subsequently, a variety of hydrothermal and solvothermal processes have been used to synthesize STO nanocuboids; they have typically involved treatment of a Sr^{2+}/Ti^{4+} bimetallic solution in base at temperatures between 120 ^{o}C and 250 ^{o}C for up to 48 hours in fixed-volume autoclaves using convection heating. This suggests that STO nanoparticles can be synthesized from a wide suite of global synthetic parameters, likely because differences in lab-specific, equipment-specific, and process-specific parameter impact the precipitation and facet growth of nanoparticles in solution.[85,86,90–92]

In developing a commercially viable STO synthesis, it is desirable to use a more efficient heating method than convection heating to reduce the overall energetic cost needed. Microwave-assisted heating has been shown to introduce heat energy more uniformly and rapidly into a reaction mixture than convection heating, thereby impacting the temperature and time profiles required to drive chemical processes to completion.[93–100] These techniques have been used extensively for organic syntheses of small molecules, where microwave reactors afford pure final products in as little as 30 minutes.[94,97] Microwave assisted heating has also been utilized to form a variety of inorganic materials of interest, including classes of oxides, sulfides, and halides.[95,96,98] Regarding STO, it was demonstrated that STO nanocuboids can be synthesized in microwave reactor without significant change to the physical properties of the final sample (**Figure 1.12**).[70] This synthesis of STO nanocuboids was carried out under milder conditions than required when using a convection heating source and was also accomplished with the use of titanium (IV) bisammonium lactato dihydroxide (TiBALD), a water-stable replacement for $TiCl_4$.[70]

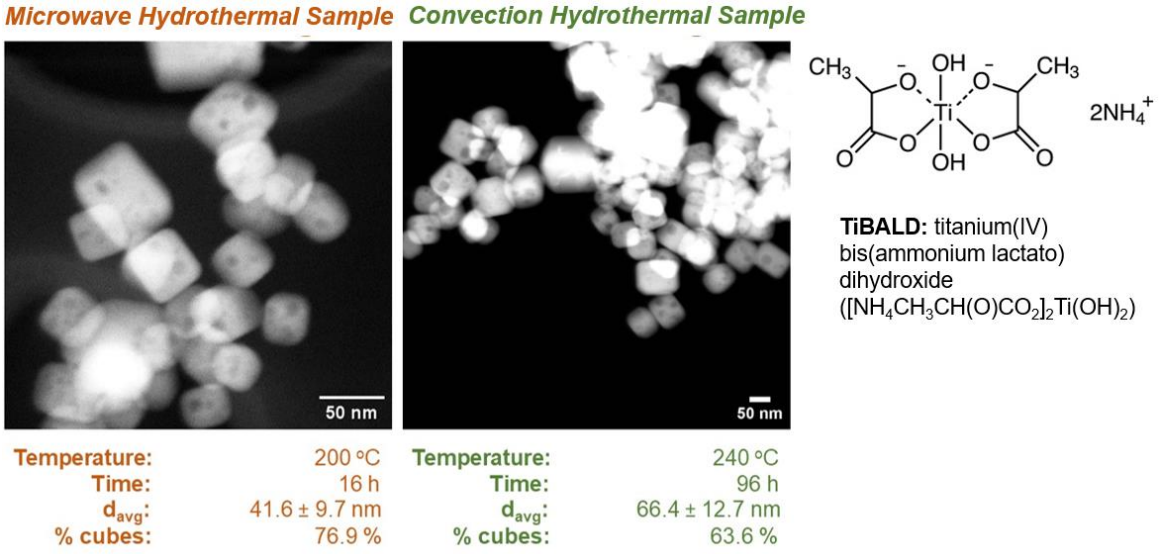

Figure 1.12. HAADF-STEM Micrographs of STO Nanocuboid Supports Synthesized Using Microwave-Assisted Heating (Left) and Convection Heating (Right). Microwave-assisted heating techniques appear to produce a higher percentage of nanocuboidal STO particles under milder conditions (200 °C, 16 h) than required for convection hydrothermal heating (240 °C, 96 h). Adapted with permission from Ref. [70]

In addition to modifications to reaction parameters, the scale of STO synthesis will need to be increased in pursuit of an eventual commercial catalyst synthesis process. Previously, a 20 gram synthesis of STO in a microwave reactor has been reported, demonstrating that these catalyst supports can be produce beyond the gram scale while retaining cuboidal character. Beyond this, other examples exist of batch-based scale-up, such as one using a stirred 4 L reactor and a convection-based heating jacket that afforded ~20 g of STO nanocuboids.[70] Some flow-based systems have been demonstrated for the synthesis of $BaTiO_3$ and $Ba_xSr_{1-x}TiO_3$ nanoparticles,[101–104] which display structural similarities to STO, suggesting that these synthetic methods could be adapted to produce STO nanoparticles. The synthesis for $Ba_xSr_{1-x}TiO_3$ produced sub-stoichiometric products at both the bench scale (5 g h^{-1}) and the pilot-plant scale (80 g h^{-1}).[105] Reference [105] utilized TiBALD as a source of Ti^{4+}, confirming that this material can be

used to scale perovskite nanoparticle syntheses.[70,106,107] Tuning global parameters, such as basicity or water-to-metal ratio influenced the composition and properties of the final product, but a one-step process was ultimately found to produce the target material. These syntheses do not select for a particular particle morphology, however, which may prove important for the preservation of desirable catalyst properties as is the case with Pt/STO. Thus, future scale-up efforts may require focus on fine-tuned control over the synthesis of catalysts and catalyst supports, while still producing material outputs that are viable for commercial use.

1.5 FOCUS AND ORGANIZATION

This Dissertation broadly studies the synthesis of STO nanocuboids and the methods by which Pt can be deposited onto these STO supports to synthesize a variety of Pt/STO catalysts. These catalysts are then used to study the upcycling of polyethylene and polypropylene into liquid products with narrow size distributions to determine which properties of Pt nanoparticle catalysts are important to waste plastic upcycling. Chapter 2 determines how previously reported STO hydrothermal syntheses that employ convection heating and TiCl4 can be modified to eliminate batch-to-batch variation such that size-controlled STO nanocuboids are consistently produced. These supports are shown to still be amenable for catalyst deposition. Chapter 3 explores explains how the choice of Sr^{2+} and Ti^{4+} sources and heating method affects Sr-Ti-OH mixture phase stability, which in turn impacts final particle morphology. Chapter 4 demonstrates how surface organometallic chemistry can be used to selectively deposit Pt onto the STO surface in a scalable fashion, and how these catalysts can then be used to upcycle polypropylene to uniform liquid products with ~20-30 carbon atom backbones. Chapter 5 demonstrates how strong electrostatic adsorption can be used to synthesize Pt/STO catalysts on large batch scales in air without specialized instrumentation, and how this catalyst can also be used to upcycle polyethylene reactants to obtain expected final liquid products. Chapter 6 shows how ALD-derived Pt/STO was used to upcycle various polypropylene samples and how these results can provide context for the upcycling results reported in Chapters 4 and 5. Chapter 7 draws conclusions from the work described in Chapters 2 through 6 and proposes appropriate directions for future study.

CHAPTER 2

Size-Controlled STO Nanocuboid Synthesis with $TiCl_4$

This Chapter was adapted with permission from "I.L. Peczak, R. M. Kennedy, R. A. Hackler, R. Wang, Y. Shin, M. Delferro, K. R. Poeppelmeier. 'Scalable Synthesis of Pt/$SrTiO_3$ Hydrogenolysis Catalysts in Pursuit of Manufacturing-Relevant Waste Plastic Solutions' *ACS Appl. Mater. Interfaces*, **2021**, *13*, 58691-58700."

2.1 ABSTRACT

An improved hydrothermal synthesis for shape-controlled, size-controlled 60 nm $SrTiO_3$ nanocuboid (STO NC) supports, which facilitates the scalable creation of platinum nanoparticle catalysts supported on STO (Pt/STO) for the chemical conversion of waste polyolefins, is reported herein. This synthetic method: 1) establishes that STO nucleation prior to the hydrothermal treatment favors nanocuboid formation, 2) produces STO NC supports with average sizes ranging from 25 – 80 nm with narrow size distributions, and 3) demonstrates how $SrCO_3$ formation and variation in solution pH prevent the formation of STO NCs. The STO synthesis was scaled-up and conducted in a 4L batch reactor, resulting in STO NCs of comparable size and morphology (m = 22.5 g, d_{avg} = 58.6 ± 16.2 nm) to those synthesized under standard hydrothermal conditions in a lab-scale 125 mL autoclave reactor. Size-controlled STO NCs, ranging in roughly 10 nm increments from the 25 nm to 80 nm, were used to support Pt deposited through strong electrostatic adsorption (SEA), a practical and scalable solution-based method. Using SEA techniques and a STO support with an average size of 39.3 ± 6.3 nm, a Pt/STO catalyst with 3.6 wt% Pt was produced and used for high-density polyethylene hydrogenolysis under previously-reported conditions (170 psi H_2, 300°C, 96h; final product: M_w = 2400, Đ = 1.03). As a well-established model system for studying the behavior of heterogeneous catalysts and their supports, the Pt/STO system detailed in this work presents a unique opportunity to simultaneously convert waste plastic into commercially viable products while gaining insight into how scalable inorganic synthesis can support transformative manufacturing.

2.2 INTRODUCTION

Owing to their critical importance in numerous industrial processes, heterogeneous catalysts and the reactions they catalyze remain one of the most actively studied areas of modern scientific research.[67,68,108] Within this field, catalyst supports have been closely studied for their ability to improve catalytic performance. These supports, typically metal oxides such as alumina or silica, are often selected for desirable physical properties such as thermal and chemical stability; they also often stabilize active catalysts on their surfaces, thus minimizing or eliminating detrimental processes such as sintering.[67,68,108] Thus, designing catalysts with superior performances requires careful investigation of both catalyst behavior, support behavior, and catalyst-support interactions.[54,109–112] In pursuit of this, model catalyst systems, with features such as high-surface area supports and clear support faceting, offer a unique opportunity to study as-yet unexplored systems in route to rational catalyst design.[67,68,108] Currently, there is significant interest in studying single-use plastic hydrogenolysis, given acute worldwide concern over plastic waste pollution. Catalytic hydrogenolysis, which can *upcycle* waste polyolefins into value-added products, is an attractive method by which to both mitigate the growing problem of plastic waste and utilize an untapped resource en route to a circular economy (**Figure 2.1**).[7,40,44,45,52,56,58,113–119]

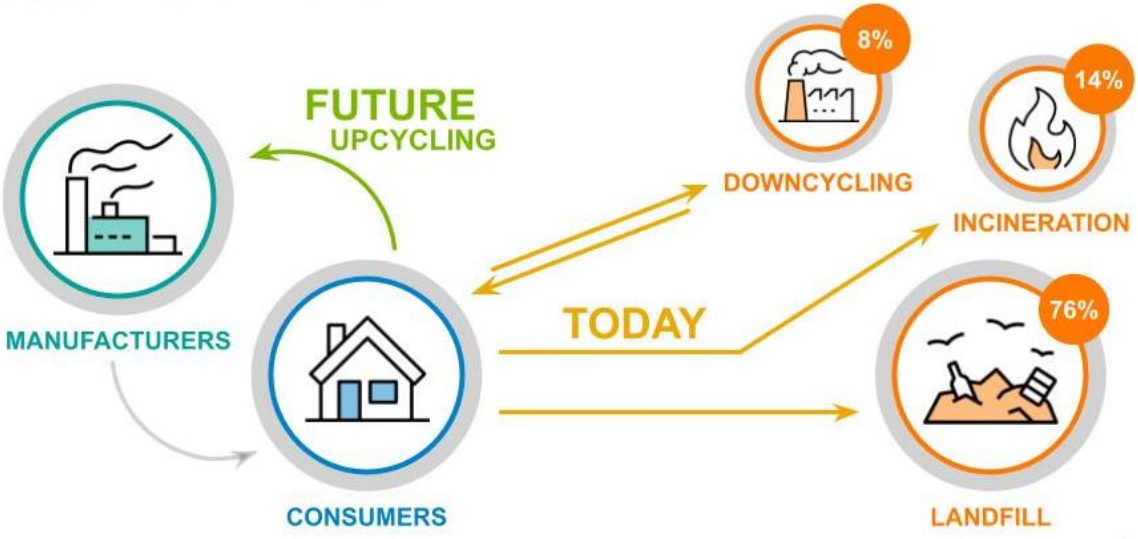

Figure 2.1. Current and Future Routes for Addressing Plastic Waste. Currently, most plastics are lost to landfills (76%), while the rest are either incinerated (14%) or downcycled (8%) to less-valuable materials. In the future, *upcycling* processes could re-direct up to 100% of post-consumer materials back to manufacturers.[113]

To that effect, Celik et al. & Hackler et al. recently investigated a system of platinum nanoparticles (Pt) deposited onto $SrTiO_3$ (STO) nanocuboids (Pt/STO) that catalyze the hydrogenolysis of high-density polyethylene (HDPE) into lubricant materials.[7,56] In addition to demonstrating superior catalytic performance to a conventional catalyst, Pt on γ-Al_2O_3, several properties of Pt/STO make it an attractive model system for catalytic study. STO nanocuboids are highly crystalline, have high thermal stability, and have well-defined {100} facets, among other properties.[7,76,120,121] Most importantly, these {100} facets exhibit a close interfacial energy match with FCC Pt, which leads to epitaxial stabilization of deposited Pt metal.[54,64,122] For these reasons and others, Pt/STO catalysts have been used to catalyze a variety of reactions such as propane oxidation and oxidative coupling of methane.[64,81–83,122] Because catalytic hydrogenolysis of polymers is both largely unexplored and potentially possesses wide-ranging economic and ecological benefits, there is strong incentive to continue studying both the Pt/STO catalyst and the STO support itself.

Previously, Rabuffetti et al. established the superiority of hydrothermal synthesis over molten-salt and solid state methods in producing STO NCs.[123] Based on that work, our group has explored the faceting, surface reconstructions, and catalyst/support interactions of a range of titanate perovskites, through the effect of metal precursors, surface directing agents (changing both surface termination and faceting), and microwave hydrothermal synthesis.[53,71,78–80,89] Other approaches have been used to control the morphology of titanate perovskite nanoparticles.[85,86,90–92,124] However, these nanoparticle syntheses can be difficult to reproduce, as the nucleation and growth processes can be highly condition-, lab-, and researcher-specific, in ways that are difficult to identify and quantify.[85,90–92]

Moreover, increasing synthetic output of STO NCs in pursuit of a commercially viable upcycling catalyst will generate additional, scale-specific challenges. First, there are several considerations that inherently complicate advanced manufacturing processes, including but not limited to: 1) demonstrating atomic-level spatial and compositional control of materials while producing at manufacturing-relevant scales; 2) tailoring processes to meet machining constraints, and 3) utilizing pathway engineering to prevent the formation of undesirable design modalities, e.g. non-target particle morphologies. Furthermore, several challenges specific to lubricant production must also be considered. For example, firms often have product-specific demands for plastic feedstocks that are not shared broadly, creating demand for varied

raw materials with differing yet equally narrow specifications. Furthermore, switching to recycled feedstocks will likely also require retooling factory equipment to account for feedstock property changes and thereby reduce the economic incentive for use of recycled materials. In total, these myriad concerns regarding both catalyst and lubricant production demonstrate the need for a catalyst synthesis method that exhibits control over STO NC physical properties (i.e. surface area, particle morphology), retains the potential to be scaled in a straightforward manner, and produces a highly-uniform upcycling product that can meet stringent manufacturer specifications.[4,125]

Herein, we report an STO hydrothermal synthesis that identifies parameters whose control is critical to the formation of nanocuboids, produces STO samples with at least 80% NCs, and explains the impact of secondary phases such as $SrCO_3$ on the formation of the primary STO NC phase. The order of addition of solutions during the creation of the Sr-Ti-OH pre-hydrothermal mixture has been investigated to determine how it can lead to the formation of either NCs or irregularly shaped nanoparticles. Through analysis of pre-hydrothermal Sr-Ti-OH particles, a dependence of hydrothermal formation of STO NCs on both the phase and size of the precursor particles was also noted. Additionally, shortening Sr-Ti-OH mixture stir time was shown to potentially decrease $SrCO_3$ formation. These modifications were incorporated into the synthetic method, and STO NCs with average sizes ranging from 25 to 80 nm with equivalent nanocuboid morphologies were synthesized by modifying the concentrations of reagents. In pursuit of synthetic scale-up to industrial scale, these STO supports were synthesized in a 4L batch reactor. The resultant STO NCs are comparable in average size and morphology to those synthesis herein in a 125 mL autoclave reactor, suggesting that with the modifications reported in this work, further scale-up of the reaction is likely attainable.

Due to the inherent limitations of scaling up atomic layer deposition, which Celik et al. and Hackler et al. utilized to generate Pt/STO catalysts,[7,56] solution-phase deposition methods were explored to find a process that can both retain some of the precision of atomic layer deposition and provide a clear path towards use on a manufacturing-relevant scale. To that effect, Pt/STO catalysts were synthesized through strong electrostatic adsorption (SEA), a charge-mediated, solution deposition method capable of depositing small Pt nanoparticles in a controlled fashion.[126,127] These Pt/STO catalysts have been tested

for HDPE hydrogenolysis and produced wax products that, while larger than those observed by Celik et al., have very low dispersity and high uniformity.

2.3 EXPERIMENTAL

2.3.1 MATERIALS AND INSTRUMENTATION

2.3.1.1 POWDER X-RAY DIFFRACTION. Diffraction experiments were conducted on a Rigaku Ultima powder x-ray diffractometer and analyzed using JADE software (Materials Data, Inc.). In preparation for analysis, solid samples were ground with a mortar and pestle. Gel aliquots were collected and spread flat on the PXRD sample holder. Crystallite size was obtained via peak broadening analysis in MDI JADE. Peak broadening was calculated via the Scherrer equation for each peak in the diffraction pattern and an average of values for the sample was taken.

2.3.1.2 ELECTRON MICROSCOPY. Nanoparticle imaging was conducted by transmission electron microscopy, using a Hitachi H8100 TEM, Hitachi HD2300, and FEI Talos F200X TEM/STEM, all operated at 200kV. These microscopes were used in coordination with the NU Atomic and Nanoscale Characterization Experimental Center at Northwestern University and the Center for Nanoscale Materials at Argonne National Laboratory. In preparation for analysis by electron microscopy, gel and solid samples (~20mg) were sonicated in ethanol (10mL) for 15 minutes. The resulting suspension was dropcast onto a lacey carbon TEM grid (Ted Pella, Inc., UC-A on Lacey 400 mesh Cu).

2.3.1.3 ELECTRON MICROSCOPY ANALYSIS. Particle size and shape were measured using ImageJ and Gatan Digital Micrograph software.[128] The face-to-face distance between opposing [100] faces of STO nanocuboids was used as a measure of particle width. Particle rounding was measured by inscribing a circle in the corner of a STO nanoparticle such that the circumference of the resulting circle traced the nanoparticle corner.[129] The radius of this circle was then used as a means of comparing corner rounding (**Figure 2.2**).

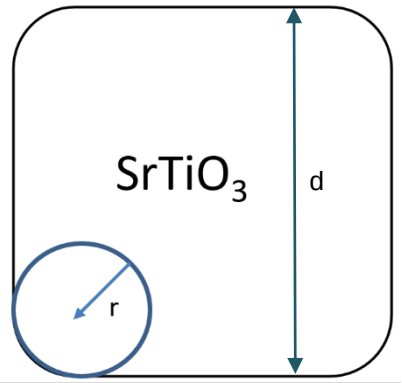

Figure 2.2 . Visual Representation of Corner Rounding Measurements for STO Nanoparticles. This method was adapted from measurements of corner rounding in supported gold nanoparticles, reported by Alpay and co-workers.[129]

2.3.1.4 HDPE HYDROGENOLYSIS. A Parr reactor and a high-throughput screening pressure reactor (SPR; Unchained Labs) at the Argonne National Laboratory's High-Throughput Research Laboratory were used for catalytic activity experiments. Activity experiments were performed under solvent-free conditions at 170 psi and 300 °C, unless otherwise noted. For the Parr reactor, the conditions were 300 mg Pt/STO, 3 g HDPE, Sigma Aldrich, M_w = 35 kDa, Đ = 3.11, 300 °C, 170 psi H_2, 96 h, with a glass liner in the reactor, as per Hackler et al.[56]

2.3.1.5 GEL PERMEATION CHROMATOGRAPHY. Samples were analyzed by GPC per Hacker et al [22]. HQL samples from hydrogenolysis of HDPE were analyzed for molecular weight (M_n and M_w) and molecular weight distribution (M_w/M_n) by high-temperature gel permeation chromatography (Agilent-Polymer Laboratories 220). 1,2,4-tricholorbenzene (TCB) containing 0.01 wt% 3,5-di-tert-butyl-4-hydroxytoluene (BHT) was chosen as the eluent at a flow rate of 1.0 mL min^{-1} at 150°C. Lubricant samples were prepared in TCB at a concentration of approximately 2.0 mg mL^{-1} and heated at 150°C for 24h prior to injection.

2.3.1.6 NOTE. All glassware was washed thoroughly with a weakly acidic (< 20 wt%) HCl solution and de-ionized water prior to use. Stir bars were stored in a weakly acidic HCl solution and thoroughly rinsed with de-ionized water prior to use.

2.3.2 SYNTHESIS

2.3.2.1 PRECURSOR SOLUTIONS

Solution A: As-received $Sr(OH)_2 \cdot 8H_2O$ (2.55 g, 10.0 mmol, Sigma Aldrich, 99.5%) was added to acetic acid (2.86 mL, 0.05 mol, Sigma Aldrich, 99.5%) in deionized water (20-60 mL) and stirred for 10 minutes.

Solution B: $TiCl_4$ (1 mL, 9.1 mmol, Sigma Aldrich, 99.5%) was added to ethanol (20 mL, absolute) in a 50 mL beaker via Luer Lock syringe and stirred for 10 minutes.

2.3.2.2 HYDROTHERMAL SYNTHESIS

Solutions **A** and **B** were mixed in a 100 mL Teflon beaker and stirred for approximately 10 minutes to ensure homogeneity (**Solution AB**). **AB** was combined with NaOH (10M or saturated) by addition of base-to-metal (BTM, i.e., introduction of NaOH into **AB** to form **AB-OH**) or addition of metal to base (MTB, introduction of **AB** into NaOH to form **OH-AB**) depending on the experiment. A mixture temperature 35-55^oC was observed immediately after combination of the bimetallic solution and NaOH. Sample was stirred for 10 minutes on a stir plate and transferred to a 125mL autoclave. Autoclave was treated in a Carbolite laboratory oven (1 ^oC/min ramp rate, 36h, 240 ^oC) and then allowed to cool ambiently to room temperature. The resulting white powder was washed repeatedly with deionized water via centrifuge (4500 rpm, 7 minutes) until the supernatant was pH 7, then dried in air in an oven (80^oC, overnight).

SAFETY NOTE: Combination of **AB** (pH ~4) and **OH** (pH ~14) generates heat and increases the resultant reaction mixture by 10-30^oC. When conducting this synthesis beyond the 125mL lab scale, *Slow MTB* addition should be employed to prevent rapid evolution of heat.

2.3.3 4L SCALE HYDROTHERMAL SYNTHESIS

Scale-up experiments were conducted at the Materials Engineering Research Facility, part of the Applied Materials Division of Argonne National Laboratory.

The solution concentrations were proportionally scaled for a 4 L reactor, with the concentrations of Sr, Ti, and NaOH halved relative to the liquid volume to decrease the concentration of chloride ions in the unlined Hastelloy® C-276 reactor.

Solution A: 38.69 g $Sr(OH)_2 \cdot 8H_2O$ was dissolved in a solution of 48.04 g of acetic acid and 640.00 g of H_2O under stirring for two hours.

Solution B: 27.62 g of $TiCl_4$ was dissolved in 504.96 g of ethanol for ten minutes.

Solutions A+**B** were mixed and stirred for 10 minutes in a 2000 mL Erlenmeyer flask. 276.85 g of 10 M NaOH solution was injected into the **AB** solution over 28 minutes at a flow rate of 10 mL/min using a syringe pump. The **AB-OH** solution was stirred using a magnetic stirrer at the maximum stir rate of the stir plate; no gelation was observed. After mixing and stirring, the **AB-OH** solution was allowed to sit for 10 minutes; the pH of the solution was 13.0, and sedimentation occurred.

The solution and sediment were transferred to a 4 L Hastelloy® C-276 reactor with an internal impeller and a heating jacket. The reactor was heated to 240 °C at a rate of 2 °C/min, and held for 12 hr, with a stir speed of 400 rpm. After the reaction, the reactor was cooled at a rate of 2 °C/min.

The precipitate and liquid were transferred from the reactor to a secondary container. The solution pH was 13.2 after the hydrothermal reaction. Initially the liquid was a light yellow color but changed to a dark orange with time. The precipitate was washed and dried.

2.3.4 Sr-Ti-OH MIXTURE SYNTHESIS

AB-OH or **OH-AB** was prepared and stirred for 50 minutes, while the pH of the solution was measured by pH paper at 5 minute intervals. The resulting product was centrifuged once (4500 rpm, 5min), and the supernatant was decanted. A white gel was recovered and immediately prepared for analysis by either PXRD or TEM to prevent decomposition.

2.3.5 PLATNIUM DEPOSITION

Pt nanoparticles were deposited via strong electrostatic adsorption, a charge-mediated solution process.[126,127] $Pt(NH_3)_4(NO_3)_2$ (PTA, Sigma-Aldrich, 60 mg) was added to a 15 mL glass vial containing a stir bar and STO nanocuboids (0.4 g) synthesized herein. Next, an NaOH solution (3mL, pH 11) was added to the vial and the resulting mixture was stirred for 2h. The suspension was then allowed to settle,

the supernatant was decanted, and the resulting product was dried in air overnight. This ligated Pt/STO was reduced in a tube furnace (5% H_2/N_2, 450^{o}C, 12h) to afford the final Pt/STO catalyst.

2.4 RESULTS & DISCUSSION

Batch-to-batch variation in size, morphology, and phase purity when following the synthesis described by Rabuffetti et al. led us to focus on steps in the synthesis that could lead to such variation. The metal and base mixing step (**Figure 2**) was identified as the step most likely to be sensitive to small changes. Thus, a series of modifications were made to improve the reliability of the synthesis by increasing control over said step. These changes result in a synthesis that produces >80% nanocuboids. First, 5 g of NaOH pellets was replaced by a 13 mL, 10M NaOH solution to facilitate the combination of NaOH (**OH**) and the bimetallic Sr/Ti mixture (**AB**) (**AB-OH**). Distinct orders of operation were then established for the combination of **AB** and **OH** to identify all possible pathways by which the **AB-OH** gel could be created (**Figure 2.3**)**.**

These pathways were defined as follows: addition rates were labeled either *fast* (i.e. component is added in under 5 seconds) or *slow* (component is added dropwise over the course of stirring), while the orders of addition were labeled either *Base-to-Metal* (BTM, NaOH is added into Sr/Ti), or *Metal-to-Base* (MTB, Sr/Ti is added into NaOH). **AB-OH** was synthesized under each of four possible pathways and treated hydrothermally (240 ^{o}C, 36 h).

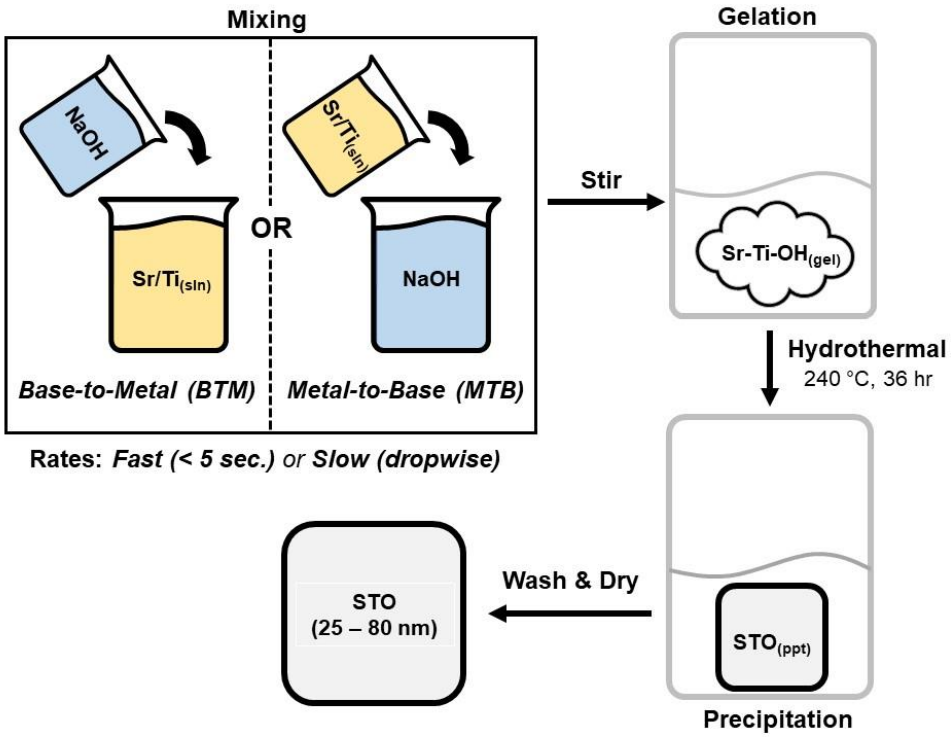

Figure 2.3. Schematic of STO NC Synthesis and Possible Orders of Operation for Sr-Ti-OH Gel Creation. The outcome of the STO synthesis is highly sensitive to the base and metal solution mixing step. Sr-Ti-OH gels can either be created via metal-to-base (MTB) or base-to-metal (BTM) addition.

Electron micrographs of the resultant STO nanoparticles are presented in **Figure 2.4**. From these micrographs, it is apparent that precursor gels synthesized under *Slow BTM* conditions (**Figure 2.4a**) afford irregularly-shaped nanoparticles, while gels synthesized under all other conditions (**Figures 2.4b-d**) afford rounded nanocuboids, with yields up to 1.5 grams.

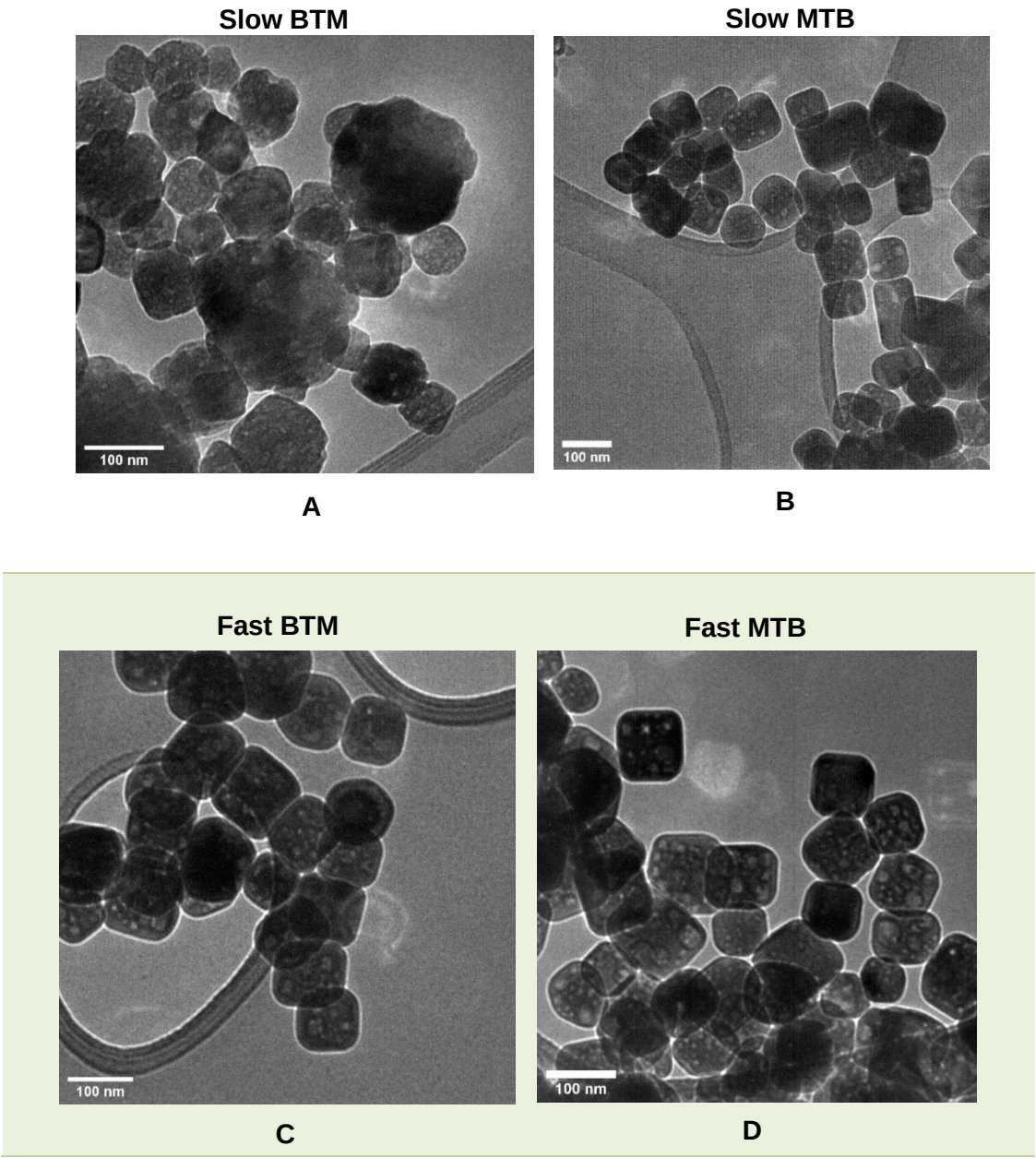

Figure 2.4. TEM-BF Micrographs of STO Nanocuboids Synthesized from Each of Four Possible Gel Creation Conditions. Each of four conditions was established through variation of the addition rate (fast or slow, i.e. combination of components in either < 5 seconds or dropwise) and the order in which components are combined (base-to-metal or metal-to-base).

To understand the driving forces behind variations in STO morphology, each **AB-OH** gel precursor was isolated and analyzed at five minute intervals of mixing without hydrothermal treatment. The

corresponding solution pHs are presented in **Figure 2.5** and display two distinct environments: one in which the pH of **AB-OH** is 14 from the start of stirring ("constant pH"), and one in which the pH increases in a stepwise fashion, reaching 14 after all NaOH has been added ("climbing pH"). This suggests that STO NC synthesis requires rapid formation of a pH 14 environment (vide infra).

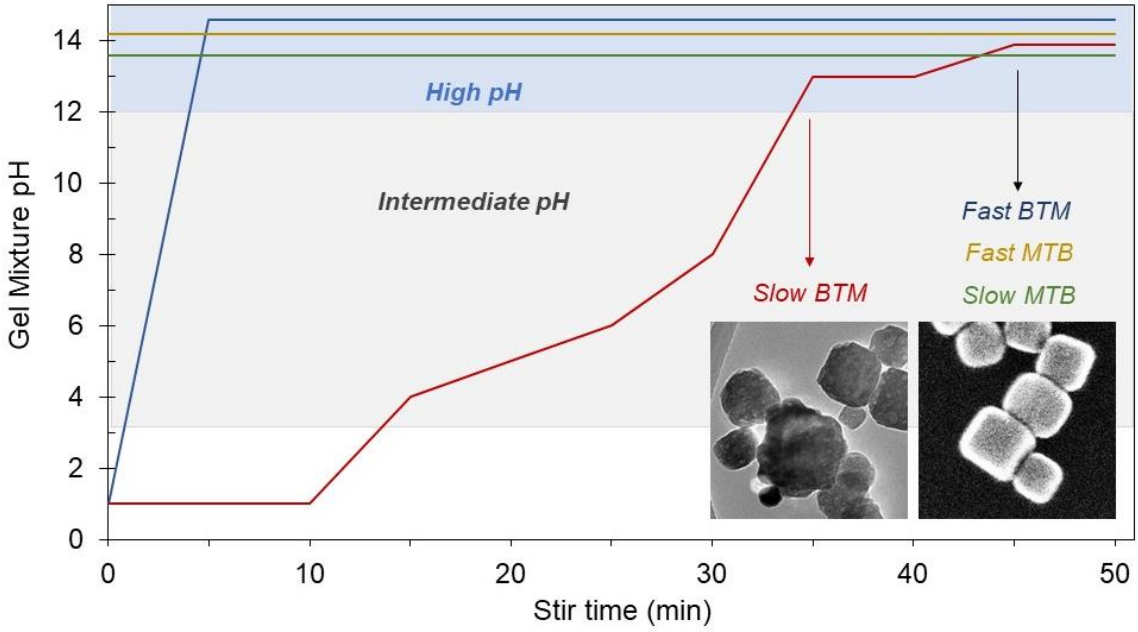

Figure 2.5. Rate of pH Change in STO Precursor Gels based on Order of Operation. Gels synthesized via *Fast BTM, Slow MTB,* and *Fast MTB* pathways show a rapid jump to pH ~14, while gels synthesized via the *Slow BTM* pathway increase over the duration of mixing from pH ~1 to pH ~14. Depending on specific reaction conditions, all temperature samples experience a temperature increase of 10 – 30°C between the start of mixing and complete incorporation of NaOH. In alkaline titanate systems, the perovskite STO phase is the most stable phase in the "high pH" region, shown here in light blue (pH 12-14).[130–134]

Next, **AB-OH** mixtures made via all four pathways were analyzed by powder x-ray diffraction. **Table 2.1** reports the phases observed in each gel environment, final particle morphology after hydrothermal treatment, and average crystallite size within the gel. In the case of *Fast BTM*, *Fast MTB,* and *Slow MTB* addition, a STO primary phase (94-99%) and less significant $SrCO_3$ secondary phase (1-6%) are observed. The average crystallite size in these environments is also comparable, ranging from 21.0 nm to around 31.3 nm. By contrast, Sr-Ti-OH gels created in a *Slow BTM* condition only show crystalline phases above pH 13, at which point a $SrCO_3$ primary phase (64%) and a STO secondary phase (36%) are observed. The average crystallite size in this sample is significantly smaller at an average of 10.7 nm. Diffraction patterns corresponding to each entry in the table are presented in the supplementary information (**Figures 2.6 – 2.9**).

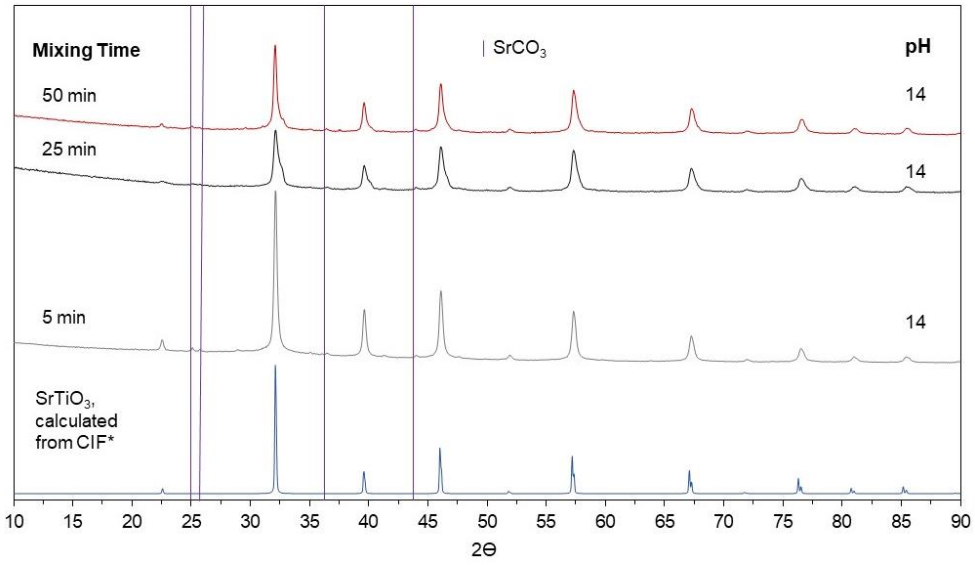

Figure 2.6. Powder X-Ray Diffraction Pattern of STO Precursor Gel Synthesized with *Fast BTM* Addition. Aliquots were removed from the reaction mixture after 5, 25, and 50 minutes, measured for pH, and spread on a sample holder for powder diffraction analysis. Peak broadening analysis via the Scherrer equation affords an average STO crystallite size of 25.2 ± 7.3 nm. The purple vertical lines pass through peaks corresponding to $SrCO_3$, but do not identify every peak corresponding to this phase.

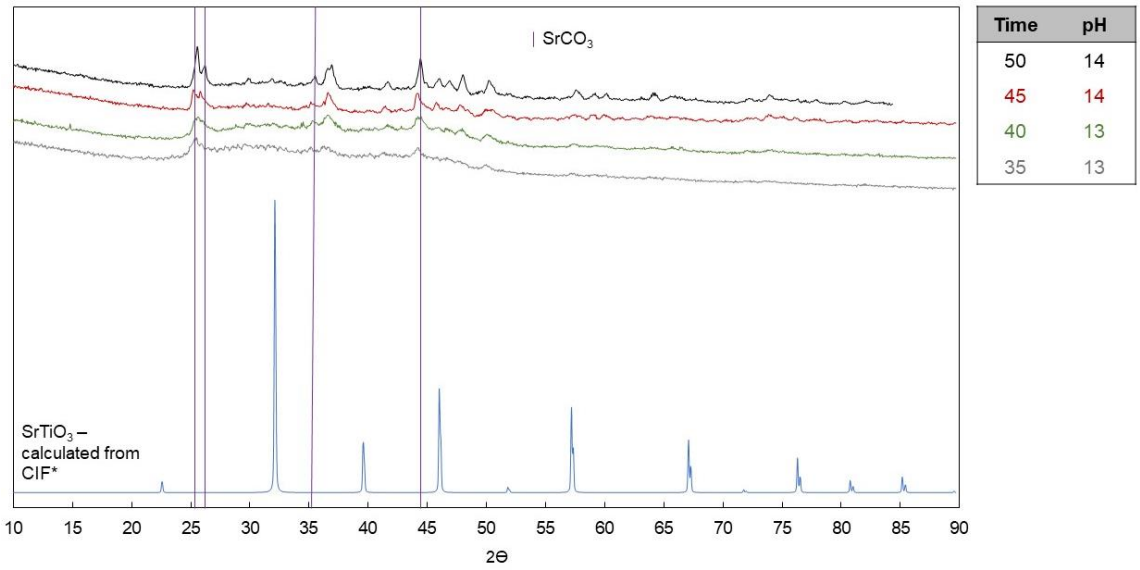

Figure 2.7. Powder X-Ray Diffraction Pattern of STO Precursor Gel Synthesized with *Slow BTM* Addition. Aliquots were removed from the reaction mixture every 5 minutes of stirring, measured for pH, and spread on a sample holder for powder diffraction analysis. No crystalline phases were observed prior to 35 minutes of stirring (pH 13). Peak broadening analysis via the Scherrer equation affords an average STO crystallite size of 10.7 ± 5.5 nm and average $SrCO_3$ crystallite size of 9.4 ± 5.6 nm. The purple vertical lines pass through peaks corresponding to $SrCO_3$, but do not identify every peak corresponding to this phase.

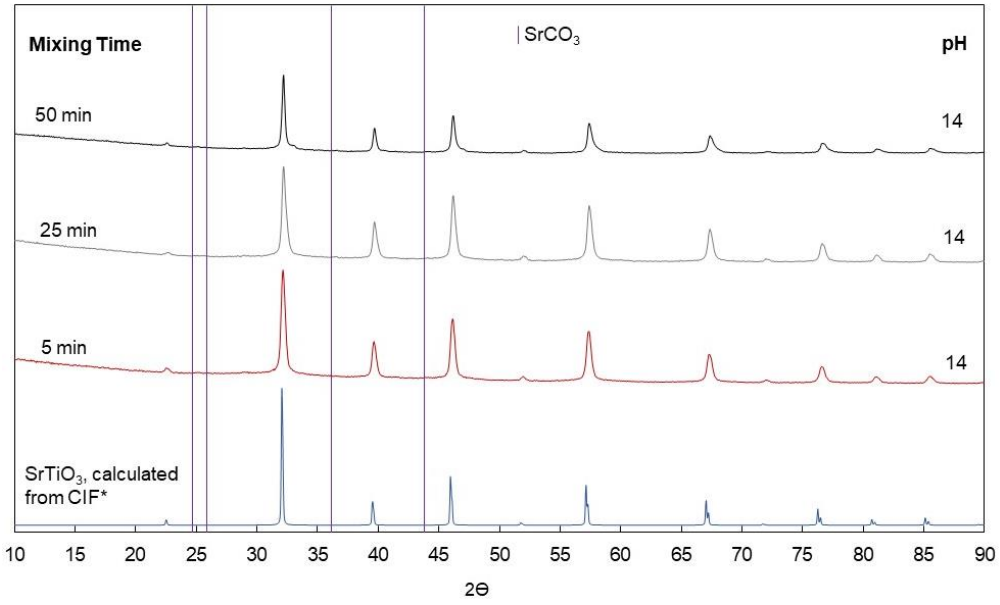

Figure 2.8. Powder X-Ray Diffraction Pattern of STO Precursor Gel Synthesized with *Fast MTB* Addition. Aliquots were removed from the reaction mixture after 5, 25, and 50 minutes, measured for pH, and spread on a sample holder for powder diffraction analysis. Peak broadening analysis via the Scherrer equation affords an average STO crystallite size of 31.3 ± 9.1 nm. The purple vertical lines pass through peaks corresponding to $SrCO_3$, but do not identify every peak corresponding to this phase.

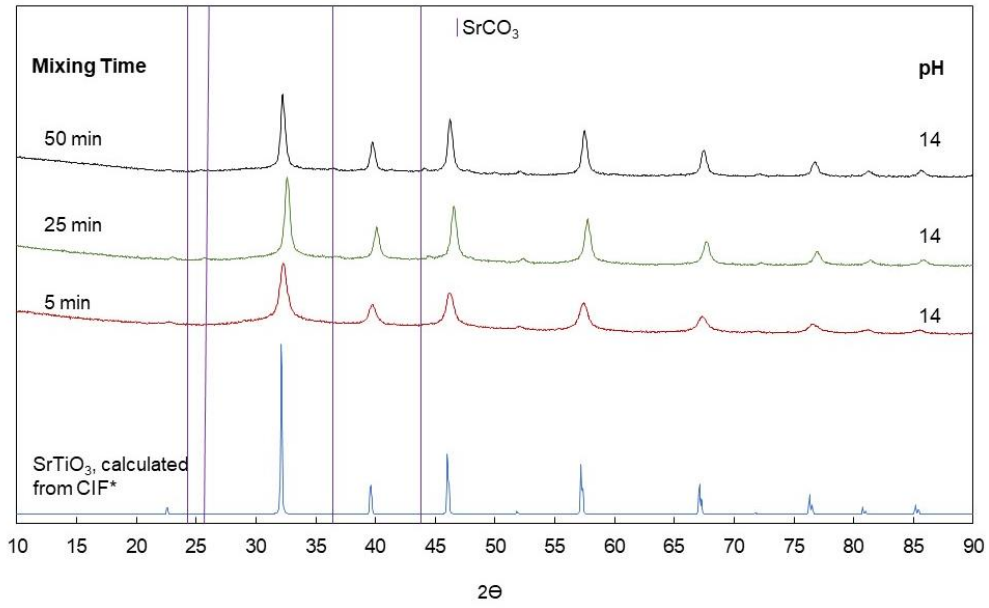

Figure 2.9. Powder X-Ray Diffraction Pattern of STO Precursor Gel Synthesized with *Slow MTB* Addition. Aliquots were removed from the reaction mixture after 5, 25, and 50 minutes, measured for pH, and spread on a sample holder for powder diffraction analysis. Peak broadening analysis via the Scherrer equation affords an average STO crystallite size of 21.0 ± 1.9 nm. The purple vertical lines pass through peaks corresponding to $SrCO_3$, but do not identify every peak corresponding to this phase.

The order of addition of the metal and base solutions during the gel creation step has a significant effect on the precursor particle formation (**Table 2.1**) and the subsequent hydrothermal formation of STO NCs (**Figure 2.4**). The optimum order, which maximizes STO NC formation and minimizes $SrCO_3$ in the precursor, is the *Fast MTB* method. A significant percent of the STO nanoparticles were NCs for the *Fast BTM* and *Slow MTB* methods, although higher percentages of $SrCO_3$ were observed in those precursor solutions than in the *Fast MTB* method. This is consistent with the original method reported by Rabuffetti et al, which specified pouring NaOH pellets into the Sr/Ti solution, approximately equivalent to the *Fast BTM* addition.

Table 2.1. Phase Identification in Pre-Hydrothermal STO Colloidal Precursors

Gel Environment	% STO	% SCO	Average STO Crystallite Size (nm)	Post-Hydrothermal Morphology
Slow BTM	36	64	10.7 ± 5.5	*Irregularly Shaped*
Fast BTM	94	6	25.2 ± 7.3	*Cuboid*
Slow MTB	97	3	21.0 ± 1.9	*Cuboid*
Fast MTB	99	1	31.3 ± 9.1	*Cuboid*

The irregular STO nanoparticles resulting from the Slow BTM method are significantly different from the STO nanoparticles from the other methods (**Figure 2.5**). Where this method differs is in how rapidly the solution pH increases, with respect to the local environment of the Sr and Ti ions. For the Slow BTM method, the pH gradually increases from a pH of ~1 to a pH of ~14 with the addition of NaOH, while for all other methods the pH rapidly jumps from 1 to 14 (**Figure 2.5**). This is significant, as the stability of various ions, complexes, and solid phases change with pH.[132–134] At low pH, Sr and Ti ions and complexes are stable in solution. At intermediate pH, Ti will condense as amorphous sol gels, which are not observable by PXRD.[135] At high pH (pH 12-14), STO is stable and will crystalize out of solution.[134] If there is a significant amount of CO_2 dissolved in solution, that may compete with STO to form $SrCO_3$ at high pH.[132,133] Significantly, if the concentration in solution of Sr and Ti is not stoichiometric, Sr or Ti may form secondary phases instead of STO, such as $SrCO_3$, $Sr(OH)_2$, or TiO_2, depending on if there is a higher concentration of Sr or Ti. In the case of the Slow BTM method, the long dwell time at intermediate pH allows the formation of titania sol gels, which pulls Ti out of solution. When the solution pH finally reaches the point that STO is stable, the solution is Ti-deficient and the Sr-rich $SrCO_3$ phase forms in addition to STO (**Table 2.1**).

Particles from **AB-OH** solutions from both *constant pH* and *climbing pH* environments were imaged by electron microscopy to observe possible morphological differences in the Sr-Ti-OH precursor under varied conditions; corresponding electron micrographs are presented below in **Figure 2.10.** Precursor gels prepared in a *constant pH* environment form aggregate nanoparticles with rough surfaces similar in size to the hydrothermally treated STO, while gels prepared in a *climbing pH* environment form an enmeshed,

irregular, fiber-like morphology that does not resemble STO nanoparticles. Elemental mapping of the gel precursors in **Figure 2.10** shows generally homogeneous distributions of strontium and titanium in the STO gel precursor irrespective of the pH environment in which it was prepared (**Figure 2.11**).

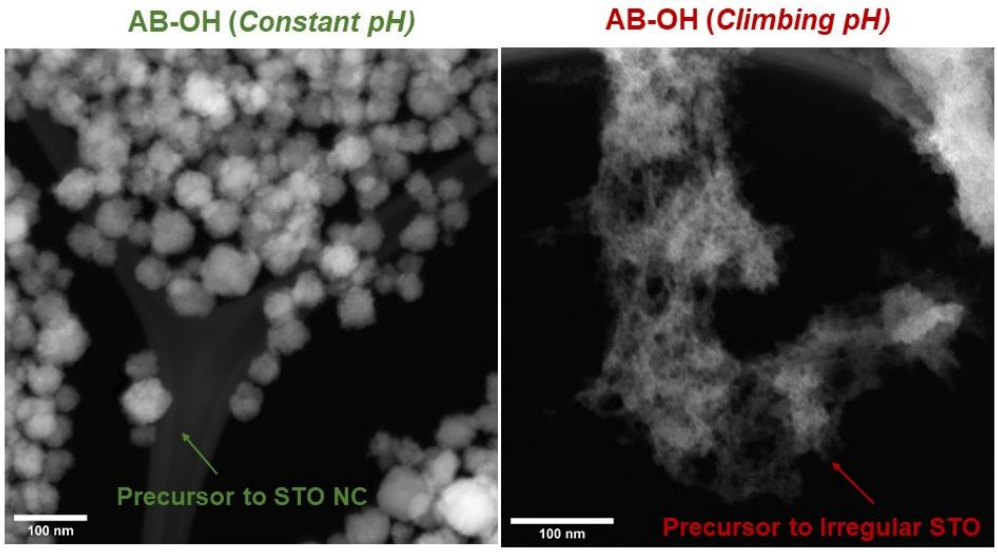

Figure 2.10. TEM-HAADF Micrographs of STO Gel Precursor in Constant pH (Left, Green) and Climbing pH Conditions (Right, Red). Images presented are representative of each gel precursor solution throughout the duration of mixing.

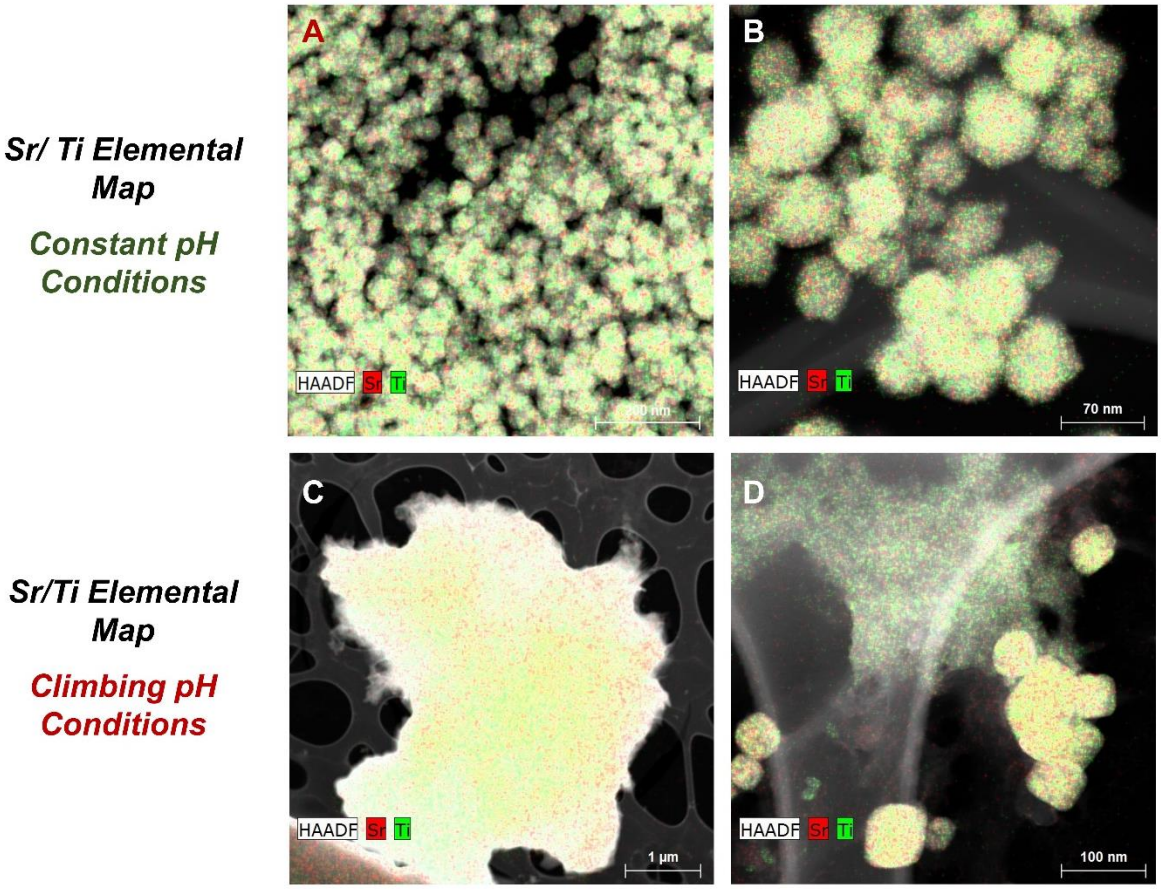

Figure 2.11. Elemental Mapping of Sr/Ti in Sr-Ti-OH Colloidal Precursors. Sr-Ti-OH precursor were elementally mapped for Sr and Ti for samples synthesized under *constant pH* conditions (top left, top right), and *climbing pH* conditions (bottom left, bottom right).

Next, the concentrations of [Sr], [Ti], and [OH] in the Sr-Ti-OH mixture were varied to determine their influence on final STO particle size. Specifically, the molarity of the 13 mL NaOH was varied, as was the amount of water used to dissolve 2.55 g $Sr(OH)_2 \cdot 8H_2O$ in **Solution A**. The results of these experiments are presented below in **Figure 2.12**. STO nanocuboids ranging from 25 nm – 80 nm are attainable when varying the volume of water from 20 – 60 mL and varying the amount of added NaOH from 13mL @ 10M to 13mL @ 25M. Both the concentration of added base and the volume of water added have significant effects on final particle size. Global synthetic conditions (i.e., values of [NaOH] and water volume

measured at the point of incorporation into the reaction mixture) and corresponding average particle sizes for each data point are reported in **Table 2.2**, along with a graphical representation of the average size and variance in **Figure 2.13.** Several representative micrographs are also reported (**Figure 2.14**).

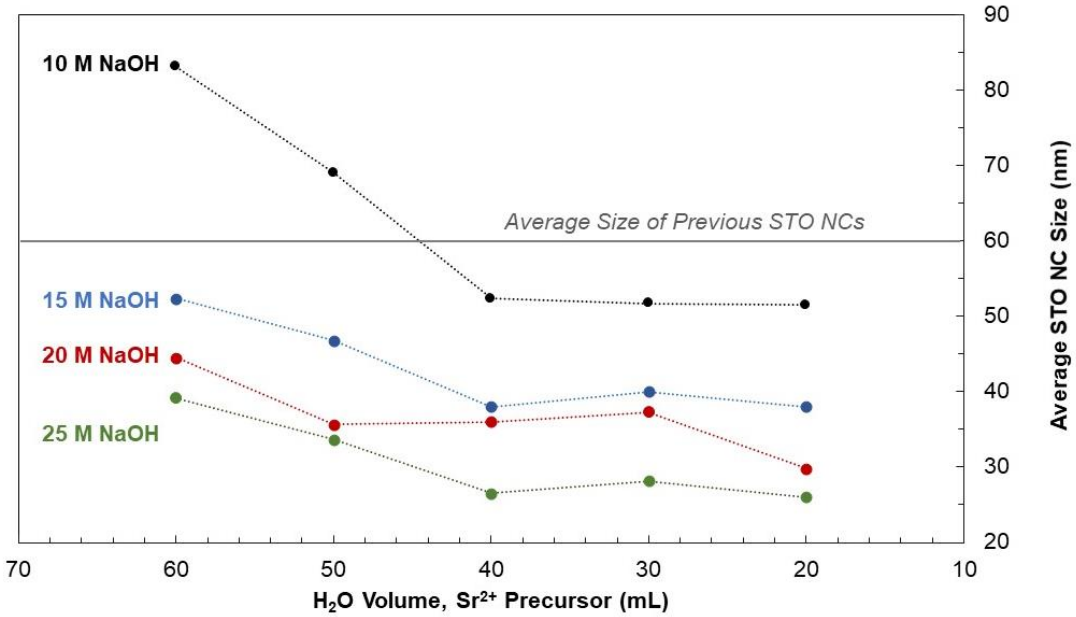

Figure 2.12. **Average Sizes of STO Nanocuboids Produced through Variation of Added H_2O and NaOH.** Variation of the molarity of added NaOH and water volume used in the reaction allows for synthesis of STO NCs ranging from 25 – 80 nm.

Table 2.2 Synthetic Conditions Varied during STO Size Variation Experiments. These results correspond to the samples shown in **Figure 6** of the paper. In each case, 9.1 mmol of both $Sr(OH)_2 \cdot 8H_2O$ and $TiCl_4$ were used. Total water volume in the solution refers to water volume added into **Solution A** at the start of the synthesis.

[added NaOH]	V_A = 60 mL	V_A = 50 mL	V_A = 40 mL	V_A = 30 mL	V_A = 20 mL
10 M	83.1 ± 14.5	69.1 ± 11.0	52.42 ± 9.1	51.72 ± 8.1	51.5 ± 11.2
15 M	52.4 ± 9.1	46.8 ± 9.2	38.0 ± 8.5	40.0 ± 11.9	38.0 ± 6.7
20 M	44.4 ± 8.0	35.7 ± 9.5	36.0 ± 10.0	37.3 ± 6.4	29.8 ± 5.3
25 M	39.2 ± 8.2	33.7 ± 7.6	26.5 ± 4.7	28.2 ± 5.2	26 ± 5.9

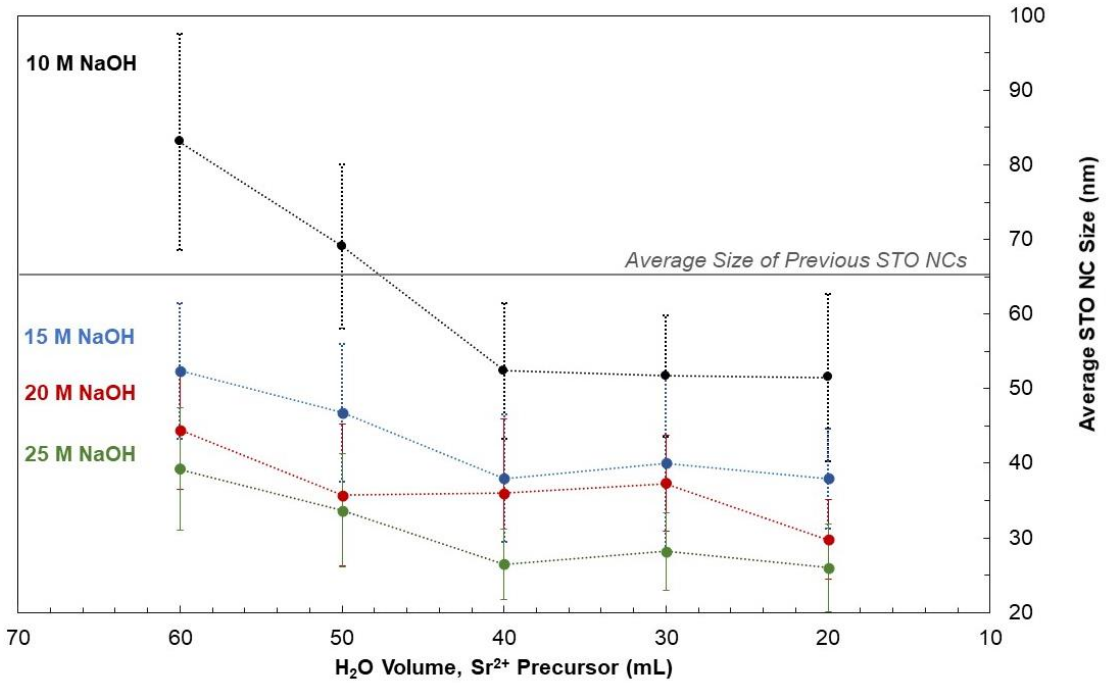

Figure 2.13 Synthetic Conditions Varied during STO Size Variation Experiments. These data and associated error bars graphically represent the information reported above in **Table 2.2** and are identical to the data presented in **Figure 2.12**.

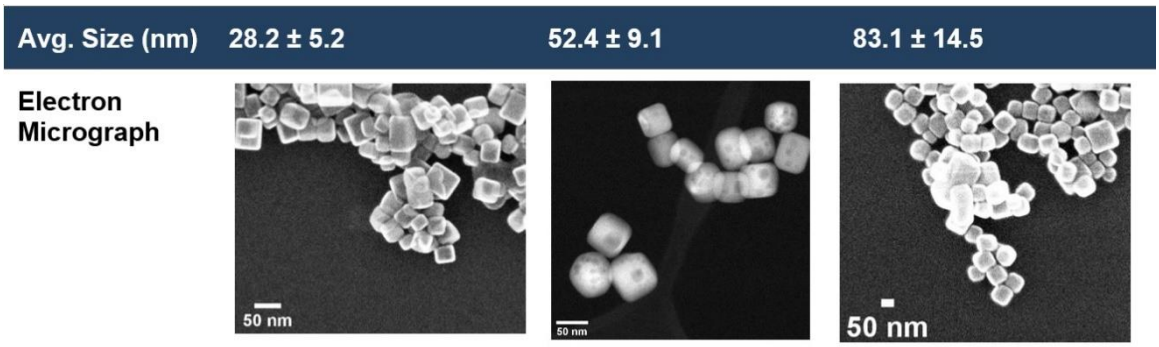

Figure 2.14. Electron Micrographs of STO NCs with Varied Average Sizes. These micrographs and their average sizes correspond to entries with the same average size and variance above in **Figure S4a**. Visually, STO NCs appear to have generally equivalent morphologies regardless of average particle size.

To probe whether particle morphology was consistent across each sample, an average measure of corner rounding was obtained by inscribing a circle into the corner of each nanocuboid, the radius of which was used as a measure of curvature (**Figure 2.2**). The data show that the ratios of particle size to corner rounding (*d:r*) are comparable, ranging from 4.0 ± 1.3 to 4.9 ± 1.3. Based on these values, STO particle morphology appears generally equivalent across all samples (**Table 2.3**).[129]

Table 2.3. Measurements of Corner Rounding In STO Nanocuboid Samples of Various Sizes. The *d:r* ratios are all within one standard deviation of each other, suggesting that the nanocuboid morphologies in these samples are generally equivalent. These samples are also generally equivalent to a sample reported by Rabuffetti et al., whose *d:r* ratio for STO NCs was 5.0 ± 1.2 (last entry, red).

Sample Size	***Radius of Curvature***	***d:r***
24.7 ± 5.1	5.0 ± 0.9	4.9 ± 1.3
39.3 ± 6.3	9.7 ± 2.7	4.0 ± 1.3
48.8 ± 6.4	9.9 ± 2.0	4.9 ± 1.2
64.0 ± 8.8	14.3 ± 2.1	4.5 ± 0.9
63.9 ± 10.0	12.6 ± 1.2	5.0 ± 1.2

The average aggregate particle size and crystallite size were measured for precursors synthesized under *constant pH* conditions, corresponding to STO NCs ranging from 25 – 80 nm (**Figure 2.15, Table 2.4**). There is a correlation between both the crystallite and particle aggregate size of the precursor particles and the size of the final STO NCs, with larger crystallites and aggregates forming larger NCs.

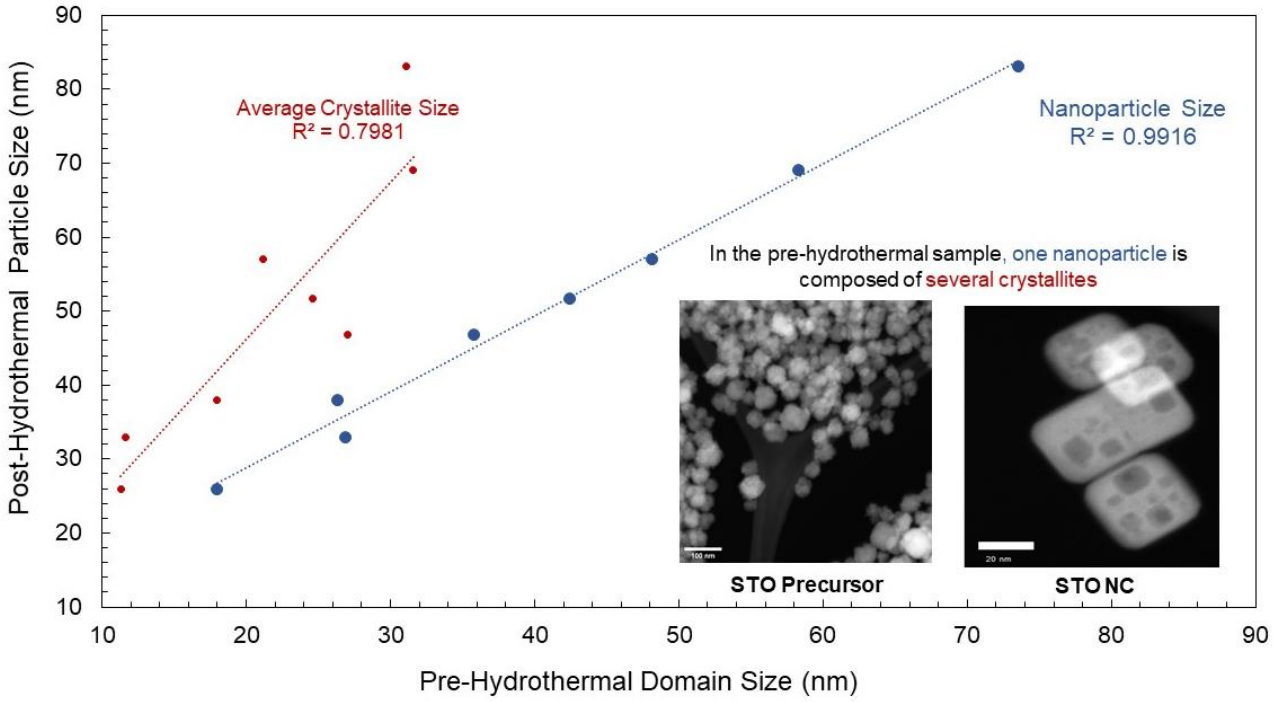

Figure 2.15. Size Measurements for Gel Precursors Compared to Final STO Nanocuboid Size. The average size of STO crystallites (red, PXRD) and particles (blue, EM) from the precursor gel are compared against the average STO NC size (**TEM-HAADF**) after hydrothermal treatment. There is a correlation between both precursor crystallite and particle sizes and the final nanocuboid size.

Table 2.4. Precursor Particle Sizes vs. Final Hydrothermal Particle Size. These data correspond to the graph in **Figure 2.15**. For each STO sample, a pre-hydrothermal particle size and a final NC size were measured through direct imaging via electron microscopy. [a] Average crystallite size for each sample was calculated via peak broadening analysis of powder x-ray diffraction patterns. [b] Average STO NC sample size was measured through direct imaging via electron microscopy as well.

Precursor		STO NC
Avg Crystallize Size (nm)[a]	Avg Particle Size (nm)[b]	Avg NC Size (nm)[b]
31.1 ± 3.1	73.5 ± 9.6	83.1 ± 14.5
31.6 ± 3.9	58.3 ± 12.0	69.1 ± 11.0
21.2 ± 1.9	48.1 ± 10.6	57 ± 10.4
24.6 ± 3.5	42.4 ± 8.6	51.7 ± 8.1
27.0 ± 2.6	35.8 ± 7.1	46.8 ± 9.2
18.4 ± 0.7	26.3 ± 5.3	38.0 ± 6.7
11.6 ± 1.7	26.9 ± 5.9	33.7 ± 7.6
11.3 ± 0.9	18 ± 4.1	26 ± 5.9

When designing a catalyst support, it is desirable to maximize surface area while retaining beneficial structural properties (e.g. faceting), increasing the potential number of catalytic sites. Particle size, which correlates inversely with surface area, can be varied over the range of 25 to 80 nm without significantly affecting STO NC morphology through control of the base and total ion concentrations (**Figures 2.2, 2.12)**. Both the concentration of base ([NaOH]) and the total ion concentration (controlled by the volume of water) affect the average particle size in the precursor and the STO NC (**Figure 2.15**), with higher ionic

concentrations (base or total) decreasing particle size. In the range of conditions probed, the concentration of base has a more significant effect on STO NC size, but the trend in the 10M NaOH samples at the highest water volumes (lowest total ion concentrations) suggests that decreasing the total ion concentration further may significantly increase the STO NC size. For the precursors that form STO NCs, there is a strong correlation between the precursor crystallite (PXRD) and particle (EM) size and the final STO NC size (**Figure 2.15**), which suggests that the NCs form directly from the precursor particles with minimal diffusion between particles. That the precursors primarily composed of $SrCO_3$ and amorphous titania (from the *Slow BTM* method) do not form STO NCs under the tested conditions is likely because the rates of precursor dissolution, diffusion, and STO formation are overall slower than the rate of STO recrystallization for the aggregates of STO crystallites. Based on these data, STO nanocuboid formation likely proceeds through separate synthesis-dependent nucleation and growth process. Initial STO nucleation at high pH likely occurs in a rapid burst fashion governed by thermodynamic and/or colloidal stability, followed by diffusion-limited facet growth during hydrothermal treatment. We believe that changing precursor concentrations (and therefore Sr^{2+}, Ti^{4+}, and OH^- concentrations) affects the minimum stable crystallite size that can form upon creation of the Sr-Ti-OH gel mixture. More specifically, lower precursor concentrations likely decrease mixture saturation and increase the minimum stable crystallite size required for STO nanoparticles to form without redissolving.

As observed in the *Slow BTM* synthesis, the formation of large amounts of $SrCO_3$ negatively affects the formation of STO NCs. $SrCO_3$ may also form by adventitious dissolution of CO_2 in solution or through variation in the Sr:Ti ratio.[136] These effects and methods to mitigate them have also been explored. In samples in which $SrCO_3$ formation is observed through powder x-ray diffraction, the final STO nanoparticles have irregular morphologies (**Figures 2.16 & 2.17**). Sr-Ti-OH mixture time was reduced from 50 minutes to 10 minutes, as this appeared to reduce the likelihood of $SrCO_3$ formation. Complete elimination of $SrCO_3$ formed from adventitious CO_2 dissolution would likely require the use of an air-free environment or degassing of the water-ethanol mixture.[85]

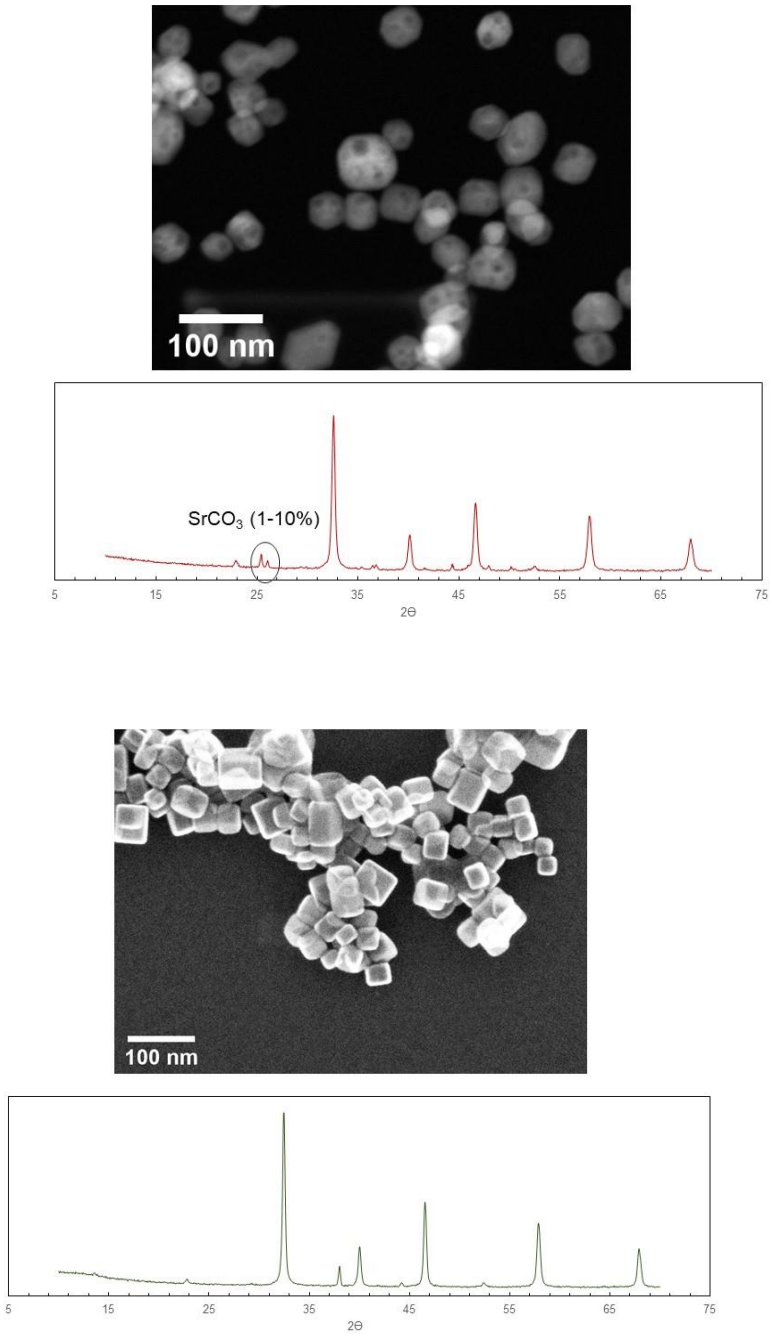

Figure 2.16. PXRD Patterns of STO Samples with and without $SrCO_3$. Samples with noticeable $SrCO_3$ secondary phase (top micrograph and diffraction pattern) correspond to final particles with irregular morphologies, indicating that $SrCO_3$ formation can hinder nanocuboid formation. STO NC samples (bottom micrograph and diffraction pattern) do not contain a $SrCO_3$ secondary phase.

Molarity of Added NaOH: **10M**

Addition Rate	10 min stir	50+ min stir
Fast	No $SrCO_3$	No $SrCO_3$
Slower	No $SrCO_3$	No $SrCO_3$

Molarity of Added NaOH: **15M**

Addition Rate	10 min stir	50+ min stir
Fast	No $SrCO_3$	$SrCO_3$ sometimes observed
Slower	No $SrCO_3$	$SrCO_3$ sometimes observed

Molarity of Added NaOH: **20M**

Addition Rate	10 min stir	50+ min stir
Fast	No $SrCO_3$	$SrCO_3$ sometimes observed
Slower	No $SrCO_3$	$SrCO_3$ sometimes observed

Molarity of Added NaOH: **25M**

Addition Rate	10 min stir	50+ min stir
Fast	No $SrCO_3$	$SrCO_3$ sometimes observed
Slower	No $SrCO_3$	$SrCO_3$ sometimes observed

Note: All glassware was washed with a weakly acidic solution (HCl) to prevent external $SrCO_3$ contamination

Figure 2.17. Conditions under which $SrCO_3$ Uptake was Observed with Longer Stir Times. The results indicate that CO_2 uptake is not significant for shorter stir times, but is significant with longer stir times (i.e. longer exposure to atmospheric CO_2).

Furthermore, we have observed that the global Sr:Ti ratio (defined based on the amounts of $Sr(OH)_2 \cdot 8H_2O$ and $TiCl_4$ added to the precursor solutions) significantly impacts nanoparticle morphology. Samples with a Sr:Ti ratio of 1.05:1 most consistently form STO NCs, while samples with higher (>1.1:1) Sr:Ti ratios form non-cubic nanoparticles (**Figure 2.18**). Previously, samples with both NC and irregular morphologies had been observed from STO syntheses using a global Sr:Ti ratio of 1:1. This could be due to decomposition of the $Sr(OH)_2 \cdot 8H_2O$ precursor from the octahydrate phase to less-hydrated phases, which was likely accelerated through grinding of the as-received reagent and storage in a desiccator (**Figure 2.19**). As such, this updated synthetic method calls for using as-received $Sr(OH)_2 \cdot 8H_2O$.

Sr:Ti Ratio

1.0 : 1	1.05 : 1	1.1 : 1

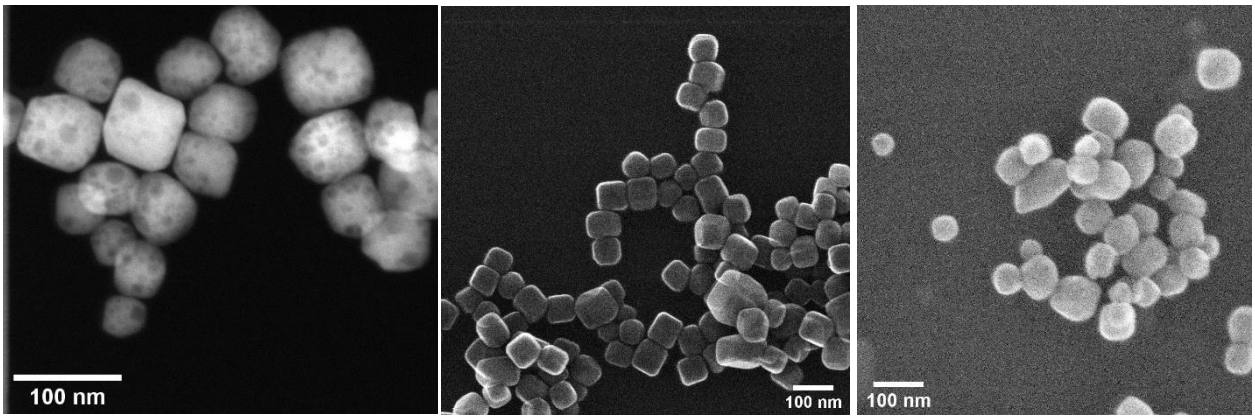

Sr:Ti Ratio

1.2 : 1	1.3 : 1	1.4 : 1

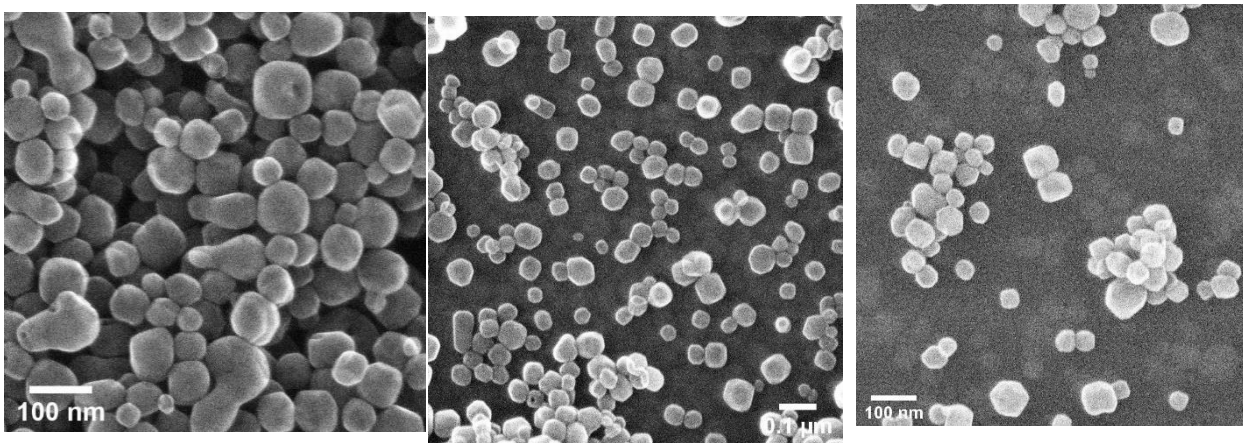

Figure 2.18. STO Nanoparticle Products Obtained Through Variation of Global Sr:Ti Ratio. The TEM micrographs above correspond to reaction mixtures with global ratios of 1:1, 1.05:1, 1.1 : 1 (top left to top right), and 1.2:1, 1.3:1, and 1.4:1 (bottom left to bottom right). The mass of as-received $Sr(OH)_2 \cdot 8H_2O$ introduced into the reaction mixture was varied from 2.43g to 3.40g, such that the overall ratio of Sr to Ti varies from 1.1 to 1.4, respectively. STO nanoparticles synthesized with global ratios of 1.05 : 1 were cuboids, while STO nanoparticles synthesized with other global ratios were irregularly shaped.

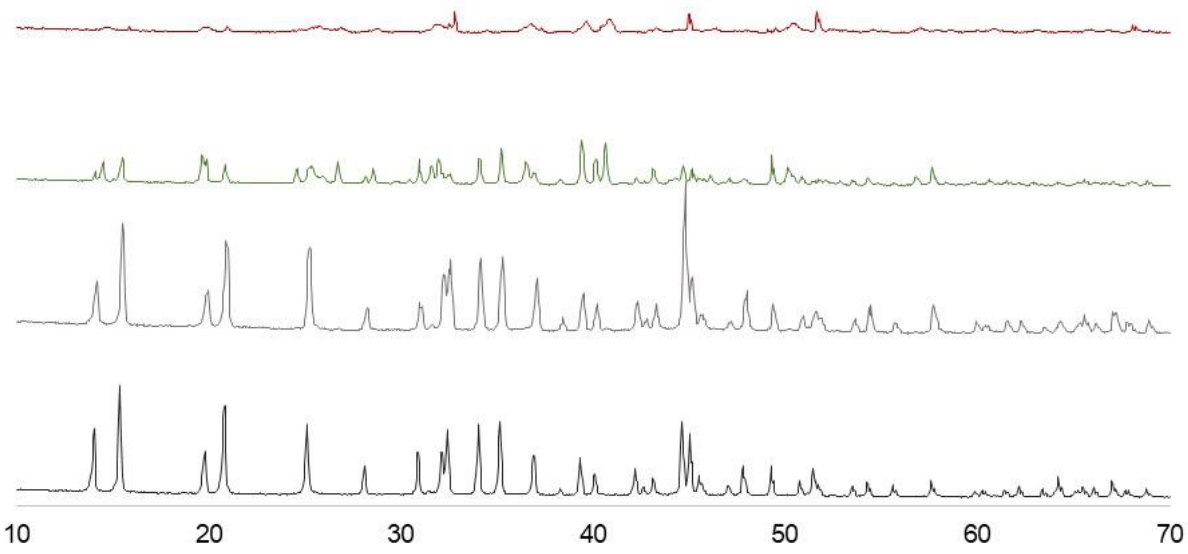

Powder Pattern	Desiccation Time (days)	% $Sr(OH)_2 \cdot 8H_2O$	% $Sr(OH)_2 \cdot H_2O$
Red	~60	0	100
Green	~20	48	52
Grey	2	100	0
Black	0	100	0

Figure 2.19. Degradation of $Sr(OH)_2 \cdot 8H_2O$ After Grinding and Desiccation. Desiccation of a ground $Sr(OH)_2 \cdot 8H_2O$ sample for two days does not cause decomposition of the octahydrate phase. However, extended desiccation on the order of one month causes significant desiccation of the octahydrate phase to a mixture of the monohydrate phase and (likely) semi-hydrate phases.

Preliminary scale-up experiments have been conducted and have demonstrated that STO nanocuboids can be synthesized at scales larger than a 125 mL autoclave. A highly-cubic STO sample (m = 22.5 g) was synthesized in a 4 L batch reactor at the Materials Engineering Research Facility (MERF) at Argonne National Laboratory; this is a 32-fold scale-up from the hydrothermal conditions reported by Rabuffetti et al. TEM micrographs of the resultant STO NCs are displayed below in **Figure 2.20**. These NCs have an average size and variance of 58.3 ± 16.2 nm, with an average corner rounding of 10.5 ± 1.7 nm, resulting in a *d:r* of 5.5 : 1. This is beyond the range of d:r ratios seen in the highly-cubic samples synthesized in a 125 mL autoclave, but within error of the higher *d:r* values from that group of samples, and therefore not indicative of a change in the Wulff shape under hydrothermal conditions. These corner rounding measurements are all also comparable to an equivalent measurement obtained for a sample synthesized by Rabuffetti et al. with the previous hydrothermal method (**Table 2.3**, *d:r* = 5.0 ± 1.2).

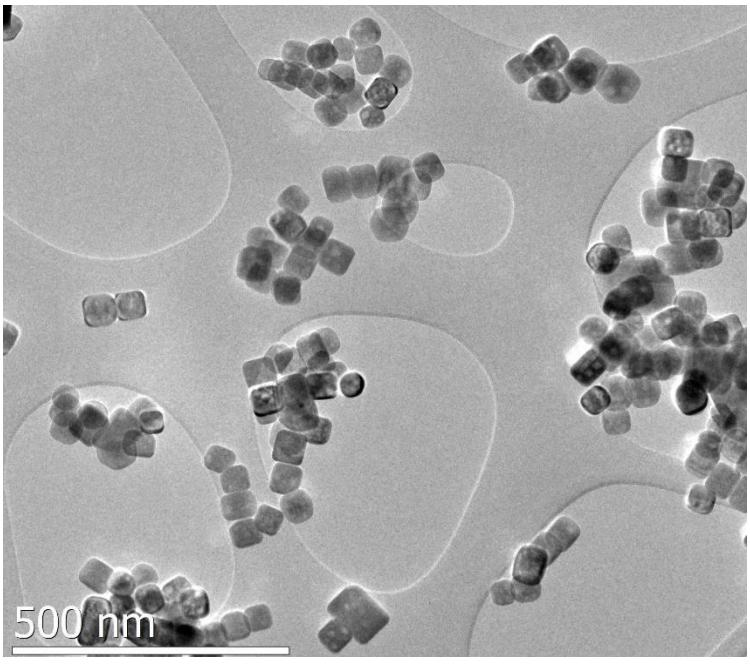

Figure 2.20. TEM-BF Micrographs of STO Nanocuboids Synthesized in a 4L Batch Reactor. This sample (m = 22.5 g) has an average size of 58.3 ± 16.2 nm. The STO NC morphology of these nanoparticles is generally equivalent to those samples synthesized in a 125 mL autoclave.

These preliminary results show that scale-up from a 125 mL autoclave reactor to a 4 L autoclave reactor can be attained without significantly altering average nanoparticle size and shape, a fact supported by the average size *d* and average ratio of size to corner rounding, *d:r*. Thus, it is likely possible to further scale-up the STO hydrothermal synthesis described herein while retaining highly cubic particle morphologies.

Size-controlled STO supports reported above have been used to construct Pt/STO catalysts through strong electrostatic adsorption (SEA), a charge-mediated, aqueous method adapted for depositing Pt onto the STO surface. Specifically, a STO nanocuboid sample with an average size of 39.3 ± 6.3 nm was used to deposit small Pt nanoparticles (< 2 nm, **Figure 2.21**) with an average diameter of 1.7 ± 0.3 nm, an average area loading of 1.1 ± 0.3 Pt atoms / nm^2, and a weight loading of 3.6 wt % Pt. The successful deposition of Pt onto the STO NC surface suggests that the improvements made to the STO hydrothermal synthesis reported herein do not significantly alter the support surfaces, thereby making them generally equivalent to samples synthesized via the hydrothermal synthesis reported by Rabuffetti et al. Furthermore, these results indicate that the SEA process is: 1) a precise deposition method that deposits Pt onto STO NCs in a controlled fashion, and 2) amenable to scale-up due to the comparatively simple equipment required to conduct the deposition, as compared to other surface-limited processes like ALD.

The above SEA-Pt/STO sample was tested for the hydrogenolysis of HDPE using the conditions described by Hackler et al.[56] After 96 hours with 11 mg of 1.7 nm Pt particles, the HDPE was converted from M_w = 35 kDa, Đ = 3.11 to a M_w = 2400 Da, Đ = 1.03 product (99% conversion to wax, 1 % gas, 0% solid and liquid), compared to similar experiments in a Parr reactor in Celik et al. with 8 mg of 2.0 nm Pt particles, which generated a M_w = 2100 Da, Đ = 1.7 product after 68 h without the use of a liner. The dispersity of the product of the SEA-Pt/STO catalyst decreased below 1.1, similar to our prior work producing upcycled liquid products from polyolefins with Pt/STO.[7,56] Notably, the dispersity decreased below 1.1 while the M_w was above 2000 Da, which we have not previously observed. This narrow dispersity demonstrates that SEA-derived Pt/STO is a selective catalyst for waste plastic hydrogenolysis. The conversion to a wax-like product was higher than previously reported; no conversion to liquids or light gases occurred, despite being observed for hydrogenolysis with previous Pt/STO catalysts. We postulate

that these differences may be due to differences in the amount of Pt atoms per square nanometer between samples. Celik et al and Hackler et al. have previously observed negligible changes in the Pt particle size and distribution after hydrogenolysis for ALD Pt/STO catalysts by electron microscopy and suggested that it is due to the epitaxial stabilization of Pt on the $SrTiO_3$ {100} facets. Based on those results, we expect that SEA Pt/STO Pt nanoparticles will be similarly stabilized. The observed low dispersity at high molecular weights will be further investigated to determine how the changes in Pt nanoparticle dispersion from ALD to SEA affect polymer/catalyst interactions and therefore the upcycled liquid products.

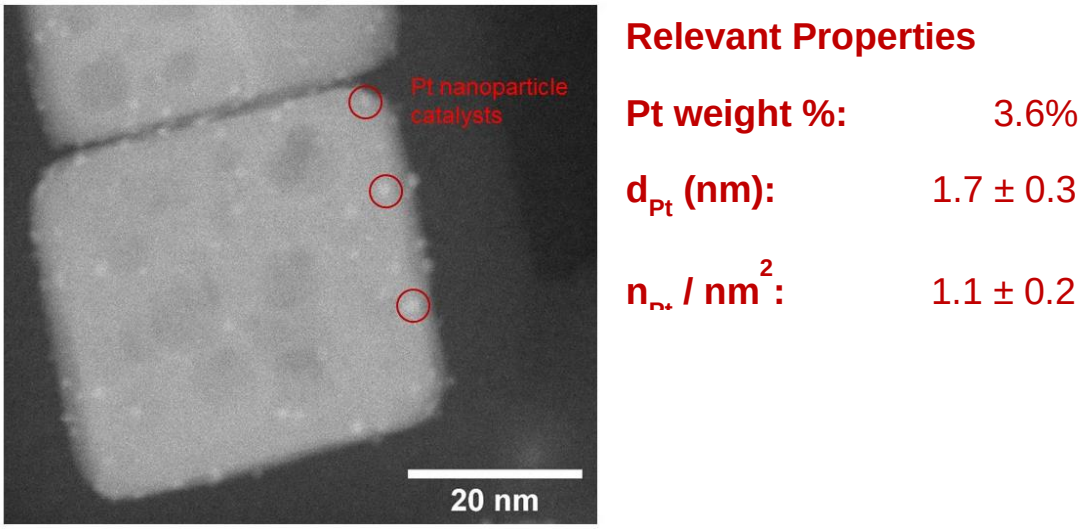

Figure 2.21 TEM-HAADF Micrograph of SEA-Derived Pt/STO Catalysts. This sample was synthesized via the updated hydrothermal synthesis and SEA deposition process reported herein. This sample has a Pt weight loading of 3.6%, an average Pt particle size of 1.7 ± 0.3 nm, and an average Pt area loading of 1.1 ± 0.2 Pt atoms per square nanometer.

2.5 CONCLUSION

Highly cubic, size-controlled STO catalyst supports have been used to generate size-controlled Pt/STO hydrogenolysis catalysts and upcycle HDPE into high-quality liquids. Several modifications to an earlier STO hydrothermal synthesis have: 1) allowed for the synthesis of STO nanocubes ranging from 25 – 80 nm in size with narrower size distributions than before; 2) ensured that nanoparticles with highly-cubic

morphologies are formed by eliminating competing effects of reaction byproducts such as $SrCO_3$, and 3) revealed that rapid formation of precursor crystallites in a pH 14 solution is required for nanocuboid formation. Analysis of the pre-hydrothermal synthetic steps established that STO NCs rapidly nucleate prior to hydrothermal synthesis, suggesting that hydrothermal treatment is primarily responsible for NC facet growth. In the future, this STO NC hydrothermal synthesis will be studied in a microwave reactor to understand the relationship between heating method and final STO morphology, and the relationship if any between these parameters and the pH control of the Sr-Ti-OH gel precursor demonstrated in this work.

We further report that the STO hydrothermal synthesis was conducted on a 4 L batch scale to afford 22.5 g of highly-cubic nanoparticles. These preliminary results demonstrate that STO can be synthesized on larger scales while retaining average particle size and a highly-cubic morphology. These findings will be used to guide conversion of the synthesis into a continuous-flow reactor in pursuit of high-throughput synthesis of shape-controlled, size-controlled Pt/STO catalysts. The construction of Pt/STO catalysts and their upcycling of HDPE into uniform wax products also demonstrate that the physical properties of these catalysts can be varied without adversely affecting hydrogenolysis. We will continue to explore the extent to which variation of properties such as support surface area impact HDPE hydrogenolysis as we pursue a commercially viable synthesis of Pt/STO catalysts for waste plastic upcycling.

CHAPTER 3

Microwave-Assisted Synthesis of $SrTiO_3$ Nanocuboids without $TiCl_4$

This Chapter was adapted with permission from "I.L. Peczak, R.M. Kennedy, A.M. Simpson, M. Delferro, K.R. Poeppelmeier. **'**Microwave-Assisted Synthesis of $SrTiO_3$ Nanocuboids without $TiCl_4$.' *Small Science,* **2023**, 220107. DOI: 10.1002/smsc.202200107."

3.1 ABSTRACT

Strontium titanate (STO) nanocuboids have been demonstrated as a novel support for Pt nanoparticle catalysts (Pt/STO). The first of many steps in commercializing Pt/STO will be developing a scalable, environmentally sustainable, and cost-effective STO nanocuboid synthesis**.** In this study, Sr-Ti-OH mixtures were synthesized from various Sr^{2+} and Ti^{4+} reagents and treated hydrothermally with convection heating and microwave-assisted heating to obtain STO nanoparticles. These experiments clarified how phase composition of the pre-hydrothermal Sr-Ti-OH mixture and choice of heating method affect final nanoparticle morphology. In Sr-Ti-OH mixtures synthesized with $TiCl_4$, STO is the most stable phase and precipitates prior to heating, while titania sol-gels are the most stable phase when other Ti^{4+} sources are used. STO crystallites always form when Sr-Ti-OH mixtures are treated by convection heating, though nanocuboids are only observed if STO precipitates in the Sr-Ti-OH mixture. If microwave-assisted heating is used, the rate at which the precursor solution is heated increases, and STO nanocuboids can form from a variety of Sr-Ti-OH mixtures regardless of mixture composition. To that effect, we report two microwave syntheses of STO nanocuboids, one which used $TiCl_4$ as a Ti^{4+} source, and another that used titanium(IV) bis(ammonium lactato) dihydroxide ($[NH_4CH_3CH(O)CO_2]_2Ti(OH)_2$), a water stable Ti^{4+} complex.

3.2 INTRODUCTION

Modern chemical industry is highly dependent on catalysts, with most chemical processes requiring their use in one or multiple steps.[137] By some accounts, over a third of the world's gross domestic product (GDP) is tied to materials generated by catalysts, ~85 % of which are heterogeneous.[137,138]

Owing to the proven success of catalysts in industrial processes, many researchers are using catalysts at the lab scale to solve unexplored problems.[139–141] One such problem is the chemical recycling of single-use plastics, as plastic pollution is a pressing global crisis that urgently needs an industrial solution.[3,8,142,143] Processing single-use plastic waste is uniquely challenging because the stable carbon-carbon and carbon-hydrogen bonds that make up these materials are difficult to break.[144] However, catalytic *upcycling* processes can potentially deconstruct plastics into uniform, value-added products, thereby converting waste into economically viable materials that close the loop of a circular economy.[31,145] Thus far, one state-of-the-art technique for waste plastic upcycling is catalytic hydrogenolysis, by which a noble metal nanoparticle catalyst (e.g. Pt, Ru) deposited on a metal oxide support (e.g. perovskites, titania, silica) selectively converts waste polyolefin samples to liquid and wax-like products.[7,39,46,56,59,114,146,147] Among such catalysts, platinum nanoparticles (Pt) on $SrTiO_3$ nanocuboid supports (STO; Pt/STO) have stood out for their demonstrated ability to selectively convert virgin and post-consumer polyethylene and polypropylene into commercially viable base oils for tribological applications.[7,46,56] Thus, continued study of Pt/STO is desirable.[42,54,60,64,79]

The development of a scalable and cost-effective synthesis for STO catalyst supports is one of many milestones that must be met if Pt/STO hydrogenolysis catalysts are to upcycle plastic waste on a scale sufficient for participation in a circular economy. Regarding STO supports, current lab-scale syntheses use reagents not suitable for eventual scale-up.[85] Of the literature reports that demonstrate hydrothermal synthesis for highly cubic STO samples (defined here and in our previous work as a batch of nanoparticles with > 80 % nanocuboids),[42] the majority use titanium tetrachloride ($TiCl_4$) as a source for Ti^{4+}.[79,80,85,87,88,90,148] Chloride ions, as well as other halides, have a demonstrated track record of acting as both inhibitors and promoters in a variety of catalytic processes. Specifically, chloride ions can be poisons

in the oxidation of CO, methane, ethane, and crotonaldehyde hydrogenation, and generally appear to deactivate platinum catalysts.[149–151] Interestingly, they also promote selective ethene epoxidation and cyclohexene hydrogenation, among other examples.[152,153] Compounding these issues, chloride ions have been shown to corrode steel-based reactors and significantly shorten equipment lifetime.[106,107,154] Thus, $TiCl_4$ restricts the application of STO and other materials as catalyst supports for polymer upcycling. Finally, the introduction of $TiCl_4$ into an aqueous reaction mixture requires the use of ethanol to stabilize the compound. Titanium (IV) chloride is reactive in air, and reagent stocks often decompose to titanium-containing oxides over time, again restricting its ability to serve as a precursor for STO synthesis. This increases the frequency with which reagents must be replaced and drives up the materials cost required to make STO. Preliminary estimations also suggest that for a hypothetical STO synthetic process, a significant amount of greenhouse gas emissions stem from the use of ethanol.[155] Thus, it is highly desirable to substitute $TiCl_4$ for an alternate Ti^{4+} source to avoid potential corrosion, increase precursor shelf life, and eliminate the use of ethanol to reduce the carbon footprint of the process.

Choosing an effective heating method for hydrothermal treatment may also impact the viability of a large-scale STO synthesis. Currently, many STO syntheses for nanocuboids use convection heating in hydrothermal treatment steps.[79,80,85,87,88,90–92,148,156] Convection heating (CH) relies on the diffusion of thermal energy through a reactor and into the reaction mixture, which may cause inhomogeneous sample heating. This can extend the heating time required to synthesize a highly cubic STO sample, consuming large amounts of energy and potentially allowing for more particles with irregular morphologies to form.

Microwave-assisted hydrothermal (MAH) heating more uniformly distributes energy throughout reaction mixtures compared to convection-based heating.[93,94,96–100,157–160] For solvents that are microwave active, e.g. water, direct delivery of microwave radiation into a reaction mixture via a magnetron-powered thermocouple causes molecular rotation. This produces uniform heating throughout the reaction medium, thereby cutting down on reaction times and making batch processes more amenable to scale-up.[93–98,157] Accordingly, microwave reactors have been used extensively in organic synthesis to synthesize small-molecule samples in as little as 30 minutes.[94] They have significantly shortened the time required to conduct transition-metal-catalyzed carbon-carbon and carbon-heteroatom bond-forming reactions, such as Heck, Stille, Negishi, and Suzuki couplings with palladium catalysts, Ullman condensations, and

carbonylations, among other processes.[98] Moreover, these small molecule heating techniques have been adapted to accelerate syntheses in adjacent fields, such as in high-speed polymerase chain reactions and enzyme-mediated organic transformations.[94,98] However, they have not been widely adopted because a limited number of solvents are microwave active, and the cost of microwave reactors is significantly higher than that of convection heating equipment.

Microwave heating is also used to produce inorganic materials, though these syntheses are less common than their organic analogs because they often require harsh reaction conditions.[93,95] Generally, microwave heating has been used to synthesize most classes of functional materials, including but not limited to oxides, halides, and sulfides.[99,100,158–160] These studies have largely focused on demonstrating proof-of-concept syntheses, which do not routinely select for certain physical properties of the product or demonstrate output beyond the lab scale. Thus, there is a continued need to investigate how MAH techniques can be used both for scale-up and the synthesis of specific nanoparticle morphologies.

In this work, a variety of Ti^{4+} and Sr^{2+} precursors were used to synthesize pre-hydrothermal Sr-Ti-OH mixtures, which were analyzed by x-ray diffraction to determine how Sr-Ti-OH phase composition impacts final STO particle morphology. The results are consistent with a previous report by Peczak et al that suggests STO nanocuboids form in a two-step process that requires 1) precipitation of STO and 2) {100} facet growth.[42] When $TiCl_4$ is not used as a Ti^{4+} precursor, nanocuboid particles generally do not form when a single-step convection heating profile is used. Additionally, STO nanocuboids were synthesized in a 1 L stirred microwave reactor to explore both reaction scale-up and the impact of heating method on final particle morphology. These syntheses were first conducted using $TiCl_4$ as a Ti^{4+} source, and then conducted by replacing $TiCl_4$ with titanium(IV) bis(ammonium lactato)dihydroxide (TiBALD), a water-stable titanium complex. From these reactions, 20 g of highly cubic STO were obtained in less time and at lower temperatures than previously required (200 ^{o}C, 8 - 16 h). Thus, we demonstrate that to synthesize STO nanocuboid samples via convection heating, a Ti^{4+} precursor must be chosen such that STO crystallites precipitate prior to heating. However, through the newly developed microwave-assisted synthesis reported herein, STO nanocuboids can now be synthesized from more Ti^{4+} sources than previously possible.

3.3 EXPERIMENTAL

3.3.1 Materials and Instrumentation

Samples were analyzed by powder x-ray diffraction and electron microscopyas described previously in *Peczak et al.*[42]

3.3.1.1 Inductively Coupled Plasma Optical Emission Spectrometry (ICP-OES)

Elemental Sr and Ti compositions in STO were measured by a Thermo iCAP 7600 Inductively Coupled Plasma Optical Emission Spectroscopy (ICP-OES) system operated through the Quantitative Bio-element Imaging Center at Northwestern University. STO samples (40 mg) were digested in aqua regia (15 mL) for 48 hours, after which 0.5 mL of the resulting solution was diluted twenty-fold with a 2 % HNO_3 / HCl solution in water (10 mL total sample volume) and analyzed. Five stock solutions were made by serial dilution from Sr and Ti standards to span a range of 1 – 40 ppm for each metal for calibration. A calibration curve was computed internally through the ICP-OES system software. Final concentration data were converted to molar amounts and divided to obtain a value of the Sr/Ti ratio. Standard deviation of the Sr/Ti ratio was computed through error propagation of the standard deviation associated with the measurements of Sr and Ti concentrations in the ICP sample. The details of this calculation are presented below in the *Statistical Analysis* sub-section.

3.3.2 $SrTiO_3$ Synthesis

3.3.2.1 Safety Note: Handle with care. Perchlorate salts are a class of potentially explosive chemicals when subjected to certain conditions. These chemicals can release a destructive amount of pressure, gas, or heat when subjected to certain conditions such as high temperature or source of ignition. These compounds also tend to be strong oxidizers. Contact with other materials may cause and/or intensify fires.

All $SrTiO_3$ nanoparticle samples were obtained by first synthesizing a Sr-Ti-OH mixture and then heating it (see scheme below). Sr-Ti-OH mixtures were synthesized from various Sr^{2+} sources ($SrCO_3$, $Sr(C_2H_4O_2)_2$, $Sr(NO_3)_2$, $Sr(OH)_2{\cdot}8H_2O$, $Sr(C_2H_4O_2)_2{\cdot}0.5H_2O$, $Sr(ClO_4)_2{\cdot}3H_2O$, $SrCl_2{\cdot}6H_2O$), and various Ti^{4+} sources ($TiCl_4$, $Ti(OCH_2CH_3)_4$, $Ti(OC_3H_7)_4$, $Ti(OCH(CH_3)_2)_4$, $Ti(OC_4H_9)_4$, $Ti(OC(CH_3)_3)_4$, $[NH_4CH_3CH(O-)CO_2]_2Ti(OH)_2$]). Hydrothermal heating was done either by convection heating or microwave heating (see below). Both techniques were used to treat Sr-Ti-OH mixtures synthesized on various scales.

(*Sr-Ti-OH mixture synthesis*) + (*heating method*) = *$SrTiO_3$ nanoparticles*

3.3.3 Sr-Ti-OH Mixture Creation with Ethanol

3.3.3.1 Lab Scale

Solution A: As-received Sr^{2+} reagents (10.0 mmol, Sigma Aldrich) were added to acetic acid (0.05 mol, Sigma Aldrich, 99.5%) in deionized water (50 mL) and stirred for 10 minutes.

Solution B: As-received Ti^{4+} reagents (9.1 mmol, Sigma Aldrich) were added to ethanol (20 mL, absolute) in a 50 mL beaker via Luer Lock syringe and stirred for 10 minutes. **Solution A** and **Solution B** were combined to make **Solution AB** and stirred for 10 minutes to ensure homogeneity. Next, **Solution AB** was added into a NaOH solution (13 mL, 10 M) to synthesize the designated **Sr-Ti-OH** mixture. In situations where a final nanoparticle synthesis was pursued, this **Sr-Ti-OH** mixture was transferred in its entirety to a hydrothermal reactor and heated, as described below. In the case of gel precursor analyses without hydrothermal heating, this Sr-Ti-OH mixture was transferred to a 50 mL Falcon tube. It was then centrifuged at 4500 rpm for 5 minutes, after which the white gel at the bottom of the centrifuge tube was separated from the supernatant, spread thin on a crucible, and analyzed by powder x-ray diffraction or electron microscopy. This was done immediately after separation to avoid gel decomposition in air. This method is derived from the process published by Peczak et al.[42]

3.3.3.2 Large Scale

Sr-Ti-OH mixtures for large scale, convection-based hydrothermal synthesis in a 4 L reactor were conducted as described previously in Peczak et al.[42]

3.3.4 Sr-Ti-OH Mixture Creation without Ethanol

3.3.4.1 Lab Scale. As-received Sr^{2+} reagents (9.1 mmol, Sigma Aldrich), were added into a 1 M solution of acetic acid (0.05 mol, Sigma Aldrich, 99.5 %) in de-ionized water (50 mL) and stirred for 10 minutes to ensure dissolution. Next, an as-received Ti^{4+} source (9.1 mmol, Sigma Aldrich) was added to the Sr^{2+} solution, and the resulting Sr/Ti bimetallic solution was allowed to stir for 10 minutes. Depending on which

Ti^{4+} source was used, either a white precipitate formed, a polymeric network formed, or no solid formed. The Sr/Ti bimetallic solution was next added to a NaOH solution (10 M, 30 mL) and stirred for 10 minutes to form the final Sr-Ti-OH mixture. In situations where a final nanoparticle synthesis was pursued, this **Sr-Ti-OH** mixture was transferred in its entirety to a hydrothermal reactor and heated, as described below. In the case of gel precursor analyses without hydrothermal heating, this Sr-Ti-OH mixture was transferred to a 50 mL Falcon tube and isolated for analysis as described above.

3.3.4.2 Large Scale. Only one Sr-Ti-OH mixture was synthesized without ethanol on a scale larger than 125 mL. $Sr(OH)_2{\cdot}8H_2O$ (77.8 g, 0.29 mol) was added into a solution of acetic acid (71.7 g, 1.20 mol) and double de-ionized water (450 g) in a 1 L beaker and stirred for 10 minutes. $[NH_4CH_3CH(O\text{-})CO_2]_2Ti(OH)_2$ (50% by weight solution in water, Sigma Aldrich, 172.18 g, 0.59 mol) was added into this solution, which then turned yellow. The resulting Sr/Ti bimetallic solution was allowed to stir for 10 minutes, after which it was added into a separate 1 L beaker containing 10 M NaOH (316 mL, 3.16 mol). The resulting gel was stirred for 15 minutes.

3.3.5 Hydrothermal Synthesis by Convection Heating

Convection-based hydrothermal heating at both the 125 mL scale and 4 L scale were conducted as described in Peczak et al.[42]

3.3.6 Hydrothermal Synthesis by Microwave Heating

Microwave experiments were conducted in a Milestone synthWAVE Single Reaction Chamber reactor. A pre-determined **Sr-Ti-OH** mixture (~800 mL) was transferred to a 1 L Teflon liner, which was inserted into the synthWAVE reactor. A heat treatment was applied consisting of: 1) a 30 minute ramp to a selected temperature (120 – 240 ^oC); 2) a hold time of 2 – 16 h with 50% maximum stir speed, and 3) a 30 min cool step back to ambient temperature. The resulting white precipitate was washed repeatedly with deionized water via vacuum filtration until the water in the Buchner funnel was pH 7. The wet powder was then removed from the funnel and dried in air in an oven (110^oC, overnight).

3.3.7 Statistical Analysis

All data presented in this work was processed as collected without any pre-processing, normalization, or removal of outliers. Data corresponding to average particle sizes is presented as the mean and standard deviation of values measured. For each measurement of average size, around 200 nanoparticles were counted. Percentages of nanocuboids per sample were calculated by counting the number of particles identified as 'nanocuboids', and dividing by the total number of particles observed in the corresponding micrograph (see below). For each calculation of the percent nanocuboids in a sample, 300 nanoparticles were considered and identified as either 'nanocuboids' or 'not nanocuboids' (**Equation 3.1**). Calculations of average particle size and percent nanocuboids were conducted in Microsoft Excel, and the relevant data were collected using ImageJ.

(Eq. 3.1): *% Nanocuboids = (# Nanocuboids Observed) / (# Total Particles Observed)*

Average crystallite size for powder x-ray diffraction samples was calculated using the Debye Scherrer equation within the MDI Jade software package.[161] Standard deviation associated with Sr/Ti ratio calculations (***r***) was measured by error propagation of the standard deviation associated with the Sr and Ti concentrations measured by ICP-OES as demonstrated below (**Equations 3.2 – 3.4**). Equations 3.2 & 3.3 were used to calculate the standard deviation associated with mass and molar amounts of both Sr and Ti, but are shown below only for Sr for conciseness.

(*Eq. 3.2*): $$\sigma_{mass\ Sr} = \sigma_{mass\ Sr} * 10^{-6} * 0.04\ g$$

(*Eq. 3.3*): $$\sigma_{mol\ Sr} = \frac{\sigma_{mass\ Sr}}{Molar\ Mass\ Sr}$$

(*Eq. 3.4*): $$\sigma_r = r\sqrt{\left(\frac{\sigma_{mol\ Sr}}{mol\ Sr}\right)^2 + \left(\frac{\sigma_{mol\ Ti}}{mol\ Ti}\right)^2}$$

3.4 RESULTS & DISCUSSION

3.4.1 Phase Composition of Pre-Hydrothermal Sr-Ti-OH Mixtures

Previously, Peczak et al demonstrated that to obtain a highly cubic STO sample after a one-step convection heat treatment, STO nanocrystals must precipitate prior to hydrothermal synthesis.[42] For the reported synthesis, which used $Sr(OH)_2{\cdot}8H_2O$ and $TiCl_4$ as starting reagents, this was accomplished by specifying an order of operations to ensure that the pre-hydrothermal Sr-Ti-OH reaction mixture ("Sr-Ti-OH") rapidly reached pH 14. Under these conditions, STO is the thermodynamically most stable phase and therefore precipitates. Subsequent hydrothermal heating is likely responsible for {100} facet growth on particles, which affords the final highly cubic product. To explore whether this phenomenon occurs in other reaction systems, Sr-Ti-OH reaction mixtures made with varied starting sources of Sr^{2+} and Ti^{4+} were synthesized without heating and then isolated and analyzed by powder x-ray diffraction. All Sr-Ti-OH mixtures were created using 10 M NaOH.

Figure 3.1 presents a graphical depiction of a 'stoplight' screening method used to compare new Sr-Ti-OH mixtures (synthesized from seven Ti^{4+} sources and seven Sr^{2+} sources with Sr(OH)2.8H2O and $TiCl_4$ serving as a control), to that previously reported by Peczak et al. By this method, Sr-Ti-OH reaction mixtures from which only crystalline STO precipitated (> 99.9 %, as determined by powder x-ray diffraction) were considered satisfactory (i.e., green, **Figure 3.2a**), as these mixtures can be converted into highly cubic products with a one-step convection heat treatment. Sr-Ti-OH reaction mixtures from which either amorphous or weakly crystalline materials precipitated (as determined by the final x-ray diffraction pattern) were considered less desirable, (i.e., red, **Figure 3.2b**).

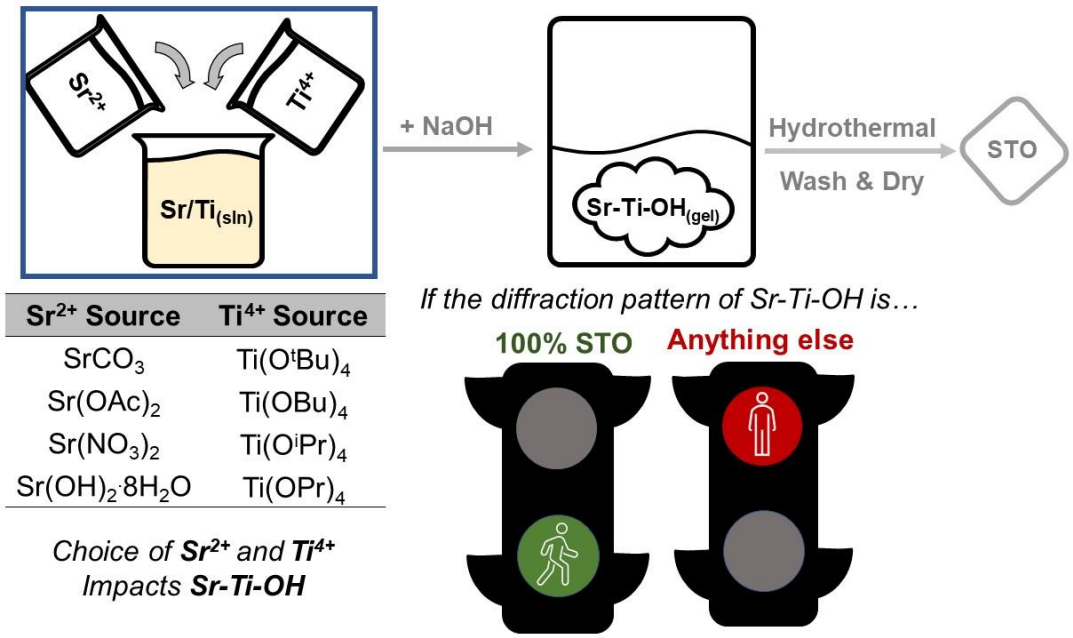

Sr^{2+} Source	Ti^{4+} Source
$SrCO_3$	$Ti(O^tBu)_4$
$Sr(OAc)_2$	$Ti(OBu)_4$
$Sr(NO_3)_2$	$Ti(O^iPr)_4$
$Sr(OH)_2{\cdot}8H_2O$	$Ti(OPr)_4$

*Choice of **Sr^{2+}** and **Ti^{4+}** Impacts **Sr-Ti-OH***

Figure 3.1. Synthesis of Sr-Ti-OH Reaction Mixtures for Screening by X-Ray Diffraction. Sr^{2+} solutions were made in 1 M CH_3COOH with one of the reagents listed in the "Sr^{2+} Source" column, and Ti^{4+} solutions were made in ethanol with one of the reagents listed in the "Ti^{4+} Source" column. These two solutions were combined and introduced into a 10 M NaOH solution. After stirring, the resulting Sr-Ti-OH mixture was centrifuged, and a gel material was removed for analysis by powder x-ray diffraction.

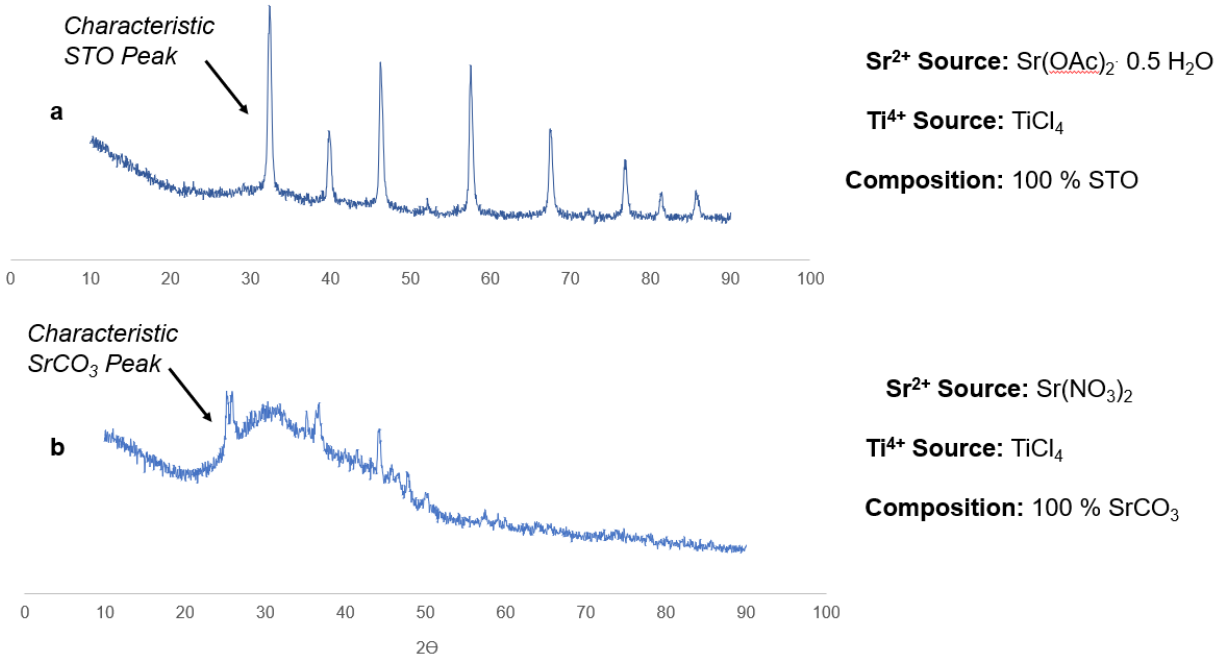

Figure 3.2. Sr-Ti-OH Mixtures for STO Samples in Figure 1 that were Highly Cubic (a) and Irregular (b) After Heating. The Sr-Ti-OH mixture characterized in **S2a** became a highly cubic STO sample after heating, while the Sr-Ti-OH mixture in **S2b** became an irregular STO sample after heating. The diffraction pattern in **S2a** corresponds to a "100 % STO" pattern that has been shown to make nanocuboids, while the diffraction pattern in **S2b** corresponds to a "weakly crystalline" pattern with a $SrCO_3$ primary phase. The "weakly crystalline" designation was assigned because of the low signal-to-noise ratio shown in the pattern.

First, $Sr(OAc)_2$, $Sr(Oac)_2{\cdot}0.5H_2O$, $Sr(NO_3)_2$ and $SrCO_3$, $Sr(ClO_4)_2{\cdot}3H_2O$, and $SrCl_2{\cdot}6H_2O$ were used to synthesize a Sr-Ti-OH reaction mixture, which was then analyzed to determine phase composition. Molar amounts of each Sr^{2+} starting reagent were chosen to meet a global ratio of 1.05 : 1 of Sr to Ti, and the average crystallite size for the primary phase of each mixture was measured by a Debye Scherrer peak broadening analysis. $TiCl_4$ was used as the Ti^{4+} source for all samples in these experiments. The findings are displayed below in **Table 3.1**. Several Sr-Ti-OH mixtures derived from various Sr^{2+} sources precipitated STO without any secondary phases. When $Sr(OAc)_2$, $Sr(OAc)_2{\cdot}0.5H_2O$,

and $SrCO_3$ were used as the Sr^{2+} source, STO crystallites precipitated from solution, while the NO_3^-, ClO_4^-, and Cl^- anions prevented STO precipitate formation. For all samples that precipitated STO, average STO crystallite sizes were between 18 – 24 nm, which is generally equivalent to those measured from Sr-Ti-OH mixtures synthesized with $Sr(OH)_2{\cdot}8H_2O$ and $TiCl_4$, as previously reported (repeated in **Table 3.1**).

Table 3.1. Variation of Sr^{2+} Source and Resulting Crystalline Composition of Final Sr-Ti-OH Mixture. All Sr-Ti-OH mixtures were synthesized with the designated Sr^{2+} reagent in 1M CH_3COOH in water, with $TiCl_4$ as a Ti^{4+} source in 20 mL ethanol, and 15 mL of 10 M NaOH as a source of base. Average crystallite size was measured in MDI Jade by peak broadening analysis.[161]

Sr^{2+} Source	% STO	% $SrCO_3$	Average Crystallite Size (nm)
$Sr(OH)_2{\cdot}8H_2O$	> 99.9	0	20.7 ± 4.6
$Sr(NO_3)_2$	18.9	81.1	23.5 ± 7.0
$Sr(OAc)_2$	> 99.9	0	24.0 ± 9.1
$Sr(OAc)_2{\cdot}0.5H_2O$	> 99.9	0	18.3 ± 6.7
$Sr(ClO_4)_2{\cdot}3H_2O$	12.0	88.0	28.3 ± 6.7
$SrCO_3$	> 99.9	0	24.4 ± 7.3
$SrCl_2{\cdot}6H_2O$	0	100	24.8 ± 5.4

Literature reports propose a variety of mechanisms by which STO nanoparticles might form,[162] and two of the most common pathways proposed are the *dissolution-precipitation* and *in situ* transformation mechanisms.[85,162] Though there is ample evidence for each process, both require Sr^{2+} and

Ti^{4+} to combine in solution. Previous reports also note that Sr^{2+} may incorporate into hydrolyzed, Ti-containing structures as a prerequisite to precipitation.[91]

The precipitation of 100 % crystalline STO from four Sr-Ti-OH reaction mixtures in **Table 3.1** suggests that in these four mixtures, STO is the most thermodynamically stable phase, as has been observed previously in analogous systems.[42] In the case of the three Sr-Ti-OH reaction mixtures with a composition of 100 % $SrCO_3$, the precipitation of this strontium carbonate crystalline phase could be the result of a decrease in Sr-Ti-OH reaction mixture pH. Sr-Ti-OH reaction mixtures are highly basic, and so a non-negligible amount of CO_2 can be uptaken from air and lower solution pH to an intermediate range, making $SrCO_3$ the thermodynamically preferred phase instead of STO. Additionally, it is possible that $SrCO_3$ precipitation occurs because anions (e.g. NO_3^-, ClO_4^-) sterically interfere with the interaction of Sr^{2+} cations and Ti^{4+} or the hydrolysis of Ti^{4+}. Such cases can allow sufficient time for the local formation of $SrCO_3$ crystallites and amorphous titania. These phases would then precipitate and leave no metal ions from which to form STO.[43] A more thorough investigation of this phenomenon would require time-resolved, pH-controlled studies that track the evolution of various strontium and titanium species.

For the mixtures in **Table 3.1**, it is possible that for Sr-Ti-OH samples in which STO does not precipitate, a change in solution pH during mixing, which would no longer make STO the dominant phase and drive the formation of other compounds, or steric interference, which would prevent the interaction of Sr^{2+} and Ti^{4+} ions, occurs. For samples that did not precipitate STO, the counterions for each strontium reagent are the conjugate base of a strong acid, meaning that their presence likely does not alter the solution pH during mixing. Thus, NO_3^-, ClO_4^-, and excess Cl^- may sterically interfere with the interaction of Sr^{2+} and Ti^{4+} in solution. A more thorough investigation of this phenomenon requires time-resolved, pH-controlled studies that track the evolution of various strontium and titanium species, as has been done previously for titania sol-gel systems.

Two of the Sr-Ti-OH mixtures in **Table 3.1** were treated hydrothermally for 36 h at 240 ^oC in a 125 mL autoclave in a convection oven. The initial Sr-Ti-OH mixtures were characterized by x-ray diffraction, and the final products were characterized by both electron microscopy (**Figures 3.2, 3.3**). While both samples had crystalline compositions of > 99.9% STO, only the sample that precipitated STO prior to hydrothermal treatment produced a highly cubic final sample. These results support the previous

conclusion that STO nanocuboids form in a two-step precipitation and facet growth process and suggest that it is independent of reagent identity. The formation of the nanocuboid shape, which changes both the chemical (e.g. surface hydroxyl concentration) and physical (e.g. faceting) properties of the nanoparticle surface, is critical for use of STO as a catalyst support because it allows for epitaxial stabilization of Pt on STO, thereby preventing sintering during catalysis. Given that a beveled nanocuboid is the Wulff shape of STO in water, a one-step convection heating profile is likely not sufficient to drive both STO precipitation and facet growth, since all STO nanoparticles should rearrange to the Wulff shape under sufficient temperature and time.

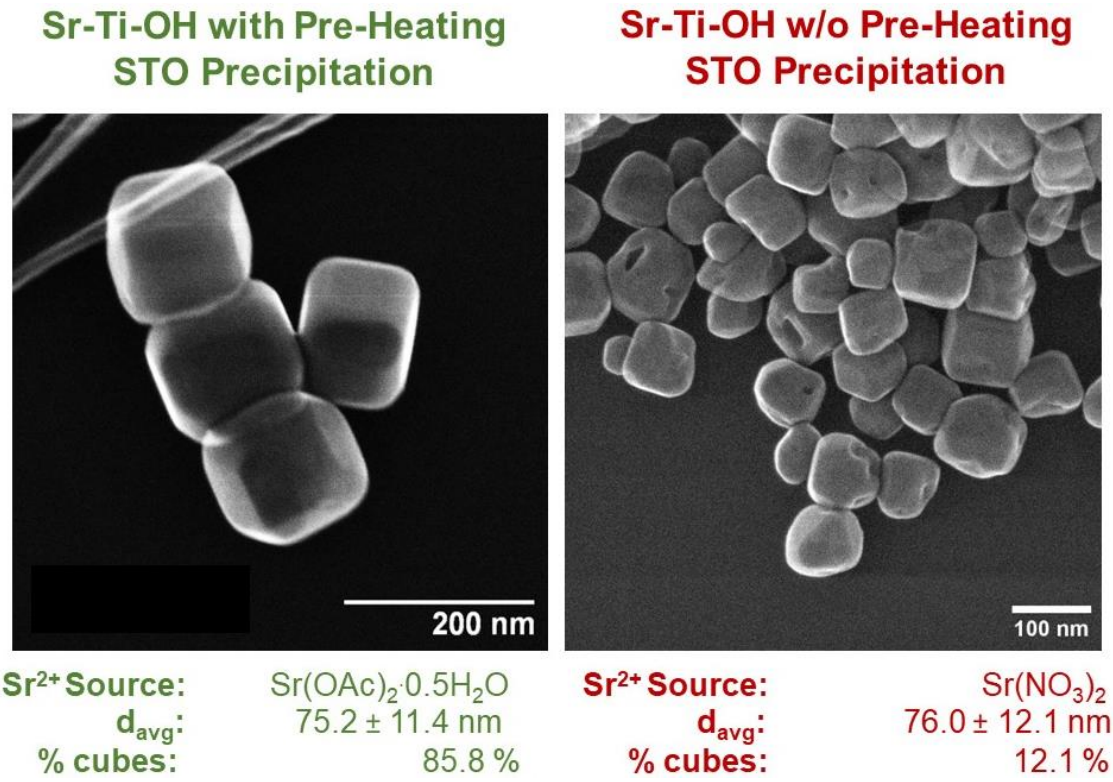

Figure 3.3. Secondary Electron STEM Micrographs of STO Samples After Hydrothermal Treatment of Sr-Ti-OH Mixtures that did (left) and did not (right) Precipitate STO Prior to Heating. The sample that precipitated STO prior to heating was synthesized using $Sr(OAc)_2$ as a Sr^{2+} source, while the sample that did not precipitate STO prior to heating was made using $Sr(NO_3)_2$ as a Sr^{2+} source. Both samples were made using $TiCl_4$ as a Ti^{4+} source. The results suggest that for unstirred convection heating in one-step heating profiles, STO nucleation prior to hydrothermal treatment is critical for the formation of highly cubic samples. For each sample above, 300 nanoparticles were imaged and analyzed to calculate the percentage of nanocuboids per sample, while 200 nanoparticles were imaged and analyzed to determine average particle size.

Next, analogous screening experiments were conducted by synthesizing Sr-Ti-OH mixtures with various Ti^{4+} sources. Four strontium reagents ($Sr(OAc)_2$, $SrCO_3$, $Sr(NO_3)_2$, and $Sr(OH)_2{\cdot}8H_2O$) were each used to synthesize gel mixtures with sodium hydroxide and one of five titanium sources: titanium ethoxide ($Ti(OEt)_4$), titanium propoxide ($Ti(OPr)_4$), titanium butoxide ($Ti(OBu)_4$), titanium tert-butoxide ($Ti(OtBu)_4$),

and titanium(IV) bis(ammonium lactato) dihydroxide (TiBALD). Titanium alkoxide sources were used because they did not require harsh conditions for dissolution in water or ethanol. The strontium sources chosen were those that successfully precipitated STO prior to heating in previous experiments. $Sr(NO_3)_2$ was also tested to determine whether samples that did not precipitate STO when mixed with $TiCl_4$ could precipitate STO when mixed with different reagents. Each mixture was separated from its supernatant by centrifugation and analyzed by powder x-ray diffraction. These Sr-Ti-OH mixtures were synthesized both with and without ethanol, and experiments are grouped as such in the top and bottom halves of **Figure 3.4**, respectively. Each strontium or titanium reagent is labeled by the anion to which it corresponds, i.e. a sample synthesized with titanium tert-butoxide is listed in the row labeled "O^tBu^-", and a sample synthesized with strontium carbonate is listed in the column labeled "CO_3^{2-}".

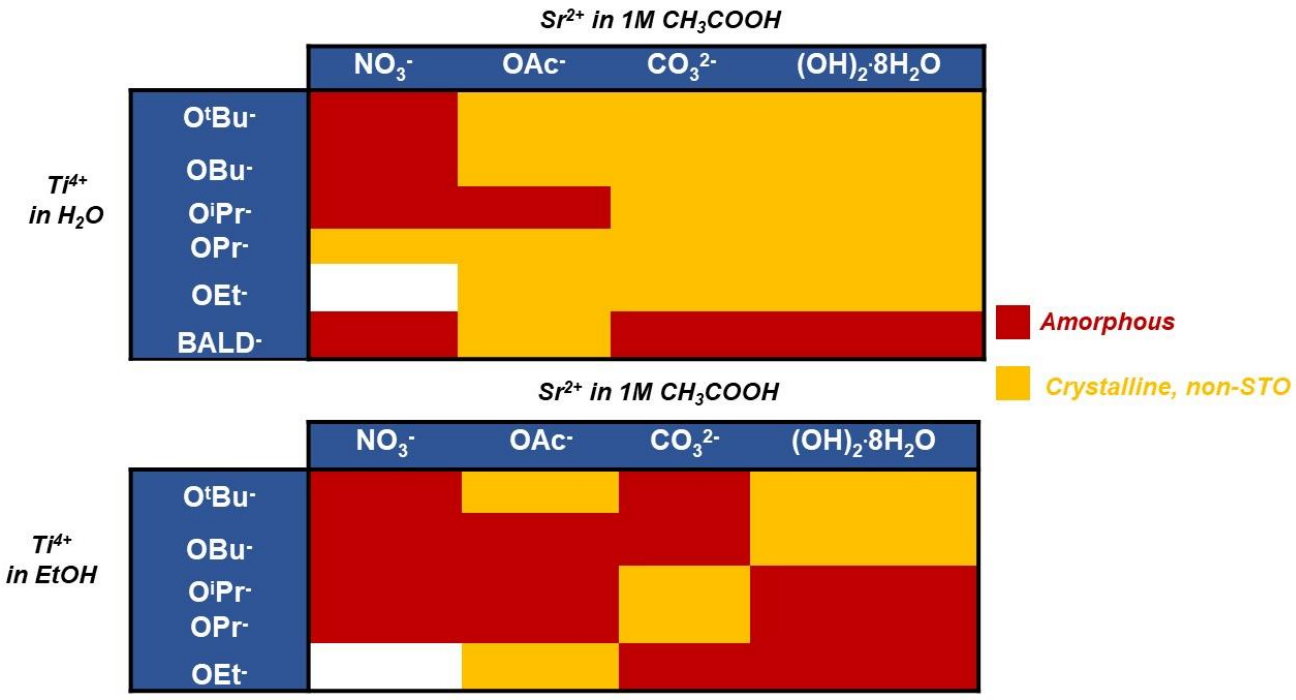

Figure 3.4. Powder X-Ray Diffraction Characterization of Sr-Ti-OH Reaction Mixture Precipitates (Varied Sr^{2+} and Ti^{4+} Sources, With and Without Ethanol as a Solvent). Six Ti^{4+} sources were tested for comparison against $TiCl_4$, which serves as a control against which to benchmark the results above.[42] None of the combinations tested precipitated STO prior to hydrothermal treatment. All samples were either amorphous, weakly crystalline, or crystallized a product other than STO. Boxes that are colored white denote a combination that was not tested. Phase determination was conducted using MDI Jade software.[161]

STO crystallites never precipitate from Sr-Ti-OH reaction mixtures that are synthesized with titanium sources other than $TiCl_4$. All permutations tested formed samples that were either amorphous, weakly crystalline, or a crystalline phase that was not STO. Of the samples that were crystalline, all observed phases were either unwanted side products, such as $SrCO_3$, or crystalline byproducts that could not be identified, likely sodium-titanium complexes. **Figures 3.2a & 3.2b** show representative diffraction patterns that are 100% STO and weakly crystalline $SrCO_3$, respectively. Additionally, the following representative diffraction patterns are provided in the supplementary information with important features

noted: an amorphous diffraction pattern (**Figure 3.5a**), a weakly crystalline diffraction pattern with phases other than $SrCO_3$ (**Figure 3.5b**), and a crystalline diffraction pattern that is likely reformed $Sr(OH)_2{\cdot}8H_2O$ (**Figure 3.5c**).

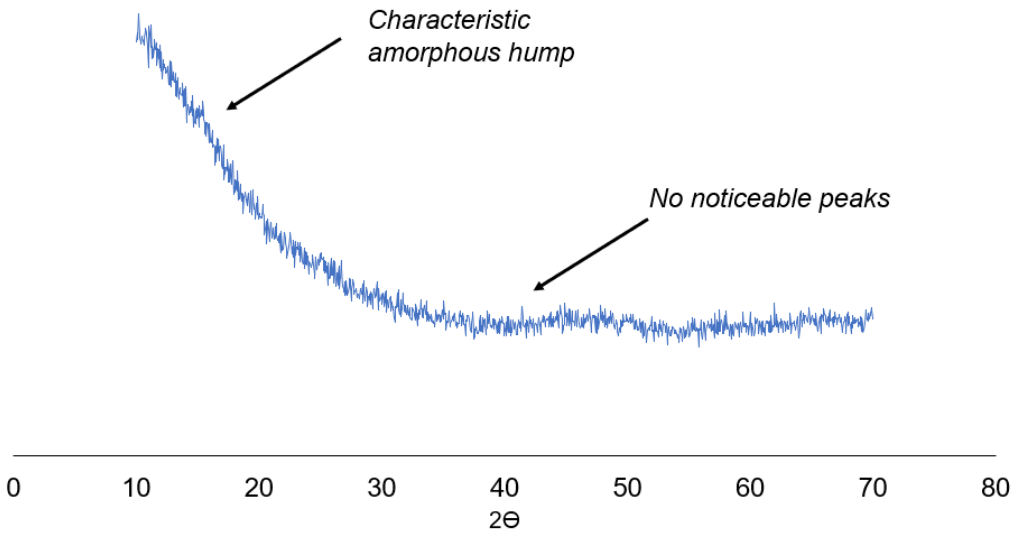

Figure 3.5a. Representative Powder X-Ray Diffraction Pattern for Sr-Ti-OH samples labeled "Amorphous". In these cases, no crystalline phase is identified in the sample after synthesizing a Sr-Ti-OH gel from the designated Sr^{2+} and Ti^{4+} sources in 10 M NaOH. All Sr-Ti-OH samples designated "amorphous" produced diffraction patterns like this one when characterized.

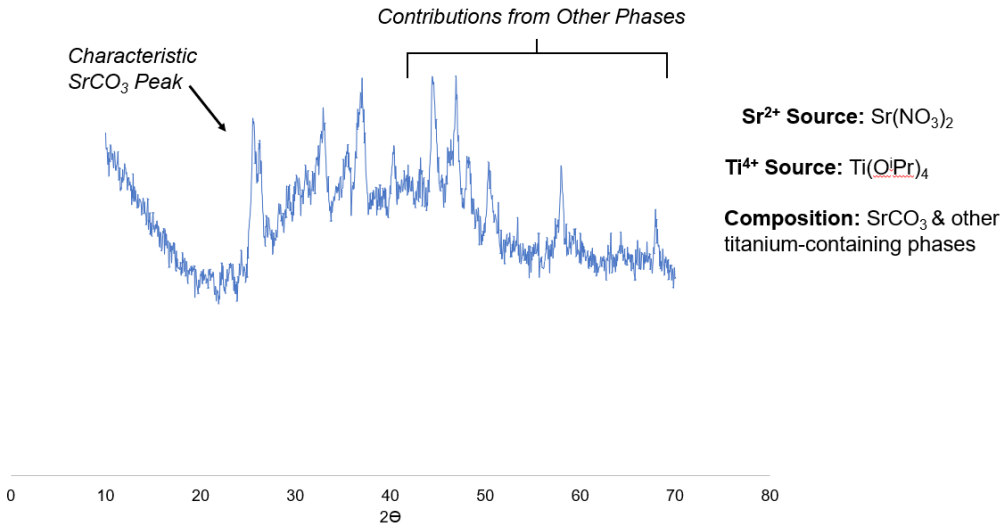

Figure 3.5b. Representative Powder X-Ray Diffraction Pattern for "Weakly Crystalline" Diffraction Pattern in Figure 2 with Phases other than $SrCO_3$. In such patterns, characteristic peaks corresponding to $SrCO_3$ are observed. However, other peaks are observed in the pattern that are likely due to titanium-containing phases, such as sodium-titanium complexes. The low signal to noise ratio also suggests that a significant portion of the Sr-Ti-OH mixture is amorphous.

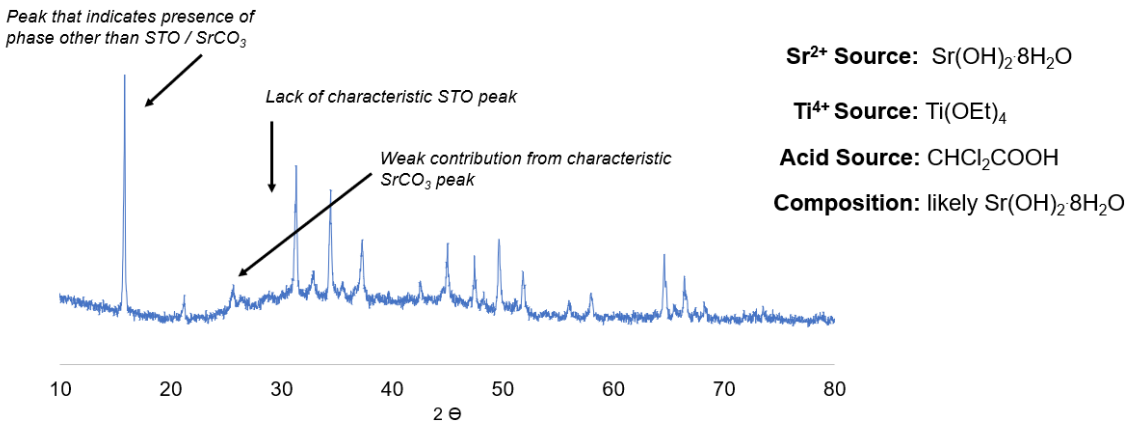

Figure 3.5c. Representative powder x-ray diffraction pattern for crystalline diffraction pattern where $Sr(OH)_2{\cdot}8H_2O$ is likely the primary phase**.** In these cases, a crystalline phase is observed upon synthesis of the Sr-Ti-OH mixture. However, there is no $SrTiO_3$ in this mixture, and the contribution from $SrCO_3$ does not explain all peaks in the diffraction pattern.

The use of $TiCl_4$ as a Ti^{4+} source appears to be crucial to precipitating STO. This is likely because generation of hydrochloric acid produces a low pH in the titanium-ethanol solution. The low pH may stabilize Ti^{4+} complexes in solution prior to mixing with NaOH and therefore prevent the creation of a solution with intermediate pH, where other phases are more stable.[163–168] Specifically, the titanium alkoxide compounds used in the experiments reported in **Figure 3.4** are known to form amorphous, polymeric networks in solution, often *sol-gel* structures, because the metal-oxygen bond is susceptible to nucleophilic attack.[169–181] For systems containing Ti^{4+} at low pH, such as Sr-Ti-OH mixtures made with $TiCl_4$, previous reports suggest that Ti^{4+} adopts a variety of soluble hydrolyzed and semi-hydrolyzed forms (e.g. $Ti(OH)_2^{2+}$, $Ti(OH)_3^{+}$, and $Ti(OH)_4$), which likely prevents other structures from forming.[135,182–184] If $TiCl_4$ is used, there are no competing anions to interfere with STO precipitation. The alkoxide ligands mentioned previously are conjugate bases to weak acids, and the weak acids likely form in solution upon creation of the Sr-Ti-OH mixture through the consumption of protons, which raises the solution pH and creates an environment ($3 < pH < 9$) in which *sol-gel* structures are more stable than STO.[42,134] Moreover,

in this pH range, $SrCO_3$ is the most stable strontium-containing phase,[134] and trace amounts of it were observed in some of the weakly crystalline powder patterns corresponding to the experiments in **Figure 3.4**. Sr-Ti-OH mixtures synthesized with the TiBALD solution do not react with water because the complexing ligands stabilize Ti^{4+} against nucleophilic attack.[156] However, the corresponding diffraction patterns were amorphous because the bidentate ligands coordinated to the Ti metal center likely stayed coordinated during mixing, preventing the interaction of Sr^{2+} and Ti^{4+} to form STO.

Based on conclusions drawn from the results in **Figure 3.4**, lowering the solution pH below 3 in a Sr/Ti solution made with titanium alkoxide complexes may drive the precipitation of STO in the final pH 14 Sr-Ti-OH mixture. Currently, an important source of acidity in the synthesis is acetic acid (pK_a = 4.76), which is used to dissolve the Sr^{2+} precursor in water. In place of acetic acid, several moderately strong acids with lower pK_a values were tested to determine whether STO could precipitate under these conditions. First, a 1 M solution in water was created with one of six acids (listed below in **Figure 3.6**), and 9.1 mmol $Sr(OH)_2{\cdot}8H_2O$ was added into this solution and allowed to dissolve. Next, one of four titanium alkoxide precursors was added into the acidic strontium-containing solution to create a bimetallic Sr/Ti solution in just water. Finally, this bimetallic solution was added to a 10 M NaOH solution to create the Sr-Ti-OH mixture. A cartoon schematic of this is presented in **Figure 3.6** to aid visualization, and the final compositions of each Sr-Ti-OH mixture as analyzed by powder x-ray diffraction are presented in **Figure 3.6** as well.

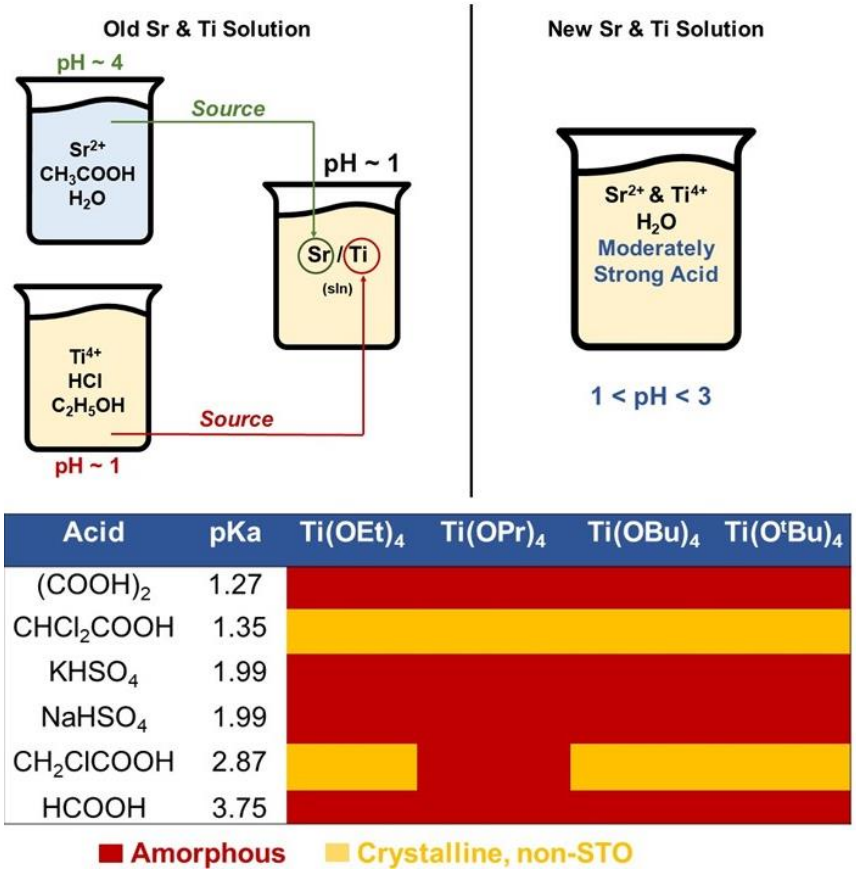

Figure 3.6. Sr-Ti-OH Reaction Mixtures Synthesized from a Bimetallic Sr/Ti Solution (no Ethanol, Acetic Acid Substituted for a Moderately Strong Acid). In place of a two-solvent bimetallic Sr/Ti solution, in which 1M CH_3COOH in H_2O dissolves an Sr^{2+} source and $TiCl_4$ is dissolved in ethanol, a Sr/Ti solution was created with only water and a moderately strong acid with a pK_a value between 1 and 4. These Sr-Ti-OH reaction mixtures were synthesized by dissolving the Sr^{2+} precursor in 50 mL water and 1M of the chosen acid in H_2O, after which the corresponding Ti^{4+} alkoxide was added. The resulting Sr-Ti-OH mixture was isolated and analyzed by powder x-ray diffraction. All samples were either amorphous or weakly crystalline. Phase compositions were determined using MDI Jade software.[161]

No Sr-Ti-OH mixture created with a moderately strong acid precipitated $SrTiO_3$ prior to heating, and final mixture composition was independent of acid pK_a. All Sr-Ti-OH mixtures were amorphous or insoluble byproducts, such as strontium oxalate, or $Sr(OH)_2{\cdot}8H_2O$ (**Figure 3.5c**). These investigations into

the phase composition of various Sr-Ti-OH mixtures may clarify why many hydrothermal syntheses for STO nanocuboids utilize $TiCl_4$ as a Ti^{4+} source. Most reported hydrothermal syntheses of STO are conducted in unstirred autoclave reactors with convection heating, and under these conditions, it is critical that STO precipitate prior to heating because heat treatment alone is not sufficient to drive STO formation and {100} facet growth.

3.4.2 STO Synthesis with $TiCl_4$ Using Microwave-Assisted Heating

STO support samples were synthesized in a 1 L microwave reactor at 200 ^oC for 8 h using $TiCl_4$ as a Ti^{4+} source to afford products with masses of 12.1 g and 21.5 g that contained 80.2 % and 82.9 % nanocuboids, respectively, with product yields of 90.3 % and 80.2 %. The output was increased from the 10 g scale to the 20 g scale by doubling the concentration of reagents used in the Sr-Ti-OH mixture. These reaction mixtures were analyzed both prior to and after hydrothermal treatment (**Figures 3.7, 3.8**) by transmission electron microscopy and powder x-ray diffraction.

The percentage of nanocuboid particles per sample is around 80% for both syntheses, which is equivalent to the percentages reported for STO samples made by convection heating. The average particle sizes are dependent on starting reagent concentration, and the particle sizes reported in **Figure 3.8** are consistent with starting reagent concentrations reported for equivalent samples synthesized by convection heating in a 125 mL reactor in Peczak et al . **Figure 3.7** shows powder x-ray diffraction patterns and electron micrographs of the pre-hydrothermal Sr-Ti-OH mixtures used for STO synthesis at the 1 L scale. These gel mixtures were analyzed and compared to Sr-Ti-OH mixtures synthesized at the 125 mL scale. Precipitation of $SrTiO_3$ nanocrystals is still observed, and the average size of these crystallites is equivalent to that observed at the 125 mL scale. The morphology of the precipitated STO particles is irregular as observed in earlier works.

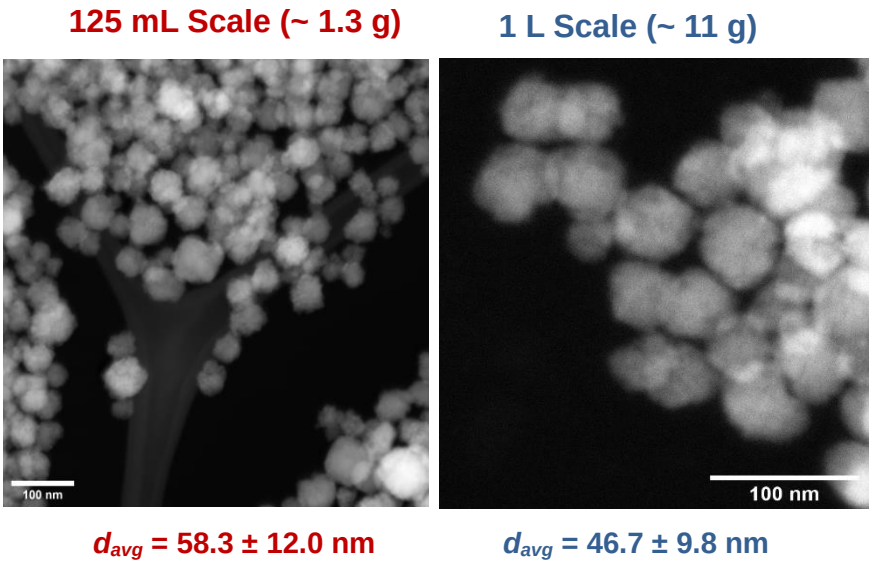

Figure 3.7a. STEM HAADF Micrographs of Sr-Ti-OH Mixtures Prior to Hydrothermal Treatment For 125 mL and 1 L Scale Syntheses. Both products are 100% crystalline $SrTiO_3$ according to analysis by x-ray diffraction.

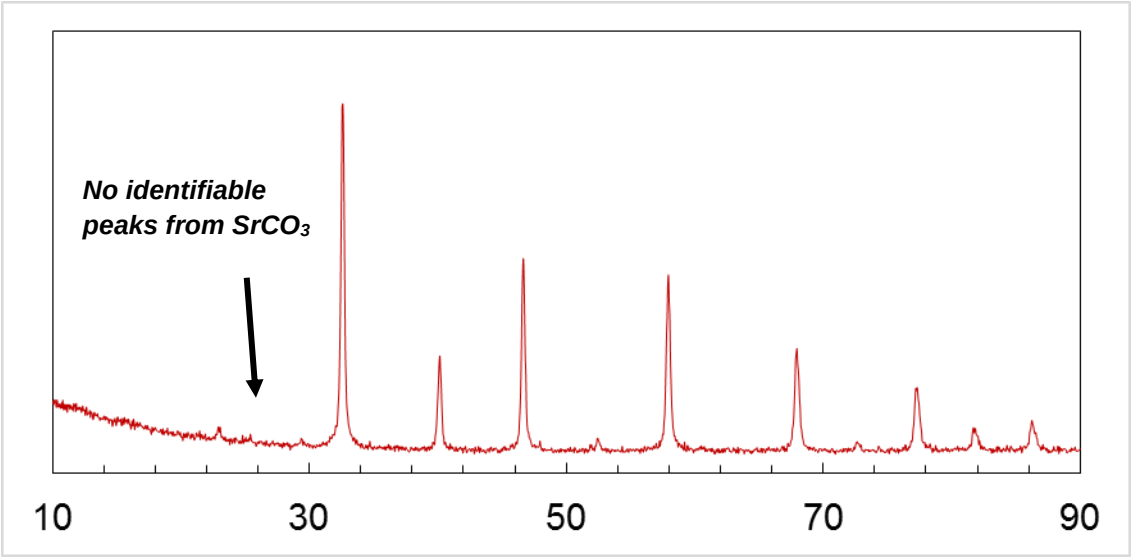

Figure 3.7b. X-Ray Diffraction Pattern of Post-Reaction MAH STO Product. This powder pattern shows a crystalline sample composed of 100% $SrTiO_3$ and no $SrCO_3$ by-product.

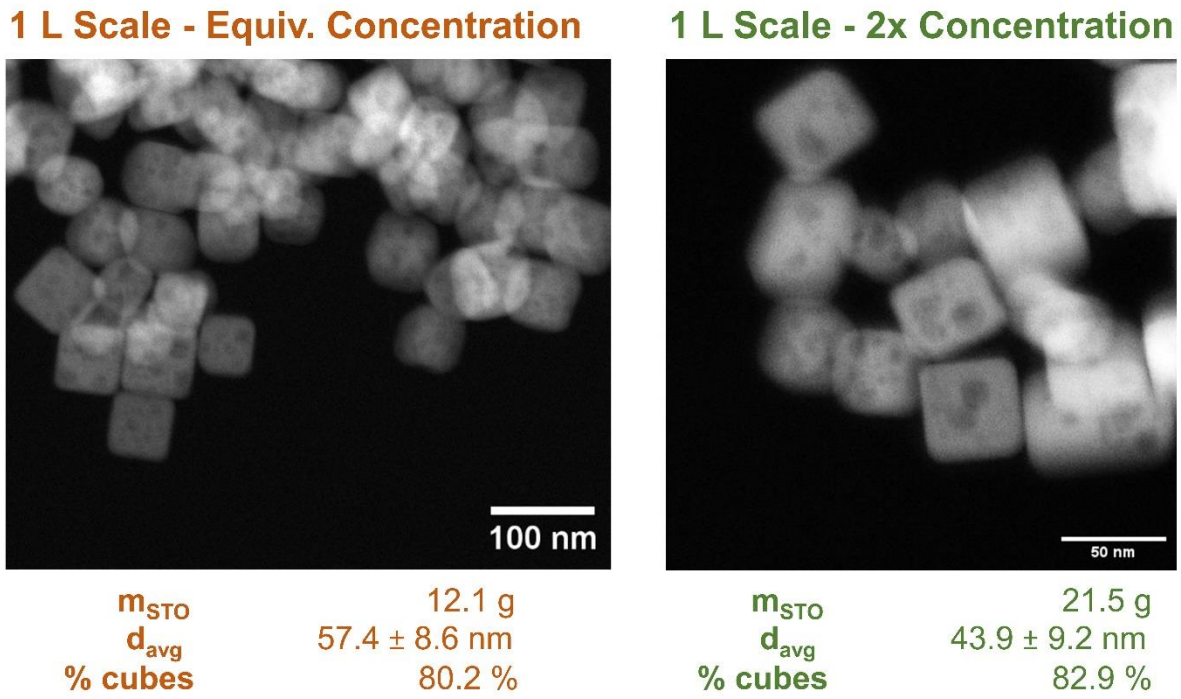

Figure 3.8. High Angle Annular Dark Field (HAADF) STEM Micrographs of MAH STO Samples Synthesized in a 1L Reactor. Two STO samples were synthesized at equivalent concentrations to the reaction mixture reported by Peczak et al. and at double this concentration, to afford highly cubic STO samples with masses of 12.1 g (90.3 % yield) and 21.5 g (80.2 % yield), respectively. The percentages of nanocuboids per sample appear to be generally equivalent for both the “Equiv. Concentration” and “2x Concentration”, and the differences are likely due to batch-to-batch variation. Shapes resembling pores in the STO material are Kirkendall voids internal to each particle and have been observed in previous works. The size decrease across samples is consistent with the previously reported relationship between starting reagent concentration and final particle size. [42]

As previously stated, because a beveled nanocuboid is the Wulff shape of STO in water, under sufficiently high temperatures and long reaction times, all $SrTiO_3$ nanoparticles in a water-based reaction medium should rearrange to this shape.[185–187] To confirm this, irregularly shaped STO nanoparticles were introduced into a pH 14 water-ethanol solution and heated hydrothermally (240 °C, 72 h). After washing, filtering, and drying, the final product was observed to be highly cubic (**Figure 3.9**).

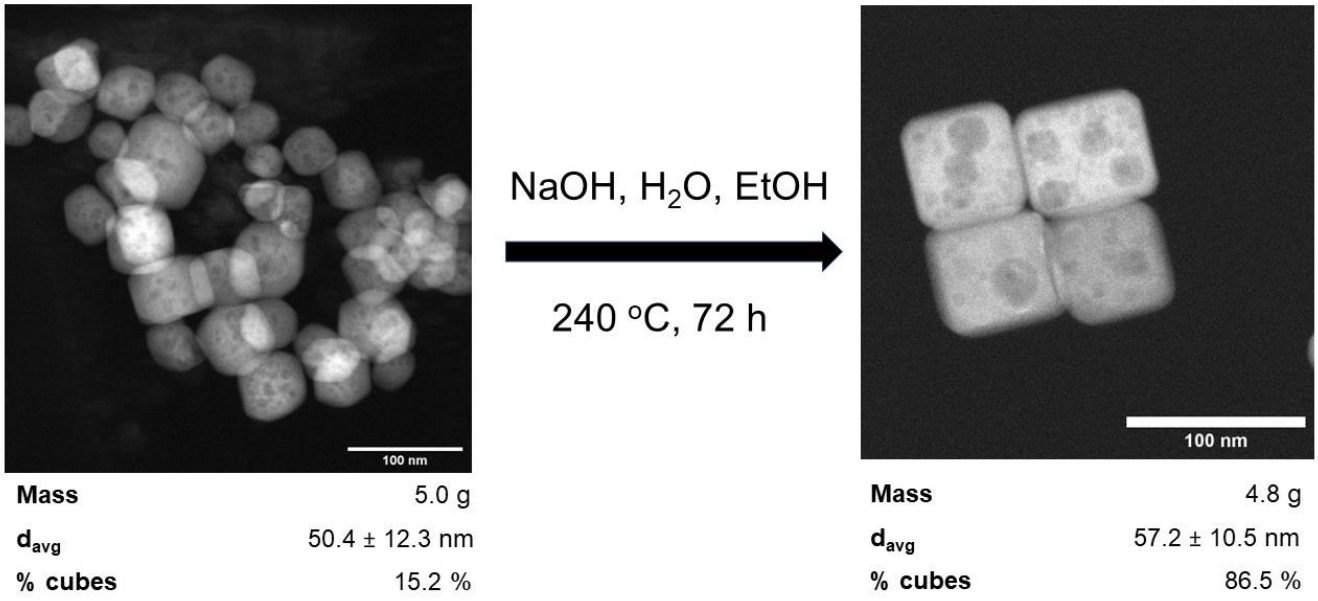

Figure 3.9. HAADF STEM Micrograph of Re-Treated STO Nanocuboid Supports. 5g of non-cubic STO nanoparticles were introduced into a supernatant with 50 mL water, 20 mL ethanol, and 13 mL of 10 M NaOH, respectively, and treated in a convection-based hydrothermal oven in a 125 mL reactor for 72 h at 240 °C (1 oC/min ramp, ambient cooling). After centrifuging and washing the sample to pH 7, the final product was analyzed by TEM and shown to be generally equivalent to previous cubic samples.

However, to further optimize the STO synthesis in pursuit of commercial viability, it is important to understand how the amount of nanocuboid particles that form per sample is affected by reaction time,

reaction temperature, heating method, and stirring. Specifically, it is important to identify the minimum temperature and time required for synthesizing highly cubic samples using both microwave heating (MAH) and convection heating (CH). Synthesizing STO materials at this minimum temperature (i.e. optimizing the temperature) will facilitate future development of an economically viable STO synthetic process. Thus, STO samples were synthesized over a range of reaction times and at several temperatures using stirred microwave heating, unstirred convection heating, and stirred convection heating in a 4 L batch reactor. In each case, average particle sizes and percent nanocuboids per sample were measured. Average STO particle sizes are tabulated in **Table 3.2** and **Table 3.3**, and a graph of percent nanocuboids per sample versus time for each condition is presented below in **Figure 3.10**. A version of **Figure 3.10** containing information on average particle size is presented in the supplementary information (**Figure 3.11**). Moreover, to aid visualization of the results conducted in this work, the experimental design used in this work is presented in the supplementary information (**Table 3.4 a & b**). Here, the three heating profiles tested on all Sr-Ti-OH reaction mixtures are presented (**Table 3.4 a**), as are lists of all seven Ti^{4+} sources and seven Sr^{2+} sources used to synthesize Sr-Ti-OH mixtures (**Table 3.4 b**).

Table 3.2. Average Particle Sizes for STO Nanoparticles Synthesized at Varied Times and Temperatures by Both Microwave Heating (*MAH-STO*) and Convection Heating (*CH-STO*).

MAH-STO			CH-STO		
Temperature	**Time (h)**	**d_{avg} (nm)**	**Temperature**	**Time (h)**	**d_{avg} (nm)**
140 °C	2	50.4 ± 12.3	120 °C	2	75 ± 20.3
	4	48.2 ± 11.3		8	61.7 ± 12.2
	8	49.6 ± 8.6		16	70.0 ± 14.6
	16	51.3 ± 13.9		32	54.7 ± 11.8
200 °C	2	47.3 ± 7.8	240 °C	2	54.4 ± 12.1
	4	47.1 ± 10.0		4	65.4 ± 13.4
	8	57.4 ± 8.6		8	64.2 ± 14.8
	16	58.9 ± 10.5		12	54.8 ± 9.8
				36	65 ± 10

Table 3.3. Average Size and % Cubes per Sample for STO Samples Synthesized in a 4 L Hydrothermal Reactor. Average STO particle size varied from 42.3 nm to 58.6 nm, while the average percent of cubes per sample increased from 5.9 % after 20 minutes, to 83 % cubes after 16 hours.

Time (h)	d_{avg} (nm)	% Nanocuboids
0.33	42.3 ± 9.1	5.9
2	49.6 ± 9.9	66.4
12	58.6 ± 16.2	77
16	53.4 ± 12.9	83

Table 3.4. Summary of Experimental Design for STO Synthesis. Presented below are tabulations of the reagents used to make Sr-Ti-OH reaction mixtures (**Equation 3.1, Table 3.4a**), and the 3 different heating profiles (**Table 3.4b, Equation 3.2**) tested for STO nanoparticle synthesis. Per **Equations 3.5** and **3.6**, all nanoparticles were synthesized by choosing one combination of Sr^{2+} and Ti^{4+} reagents, and one heating method from **Tables 3.4a** and **3.4b**, respectively.

Eq. 3.5: *(Sr^{2+} source) + (Ti^{4+} source) + (NaOH) = Sr-Ti-OH mixture*

***Eq. 3.6*:** (*Sr-Ti-OH mixture*) + (*heating method*) = *$SrTiO_3$ nanoparticles*

3.4a. Sr^{2+} and Ti^{4+} Reagents

Sr^{2+} Sources Used	Ti^{4+} Sources Used
$Sr(OH)_2{\cdot}8H_2O$	$TiCl_4$
$Sr(NO_3)_2$	TiBALD
$Sr(OAc)_2$	$Ti(O^tBu)_4$
$Sr(OAc)_2{\cdot}0.5H_2O$	$Ti(O^tBu)_4$
$Sr(ClO_4)_2{\cdot}3H_2O$	$Ti(OiPr)_4$
$SrCO_3$	$Ti(OPr)_4$
$SrCl_2{\cdot}6H_2O$	$Ti(OEt)_4$

3.4b. Heating Methods

Identifier	Heating Method	Max Time (h)	Reactor Volume (L)	Max Temperature (°C)	Ti^{4+} Source	Output (g)
A	Convection	36	0.125	240	$TiCl_4$	1.5
B	Convection - Heating Jacket	16	4	240	$TiCl_4$	20
C	Microwave Radiation	16	1	200	$TiCl_4$	20
D	Microwave Radiation	16	1	200	TiBALD	20

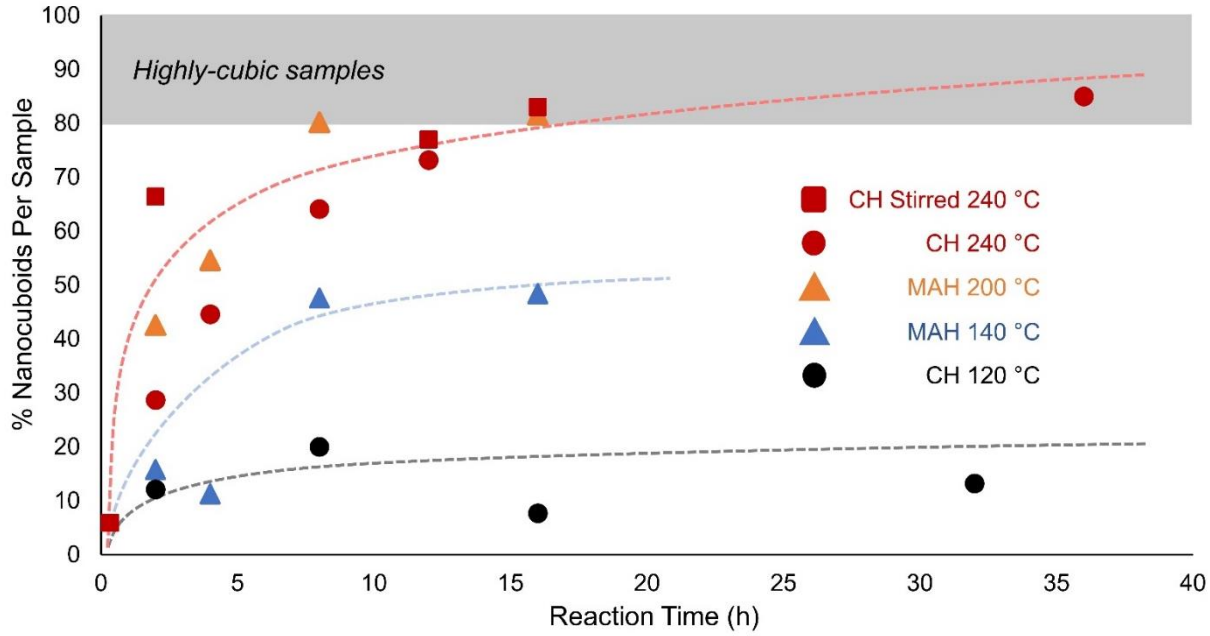

Figure 3.10. Percent Nanocuboid Particles for STO Samples Synthesized by Either Microwave Heating (*MAH-STO*) or Convection Heating (*CH-STO*) with and without Stirring at Various Temperatures and Times. The percent nanocuboids per sample appears to evolve similarly independent of heating method. Red circular markers were used for CH-STO data at 240 °C, triangular markers were used for MAH-STO data, and a black circle was used for CH-STO data collected at 120 °C. For each data point, 300 nanoparticles were analyzed to determine the percent nanocuboids per sample. Dotted curves have been included to guide the reader.

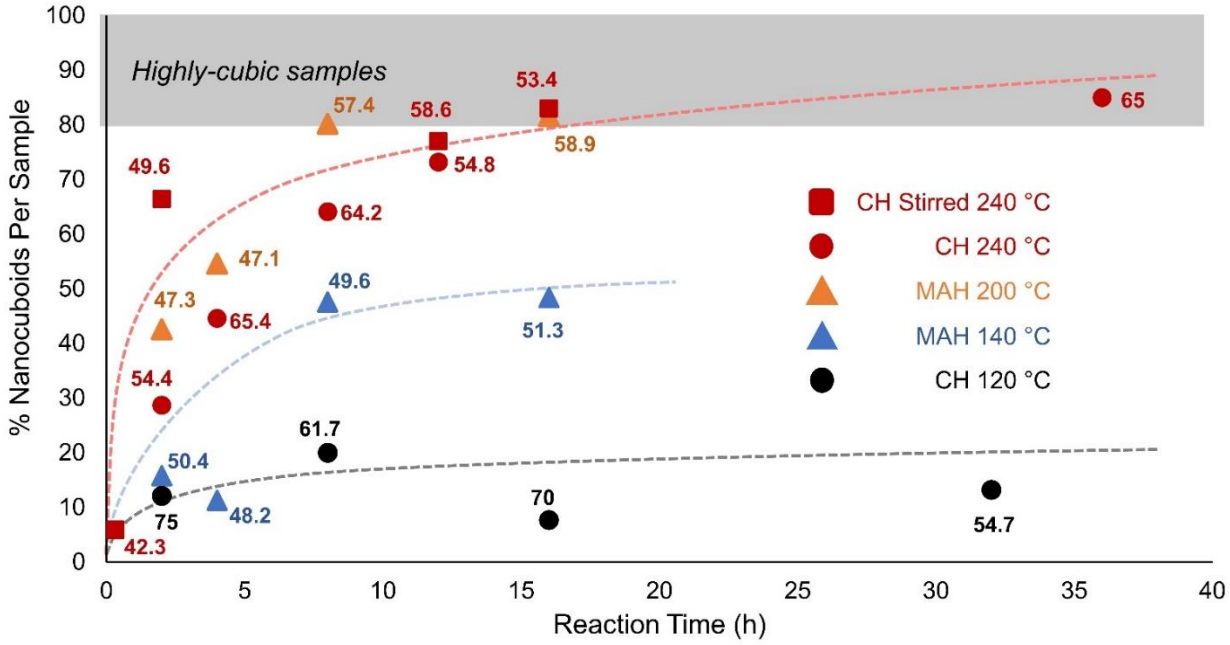

Figure 3.11. Percent Nanocuboid Particles and Average Particle Sizes for STO Samples Synthesized by Either Microwave Heating (*MAH-STO*) or Convection Heating (*CH-STO*) with and without Stirring at Various Temperatures and Times. This figure is equivalent to **Figure 3.10**. However, data labels (number closest to each point) have been added to show the average particle size (in nanometers) of each STO sample analyzed. At least 200 nanoparticles were measured to compute a mean value for each data point.

The final average STO particle size appears slightly smaller for samples synthesized with microwave heating and stirred convection heating than for unstirred convection heating (between 50 – 60 nm for MAH samples and 42-59 nm for stirred CH samples, versus between 55 - 75 nm unstirred CH samples). The variance in average size appears generally equivalent across all samples. The smaller average size of the pre-hydrothermal STO particle (**Figure 3.7**) may explain why MAH-STO samples are smaller than CH-STO samples, since based on previous reports, facet growth appears to increase particle size by around 15 – 30 % of the pre-heating particle size.[42] Beyond observations of differences in average particle size, we have previously established that varying the concentration of Sr^{2+}, Ti^{4+}, and OH^- in solution affords control over final nanocuboid average size, which determines the surface area per gram support available for deposition. In general, increasing Sr^{2+}, Ti^{4+}, and OH^- concentrations drives formation of smaller nanocuboids. By applying this methodology to the microwave-assisted heating methods developed herein, MAH-STO could be synthesized both on 10 and 20 g scales with average sizes between 20 – 80 nm. [42]

To synthesize a highly cubic STO sample, a pre-hydrothermal mixture must be treated for 8 h at 200 ^oC when using microwave-assisted heating, compared to around 18 h at 240 ^oC when using unstirred convection heating. In a 4 L, stirred convection batch reactor at 240 ^oC, the Sr-Ti-OH reaction mixture must be treated for around 12 hours to attain said highly cubic sample. This is less time than is required for an unstirred reactor, but these reaction conditions are still harsher than those used for microwave heating (8 h at 200 ^oC). Thus, while both stirring and heating increase energy distribution throughout a reaction system, microwave heating seems to have a larger contribution towards speeding up nanocuboid formation than does stirring. Moreover, increased energy distribution in microwave heating likely facilitates STO crystallite precipitation and {100} facet growth at lower temperatures than is possible in convection heating.

For unstirred samples at lower temperatures (120 ^oC for CH, 140 ^oC for MAH), reaction times of up to 36 h for unstirred convection heating, and 16 h for microwave heating, were insufficient for the formation of highly cubic samples. Moreover, unstirred convection heating of a Sr-Ti-OH mixture at 120 ^oC for 64 hours was also insufficient to form a highly cubic sample, producing only 10.6 % nanocuboids (**Figure 3.12**).

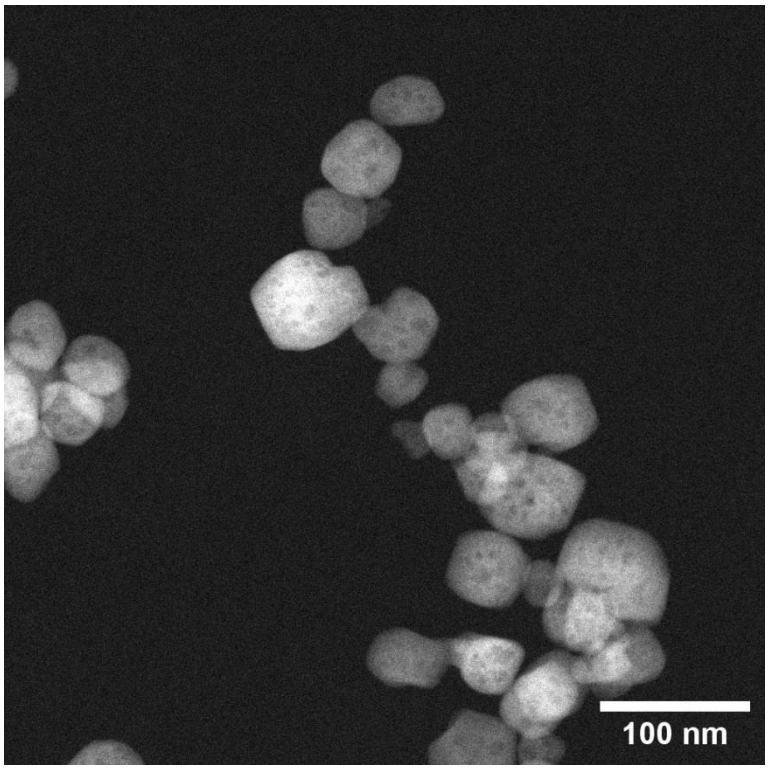

d_{avg}	42.7 +/- 10.8 nm
% Cubes	10.6 %

Figure 3.12. Electron Micrograph of $SrTiO_3$ Samples Treated Hydrothermally for 64 hours at 120 ^oC Under Previously Reported Lab Scale Conditions with Convection Heating. These samples do not meet the threshold for "highly cubic" established by Peczak et al as they have 10.6% cubes per sample. The average particle size is 42.7 ± 10.8 nm.

At higher temperatures (240 ^oC for CH, 140 ^oC for MH), the evolution of percent nanocuboids per sample versus reaction time is equivalent for both heating methods. Large increases in the percent nanocuboids

per sample are observed early on, and eventually, additional time causes less pronounced changes in the percent nanocuboids per sample, which stops increasing at around 80 – 90 % depending on the batch. The differences in sizes between average $SrTiO_3$ crystallites and final nanocuboid size are comparable to those observed in previous work.[42] This suggests that in both convection heating and microwave-assisted heating syntheses, STO nanocrystals precipitate prior to heat treatment, and {100} facets grow directly on individual particles during hydrothermal heating, with limited diffusion between particles. As previously noted by Peczak et al, the size of these precipitated STO nanocrystals heavily influences final STO nanocuboid size.[24] Facet growth appears to increase particle size by up to 30 % from that of the precipitated crystallite, but not further. As a result, changing heating method, reaction time and temperature, may change the progression towards a final nanoparticle size, but not change its value. This is not the case with other materials, where higher temperatures and longer reaction durations can influence increase particle size.

Finally, elemental analysis of STO synthesized on 1 g, 10 g, and 20 g scales shows that all reported samples contain Sr and Ti in around a 1:1 ratio independent of STO output (**Table 3.5**). This confirms that increasing reaction scale likely does not create any dispersion-related issues that could impact STO precipitation and facet growth. Moreover, deficiencies of Sr and Ti in $SrTiO_3$ often leads to the formation of extended structures and Ruddlesden-Popper phases, such as Sr_2TiO_4. Examples of this are well-documented for $SrTiO_3$.[188] These results all suggest that the chemistry and mechanisms governing the formation of STO nanocuboids are independent of the heat treatment method used. Thus, MAH STO samples will likely have surface chemistry comparable to that of previously synthesized CH STO samples, making them viable candidates for $Pt/SrTiO_3$ catalyst synthesis.

Table 3.5. Elemental ratio of Sr/Ti for STO samples synthesized on 1 g, 10 g, and 20 g scales. Sr/Ti ratios were calculated based on Sr and Ti concentrations obtained from measurements by inductively coupled plasma optical emission spectrometry (ICP-OES). Standard deviations were calculated by error propagation techniques. The details of these calculations are presented in the *Statistical Analysis* subsection of the Experimental section.

Sample	Scale	Sr:Ti
CH-STO	1 g	1.04 ± 0.06
MAH-STO	10 g	0.96 ± 0.02
MAH-STO-TiBALD	20 g	0.98 ± 0.01

3.4.3 Microwave STO Synthesis without Ethanol with TiBALD as a Ti^{4+} Source

Next, a new synthetic route to STO supports was created by replacing $TiCl_4$ and ethanol with an equimolar amount of $[NH_4CH_3CH(O\text{-})CO_2]_2Ti(OH)_2$] (TiBALD). This new Sr-Ti-OH mixture was treated in both a microwave reactor and a convection hydrothermal oven, and the resulting samples were analyzed by both electron microscopy and x-ray diffraction (**Figures 3.11, 3.14**).

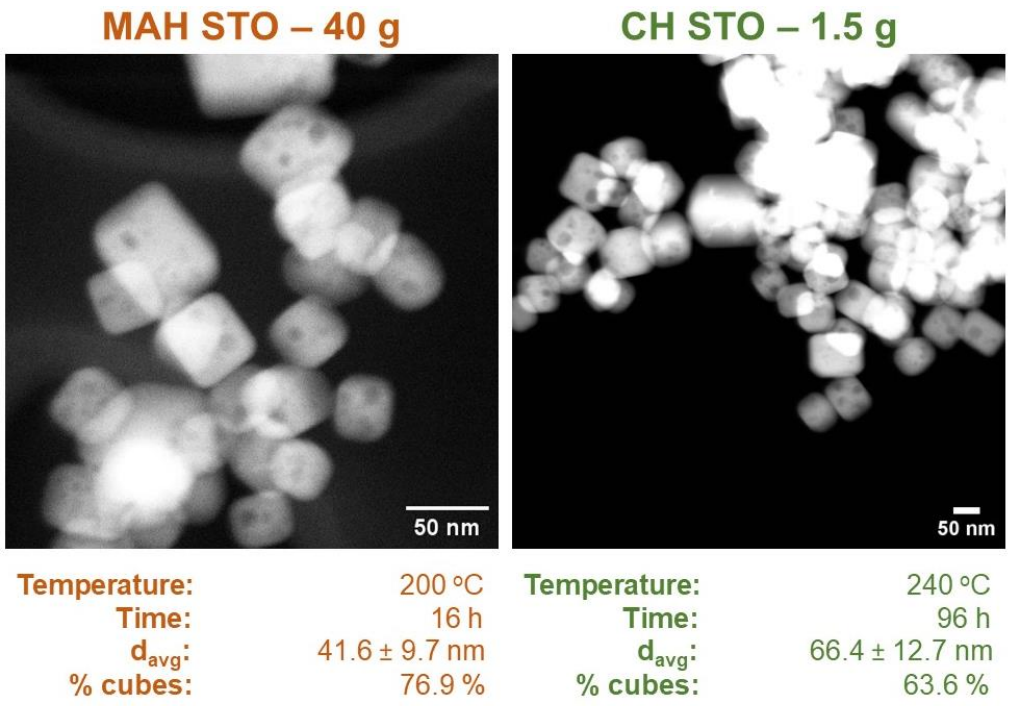

Figure 3.13. HAADF STEM Micrographs of STO Supports Synthesized by Microwave-Assisted Heating and Convection Heating Using TiBALD as a Ti^{4+} Source. Both samples are > 99.9% STO by powder x-ray diffraction. While the STO sample treated by MAH was highly cubic after heating, the unstirred CH sample was not highly cubic despite being treated at higher temperatures and longer reaction times. For both the MAH-STO and CH-STO samples, 200 nanoparticles were analyzed to determine average nanocuboid size, and 300 nanoparticles were analyzed to determine the percent of nanocuboids in the sample.

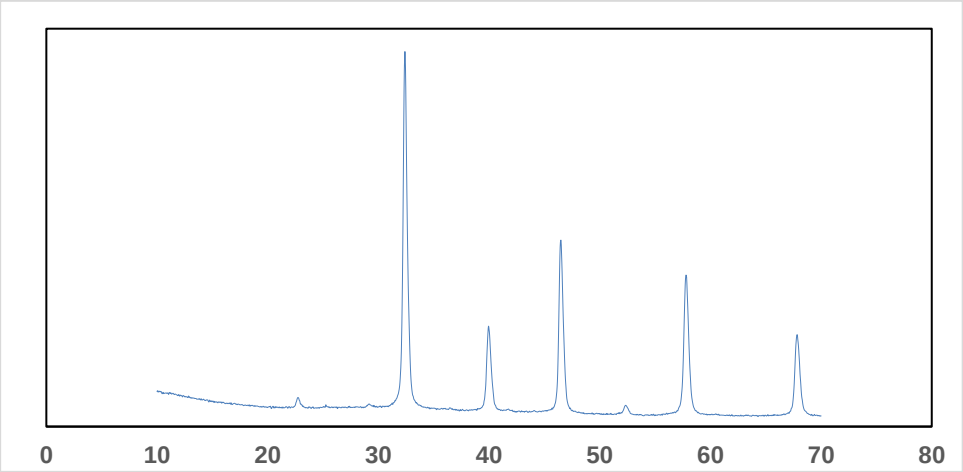

Figure 3.14. Powder X-Ray Diffraction Pattern of STO Nanoparticles Synthesized Using TiBALD. The final STO sample is 100% crystalline STO with no secondary phases detectable by PXRD.

In both reactions, the final product is > 99.9% crystalline $SrTiO_3$ with no secondary phases (**Figure 3.14**). When using convection heating, treatment at 240 ^oC for 96 h was insufficient to produce highly cubic STO, with the final percent of nanocuboids in the sample reaching 63.6 %. By contrast, microwave heating at 200 ^oC for 16 h afforded a final STO sample with 76.9 % nanocuboids, which is slightly less than required for a highly cubic STO sample (80 % nanocuboids). This is likely one of the first reports of an STO hydrothermal synthesis that produces a cubic final sample on a 20+ g scale without the use of $TiCl_4$ as a Ti^{4+} source. The pre-Sr-Ti-OH reaction mixture for this sample was amorphous despite having a final pH of 14 (**Figure 3.15**). It is likely that for this reaction system, microwave heating and stirring are sufficient to allow both the precipitation of STO and facet growth during heating. This is not the case when the sample is treated via convection heating, which is consistent with previous observations about the impact of Sr-Ti-OH mixture pH variation and STO precipitation on final particle morphology.

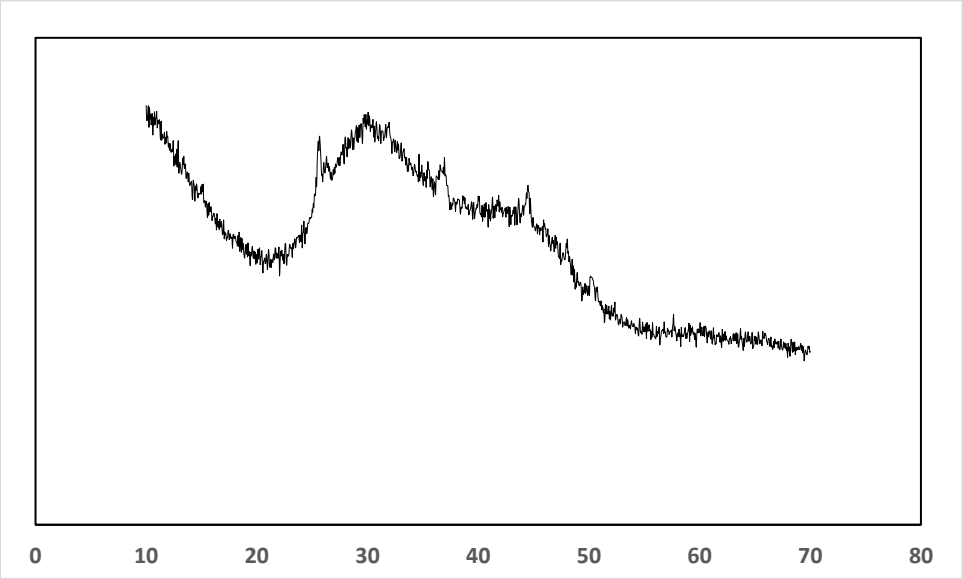

Figure 3.15. Powder X-Ray Diffraction Pattern of Sr-Ti-OH Gel Precursor Synthesized with TiBALD as a Ti^{4+} Source. The precursor sample is largely amorphous with traces of weakly crystalline $SrCO_3$.

3.5 CONCLUSION

The synthesis of $SrTiO_3$ nanocuboid supports was investigated to both understand the composition of the Sr-Ti-OH reaction mixture prior to heating and determine the impact of heating on STO particle morphology by developing a synthetic route based on microwave heating. Phase stability studies of various Sr-Ti-OH mixtures prior to heating demonstrate STO nanocuboid formation proceeds through a two-step precipitation and facet growth process. When any Ti^{4+} source other than $TiCl_4$ is used, STO does not precipitate prior to heating because titania sol-gel structures are more thermodynamically stable. This is likely because the solution pH increased to an intermediate range ($3 < pH < 9$). When one-step convection heating profiles are used, STO must precipitate prior to heating to obtain a highly cubic sample. Next, the impact of heating method chosen on the final STO sample was investigated by testing microwave-assisted heating for hydrothermal treatment. Two syntheses were developed that produce around 20 g highly cubic STO under milder conditions than previously possible (200 ^{o}C, up to 16 h), using both $TiCl_4$ and titanium(IV) bis(ammonium lactato)dihydroxide as Ti^{4+} reagents. The latter is one of the first examples of a synthesis for highly cubic STO without the use of titanium tetrachloride and ethanol.

Overall, the results demonstrate that rational design of STO catalyst supports for commercial applications is possible. The insights gained from investigating how different Ti^{4+} sources impact STO formation may be also applied to other materials such as lithium titanium oxide anodes, whose syntheses also rely on similar reagents.[189–191]

CHAPTER 4

Polyolefin Hydrogenolysis by ALD-Derived Pt/STO

This Chapter was adapted with permission from "R.A. Hackler, J.V. Lamb, I.L. Peczak, R.M. Kennedy, U. Kanbur, A.M. LaPointe, K.R. Poeppelmeier, A.D. Sadow, M. Delferro. 'The Effect of the Macro- and Microstructure on Catalytic Hydrogenolysis of Polyolefins' *Macromolecules,* **2022**, 55, 15, 6801–6810"

4.1 ABSTRACT

Polyethylenes of varying molecular weight and branch density, as well as polypropylenes of varying molecular weight and tacticity were catalytically converted to lower molecular weight liquid products to showcase how these various properties in a mixed waste plastic stream could affect the final product. A Pt nanoparticle on strontium titanate nanocuboids (Pt/STO) catalyst was used under solvent-free conditions in presence of 170 psi of H_2 at 300 °C for hydrogenolysis. The initial molecular weight of polyethylene was found to have a moderate effect on yield to the final product (ranging from 55 wt% for M_n ~ 7,600 Da to 67 wt% for M_n ~ 50,950 Da). The microstructure, defined as the length and density of branches in a polymer, of higher molecular weight polymers was the dominant factor in determining yield (ranging from 67 wt% for M_n ~ 50,950 Da for linear low-density polyethylene (LLDPE) with C_2 branches to 97 wt% for M_n ~ 38,850 Da for LLDPE with C_6 branches). The same products, polydispersity (M_n = C_{29} – C_{46}, $Đ$ = 1.1 – 1.6), and distribution of undesired light gases (C_1-C_4 ≈ 90 mol%, C_5-C_8 ≈ 10 mol%) are obtained from conversions of PE of varying molecular weight. The tacticity of polypropylene at a given molecular weight had a significant effect on the molecular weight of the final product while not strongly affecting conversion. Hydrogenolysis of isotactic polypropylene (iPP) produced ≈ C_{18} with a wider polydispersity ($Đ$ ~ 1.4) compared to the narrow ≈ C_{64} ($Đ$ ~ 1.0) and ≈C_{54} ($Đ$ ~ 1.0) products from atactic (aPP) and syndiotactic (sPP) polypropylene, respectively. The stereochemistry of the methyl groups dictates the shape and structure of the polymer in the melt, which in turn affects how the hydrocarbon chain interacts with the catalyst surface thereby impacting the number of C–C scissions. These results show how various characteristics such as molecular weight and structure of a waste plastic stream could affect the final product.

4.2 INTRODUCTION

Plastics have become an increasingly problematic material in recent decades due to the lack of effective post-consumer processing.[144] Without an effective and economically viable infrastructure to deal with plastics and in particular single-use polyolefins, most of these hydrocarbons will simply be discarded.[8] This has been the case for several decades and continues to be the case today, with global plastic production topping 330 million metric tons (Mt) in 2016.[143] Current recycling infrastructure satiates only 8.8% of post-consumer plastic supply in the U.S.[144] One of the most harmful consequences of plastic disposal is the generation of microplastics in various ecosystems, the most studied thus far being aquatic environments.[192,193] While coastal urban areas are thought to contribute a vast majority of ocean plastic waste, watersheds, rivers, and streams from inland populations also act as pathways for microplastic debris.[143]

One of the main wrinkles in the plastics problem is the myriad of plastics circulating in society. These plastics vary greatly in molecular weight, in branching, and in overall structure. Modern solutions to the global plastic waste crisis will inevitably require a means to combat a mixed and varied polymer waste stream to be sufficiently effective. Previous studies on low-temperature (<350 °C) catalytic conversion of plastics have primarily focused on at most a few different plastics.[7,114,118,194] Catalytic hydrogenolysis studies on polyethylene (PE) thus far, for example, have investigated the effect of PE molecular weight on conversion and product size while concluding equivalent products can be achieved independent of PE characteristics.[7] For polypropylene (PP), Rorrer *et al.* noted the impact of viscosity and size for PP feedstock and number of C-C scission events required.[43] On the stereochemistry front, Kots *et al.* recently proposed a loss of stereochemical information was a necessary prerequisite for PP hydrogenolysis, and that their Ru/TiO_2 catalyst had a proclivity towards demethylation along the polymer backbone, leading to increased methane production.[36] This is in contrast to the work of Jaydev *et al.* where their Pt/C system produces negligible amounts of methane.[195] In pyrolysis studies that investigated different plastic types, it was found that the structure of the polymer also impacted the molecular weight of the product and kinetics of the reaction.[196,197] However, it is unclear how mixed polyolefins of varying types, sizes, and branching affect the physical properties of the product, the purity, and the economic value in these systems. Recent efforts by Chevron Phillips,[198] BASF,[199] and ExxonMobil[200] in scaling up pyrolysis shows

that despite these uncertainties, pyrolysis is economically feasible in the market, and that this is in part due to conversion to liquid fuel, for example, nearing 80% yield.[201] Still, it is necessary to investigate the effect of polymer microstructure in chemical recycling processes. Microstructure is defined as the length and density of branches along the polymer backbone. The results presented within show certain properties, such as stereochemistry in branching, can affect the reaction mechanism and thus the molecular weight and microstructure of the final product. Other properties, such as molecular weight, appear to have little to no effect on the final product across all polyolefin feedstocks and therefore are less of a concern when evaluating catalyst design.

4.3 EXPERIMENTAL

4.3.1 *Catalytic Hydrogenolysis*

In a Parr autoclave reactor (100 mL, Series 4590 Micro Reactor), 300 mg of Pt/STO catalyst (~10 wt% Pt comprised of ~2 nm Pt nanoparticles) and ~3 g of the corresponding polymer was placed inside a glass sleeve inside the reactor. The dimensions of the glass sleeve and the impeller ensured that mixing of the molten plastic and the catalyst took place and are highlighted in **Scheme 4.1**. The gas lines, valves, and reactor were flushed with He. The reactor was then heated to 300 °C at roughly 5 – 10 °C/min ramp and then allowed to stand until a stable temperature was established for 30 min. Then, the reaction mixture was agitated with an impeller at 800 rpm. Comparisons between hydrogenolysis products from different stirring rates (800 and 1,700 rpm) show negligible impact on the product distribution, as the reaction is still within mass transfer limitations (Table S1). Finally, the reactor was flushed and charged with H_2 (UHP) to 170 psi for 72 h unless otherwise stated. The polyolefins that underwent hydrogenolysis include linear low density polyethylene (**1**, LLDPE, Sigma Aldrich, 1.0g/10 min. melt index), bubble wrap (**2**, LDPE, Amazon), LLDPE of varying molecular weight provided by Dow Chemical (**3**, Engage 8100, **4**, Engage 8200, and **5**, Affinity GA 1875, octene mol% 13), atactic (aPP, **6**, Scipoly, average M_n ~1,600), isotactic (iPP, **7**, Sigma Aldrich, average M_n ~ 6,000 Da), and syndiotactic PP (sPP, **8**, as synthesized previously[19]), and isotactic PP with random distributions of PE at 12 wt% (**9**, Vistamaxx 8780, ExxonMobil). A physical mixture of **1** and **7** was used to produce **10**, as listed in Table 1.

Hydrogenolysis was also conducted using D_2 (UHP) under the same conditions (170 psi D_2 with 3g iPP, 300 mg Pt/STO catalyst, and 300 °C for 72 h) to determine the extent of dehydrogenation, C – C bond cleavage, and skeletal rearrangement mechanisms.

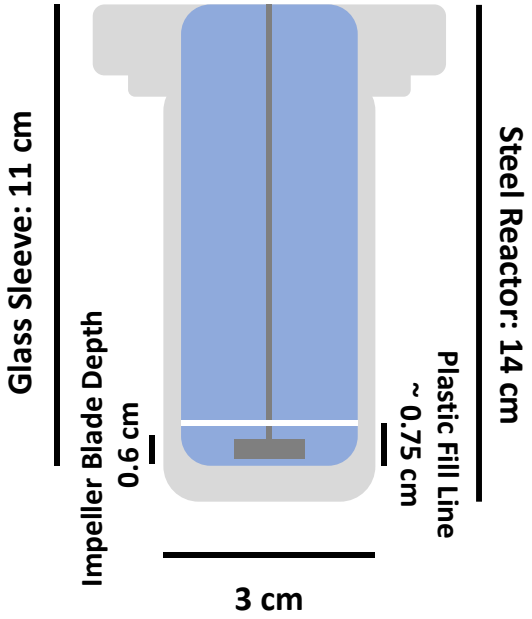

Figure 4.1: Hydrogenolysis reactor setup with relevant dimensions of the reactor, impeller, and plastic melt height. Under reaction conditions, plastic fill line lies above the impeller blades at the beginning of the reaction.

4.3.2 Polymer and Liquid Product Characterization

After the reaction, the reactor was cooled to 150 °C and the headspace was evacuated to a gas chromatograph (Agilent 6890N) with a capillary column (Agilent, HP-Plot Al_2O_3-S, 25 m x 0.320 mm x 8.0 µm) and a flame ionization detector. After GC analysis, the reactor was cooled to room temperature and vented to atmosphere. The liquid product found between the walls of the reactor and the walls of the glass sleeve was extracted and washed with n-hexane. The liquid product was then filtered through silica

gel (Davisil Grade 646, Millipore Sigma) to remove any catalyst particles, and any remaining n-hexane was evaporated under low vacuum (~100 mbar) at ~55 °C.

The starting polymers and resulting hydrogenolysis products were analyzed for molecular weight (M_n and M_w) and molecular weight distribution (*Đ*) by matrix-assisted laser desorption/ionization (MALDI) mass spectrometry and high-temperature gel permeation chromatography (HT-GPC). MALDI-TOF-MS experiments were carried out on a Bruker UltrafleXtreme MALDI-TOF/TOF spectrometer, equipped with a Smartbeam-II™ laser (2 kHz repetition rate). The mass spectra were acquired in both linear positive and reflector positive ion mode. 1000 laser shots were utilized for each measurement. The MALDI-TOF spectra were analyzed, average molecular weights and polydispersity were calculated using the Bruker PolyTools software. Stock solutions of products were prepared in tetrahydrofuran at a 0.5 mg/mL concentration, and a stock solution of saturated silver nitrate was prepared in acetonitrile. Final sample solutions for spotting were prepared by mixing equal volumes (0.2 mL) of stock solutions of alkanes and silver nitrate. The 2,5-dihydroxybenzoic acid (DHB) matrix solution was prepared in a 3:2 (*v*:*v*) mixture of tetrahydrofuran and methanol at a 10 mg/mL concentration. The dried-droplet method of sample deposition was employed, where 0.5 µL of the sample solution was deposited on the stainless-steel sample plate, followed by 0.5 µL of the matrix solution. The solvents evaporated by air-drying. HT GPC experiments were carried out on an Agilent PL220 equipped with RI and viscometer detectors. Monodisperse polyethylene standards (ranging from ~300 Da to 120 kDa) were used to build the calibration curve. The column set included 3 Agilent PL-Gel Mixed B columns and 1 PL-Gel Mixed B guard column. 1,2,4-trichlorobenzene (TCB) containing 0.01 wt% 3,5-di-tert-butyl-4-hydroxytoluene (BHT) was chosen as the eluent at a flow rate of 1.0 mL/min at 150 °C. The lubricant samples were prepared in TCB at a concentration of ~1.0 – ~4.0 mg/mL and heated at 150 °C for 24 h prior to injection.

Solution-phase Nuclear Magnetic Resonance (NMR) spectra were collected using a Bruker Avance III 500 MHz NMR spectrometer (11.7 T) at 120 °C in 1,1,2,2-tetrachloroethane-d_2 and referenced internally to residual solvent signals. ^{1}H spectra (500 MHz) were recorded with 32 scans, ^{13}C{^{1}H} spectra (125 MHz) with ~9500 scans, and ^{2}H spectra (77 MHz) with 600 scans. Spectra were analyzed using MestReNova (v11.0.1, Mestrelab Research S.L.).

The branching density of hydrogenolysis products derived from PE were determined using ^{1}H NMR via the following formula: # branches per 1000 C = (CH_3/3)/(($CH + CH_2 + CH_3$)/2) x 1000. CH_3, CH_2, and CH refer to the integrations obtained for methyl, methylene, and methine resonances, respectively.[202,203]

4.4 RESULTS AND DISCUSSION

The Pt/STO catalyst was synthesized using a hydrothermal synthesis for STO production and an atomic layer deposition (ALD) method for the Pt nanoparticles, both described previously.[7] Hydrogenolysis of the various polyolefins was done using Pt/STO (10 wt% Pt, 2 nm nanoparticles) under identical conditions (300 °C, 170 psi H_2, 72 h) to accurately compare the effects of molecular weight and polymer structure. An extended run time of 72 h was chosen to guarantee all polymer samples reach the molecular weight asymptote, as seen previously in Pt/STO hydrogenolysis.[7] Larger polyolefins require a longer reaction time to ensure they reach this minimum molecular weight. Control experiments were previously performed[7] and showed bare STO to not contribute catalytically beyond background thermal degradation. Performing the reaction with Pt/STO in the absence of H_2 resulted in a much smaller and narrower product (M_n ~ 1,630 Da, $Đ$ ~ 2.0) compared to thermal degradation, however aromatics formed as confirmed via ^{1}H NMR (see Figures S1-S2 in SI). All the reported M_n, M_w, and $Đ$ were measured in-house via HT GPC.

4.4.1 Polyethylene

Standard (Sigma Aldrich) and commercial (Dow Chemical) polyethylene of varying molecular weight, branching, and polydispersity were evaluated for hydrogenolysis with reaction conditions held constant at 170 psi H_2, 300 °C, and 72 h run time (**Table 4.1** and **Figure 4.2**). The % yield is the mass of the liquid/waxy product with respect to the initial plastic mass. Conversion is defined as the wt% of starting polymer that has undergone an observable amount C – C bond scissions such that the product is distinct from the starting material, in which case all polymers studied had > 99% conversion. Based on ^{1}H and ^{13}C{^{1}H} NMR (see **Figures 4.2** – **4.3** in SI), the Sigma LLDPE (**1**) is likely an ethylene-1-butene copolymer. The commercial LLDPE polymers were prepared by using 1-octene as a co-monomer, with **3 – 5** having the same octene content (13% mol). Despite the differences in starting M_n (7,600 – 50,950

Da), their respective liquid hydrogenolysis products were essentially indistinguishable in terms of molecular weight (**Figure 4.4**, M_n ~ 550 Da), polydispersity (*Đ* ~1.4), and structure (degree of branching per 1000 C = DB_f = 160 – 180, ^1H and $^{13}C\{^1H\}$ NMR in figures S6 – S18 in SI), with yield to liquid products being the main difference. The yield to liquid product vs. light gases, however, is directly related to the molecular weight of the starting polymer in LLDPE (**Figure 4.5**). The affinity between the catalyst surface and larger hydrocarbon chains, as established previously,[7] shifts the molecular weight in the polymer population until the product is sufficiently small. The smaller hydrocarbons become volatile under reaction conditions and likely establish an equilibrium between the melt and vapor.

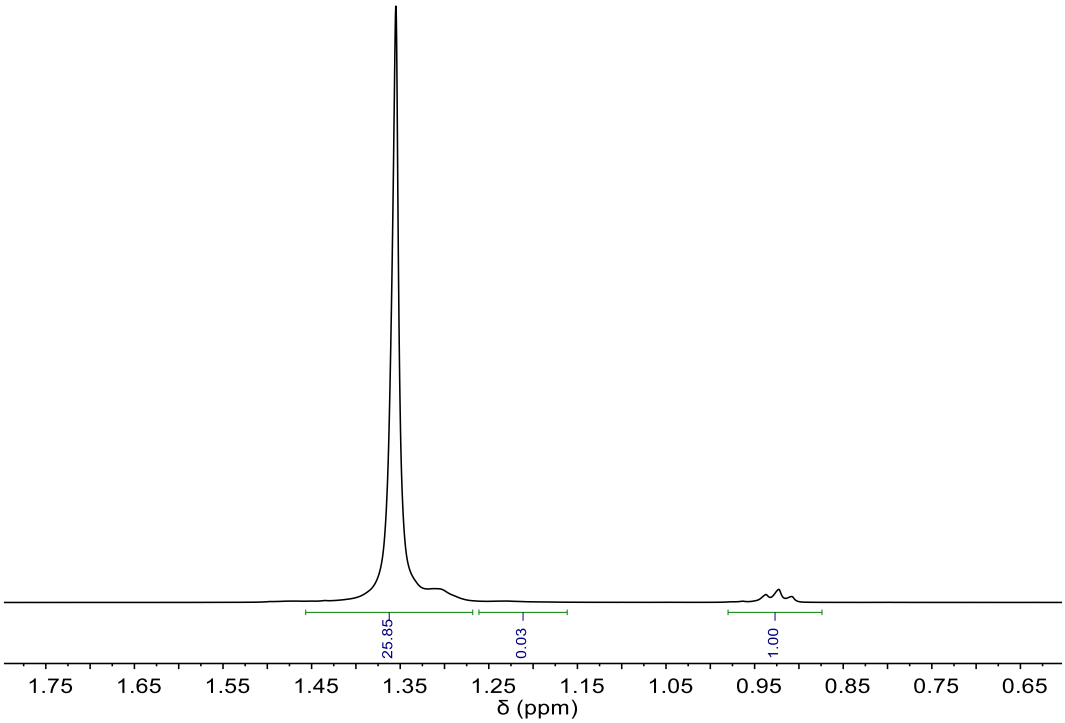

Figure 4.2. ^1H NMR spectrum (1,1,2,2-tetrachloroethane-d_2, 120 °C, 500 MHz) of LLDPE (**1**). $N_{branches/C}$ = 0.03.

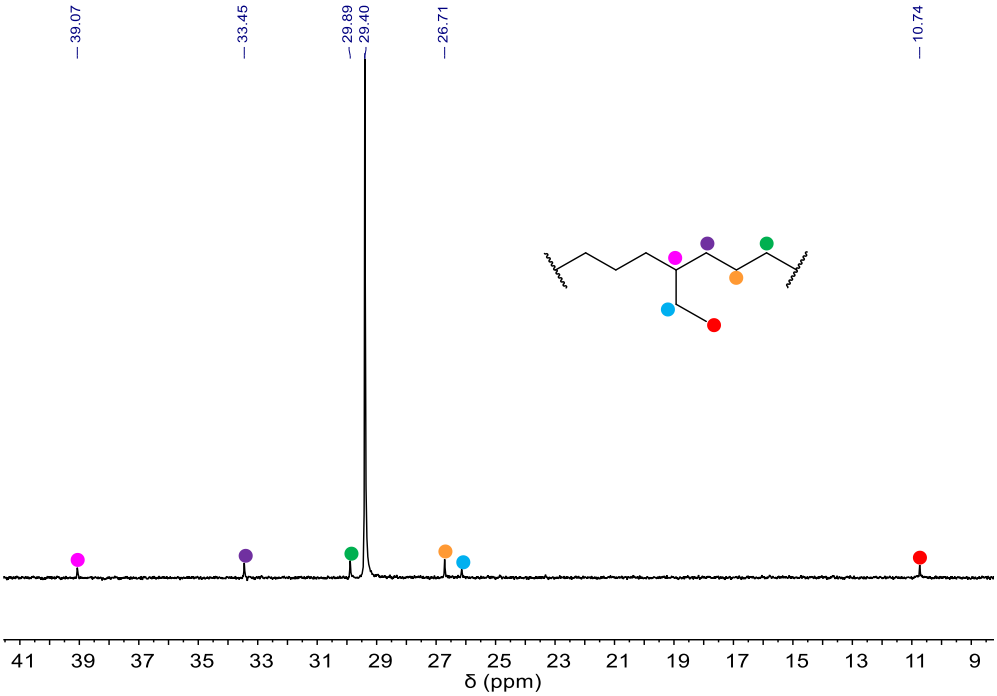

Figure 4.3. $^{13}C\{^{1}H\}$ NMR spectrum (1,1,2,2-tetrachloroethane-d_2, 120 °C, 500 MHz) of LLDPE (**1**).

Table 4.1. Polymer samples before and after catalytic hydrogenolysis, with corresponding structural properties as determined by gel permeation chromatography (GPC) and ^{1}H NMR.

Sample #	Polymer	M_{n0} (Da)[a, b]	$Đ_0$ [c]	M_{nf} (Da)[d]	$Đ_f$ [c]	DB_f [e]	Conversion (wt%)[f]	Yield (wt%) [g]	Light Gases (%)
1	LLDPE	38,850	2.7	440	1.4	150	> 99	97	< 3
2	Bubble Wrap/LDPE	13,050	5.1	590	1.0	140	> 99	97	< 3
3	Engage 8100 (LLDPE)	50,950	2.1	400	1.6	160	> 99	67	< 33
4	Engage 8200 (LLDPE)	33,950	2.2	650	1.1	180	> 99	62	< 38
5	Affinity 1875 (LLDPE)	7,600	2.4	350	1.6	170	> 99	55	< 45
6	aPP	1,600	4.2	900	1.0	-	> 99	76	< 24
7	iPP	6,000	2.2	250	1.4	-	> 99	77	< 23
8	sPP	4,250	1.7	750	1.0	-	> 99	75	< 25
9	12 wt% PE/iPP	26,550	2.5	360	1.2	-	> 99	74	< 26
10	LLDPE + iPP	Mixture	Mixture	800	1.2	-	> 99	99	< 1

[a] M_n = number-average molecular weight (g/mol). [b] $_0$ = initial property value prior to hydrogenolysis. [c] $Đ$ = polydispersity. [d] $_f$ = final property value after hydrogenolysis. [e] DB = # branches per 1000 C.[6] [f] conversion is defined as the wt% of starting polymer that has undergone an observable amount of hydrogenolysis [g] wt% yield of liquid/wax product with respect to initial plastic mass.

phase with the remaining hydrocarbon chains until they reach < 900 Da (< C_{60}s), vapor pressure builds according (> 0.67 Torr at 300 °C for a C_{64} and below) to the Antoine equation and trends for n-alkanes,[204] and C-C scission events cease. If the volatile product condenses away from the catalyst while the reaction is still underway, then the size and structure of the product would dictate volatility, and therefore may explain the termination of hydrogenolysis in PE samples. PE with short branches and/or fewer branches may be a unique case where the number of potential structures after hydrogenolysis is limited by virtue of the small number of unique cleavage sites (**Scheme 4.2**, Scenario 3 most common), as in the case with (**1**). As hydrogenolysis progresses, fewer and fewer internal branches can undergo C – C scission to light gases. Polyolefins that yield high gas production may indicate a preference towards scission across the branching points (**Scheme 4.2**, Scenarios 1 and 2). This is evident in the case of using butene (**1**) vs. octene (**3 – 5**) as a co-reactant in LLDPE synthesis; an abundance of accessible methylene groups in C_6 branches leads to different hydrogenolysis scenarios when compared to only C_2 branches.

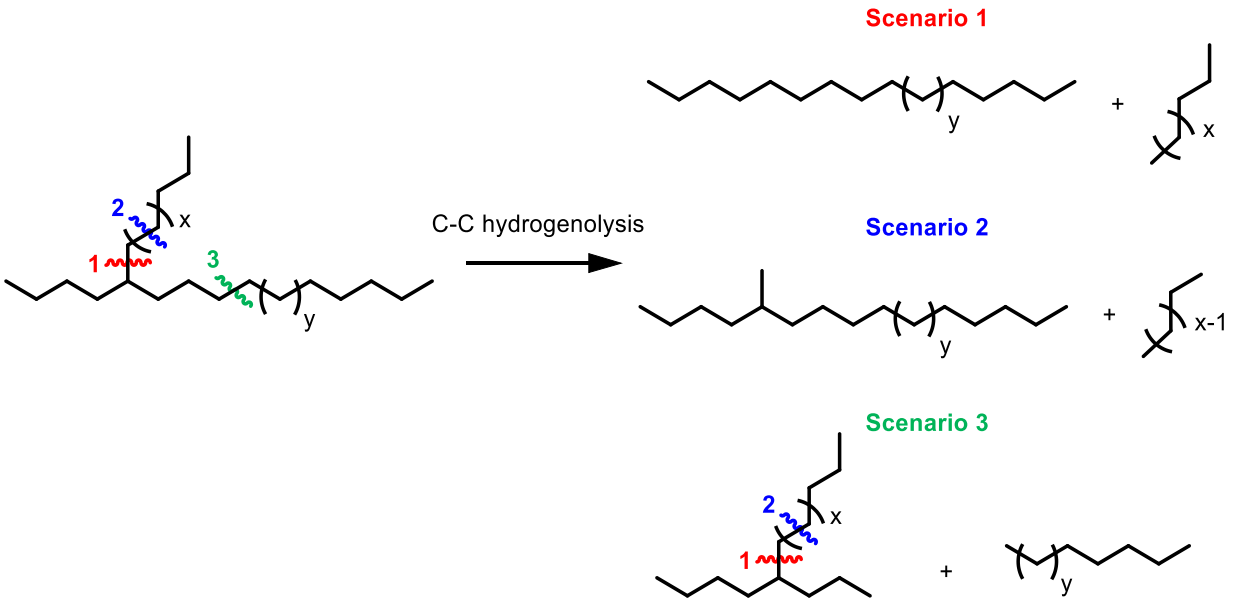

Scheme 4.2. Potential and unique C – C bond cleavage sites along the PE backbone.

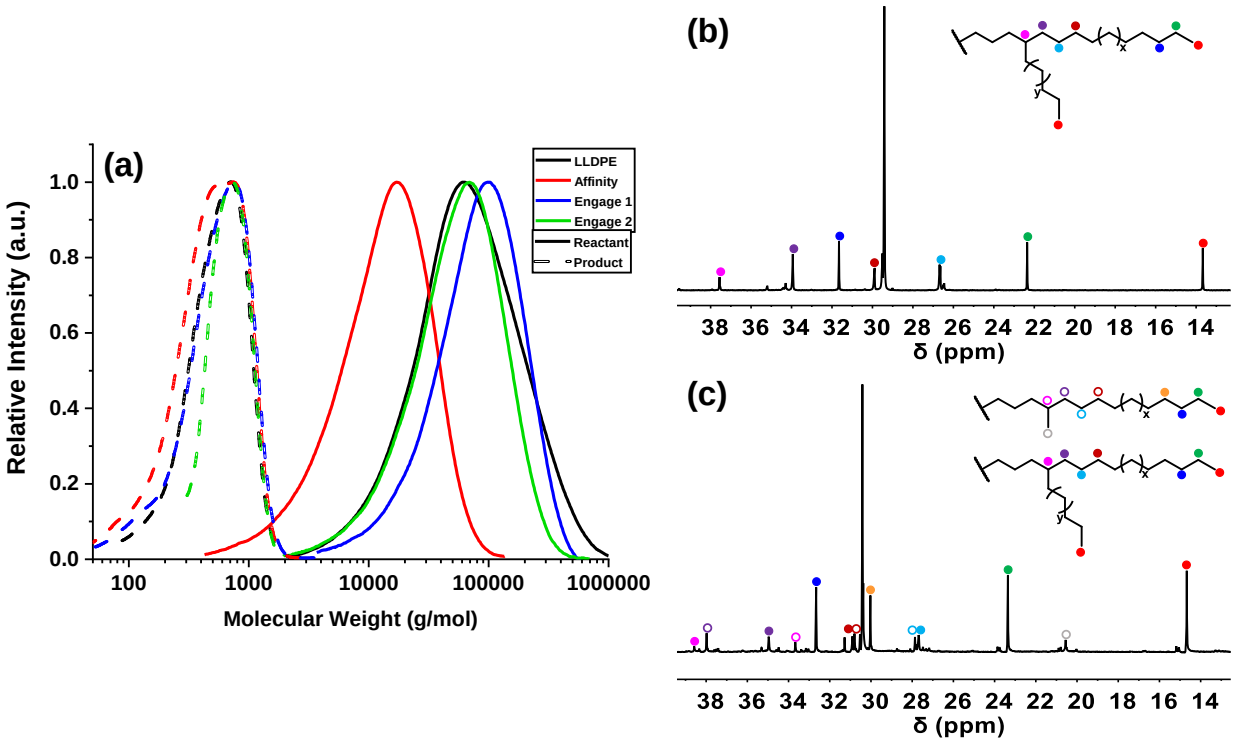

Figure 4.4. (a) Molecular weight distribution plots for starting (solid) and hydrogenolyzed (dashed) polyethylene of varying molecular weight and branching, as determined by GPC. Hydrogenolysis was done at 300 °C for 72 h under 170 psi H_2. Horizontal scale is logarithmic. (b) $^{13}C\{^1H\}$ NMR spectrum of Affinity polyolefin prior to hydrogenolysis. (c) $^{13}C\{^1H\}$ NMR spectrum of Affinity polyolefin after hydrogenolysis.

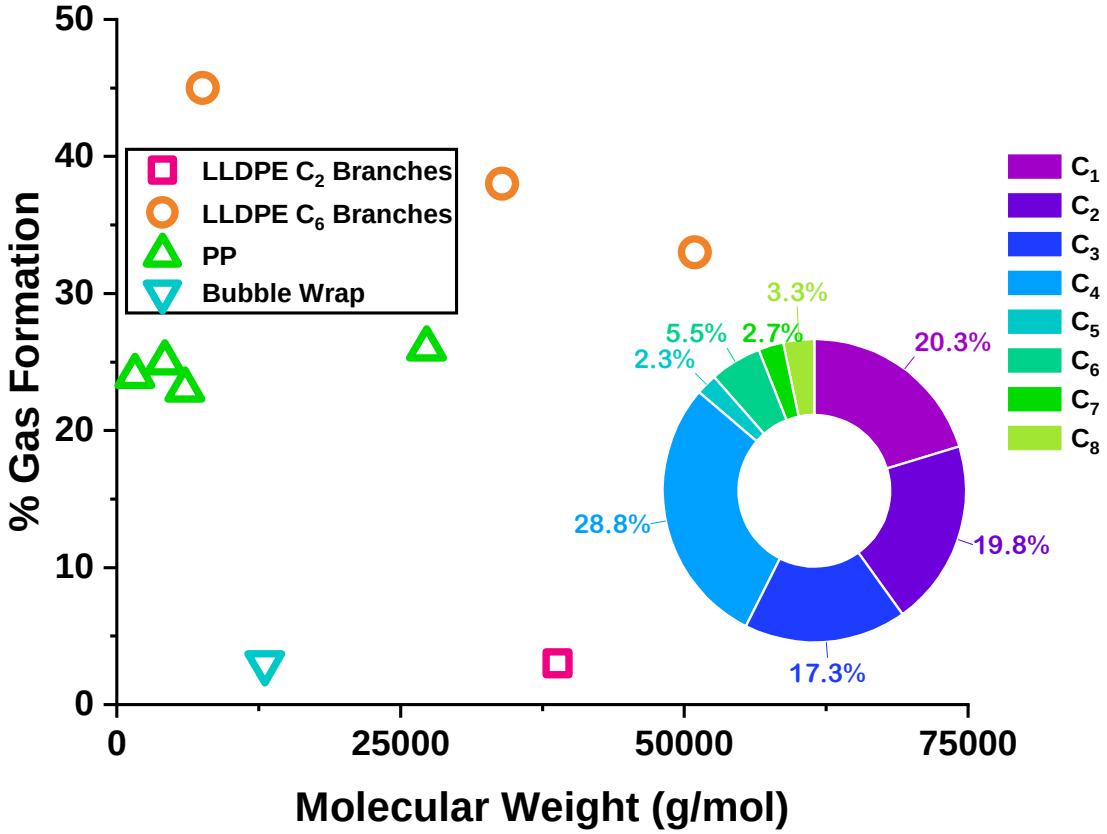

Figure 4.5. Gas formation wt% (with respect to initial mass) as a function of starting polyolefin molecular weight. Polyolefins are differentiated in color by their overall structure; LLDPE (magenta), LLDPE Dow (orange), PP (green), and bubble wrap/LDPE (blue). Inset: Representative distribution of light gases after hydrogenolysis of LDPE as determined by GC. C_1 – C_4 make up the bulk of the hydrocarbons in the headspace. All hydrogenolysis experiments follow a similar distribution of light gases after 72 h.

^{1}H and $^{13}C\{^{1}H\}$ NMR analysis of the PE commercial samples before and after hydrogenolysis show very few changes to the microstructure (**Figure 4.4b-c**), with few scissions under Scenario 2 of **Scheme 4.2**. An increase in the degree of branching between the starting polymer and final product can be attributed to the higher number of terminal methyl groups relative to methylene units after C – C bond scission on the polymer backbone. Only a small increase in additional signals in the ^{13}C NMR are observed due to C – C bond scission at the *β*-carbon of the minor branch.[36]

4.4.2 Polypropylene

Although the atactic (**6,** aPP), isotactic (**7,** iPP), and syndiotactic (**8,** sPP) polypropylenes had similar molecular weights and polydispersity (Đ), their liquid hydrogenolysis products were strikingly different (**Table 4.1** and **Figure 4.6**).

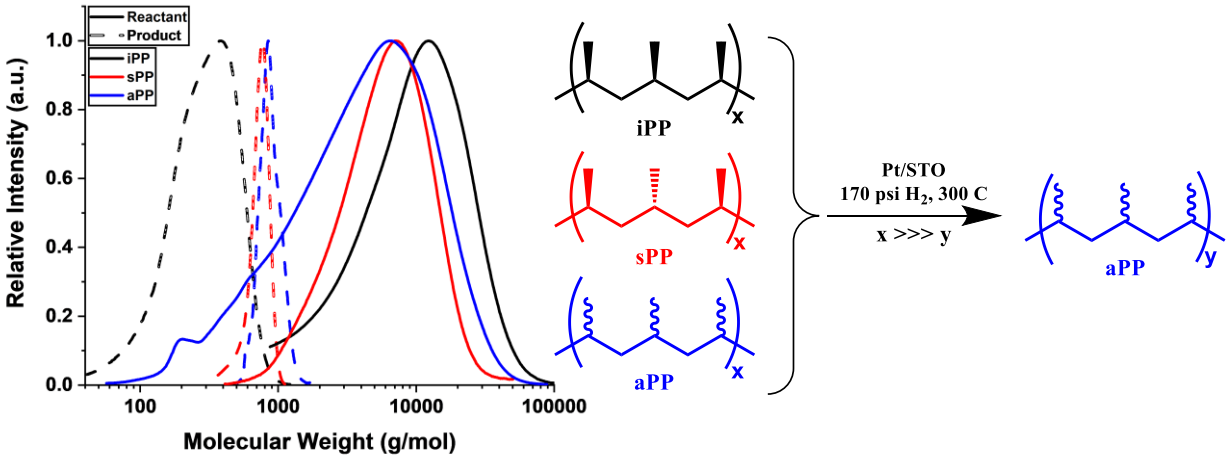

Figure 4.6. Molecular weight distribution plots for isotactic (black, iPP, product M_n ~ 6,000 Da), syndiotactic (red, sPP, product M_n ~. 4,250 Da), and atactic (blue, aPP, product M_n ~ 1,600 Da) polypropylenes for the starting polymers (solid) and resulting products (dashed) after hydrogenolysis, as determined by GPC. Hydrogenolysis was done at 300 °C for 72 h under 170 psi H_2 to produce smaller polypropylene fragments with epimerized stereocenters. Horizontal scale is logarithmic.

Namely, the aPP and sPP liquid products (**6** and **8)** were roughly equal in size (M_n ~ 800 Da) and in polydispersity (*Đ* ~ 1.1), whereas the iPP product (**7**) was significantly smaller (M_n ~ 250 Da) and broader (*Đ* ~ 1.4) under the same reaction conditions. The iPP chains may develop helical conformations due to the stereochemistry of the methyl branches,[205] although it is unclear if this structure persists in the melt and how it influences the interaction with the catalyst surface under reaction conditions. The sPP and aPP polymers do not have the same tertiary structure, and so their interaction with the surface during C-C scission events likely leads to larger hydrocarbon fragments. This is interesting considering the epimerization of stereocenters in the final product as the reaction progresses, which is discussed later. In addition, the rate of diffusion of a pure iPP melt (3.42E-3 nm^2/Monte Carlo step) is also greater than that

of pure an aPP (2.35E-3 nm^2/Monte Carlo step) or sPP melt (2.98E-5 nm^2/Monte Carlo step),[206] which may also shift the product distribution to smaller hydrocarbons due to enhanced mobility of shorter species. This also suggests mixing rates may affect product distribution as well. Despite this trend to smaller products for iPP the yield to liquid products is similar for all microstructures (75 – 77 wt% with respect to starting polymer weight as shown in **Figure 4.7a**), and comparable to pyrolysis yields to liquid fuels.[201] Consistent rates for liquid production are likely the result of similar branching structures (i.e. mostly methyl branches, no long-chain branches) and reaction conditions,[7] in contrast to the molecular weight dependence in PE. The polydispersity of the product is also unaffected by the starting polydispersity across all polyolefins, as all polyolefins convert towards a smaller polydispersity.

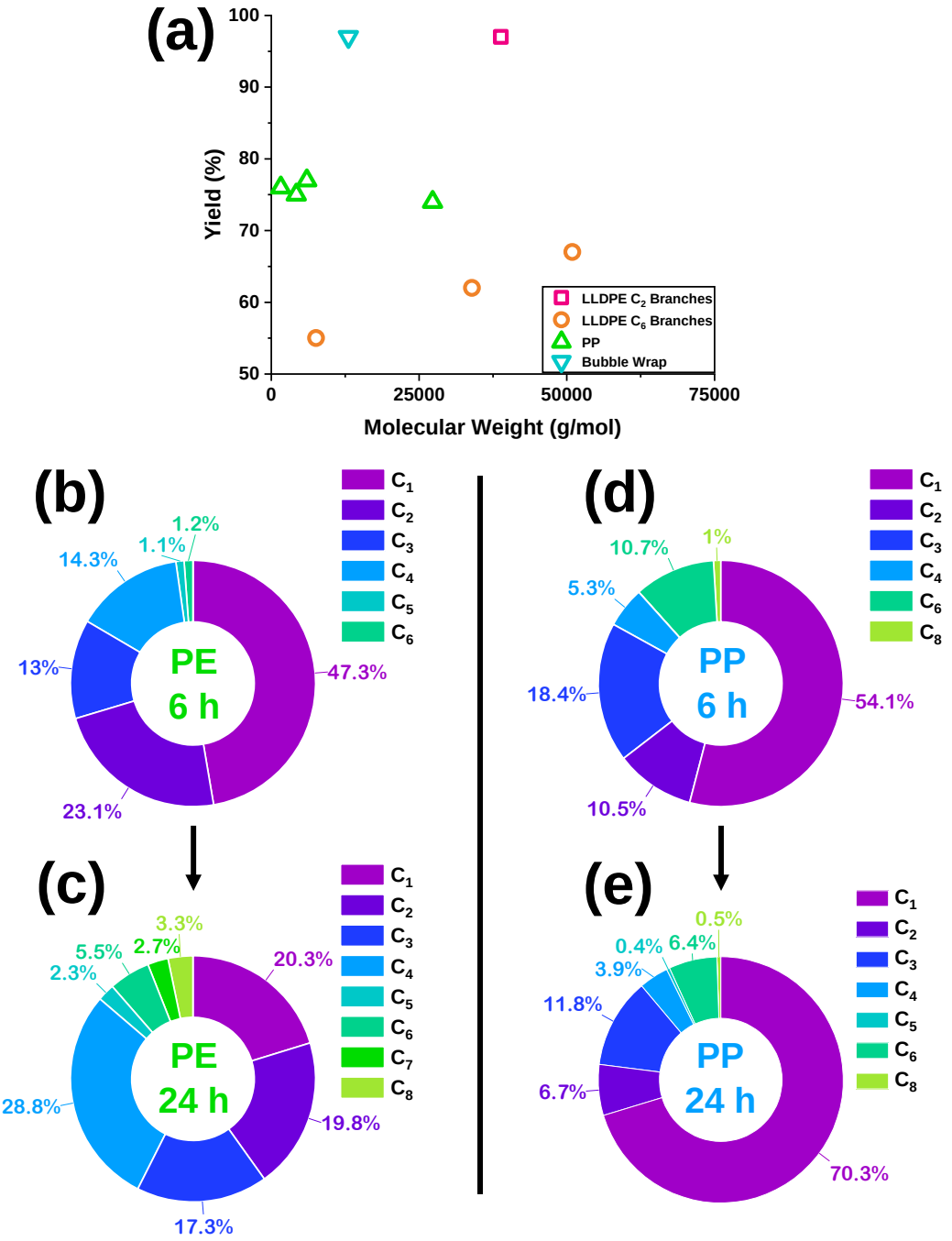

Figure 4.7. (a) Liquid/wax yield for various polyolefins as a function of molecular weight. (b, c, d, e) distribution of light gases (C_1 – C_8) for LLDPE (**1**) at 6 h, LLDPE (**1**) at 24 h, PP at 6h, and PP at 24 h, respectively. Shorter reaction times were utilized for GC evaluation, as all noticeable changes in the distribution of light gases were within 24 h.

It is worthwhile to note the population of smaller hydrocarbons in the virgin aPP polymer that is not present in the hydrogenolysis product, as shown in the GPC and MALDI (**Figures 4.8** and **4.9**). This hydrocarbon population either undergoes a chain lengthening side reaction to occupy the larger hydrocarbon species or undergoes enough C-C scissions to occupy the volatiles fraction not characterized by GPC. In any case, the fate of these smaller hydrocarbon species does not greatly alter the yield of gaseous hydrocarbons when compared to sPP gas yields.

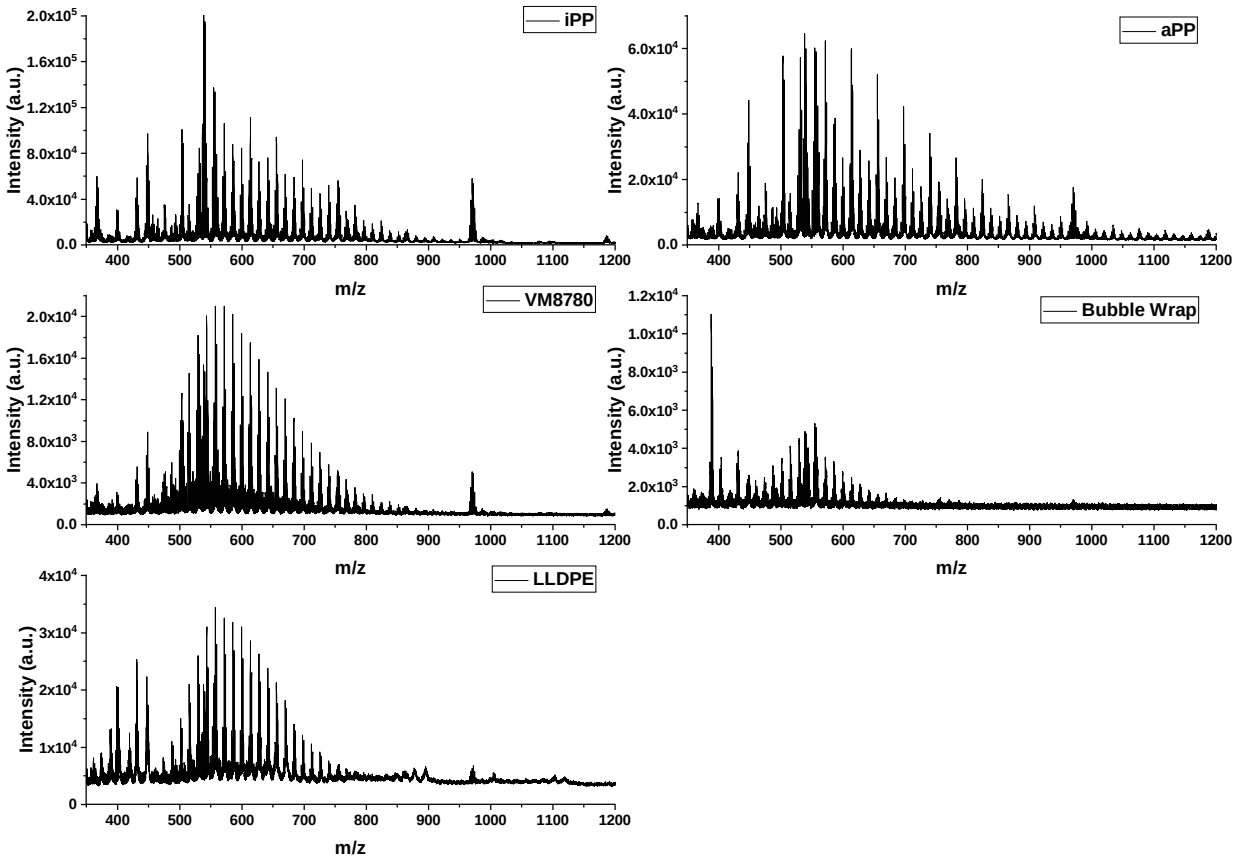

Figure 4.8. Mass spectrometry plots for various polymers (iPP, aPP, VM8780, bubble wrap/LDPE, and LLDPE) after catalytic hydrogenolysis as determined by matrix-assisted laser desorption/ionization (MALDI) mass spectrometry.

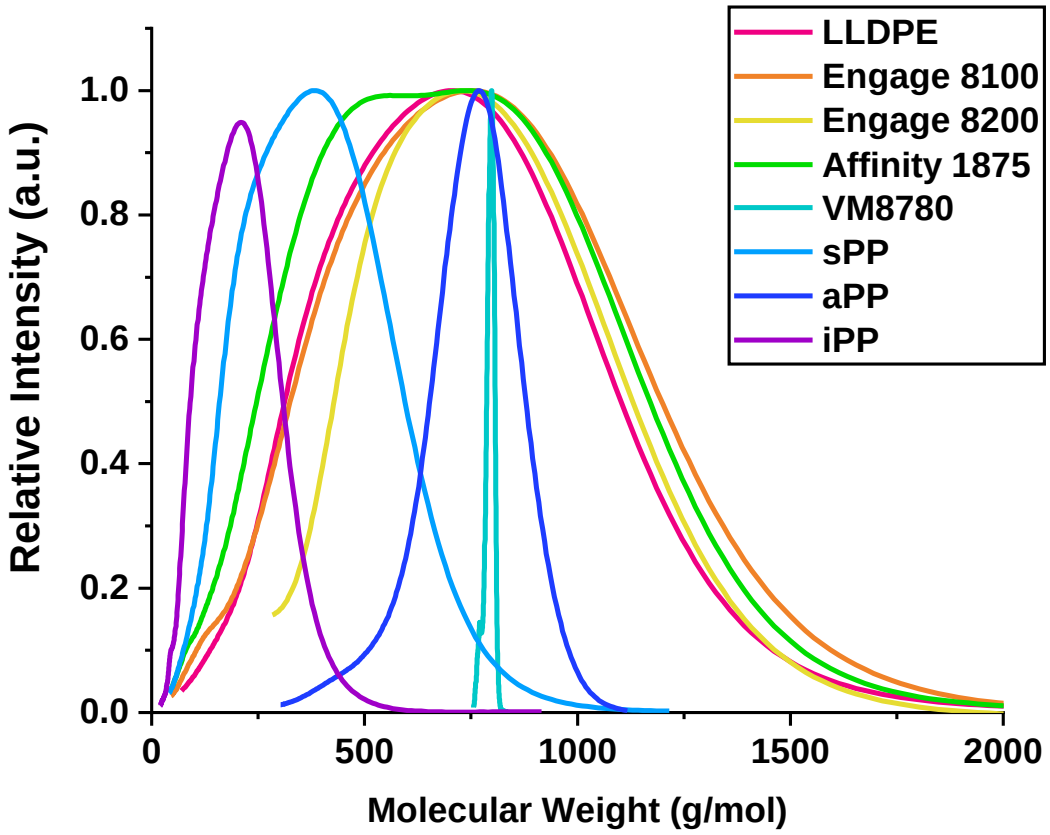

Figure 4.9. Molecular weight distribution plot for catalytic hydrogenolysis products from various polyolefins, as determined by GPC.

For all PP microstructures, racemization of the stereocenters is observed, as evidenced by the methyl region of the $^{13}C\{^{1}H\}$ NMR spectrum (**Figure 4.10e**, ~ 20 ppm), which is like that of aPP. It is likely that this occurs via dehydrogenation or formation of vinylidene followed by non-stereoselective rehydrogenation (overall scheme in Figure **4.10a**, D_2 NMR experiment in **Figure 4.10f**).[36] Re-hydrogenation would lead to the reintroduction of a stereocenter of either configuration, leading to a proliferation of methyl peaks in the $^{13}C\{^{1}H\}$ NMR spectrum around ~ 20 ppm where nearly uniform methyl signals from virgin iPP and sPP split and resemble aPP signals. Furthermore, an abundance of additional signals 35 – 40 ppm suggests skeletal rearrangement is also in play beyond the simple demethylation that other catalytic systems have observed.[36] The contribution of methane relative to other light gases

from headspace GC analysis does increase from 6 to 24 h (54 to 70 mol%, Figure **4.7d-e**), whereas methane's contribution decreases over time in PE hydrogenolysis (47 to 20 mol%, Figure **4.7b-c**), and suggests C – C bond scission at tertiary carbons does occur. However, the removal of methyl groups on the PP backbone is insufficient to explain the additional ^{13}C signals. This also suggests demethylation, beyond what occurs in PE, appears to take place in the later stages of hydrogenolysis. Skeletal rearrangement is likely to occur during the first 6 hours, as an abundance of tertiary carbons would lead to a higher likelihood of carbocation formation. The active site for skeletal rearrangement is unclear, however, as the TiO_2-terminated STO surface is not known for harboring Brønsted acid sites[207] that can initiate extensive isomerization.[208]

Hydrogenolysis with D_2 was performed on iPP to help elucidate the hydrogenolysis pathways. Reaction conditions were unchanged, and the resulting product was similar in structure (as evidenced by $^{13}C\{^1H\}$ NMR in the SI) and molecular weight (M_n ~ 300, $Đ$ ~ 1.3, yield = 69 wt%) to the H_2 experiment. Relative integrations from ^1H and ^2H NMR reveal increases in CH, CD, and CX_3 signal (X being any combination of H and D) relative to H_2 hydrogenolysis of iPP (**Table 4.2**).

Table 4.2. NMR analysis of the products produced from iPP in the presence of H_2 or D_2. Total integration set equal to 1 for each spectrum.

Sample	**Relative integrations**		
	CX	**CX_2**	**CX_3**
^2H NMR iPP + D_2	0.14	0.16	0.7
^1H NMR iPP + D_2	0.14	0.26	0.6
^1H NMR iPP + H_2	0.06	0.41	0.53

An increase in these signals can occur when deuterium is incorporated during either hydrogenolysis and/or re-hydrogenation. The ^{2}H NMR signal from CD and CX_2 being roughly equal and significantly smaller than the CX_3 signal suggests hydrogenolysis occurring across methylene units in the reaction mixture (yellow to blue in Figure 5) to produce chains with either deuterated methyl groups, or deuterated methylene groups that can go on to either produce light gases or undergo skeletal rearrangement. A corresponding decrease in signal from methylene units in ^{1}H NMR when all other signals increase suggests re-distribution of hydrogen at CH_2 to methane and methine units. An inverse isotope effect may account for this re-distribution, as an deuterium on the Pt surface is known to increase the rate of hydrogenolysis and isomerization vs. hydrogen,[209] and hydrogenolysis rates are fastest for methylene-associated C – C bonds.[210] It should also be noted, however, that other characteristics such as local chain configurations and steric hindrance may play a role in the role and extent of hydrogenolysis within a given run time. These phenomena will also depend on catalyst used, as Ertem *et al.*[194] observed only partial hydrogenolysis for Pt/SiO_2 compared to $PtRe/SiO_2$ at 170 °C and 500 psi D_2. While the products described herein from H_2- and D_2-hydrogenolysis of iPP look relatively equal within 72 h, this does not capture kinetic differences from using D_2 and may not hold true for other polymer systems.

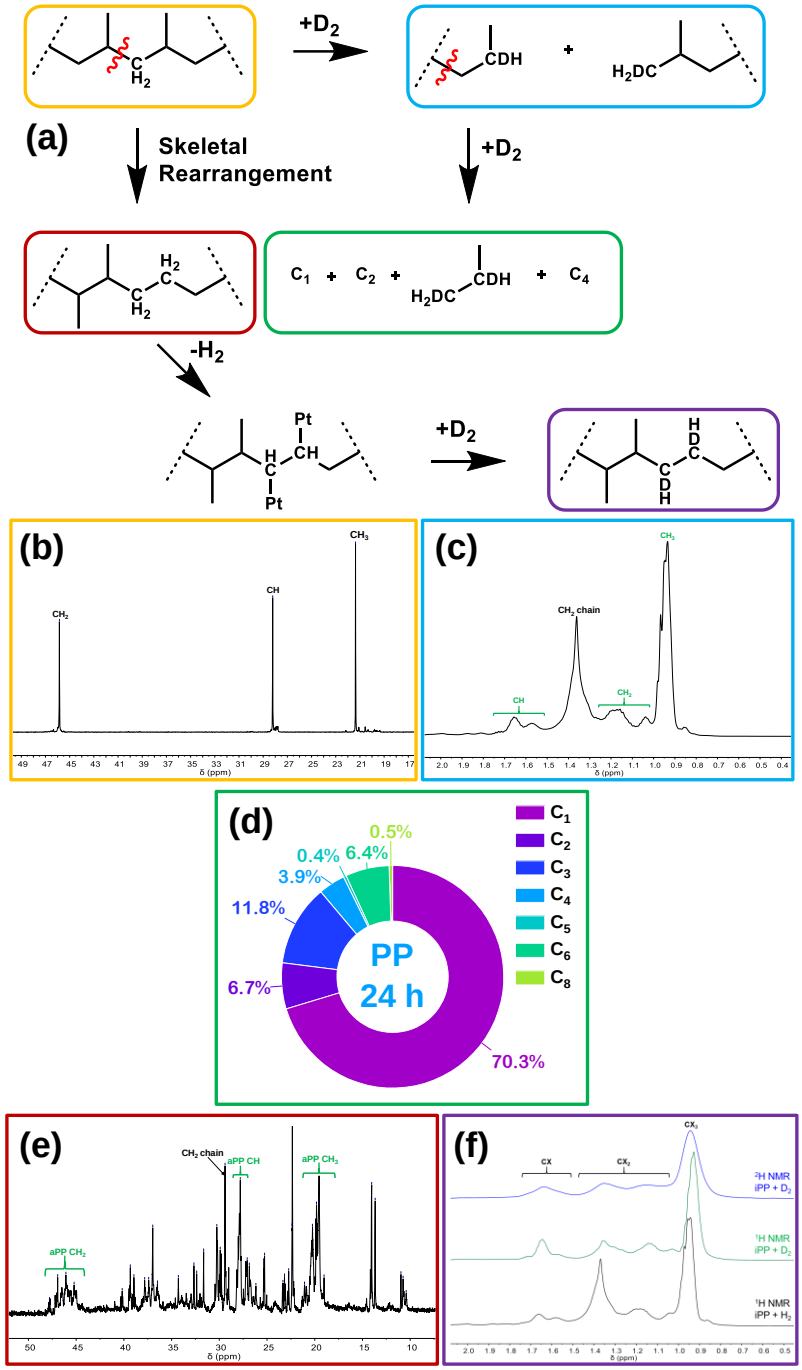

Figure 4.10. (a) Sequential pathways for C – C bond cleavage of iPP (b, orange, $^{13}C\{^{1}H\}$ NMR) via hydrogenolysis to liquid (c, blue, ^{1}H NMR) and gas (d, green, GC) products. Skeletal rearrangement (e, red, $^{13}C\{^{1}H\}$ NMR) of the starting iPP prior to dehydrogenation and re-hydrogenation (e, purple, ^{1}H and ^{2}D NMR) is also shown, showcasing the proliferation of C signals and spread of D_2 incorporation.

4.4.3. Polyethylene-Isotactic Polypropylene Copolymer

A randomly distributed iPP-co-PE co-polymer (Vistamaxx, ExxonMobil, 12 wt% ethylene, M_n ~ 26,550 Da, *Đ* ~ 2.5) was also evaluated to determine if co-polymers differed compared to mixed polymer streams (**Figure 4.11**). This copolymer is used in thermoplastic compounding and injection molding applications due to its high elasticity.[211] In contrast to the iPP, the hydrogenolysis product of the co-polymer had a molecular weight in between iPP and the sPP/aPP products (M_n ~ 360 Da), while being narrower in distribution (*Đ* ~ 1.2) than the iPP product (**7**). A break in the rigid iPP structure by segments of flexible PE[205] may allow for more uniform surface structures to develop onto the catalyst surface if the helical structures as described previously persist in the melt. Despite the copolymer having a significantly higher molecular weight than the iPP, its hydrogenolysis product is also closer to the PE products in M_n. Conversion (> 99 wt%) and yield to liquid products (74 wt%) is also nearly equivalent to iPP experiments. A significant increase in CH_2 signal (1.4 ppm) from ^{1}H NMR after hydrogenolysis is concurrent with all PP experiments and suggests a similar skeletal rearrangement with minimal demethylation. These results suggest that the copolymers do not undergo significantly different hydrogenolysis mechanisms, but that polymer dynamics on a larger scale may affect yield and gas production.

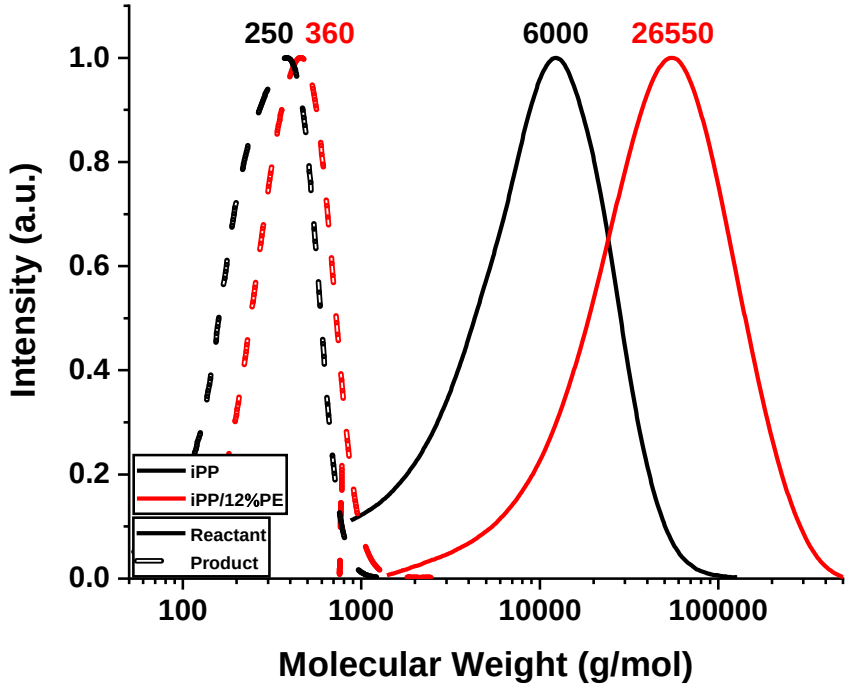

Figure 4.11 Molecular weight distribution plots for 12 wt% polyethylene in VistaMaxx iPP-co-PE and isotactic polypropylene for comparison, as determined by GPC. Starting polymers (solid) and hydrogenolysis products (dashed) show the impact structure can have on the final product. Horizontal scale is logarithmic.

4.4.4 Physical Mixture of LLDPE and iPP.

Finally, a physical mixture of LLDPE (Sigma) and iPP (**10**) was used in a 1:1 mass ratio to evaluate the extreme ends of a mixed polymer feedstock in both molecular weight and structure (**Figure 4.12**). The resulting product was uniform in size (M_n ~ 800 Da) and distribution ($Đ$ ~ 1.2) with no discernible characteristics of either starting polyolefin according to GPC. While the polydispersity is lower than that of the individual polyolefins after hydrogenolysis, the final molecular weight is markedly higher. It is likely that the polymer dynamics and viscosity in a mixed system slowed the collective rate of hydrogenolysis such that the reaction time or hydrogen pressure were insufficient to bring the hydrocarbon species to the lower molecular weight range. It is possible competitive adsorption between different polymer identities could also play a role in the dynamics and molecular weight of the final product, although one may expect such a bias to persist towards the later stages of hydrogenolysis and result in a broader or even bi-modal

distribution in the GPC. Conversion (> 99 wt%) and yield (99 wt%) at these reaction conditions, however, were higher than the individual polyolefins and thus suggest additional characterization of the polymer dynamics is needed to optimize this system given a wide and varied feedstock stream.

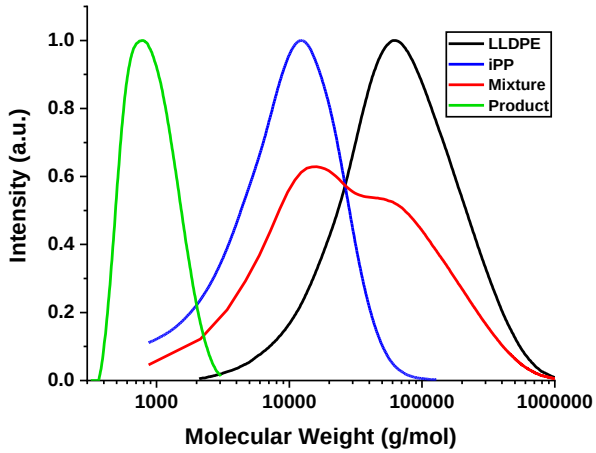

Figure 4.12. Molecular weight distribution plots for virgin LLDPE (black), virgin iPP (blue), a physical mixture of the virgin polyolefins (red) and the corresponding hydrogenolysis product (green), as determined by GPC. Horizontal scale is logarithmic.

4.5 CONCLUSIONS

The survey of polyolefins conducted within show various properties of the polymer source must be accounted for when performing hydrogenolysis. While properties such as the degree of branching and molecular weight can have an impact on how the final product performs for certain applications,[56] these properties do not affect hydrogenolysis in polyethylene samples. That is not the case in polypropylene samples, however, and so pre- or post-catalytic sorting may be needed if a pure product is desired. The copolymer results also suggest structural motifs installed during polymer synthesis could be used to deconstruct post-consumer plastics more effectively. Mixed polyolefin feedstocks will also require additional testing to optimize reaction conditions to bring the molecular weight down to lubricant base oil ranges. These results will direct future efforts in catalyst design principles in attempts to effectively convert post-consumer plastic waste into higher value commodity goods. Evaluations on molecular dynamics, reaction mechanisms, polymer-surface interactions through solid-state NMR, and variations on PP/PE mixtures will help facilitate this design effort.

CHAPTER 5

Solution-Phase Platinum Deposition by SOMC and Related Upcycling

This Chapter was adapted with permission from "K. E. McCullough, I.L. Peczak, R.M. Kennedy, Y-Y. Wang, J. Lin, A.L. Paterson, F.A. Perras, J. Hall, A.J. Krpof, R.A. Hackler, Y. Shin, J. Niklas, O.G. Poluektov, J. Wen, W. Huang, A.D. Sadow, K.R. Poeppelmeier, M. Delferro, M.S. Ferrandon. 'Synthesis Of Platinum Nanoparticles On Strontium Titanate Nanocuboids *Via* Surface Organometallic Grafting For The Catalytic Hydrogenolysis Of Plastic Waste' *J. Mater. Chem. A*, **2023**, 11, 1216-1231.**"**

5.1 ABSTRACT

$Pt/SrTiO_3$ (Pt/STO), prepared on small scale by atomic layer deposition (ALD), is a capable heterogeneous catalyst for the selective hydrogenolysis of polyolefins to hydrocarbon oils, providing a promising approach for upcycling plastic waste. However, because deposition by ALD is costly and resource-intensive, a new synthesis of Pt/STO is needed to effectively scale catalyst production and pursue the commercialization of upcycling processes. To that effect, this work details a scalable deposition method for Pt/STO made by surface organometallic chemistry (SOMC) techniques using Pt(II) acetylacetonate or and trimethyl(methylcyclopentadienyl)platinum. The STO support was calcined (550 °C), treated with ozone (200 °C), and finally steamed (200 °C) to afford a clean STO surface populated with only hydroxyl groups. Pt precursors were dissolved in toluene and deposited onto STO. After reduction at 300 °C, the STO support was decorated with 1.0–1.5 nm Pt nanoparticles. The size and loading of these nanoparticles were varied by employing a multi-cycle deposition and oxidation and/or reduction process designed to ALD techniques. These Pt/STO catalysts hydrogenolyzed isotactic polypropylene into liquid products (>95% yield) with average molecular weights of 200–300 Da (~25 carbon atoms) and narrow size distributions at 300 °C and 180 psi H_2.

5.2 INTRODUCTION

Single-use plastics constitute an important cornerstone of the current chemical economy because of their wide-ranging use in many critical industrial sectors. As many as 400 million metric tons of plastics are produced globally each year to meet consumer needs in textiles, medical and construction equipment,

and food and beverage products, among other uses.[3,5,8,142–144] Modern society lacks the infrastructure to process post-consumer plastics efficiently and economically, meaning that up to 80% of these products are discarded to landfills. A minority of plastic waste is downcycled, *via* traditional mechanical recycling, which prevents recovery of their inherent chemical value.[8,144] While several chemical recycling approaches have been proposed, there are barriers to their broad implementation at scale. For example, pyrolysis, a high-temperature (~500 °C) decomposition process in an oxygen-free environment, can successfully break down plastics at various industrial scales but it (1) is inherently unselective and tends to afford wide product distributions, and (2) the value of these products is intimately related to the current price of crude oil, which limits the process' economic upside.[13,145,212,213] Overall, developing an economically viable method for chemical recycling will require a process that selectively creates value-added products across a wide range of starting plastics. Ideally, these chemical upcycling techniques should simultaneously recoup the inherent chemical value built into single-use plastics and create a uniform product that can meet a particular commercial need.

At the laboratory scale, a promising upcycling technology is catalytic hydrogenolysis, in which waste polyolefins are selectively converted into liquid and wax-like products using metal nanoparticle catalysts deposited on a metal oxide support.[7,31,39,42,43,45,114,146,147] We have previously reported such a system in which platinum (Pt) on $SrTiO_3$ nanocuboid (STO; Pt/STO) catalysts convert various high-density polyethylene, low-density polyethylene, polypropylene, and waste plastic streams into highly uniform liquid and waxlike lubricant products with 60–80 carbon atom backbones.[7,42,46,56] Recent efforts to model a conceptual pilot plant for this process have shown that Pt/STO upcycling at a scale of 250 Mt day^{-1} could profitably generate lubricant materials while reducing process emissions relative to current industrial methods.[59] These results incentivize further study of Pt/STO upcycling, part of which involves scale-up of Pt/STO catalyst synthesis to the kilogram and ton scales. STO nanocuboids have also previously been investigated as a model catalyst support, and as a bridge between templates for surface science studies and performance-oriented, high surface area supports, and the work developed here may also affect innovation of other M/STO catalyzed processes.[7,42,54,60,64,80]

Scaling up the Pt/STO synthesis will require establishing new procedures for support synthesis and Pt deposition. We have previously explored such methods for the scale-up of the STO synthesis, demonstrating that 20+ g of support can be synthesized in a 4 L batch reactor without significant changes to support physical properties nor impact on products of hydrogenolysis when used in a final Pt/STO catalyst.[42] Currently, Pt nanoparticles are introduced onto STO supports *via* atomic layer deposition (ALD), a well-established technique that deposits metals from a gaseous precursor in a precise fashion.[7,60] This process, however, requires highly specialized instrumentation, making it difficult to increase output beyond the gram scale in a short period of time. It is, therefore, necessary to develop a Pt deposition method that retains the precision and tunability of ALD while also facilitating an increase in the output of Pt/STO. Such a deposition method would likely be based on a solution-phase process. Several types of solution-based processes are attractive alternatives to ALD and have found applications in numerous areas of industrial importance not limited to waste plastic upcycling.[67,214]

Solution atomic layer deposition (sALD) is one attempt to develop such a process. Starting from dissolved metal precursors, sALD proceeds *via* the same surface-limited chemistry as conventional, vapor-phase ALD, but improves on the process by both increasing deposition yield and eliminating the need for precursors that are stable in the vapor phase, which are often prohibitively expensive.[215–217] Several sALD systems have been reported for the deposition of inorganic and organic thin films on common metal oxide supports (*e.g.* titania, silica), among other exploratory examples.[215–219]

Another promising synthetic method analogous to ALD is surface organometallic chemistry (SOMC), in which organometallic precursors are chemisorbed onto catalyst support surfaces.[220] Straddling homogeneous and heterogeneous catalysis, this technique generates supported catalysts with single, well-defined active sites without uncontrolled deposition and molecular degradation.[220–223] These active sites also lend themselves well to spectroscopic and kinetic characterization, facilitating the optimization of activity and selectivity.[220] Unlike ALD, SOMC is also scalable and an appealing target for large-scale catalyst deposition. In the last forty years, SOMC-derived supported catalysts have been tuned through precursor engineering and support control to optimize catalyst activity and selectivity for processes as wide-ranging as metathesis, polymerization, hydrogenation, and hydrogenolysis, among others.[220–

[225] These works largely focus on grafting onto amorphous silica, a support that is desirable because of its high surface area and high density of surface hydroxyls available for bonding. Many seminal SOMC systems have been developed around early transition metal (*e.g.*, Ti) complexes. Late transition metals form weaker M–O bonds relative to early transition metals, and under hydrogen treatment during SOMC form metal nanoparticles on the catalyst surfaces.[220] For example, SOMC-derived Cu/ZrO_2 catalysts have shown selectivity for the conversion of carbon dioxide to methanol. This selectivity is partially attributed to the activation of CO_2*via* interaction with Zr(iv) Lewis acid sites in close proximity to deposited Cu particles. Importantly, an SOMC-derived synthesis is integral to this mechanism since it allows for the introduction of highly dispersed and isolated Zr(iv) sites.[220] Comparable activity has been shown for $Cu/Ti@SiO_2$, whose SOMC synthesis affords a high density of Ti(iv) isolated sites. SOMC techniques have also been used to synthesize $PtGa@SiO_2$ alloyed nanoparticles, which show high selectivity for alkane dehydrogenation. Additionally, high-throughput screening techniques have been used to synthesize >100 possible SOMC catalysts for testing in dry reforming of methane.[66] Together, these results show that SOMC can produce small, supported nanoparticles for catalysis, with the potential to synthesize a broad range of bimetallic systems.[220]

In this work, we report the synthesis of a supported platinum nanoparticle catalyst *via* SOMC grafting onto STO nanocuboids (**Fig. 5.1, 5.2**). We have studied surface treatment *via* calcination, ozonolysis, and steaming of the STO nanocuboids to influence surface hydroxyl density and clean the STO surface. The rationale for using this pre-processing method is consistent with other studies of analogous zeolite supports in which pre-reaction processing influences reaction selectivity.[139,226–230] Then, the SOMC grafting of Pt precursors was studied, along with chemical treatments to generate Pt nanoparticles from the SOMC materials. All Pt/STO catalysts prepared in these ways were investigated in hydrogenolysis of isotactic polypropylene to provide liquid products with narrow dispersity, replicating the outcomes from ALD materials.

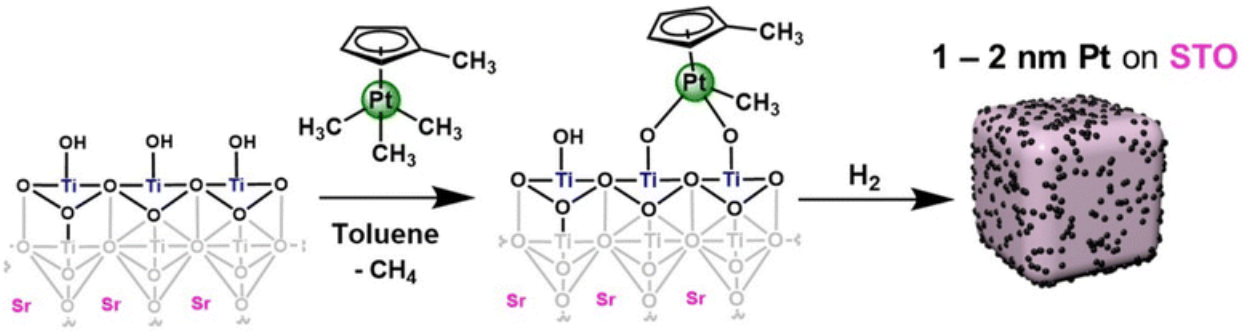

Fig. 5.1 Stepwise SOMC synthesis of Pt/STO catalysts. Pt (green) is deposited onto a STO nanocuboid (surface termination shown) in toluene under heating *via* trimethyl(methylcyclopentadienyl)platinum(IV) ($MeCpPtMe_3$). $MeCpPtMe_3$ bonds to hydroxyl groups on the STO surface, at which point the sample is placed in a reducing environment ("H_2") to afford a sample with 1 – 2 nm Pt nanoparticles on the STO nanocuboid support (right).

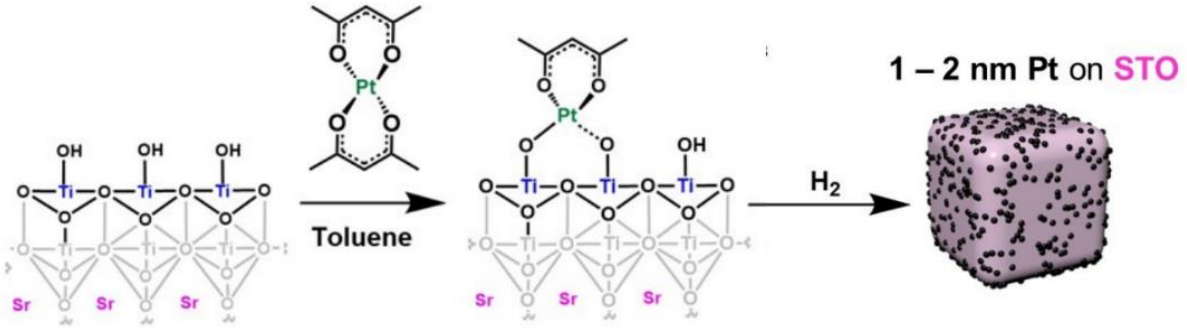

Fig. 5.2 Stepwise SOMC Synthesis of Pt/STO Catalysts. Pt (green) is deposited onto a STO nanocuboid (surface termination shown) in toluene under heating via platinum(II)acetylacetonate ($Pt(acac)_2$). $Pt(acac)_2$ bonds to hydroxyl groups on the STO surface, at which point the sample is placed in a reducing environment ("H_2") to afford a sample with 1 - 2 nm Pt nanoparticles on the STO nanocuboid support (right).

5.2 EXPERIMENTAL SECTION

5.2.1 Materials

Isotactic polypropylene (i-PP), number-averaged molecular weight (M_n) = 5000 Da, weight-averaged molecular weight (M_w) = 12 000 Da, was obtained from Sigma-Aldrich and used as received.

5.2.2 Synthesis of $SrTiO_3$ Nanocuboids

The procedure for the synthesis of large-scale STO nanocuboids was reported by Peczak *et al.*[42] The solution concentrations were proportionally scaled for a 4 L reactor, with the concentrations of Sr, Ti, and NaOH halved relative to the liquid volume to decrease the concentration of chloride ions in the unlined Hastelloy C-276 reactor. Solution A was prepared with 38.69 g of $Sr(OH)_2 \cdot 8H_2O$ dissolved in a solution of 48.04 g of acetic acid and 640.00 g of H_2O under stirring for 2 h. A solution B was prepared with 27.62 g of $TiCl_4$ dissolved in 504.96 g of ethanol for 10 min. The two solutions A and B were mixed and stirred for 10 min in a 2000 mL Erlenmeyer flask; 276.85 g of 10 M NaOH solution was injected into the AB solution for 28 min at a flow rate of 10 mL min^{-1} using a syringe pump. The AB–OH solution was stirred using a magnetic stirrer at the maximum stir rate of the stir plate; no gelation was observed. After mixing and stirring, the AB–OH solution was allowed to sit for 10 min; the pH of the solution was 13.0, and sedimentation occurred. The solution and sediment were transferred to a 4 L Hastelloy C-276 reactor with an internal impeller and a heating jacket. The reactor was heated to 240 °C at a rate of 2 °C min^{-1} and held for 2 h with a stir speed of 400 rpm. After the reaction, the reactor was cooled at a rate of 2 °C min^{-1}. The precipitate and liquid were transferred from the reactor to a secondary container. The solution pH was 13.2 after the hydrothermal reaction. Initially, the liquid was a light-yellow color but changed to dark orange with time. The precipitate was washed with vacuum filtration and dried in air overnight (12 h, 110 °C).

5.2.3 Treatments of $SrTiO_3$ Nanocuboids

Prior to Pt deposition, STO supports were treated through a mixture of calcination in air, ozonolysis, and steaming. STO nanocuboids (~300 mg at a time) were calcined in air between 350 °C and 550 °C for 4 h. STO samples were then introduced into a fixed bed flow reactor and treated with a flow (400 sccm) of ozone in oxygen (8% O_3) using an ozonolyzer (Pacific Ozone, Evoqua Water Technologies LLC) at a constant temperature (200 °C) for 2 h. Samples were then treated with steam at 200 °C for 2 h.

5.2.4 Deposition of Pt onto STO Nanocuboids

Vacuum-dried STO nanocuboids (200 °C, 12 h) were suspended in a solution of trimethyl(methylcyclopentadienyl)platinum(iv) ($MeCpPtMe_3$) (Sigma Aldrich, 98%) or platinum(ii)acetylacetonate ($Pt(acac)_2$) (Sigma Aldrich, >99.98%) in toluene (target 2 wt% Pt) at various temperatures for 72 h under an inert atmosphere in a N_2-filled glovebox, washed and filtered three times with toluene and once with pentane to remove physisorbed precursor, and then vacuum dried at 60 °C overnight. The sample was either calcined at 300 °C in air for 4 h, and/or reduced under 10% hydrogen at 300 °C for 4 h. In order to increase the amount of Pt loaded onto the STO surface, a multi-cycle (*i.e.* multiple cycles of deposition and reduction) approach was implemented. In a one-cycle (1c) deposition and reduction process, STO samples were introduced into a toluene solution for Pt metalation and then reduced to afford metal Pt nanoparticles as above. The reduction treatment of the ligated Pt/STO catalyst regenerates surface hydroxyls, which creates more available sites for deposition and removes any ligands bound to the Pt metal. Afterward, the 1c-sample was vacuum dried (200 °C, 12 h) and reintroduced into a glovebox to be used for an additional round of deposition and reduction to give the two-cycle (2c) sample. Repeating this process again produced the three-cycle (3c) sample.

5.2.5 Characterization

5.2.5.1 Nuclear magnetic resonance (NMR) titration

STO samples were introduced into a solution with an excess of $MgBn_2(THF)_2$ (synthesized by Shrock[231]) and a cyclohexane internal standard (C_6H_6, Sigma-Aldrich-Millipore, 99%, A.C.S. reagent) allowed to react in a J-Young tube while being processed on a 500 MHz Bruker NMR spectrometer with multinuclear broadband observe probes (2.5, 5, or 10 mm tube diameter). OH^- site density was calculated through the

integration of toluene peaks relative to the cyclohexane standard. Calculation of the absolute amount of toluene in each sample was then taken as a measure of the absolute number of hydroxyls on the STO surface and used to determine mmol of OH per square nanometer of support.

5.2.5.2 NMR Characterization

Solution NMR experiments were conducted using a Brucker UltraShield AVANCE 600 MHz spectrometer (^{1}H = 600 MHz) and spectra were analyzed using MestReNova (v14.1.1-24571). NMR analysis of i-PP derived liquid samples were carried out in 1,1,2,2-tetrachloroethane-d_2 at 395 K (122 °C). Dynamic nuclear polarization (DNP)-enhanced ^{17}O solid-state NMR experiments were carried out on the bare STO nanocuboids to characterize their surface termination. STO materials were surface-enriched with ^{17}O by first partially dehydroxylating them at 300 °C overnight, rewetting them with 40% ^{17}O-water in a dry atmosphere, and then removing excess water at room temperature under vacuum overnight. This process partially exchanges oxide and hydroxide centers from the surface. The procedure was repeated to surface ^{17}O-enrich a sample of anatase titania that was used as a reference. The material was then wetted with a 16 mM solution of the TEKPol biradical polarizing agent in either fully protonated or fully deuterated 1,1,2,2-tetrachloroethane (TCE),[232] packed into a 3.2 mm sapphire rotor and inserted into the pre-cooled (100 K) low-temperature MAS probe installed from a Bruker AVANCE III 400 MHz/263 GHz MAS-DNP spectrometer. Measurements were carried out using three approaches, namely, (1) a ^{17}O{^{1}H} PRESTO-II experiment excites exclusively hydroxyl ^{17}O species,[233,234] (2) a ^{17}O{^{1}H} D-RINEPT-SR4$_1^2$(tt) experiment excites both hydroxyls and oxide ^{17}O centers that are near ^{1}H nuclei,[235] and (3) a ^{17}O direct DNP experiment that reveals all surface ^{17}O centers,[236] regardless of ^{1}H locality. The MAS spinning frequency was set to 13.888 kHz and ^{17}O pulses utilized effective RF powers of 25 kHz. ^{1}H RF powers were of 100 kHz for hard and CW pulses and 132 kHz for the tanh/tan adiabatic SR4$_1^2$ pulses used in the D-RINEPT-SR4$_1^2$(tt) experiments. Recycle delays were set to 2 s and 8 s for the indirect and direct DNP experiments performed on the STO, respectively, and 10 s in the case of anatase TiO_2. Quadrupolar Carr–Purcell Meibook–Gill (QCPMG) was applied for sensitivity enhancement.[237] 34 echoes were acquired, with a spikelet separation of 694 Hz. PRESTO spectra were acquired in 2048 and 768 scans for STO and TiO_2, respectively, with 2 rotor cycles of recoupling and INEPT spectra were acquired in 8192

and 1536 scans with 32 rotor cycles of recoupling. Direct DNP experiments utilized a 6.94 kHz spikelet separation, recycle delays between 1 and 256 s and acquired in 256 scans. Through-space $^{17}O\{^{1}H\}$ heteronuclear correlation experiments were measured using the D-RINEPT-SR4$_1^2$(tt) pulse sequence and 100 kHz ^{1}H frequency-switched Lee-Goldburg homonuclear decoupling.[238] 672 scans were acquired for each of the 16 t_1 increments of 130.672 μs and the QCPMG spikelet separation was increased to 2.315 kHz.

$^{1}H\{^{195}Pt\}$ experiments were carried out using a sideband-selective perfect-echo (PE)-RESPDOR experiment using an Agilent DD2 400 MHz spectrometer equipped with a Samoson 1.7 mm fast-MAS probe.[239] Samples were packed into 1.7 mm rotors in an inert atmosphere and spun to 40 kHz using pressurized nitrogen. Hard ^{1}H pulses utilized a 100 kHz RF field while the sideband-selective, 50 μs, ^{195}Pt pulses were applied with a 13 kHz RF power. The total recoupling time was equal to 1.2 ms. Sub-spectra were acquired in either 2048 or 16 384 scans with a 1 s recycle delay. The ^{195}Pt offset frequency was first stepped in 10 kHz increments around −2000 ppm to find a spinning sideband and was then stepped in 40 kHz increments to measure the intensities of the neighboring spinning sidebands.

5.2.5.3 Density Functional Theory

Density-functional theory (DFT) calculations of ^{17}O magnetic shielding and electric field gradient tensors were carried out using CASTEP (version 2018).[240] The default “on-the-fly” ultrasoft pseudopotentials were used together with the exchange-correlation functional of Perdew, Burke, and Ernzerhof (PBE).[241,242] Structures were first geometry optimized with convergence tolerances of 2×10^{-5} eV per atom in total energy, 0.05 eV $Å^{-1}$ in forces, and 0.002 Å in maximum atomic displacement. Geometry optimization calculations used kinetic energy cutoffs of 489.8 eV, a *k*-point grid density of 0.08 $Å^{-1}$, and the Grimme D2 dispersion scheme.[243] Shielding calculations used the gauge-including projector augmented-wave (GIPAW) method as implemented within CASTEP.[244,245] The kinetic energy cutoff was increased to 700 eV and the *k*-point grid density was set to 0.03 $Å^{-1}$. ^{17}O magnetic shielding constants converged to within 1 ppm and were converted to chemical shifts using a reference shielding of 187.065 ppm calculated using SrO and TiO_2.

5.2.5.4 Electron Microscopy

Nanoparticle imaging was conducted by scanning transmission electron microscopy, using a FEI Talos F200X TEM/STEM operated at 200 kV. Aberration-corrected high-resolution transmission electron microscopic images were acquired using the Argonne Chromatic Aberration-corrected TEM (ACAT), a FEI Titan 80-300 ST with an image corrector to correct both spherical and chromatic aberrations. These microscopes were used in coordination with the Center for Nanoscale Materials (CNM) at Argonne National Laboratory. In preparation for analysis by electron microscopy, powdered samples (~20 mg) were sonicated in ethanol (10 mL) for 15 minutes. The resulting suspension was dropcast onto a lacey carbon TEM grid (Ted Pella, Inc., UC-A on Lacey 400 mesh Cu). Particle size and shape were measured using ImageJ and Gatan Digital Micrograph software.[128] The face-to-face distance between opposing [100] faces of STO nanocuboids was used as a measure of particle width.

5.2.5.5 Brunauer–Emmet–Teller (BET) Surface Area Measurements

The catalyst surface area was determined by nitrogen adsorption using a Micromeritics ASAP 2010 instrument. Each sample was degassed by heating at 150 °C under vacuum prior to measuring the surface area. Five data points were measured for an accurate evaluation of surface area.

5.2.5.6 X-ray Absorption Fine Structure (XAFS)

XAFS spectroscopy measurements were completed at the 10ID beamline at the Advanced Photon Source (APS) of Argonne National Laboratory. The beam was generated *via* an undulator source with a liquid N_2-cooled Si(111) double crystal monochromator (DCM) and harmonic rejection mirror. Spectra were collected in fluorescence mode using Soller slits and a Zn filter with a fluorescence ionization chamber. Simultaneous measurement of the Pt foil was completed and calibrated to 11 562.76 eV at the zero-crossing of the second derivative. Samples were diluted with SiO_2 and pressed into self-supporting wafers at a 45° angle and placed within an *in situ* gas cell as described in detail in a previous report.[246]

Spectra were measured under He flow (200 mL min^{-1}) at room temperature before and after reduction (3.5% H_2/He, 250 °C, 10 minutes, 50 mL min^{-1}) to remove surface oxide species formed in the samples upon contact with air. Data processing (includes normalization, background subtraction calibration, and fitting) was performed using the Demeter/Athena/Artemis suite of XAFS analysis software.[247]

5.2.5.7 Electron Paramagnetic Resonance Spectroscopy (EPR)

Continuous wave (CW) X-band (9–10 GHz) EPR experiments were carried out with a Bruker ELEXSYS II E500 EPR spectrometer (Bruker Biospin, Billerica, MA), equipped with a TE_{102} rectangular EPR resonator (Bruker ER 4102ST). Field modulation at 100 kHz in combination with lock-in detection leads to first derivative-type CW EPR spectra. Measurements were performed at 15 K. A helium gas-flow cryostat (ICE Oxford, UK) and an ITC (Oxford Instruments, UK) was used for temperature control. Data processing was performed using Xepr (Bruker Biospin, Billerica, MA) and MatlabTM R2018b (MathWorks) environment.

5.2.5.8 Thermogravimetric Analysis (TGA)

TGA was carried out using a TGA Discovery (TA Instruments) coupled with a mass spectrometer (QMS200, Stanford Research Systems) with 10 mL min^{-1} N_2.

5.2.5.9 Powder Diffraction (PXRD)

The crystalline phase compositions of the samples were determined by PXRD using a Bruker Diffractometer D8 Advance operating with the following parameters: Cu Kα radiation of 40 mA, 40 kV, K_λ = 0.15418 nm, 2θ scanning range of 20–60°, a scan step size of 0.0018° and a time of 1 s per step. The sample was placed on a zero-background silicon holder (MTI Corp.) for analysis.

5.2.5.10 Inductive Coupled Plasma Optical Emission Spectrometry (ICP-OES)

Metal analysis was performed at the Northwestern University Quantitative Bio-element Imaging Center. Quantification of Pt, Sr, and Ti was accomplished using ICP-OES of acid-digested samples.

5.2.5.11 Catalytic Hydrogenolysis of i-PP Using Pt/STO

Hydrogenolysis experiments were performed in 100 mL Parr autoclaves equipped with an overhead stirrer and thermocouple extending to just above the melted polymer. i-PP (3 g) and Pt/STO catalyst (300 mg) were loaded into a glass liner in the reactor. The autoclave was sealed, and then evacuated and refilled with mixed gas (9 : 1 ratio of H_2 : He) three times. The reactor was pressurized with mixed gas (9 : 1 ratio of H_2 : He) at 827 kPa at room temperature, and then heated to 300 °C (1.2 MPa). After 24 h, the reactor was allowed to cool to room temperature. The gas in the headspace was directly injected into a gas chromatograph (GC) for analysis (see below). The remaining gas in the headspace was slowly released. The liquid products were collected and fractionated based on their location either outside the liner (OL) or inside the liner (IL). OL-products were directly collected by pipette, while IL-products were extracted with *n*-hexane (HPLC grade) warmed at 55 °C. The extracted solution was filtered through silica gel, and the solvent was removed using a rotary evaporator. Both OL- and IL-products were analyzed by ultra-high pressure liquid chromatography (UHPLC), NMR, and thermogravimetric analyzer-differential scanning calorimetry (TGA-DSC). In the manuscript, the total amount of liquid is the sum of OL and IL.

5.2.5.12 Liquid Species Analysis

A Waters Corporation UHPLC system equipped with the ACQUITY AQT XT45 (1.7 μm, 4.6 mm, 150 mm) analytical column was used to characterize the M_n and M_w of the soluble products. The calibration standard included research-grade, pure alkane species individually (*n*-octane, *n*-nonane, *n*-decane, *n*-dodecane, *n*-hexadecane, *n*-octadecane, *n*-eicosane, *n*-tetracosane, *n*-octacosane, *n*-dotriacontane, and *n*-hexatriacontane, 1 mL, 50 mg mL^{-1}). A calibration curve and representative spectrum are presented in the ESI (**Fig. 5.3**). OL- and IL-products were dissolved in *n*-hexane (1 mL, 50 mg mL^{-1}) and injected for analysis.

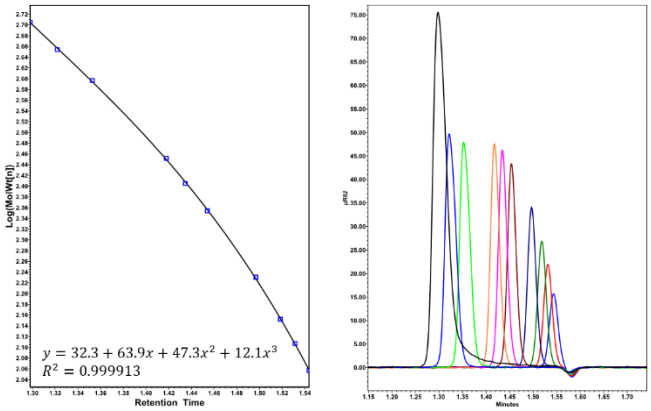

Fig. 5.3 *i-PP*-Derived Liquid Sample Analysis. The calibration curve used to benchmark polymer upcycling products in liquid sample analysis is presented on the left of this figure, and a sample high-pressure liquid chromatography output is presented on the right. A more extensive description of this analytical technique is presented in the Experimental section of the main manuscript under the same title.

5.2.5.13 Quantification of Gas Species

The volatile products were sampled by connecting the autoclave to a GC sampling loop and analyzed simultaneously using a GC-flame ion detector (FID) and a GC-thermal conductivity detector (TCD) installed on a HP 5890 gas chromatograph. A Supelco 60/80 Carboxen 1000 (15′ × 1/8″ × 2.1 mm) packed column (GC-TCD) was used to measure the ratio of H_2 to He (internal standard) to quantify H_2 in the headspace after an experiment. An Agilent GS-Gaspro (15 m × 0.32 mm × 0.00 μm) capillary column was used to separate and quantify the C_1–C_9 hydrocarbon species by GC-FID. Quantification of volatile hydrocarbons was conducted by using a calibrated gas tank (Matheson, C_1–C_4 hydrocarbons gas tank) and pure small molecular weight alkanes solvent vapor (Sigma-Aldrich, HPLC grade, *n*-pentane, *n*-hexane, *n*-heptane, and *n*-octane). A graphical display of a calibration curve is presented in the ESI (**Fig. 5.4**).

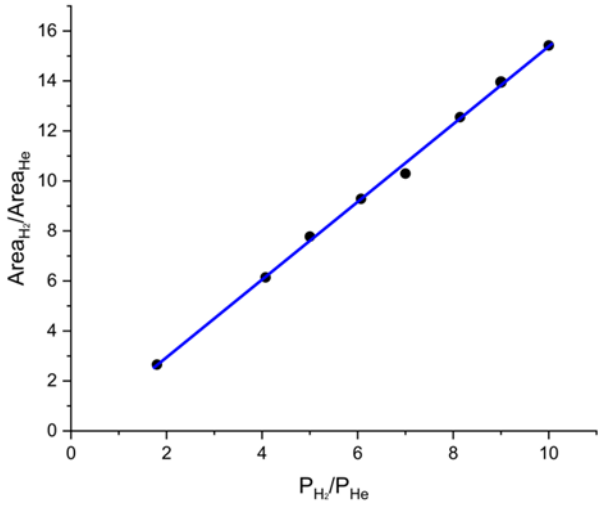

Fig. 5.4 Gas Species Quantification and H_2 Consumption Analysis. The calibration curve used to quantify gaseous species and hydrogen consumption in this work is presented above. A more extensive description of this analytical technique is presented in The Experimental section of the main manuscript under the same title.

5.2.5.14 TGA-DSC Analysis

i-PP derived samples were analyzed simultaneously by TGA and DSC configuration, installed on a Netzsch (STA 449F1) equipped with Al_2O_3 crucible (volume 85 µL) with lid. The instrument calibrations (weights, temperature, and sensitivity) were performed using calibration sets (serial #14565) provided by Netzsch. An empty Al_2O_3 crucible served as reference. A 3 mg sample was placed in the sample crucible, covered by a lid. The sample was heated from 40 to 550 °C with 3 °C min^{-1} in a streaming nitrogen atmosphere (purge: 20 mL min^{-1}; protective: 20 mL min^{-1}) to suppress oxidation. The total instrumental runtime was 3 h. Analysis of DSC peaks was carried out using Proteus Thermal Analysis Software (Ver 8.0.2) from Netzsch.

5.3 RESULTS AND DISCUSSION

5.3.1 Preparation of STO nanocuboids Prior to Surface Modification Studies

Strontium titanate ($SrTiO_3$, STO) nanocuboids (nano-rectangular prisms) were synthesized hydrothermally as per the scaled-up method described in Peczak *et al.* at 240 °C for 2 h.[42,123] The STO nanocuboids have an average size of 45 ± 10 nm and an average shape of a cube composed of (100) facets, with rounded edges. 70 to 75% of nanoparticles in the STO sample take this shape, though the batch is 100% crystalline $SrTiO_3$ by powder X-ray diffraction. Previous work has demonstrated that hydrothermally synthesized STO nanocuboids predominantly have a Ti rich, $\sqrt{13}$ by $\sqrt{13}$, 33.3° rotated TiO_2 double layer reconstruction on the surface of the {100} facets,[42,76,78,81–83,123,186,187,248] and that upon annealing at elevated temperatures, the rounded corners between these {100} facets reform into {110} facets.[78] Additionally, bulk STO has a close lattice match with platinum, which can result in a high degree of epitaxial stabilization of platinum nanoparticles on the support surface.[54,60,122] Previously, platinum nanoparticles with narrow size distribution and a range of sizes were synthesized on STO nanocuboids by atomic layer deposition (ALD).[7,54,54,60,249] These ALD-derived Pt/STO catalysts synthesized show no signs of immediately evident $SrCO_3$ buildup at room temperature or typical reaction conditions (200–300 °C), per results collected *via* X-ray diffraction (**Fig. 5.5**), though some carbonate desorption was observed at high temperatures (**Fig. 5.6**).

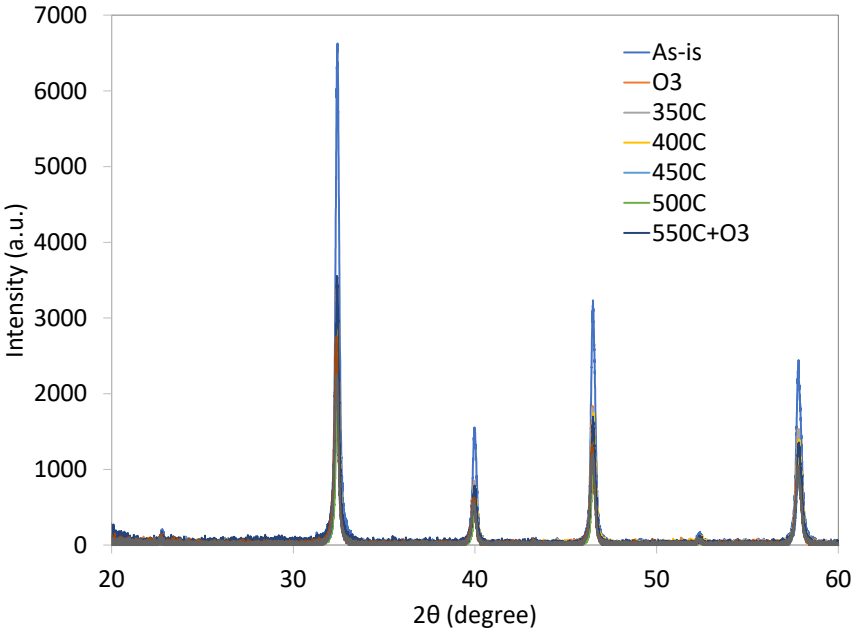

Fig. 5.5 Diffraction patterns of $SrTiO_3$ after Various Treatments. Patterns were collected by power x-ray diffraction, and all correspond to crystalline strontium titanate.

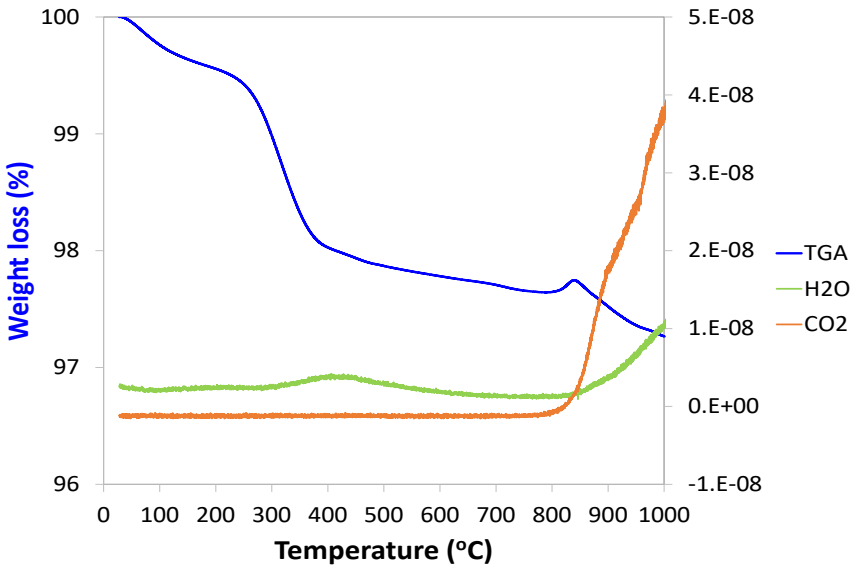

Fig. 5.6 Thermogravimetric analysis (TGA) of as-prepared STO supports. The data show 0.5 % by mass of carbonate desorption above 800 °C, which would indicate a minority surface species (e.g. $SrCO_3$) present after synthesis that does not significantly affect the STO surface. This is consistent with previous observations about $SrCO_3$ formation in Peczak et al.[42]

In atomic layer deposition, ozone treatment is used to clean the STO surface because as-synthesized STO nanocuboids can have a range of adventitious species on the surface, including hydroxyls as part of the surface termination, adsorbed water, or ions (e.g. sodium, chloride, hydroxide, acetate, carbonate) from the hydrothermal solution, as suggested in Peczak et al.[42] Carbonates, for example, can form during the STO synthesis when inhomogeneity in the pre-heating Sr–Ti–OH mixture creates local environments with intermediate pH (e.g. 3 < pH < 9). In this range, strontium carbonate is more thermodynamically stable than strontium titanate. [42,132–134] The concentration of the adsorbed ions from the reaction mixture can be significantly decreased by washing and drying the nanoparticles post-synthesis. However, such post-reaction processing still allows for some species, such as hydroxyls and water, to remain on the surface. Variation in the concentration of hydroxyls and water on the surface, both between batches and between individual cuboids, can result in inhomogeneity in the grafting of catalyst precursors on the surface of the support. To minimize this effect, various pre-treatments can be performed to burn or desorb species on the surface or to selectively re-introduce desired surface species. Here, calcination and ozonolysis were used for the former, and steam for hydroxyls.

5.3.2. Surface Modification through Calcination

STO nanocuboids were calcined for 4 h at temperatures between 350 °C and 550 °C. Particle size and the relative amount of nanocuboid particles are statistically equivalent in the as-synthesized sample and post-calcination samples (**Fig. 5.7** and **Table 5.1**).

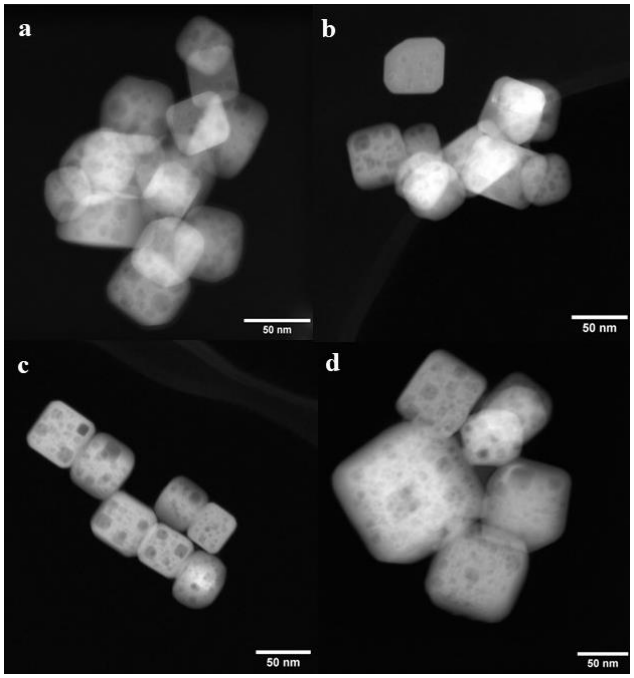

Fig. 5.7 TEM images of as-prepared STO (a) and STO after calcination at 350 °C (b), 450 °C (c), and 550 °C (d). All samples, regardless of calcination conditions or lack thereof, appear to have average sizes of around 45.0 ± 10.0 nm and contain between 70 – 75 % nanocuboid particles per sample. Measurements of these two parameters corresponding to each sample are presented in the supplementary information.

Table 5.1. Average size of STO nanocuboids and average amount of nanocuboid particles per sample analyzed for an as-synthesized support sample, and samples that had been calcined at 350 ^{o}C, 450 ^{o}C, and 550 ^{o}C.

Calcination Temperature (^{o}C)	Average STO Particle Size (nm)	% Cubes
As-prepared (no calcination)	45.9 ± 9.7	74.2
350	45.7 ± 11.1	71.4
450	42.1 ± 9.9	72.1
550	42.6 ± 9.1	73.5

Calcination of as-synthesized STO nanocuboids at 350 °C and 550 °C desorbed most surface species, which generally desorb between 200 °C and 600 °C, as seen by TGA of the calcined materials (**Fig. 5.8**). These results demonstrate that calcination at 550 °C exhibits the lowest weight loss of desorbed species, indicating that this surface is the least contaminated and therefore cleanest. At around 550 °C, the surface area of the STO sample has decreased 37% from the as-synthesized sample even though particle morphology does not visibly change. This likely stems from the coalescence of individual STO nanocuboids (**Table 5.2**). To avoid this and ensure that the STO support surface area was sufficiently high for catalyst deposition, calcination treatments were not carried out at temperatures higher than 550 °C.

Table 5.2. BET Surface Area of STO supports After Calcination at Various Temperatures. Catalyst surface area was determined by N_2 adsorption. Prior to surface area measurements, each sample was degassed by heating under vacuum at 150°C. Five data points were collected to ensure accuracy.

Calcination Temperature (ºC)	BET Surface Area (m^2 / g)
As-prepared (no calcination)	26.5
350	22.9
450	17.0
550	16.7

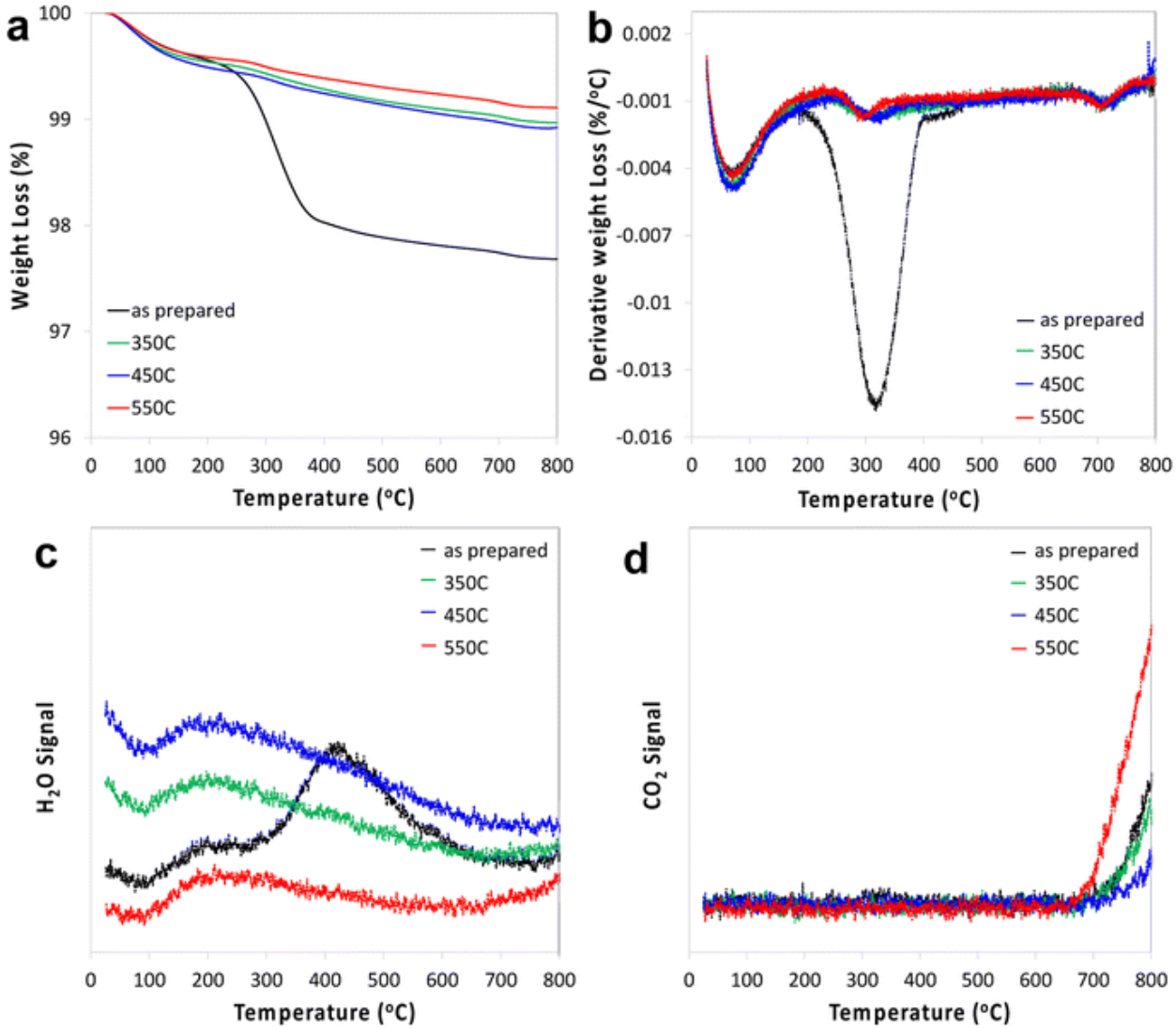

Fig. 5.8 TGA (a), 1st derivative (b), water signal (c) and CO_2 signal (d) of STO as prepared and after calcination at 350 °C, 450 °C and 550 °C.

5.3.2 Effect of Calcination on $MeCpPtMe_3$ Grafting

One cycle of platinum was deposited at room temperature on STO samples calcined at 350 °C or 550 °C, using the $MeCpPtMe_3$, the organometallic precursor used for ALD of Pt, resulting in Pt/STO samples with weight loadings of 0.019 wt% and 0.13 wt%, respectively. It appears that the Pt particle size is uneven on the STO calcined at 350 °C, while it is more uniform when deposited on STO calcined at 550 °C (**Fig. 5.9**). Uneven deposition on otherwise equivalent samples is likely due to remaining surface species that interfere with Pt grafting, making calcination at 550 °C the preferred temperature. However, the weight

loading of Pt is still low relative to previously reported ALD deposition and can likely be increased through additional pre-deposition surface treatments.

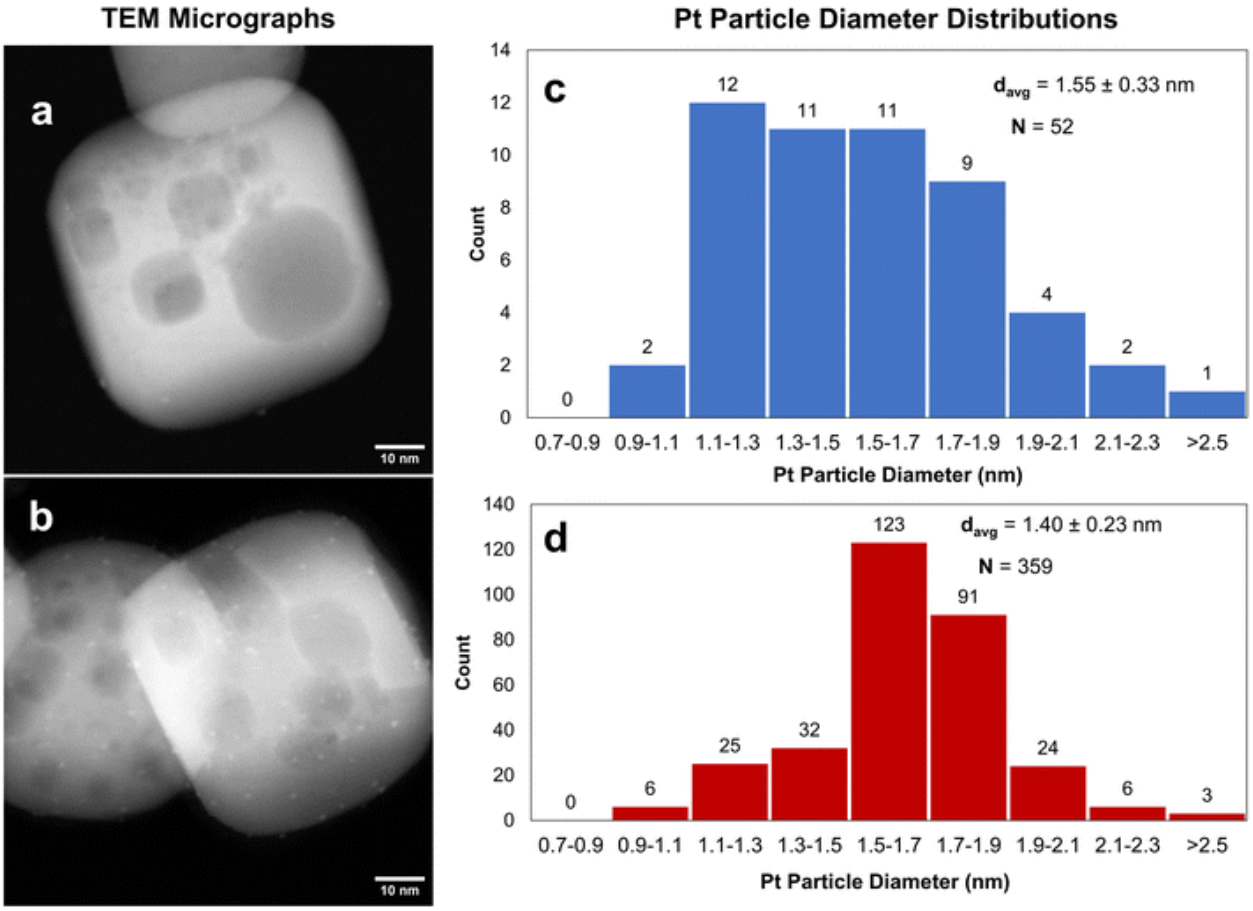

Fig. 5.9 1cPt/STO using STO pre-calcined at 350 °C (a) and at 550 °C (b). Metalation of $MeCpPtMe_3$ at 25 °C. Pt particle size distributions for the samples presented in (a) and (b) are provided in the adjacent histograms in (c) and (d), respectively.

5.3.3 Surface Modification Through Ozonolysis

A similar effect to calcination can be achieved at lower temperatures using stronger oxidants, such as ozone through ozonolysis. The lower temperature of ozonolysis can be beneficial if there are other properties, such as phase transitions or sintering, that would be accelerated at higher temperatures. In this work, both processes were used in sequence to ensure that STO support surfaces were sufficiently clean for Pt deposition. Additionally, because ozone treatment at 200 °C was previously used to deposit Pt by ALD,[7] the use of ozonolysis in this work enables a comparative study between ALD- and SOMC-derived Pt deposition methods. Ozone treatment at 200 °C was used to treat the STO surface after calcination prior to catalyst deposition. Pt deposition was conducted *via* SOMC of $MeCpPtMe_3$ at 65 °C on STO supports treated by both calcination and a combination of calcination and ozonolysis. Ozone treatment did not significantly affect final Pt particle size, as final particle sizes for both samples were 1.3 nm (**Fig. 5.10**), and Pt weight loadings were similar (0.13 wt% without ozone and 0.12 wt% with ozone).

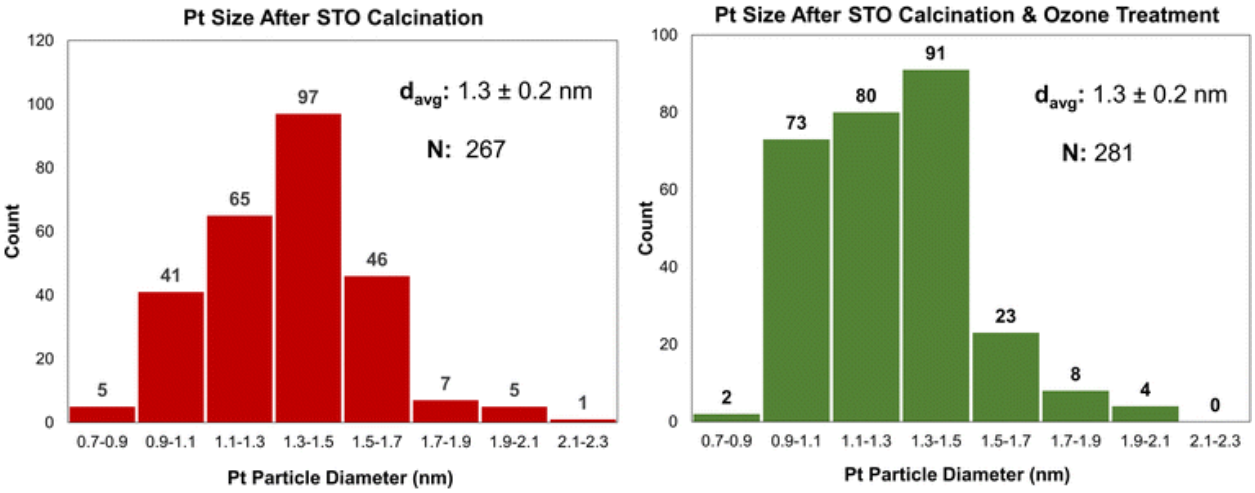

Fig. 5.10 Platinum particle size distributions for SOMC 1cPt/STO prepared with STO that had been calcined at 550 °C and steamed at 200 °C (red, average size of 1.3 ± 0.2 nm) and with an additional ozone treatment at 200 °C between the calcination and steaming steps (green, average size of 1.3 ± 0.2 nm). Metalation of $MeCpPtMe_3$ at 65 °C.

5.3.4. Effect of Steam Treatment

Any combination of calcination and ozonolysis likely leads to significant dehydroxylation, meaning that hydroxyls must be replenished prior to SOMC grafting. Steam treatment at elevated temperatures can be used to re-introduce controlled concentrations of surface hydroxyls.[250] NMR titration of surface hydroxyls on STO nanocuboids with $Bn_2Mg(THF)_2$ on samples calcined at 550 °C and then steam-treated at temperatures ranging from 100 °C to 500 °C revealed that the hydroxyl concentration reaches a maximum of 17.3 OH per nm^2 at 200 °C (**Fig. 5.11**).

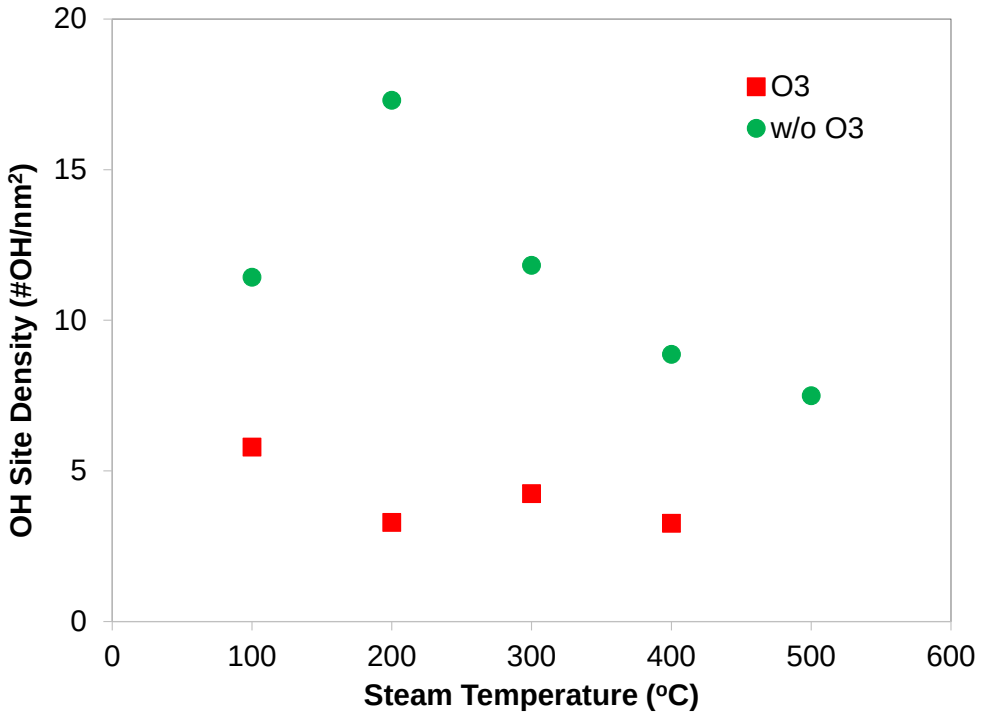

Fig. 5.11 NMR titration of surface hydroxyls per nm^2 on STO with $Bn_2Mg(THF)_2$ in C_6D_6 and cyclohexane. The STO was calcined at 550 °C followed by steam for 2 h ranging from 100 °C to 500 °C (green dots). The STO was calcined at 550 °C followed O_3 treatment at 200 °C for 2 h and by steam for 2 h ranging from 100 °C to 400 °C (red square).

The presence of O_3 did not significantly affect surface hydroxyl concentrations. Below that temperature, the number of reconstituted hydroxyls is low, and above that temperature, the formation of hydroxyls is increasingly in competition with the reverse dehydration reaction to form a bridging oxygen, shifting the equilibrium toward low hydroxyl concentrations.[251,252] Steam treatment at 200 °C was selected to use as a post-treatment of ozonolysis. TGA confirms a higher loss of water when ozone is used in between the calcination at 550 °C and the steam treatment at 200 °C (**Fig. 4.12**). It is likely that the increased oxidizing power of ozone is leading to re-arrangement and stabilization of the surface, making it more prone to reaction with water to form hydroxyls.

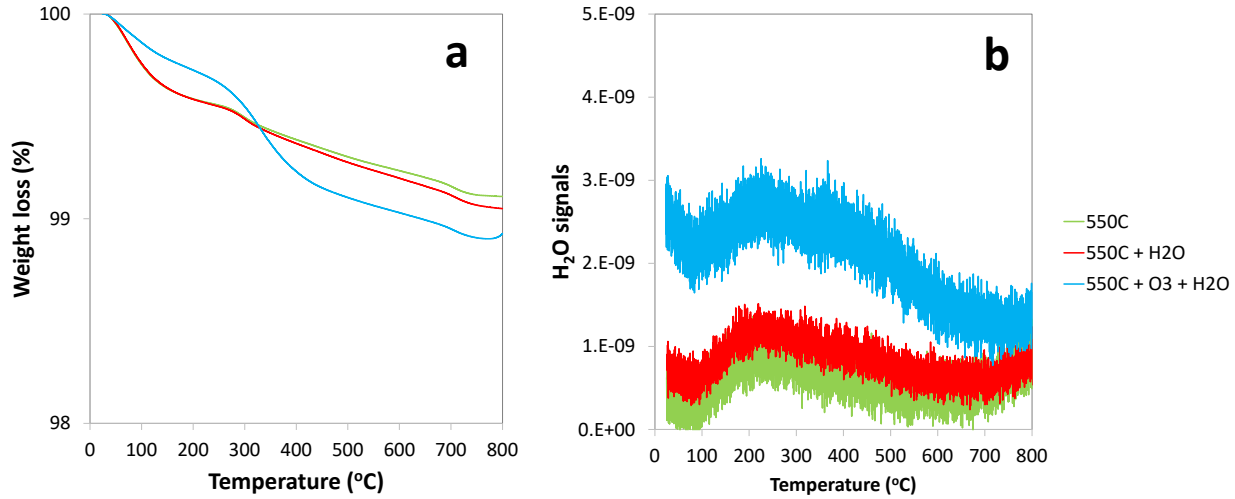

Fig. 5.12 TGA curve (a) and H_2O signals (b) of STO at various treatments.

DNP-enhanced ^{17}O solid-state NMR was carried out to characterize the structure of the formed hydroxy species and surface termination. Three experiments, PRESTO, D-RINEPT-SR4$_1^2$(tt), and direct DNP, were conducted to selectively detect hydroxyl species, all oxygen centers near ^1H spins, and all oxygen centers regardless of environment, respectively. The D-RINEPT-SR4$_1^2$(tt) experiment revealed two major surface environments resonating near 500 and 100 ppm at 9.4 T, the latter of which could be assigned to hydroxyls using the PRESTO measurement (**Fig. 5.13**). Plane-wave DFT calculations were carried out on

the *c*(4 × 4)[253] and $\left(\sqrt{13}\times\sqrt{13}\right)\mathrm{R}33.7°$ terminations of STO,[254] in addition to three hydrated variants of the (2 × 1) termination,[255,256] to predict the ^{17}O chemical shifts and quadrupolar coupling parameters for various surface environments. These calculations revealed that the signal around 500 ppm can be attributed to surface oxygen species in the TiO_2 double layer, with potentially a shoulder from the Sr layer. No evidence for Sr–OH species was detected, meaning that, as expected, the Pt grafting sites are Ti–OH species. The ratio of the Ti–O–Ti and Ti–OH signal intensities was similar in a direct DNP experiment and was not affected by the solvent protonation level. ^{17}O{^{1}H} HETCOR experiments revealed that the major correlation for the oxide resonances was from a neighboring Ti–OH species, and this was not affected by the application of a longer recoupling time in protonated TCE (*i.e.* no correlations to solvent were observed, **Fig. 5.13**). This indicates that hydroxyls are found homogeneously on all STO facets and that significant defects are present in the usually hydrophobic $\left(\sqrt{13}\times\sqrt{13}\right)\mathrm{R}33.7°$ surfaces, in agreement with the high average hydroxyl density.

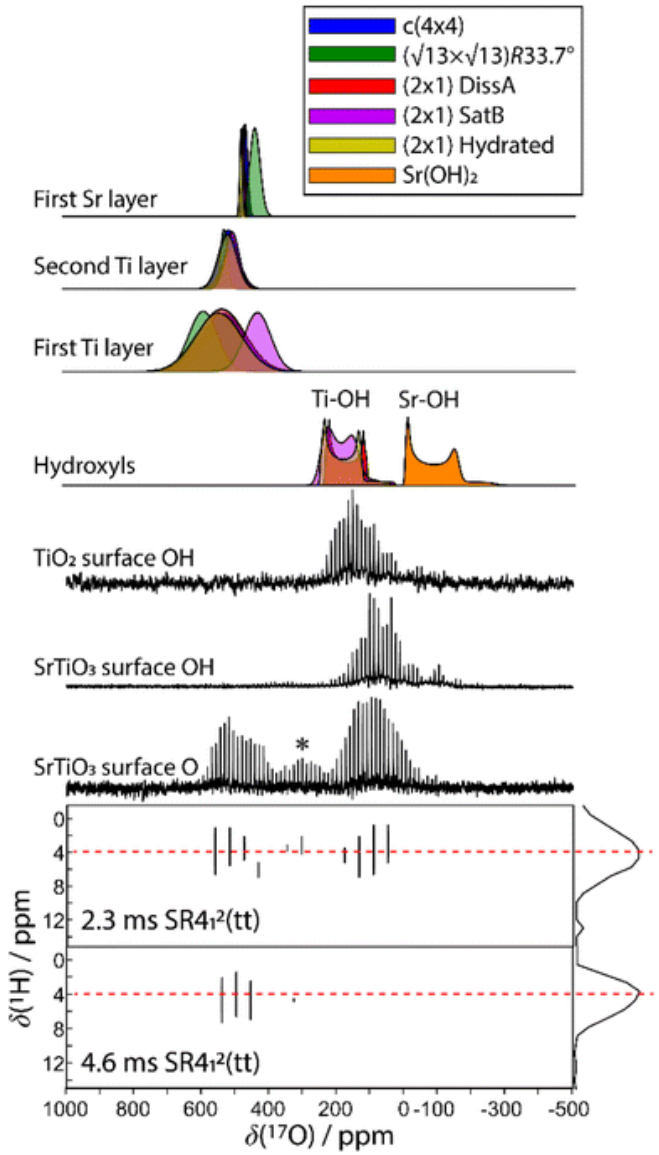

Fig. 5.13 Experimental (black) D-RINEPT-SR4$_1^2$(tt) (bottom) 1D and 2D^{17}O{^{1}H} spectra and ^{17}O{^{1}H} PRESTO spectra acquired on STO and anatase titania. Simulated spectra are shown on the top corresponding to the parameters calculated using plane-wave DFT for various surface terminations, as indicated on the figure. An asterisk is used to mark the position of a spinning sideband.

5.3.5. Effect on Pt Precursor and Solution Temperature on Grafting

The amount of Pt loading *via* SOMC can be increased by changing the starting Pt complex that is grafted to the STO surface. $Pt(acac)_2$ and $MeCpPtMe_3$ are two common platinum precursors used in catalyst synthesis.[255–258] In addition to traditional methods such as wet impregnation, incipient wetness, and co-precipitation, these precursors have been used for ALD of Pt nanoparticles on oxide surfaces,[63] with $MeCpPtMe_3$ specifically used to grow Pt nanoparticles of a range of sizes through cyclic growth on STO nanocuboids.[7,54,60,63,80] On STO calcined at 550 °C, ozone and steam treated at 200 °C, grafting at 50 °C of $Pt(acac)_2$ was more efficient (0.50 wt% Pt) than the grafting using $MeCpPtMe_3$ (0.12 wt%), which is expected due the covalent nature of the Pt–C bond in the latter.

Solid-state NMR $^{1}H\{^{195}Pt\}$ perfect-echo RESPDOR experiments (**Fig 5.14**) were performed on a sample of $MeCpPtMe_3$ grafted onto STO. Correlations were observed in the sideband-selective experiment corresponding to a uniform Pt environment characterized by an isotropic ^{195}Pt chemical shift of −2100 ± 100 ppm, a tensor span of 1600 ± 200 ppm, and a skew of −0.8 ± 0.2. These parameters are similar to those measured in a $MeCpPtMe_3/Zn–SiO_2$ catalyst,[259] suggesting that it adopts a similar bipodal coordination environment. This is consistent with the observation that after grafting of $MeCpPtMe_3$ onto STO supports, the final Pt loading (0.5 wt%) was lower than that obtained with $Pt(acac)_2$ (2 wt%), as a bipodal mode of grafting consumes surface hydroxyls that would otherwise be available for additional Pt deposition. No evidence of monopodal or tripodal Pt species was detected.

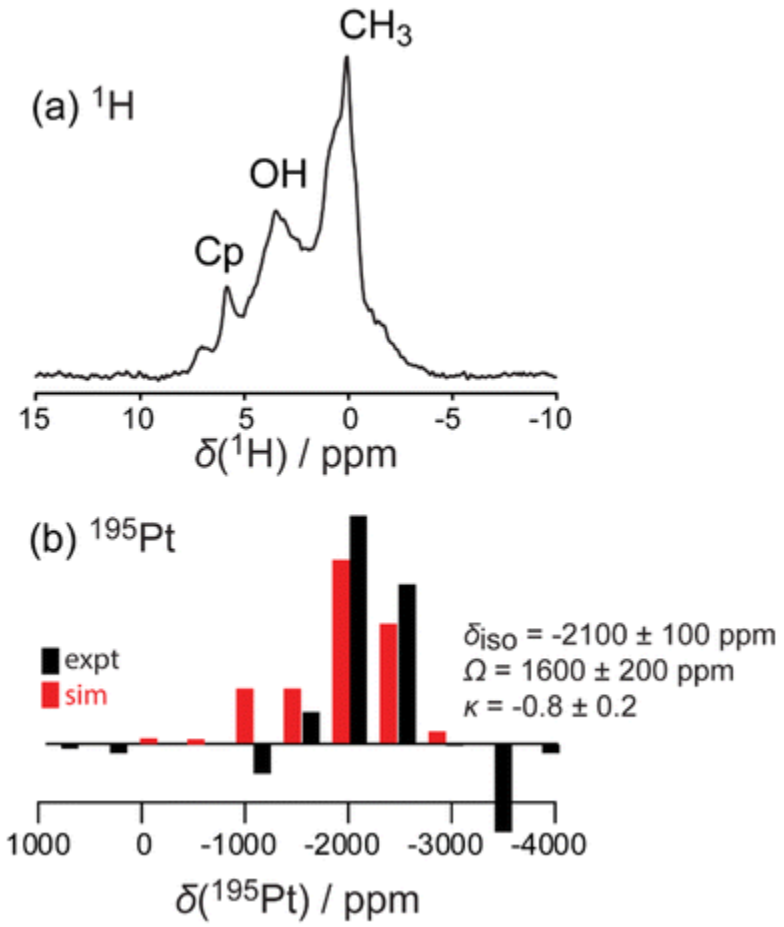

Fig. 5.14 Simulated (red) and experimental (black) ^{1}H MAS (a) and ^{1}H{^{195}Pt} perfect-echo RESPDOR (b) solid-state NMR spectra acquired on a MeCpPtMe$_3$/STO material.

EPR spectroscopy confirmed the presence of Ti(iii) on STO both as synthesized and after calcination (**Fig. 5.15**). The observation of Ti(iii) in these samples is consistent with previous reports that show Ti(iii) evolution in STO after treatment in both reducing environments and high-temperature annealing environments. It has been proposed that such an environment can introduce oxygen vacancies into the STO crystal lattice, leading to a reduction of Ti^{4+} to Ti^{3+} to preserve electrical neutrality.[260] Overall, Ti(iv)

appears to be the dominant Ti species, though paramagnetic effects from Ti(iii) overwhelm the NMR signals for ^{1}H and ^{195}Pt.

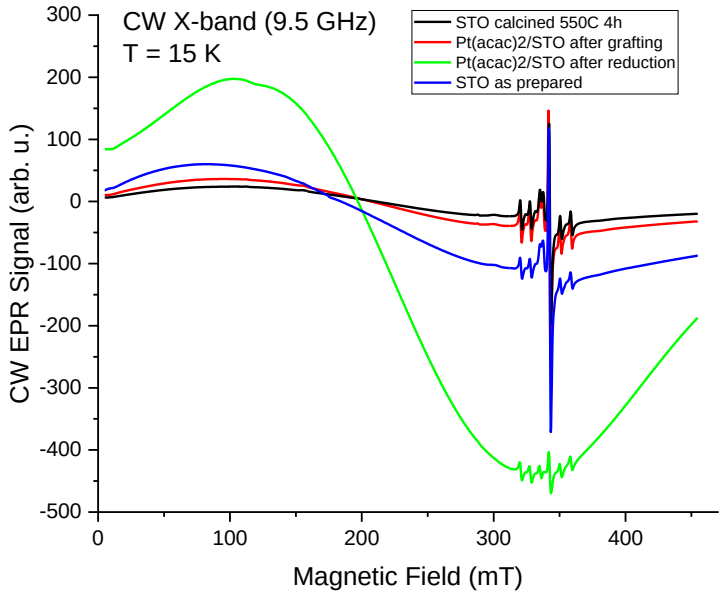

Fig. 5.15 Continuous wave (CW) X-band EPR Spectra of Calcined STO, $Pt(acac)_2$ on STO after grafting, $Pt(acac)_2$ on STO after reduction, and as prepared STO (black, red, green, and blue respectively) at cryogenic temperatures (T = 15 K). The intense broad EPR signal centered around 220 mT is due to ferromagnetically coupled electron spins, which we assign to Ti(III) ions in the STO support.

5.3.6. Metalation Temperature for $Pt(acac)_2$ Deposition

After STO nanocuboids were calcined at 550 °C and treated by ozonolysis and steaming (both at 200 °C), $Pt(acac)_2$ was grafted onto the STO nanocuboids in toluene at temperatures ranging from 50 °C to 120 °C for 72 h. The Pt loading was slightly affected by solution temperature for $Pt(acac)_2$, with 0.50 wt% Pt deposition being observed at 50 °C, and increasing slightly to 0.54 wt% at 80 °C and 0.55 wt% at 120 °C (**Fig 5.16**). A metalation temperature of 90 °C was also tested, and average Pt particle size was comparable to that observed for depositions carried out at 80 °C (**Fig. 5.17**). A metalation temperature of

120 °C led to larger particles, however, which are thought to be less active for polyolefin hydrogenolysis.[7] Thus, metalation at 80 °C was selected for further experiments.

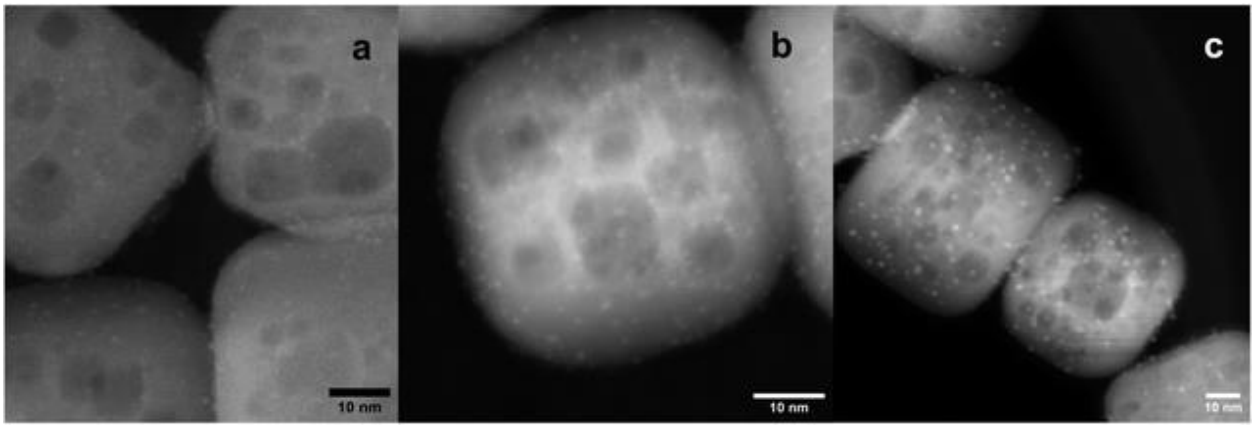

Fig. 5.16 STEM HAADF micrographs of SOMC 1cPt/STO calcined at 550 °C, followed by O_3 and steam treatment at 200 °C, made at a 50 °C (1.2 ± 0.3 nm; (a)), 80 °C (1.3 nm, (b)), and 120 °C (1.8 nm, (c)).

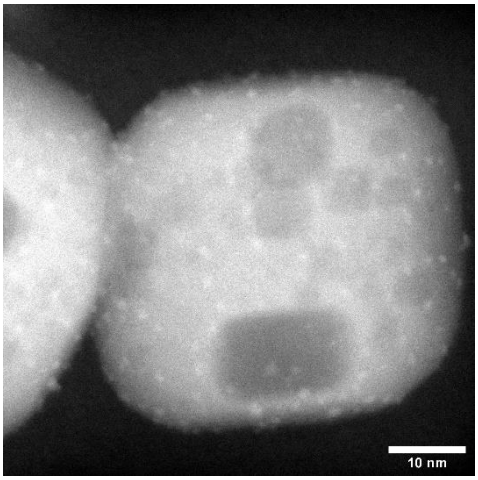

Fig. 5.17 STEM HAADF micrographs of SOMC 1c-Pt/STO calcined at 550 °C, followed by O_3 and steam treatment at 200 °C, made at 90 °C (1.5 ± 0.4 nm).

5.3.7. Multiple-Cycle Deposition

One of the unique features of the self-limiting ALD processes is that particles or layers of a desired size or thickness can be grown by repeating the growth cycle a specific number of times.[60,249] SOMC is also a self-limiting deposition process, and it should be possible to perform additional cycles of grafting to deposit controlled amounts of Pt on the surface until a desired particle density or size is reached. We observed the Pt surface loading increase from 0.90 Pt atoms per nm^2 after one cycle to 1.66 Pt atoms per nm^2 after two cycles. Interestingly, the average Pt nanoparticle diameter was independent of the number of cycles at 1.3 ± 0.3 nm, 1.2 ± 0.39 nm, and 1.5 ± 0.35 nm after the 1, 2, and 3 cycles (**Table 5.3**). Instead, increases in Pt loading are driven by new nanoparticle formation. The cycle-by-cycle growth behavior of SOMC under reducing conditions is different from analogous ALD depositions, where oxidizing conditions appear to favor particle growth over new nucleation on subsequent cycles.[63,249]

Table 5.3 Average Pt particle size, measured from STEM-HAADF images, and loadings measured by ICP. Pt particle size ranges estimated from EXAFS fit results from **Table 5.6** (see below). STO calcined at 550 °C followed by O_3 and H_2O at 200 °C. Metalation of $Pt(acac)_2$ at 80 °C.

	Average diameter ± SD (nm)	**Particle range[a] (nm)**	**Pt loading (wt%)**	**Pt/Ti**
1cPt_red/STO	1.3 ± 0.30		0.562	0.0224
2cPt_red/STO	1.2 ± 0.39	1.3–1.8	1.082	0.0446
3cPt_red/STO	1.5 ± 0.35		1.636	0.0365
2cPt_red/STO_spent	1.8 ± 0.89	1.3–1.9	1.204	0.0443
2cPt_calc/STO	0.8 ± 0.22		0.884	0.0374
2cPt_cal + red/STO	1.0 ± 0.20	1.1–1.9	0.936	0.0374
2cPt_cal + red/STO_spent	1.3 ± 0.49	1.0–1.3	0.960	0.0214

a The number of atoms per particle was calculated using estimations described by Jentys[261] and assuming a spherical particle shape.

After the Pt precursor is grafted to the STO nanocuboid surface (two cycles), the excess precursor is washed off with toluene and the pre-catalyst is dried before forming Pt nanoparticles. Like ALD,[63] Pt nanoparticles can be formed *via* oxidation or reduction of the grafted species to remove the stabilizing ligands. In both the oxidizing and reducing cases, the individual Pt atoms are mobile on the oxide surface and nucleate to form nanoparticles. In the case of ALD at sub-atmospheric pressures, under oxidizing conditions, PtO_x/Pt^0 core–shell particles form, while a metallic Pt^0 particle forms under reducing

conditions.[63,249] The mobility of the Pt species can be modified by adjusting the partial pressure of the oxidant or reductant.[258] Here, the grafted Pt species were either annealed under air at 300 °C or reduced under hydrogen at 300 °C for 4 h or annealed at 300 °C under air followed by reduction at 300 °C for 4 h. An annealing temperature of 300 °C was chosen to remove organics according to TGA (**Fig. 5.18**).

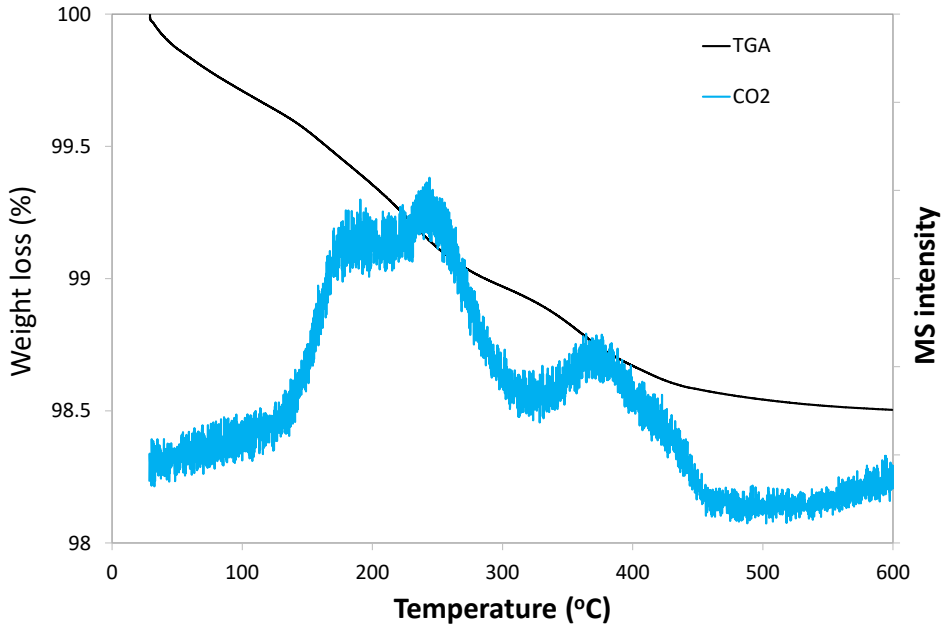

Fig. 5.18 TGA of 2cPt/STO with the second deposition of $(Pt(acac)_2$ is only dried.

The average particle sizes and distributions for all three conditions are summarized in **Fig. 4.19** and **Table 4.3** along with the Pt loadings. Oxidizing before reducing lowers the average Pt particle size from 1.2 to 1.0 nm compared to reduction only, indicating that PtO_x may be better stabilized onto STO, also shown by the Pt/Ti ratio of 0.374 that remains constant after reactions. The higher Pt/Ti ratio in the reduced sample only may be due to the higher reduction of Pt species compared to the calcined and reduced samples (**Fig. 5.19** and **Table 5.3**). A layer of PtO_x in contact with the support would favor stronger binding compared to Pt^0.[249,262]

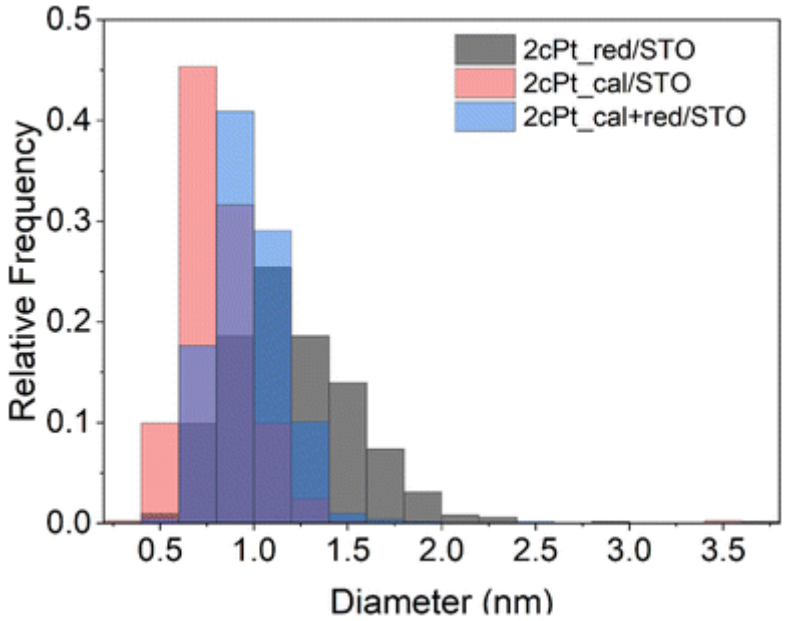

Fig. 5.19 Pt particle size distribution of 2cPt/STO after calcination, reduction and both oxidation at 300 °C followed by reduction at 300 °C. STO support has been calcined at 550 °C followed by separate O_3 and steam treatment both at 200 °C.

Both Pt/STO catalysts mentioned in **Fig. 5.19** were examined by high-resolution transmission electron microscopy (HRTEM) to examine the interface between the Pt catalyst and STO support. The results are presented below in **Fig. 5.20**. These micrographs demonstrate cube-on-cube epitaxy between the Pt metal {100} facet and {100} STO support facet. However, planar epitaxy between the Pt metal {101} facet and the {100} facet was observed in some images. Image analysis suggests that the epitaxy shown in **Fig. 5.20** represents a minor portion of all Pt/STO catalyst–support interactions. This epitaxial stabilization is likely responsible for the high stability of deposited Pt nanoparticles against sintering. Although previous reports of Pt/STO synthesized by ALD show a larger relative amount of cube-on-cube epitaxy in comparable samples,[54,62,80] these results are generally consistent with observations that smaller average sizes for deposited nanoparticles lead to distortions in epitaxial stabilization.[62,263] Such distortions include but are not limited to planar epitaxy, as is the case here, or existences as twinned particles, as

was observed in some images corresponding to the experiment in **Fig. 5.20**. An example of such epitaxy is presented in the ESI (**Fig. 5.21**).

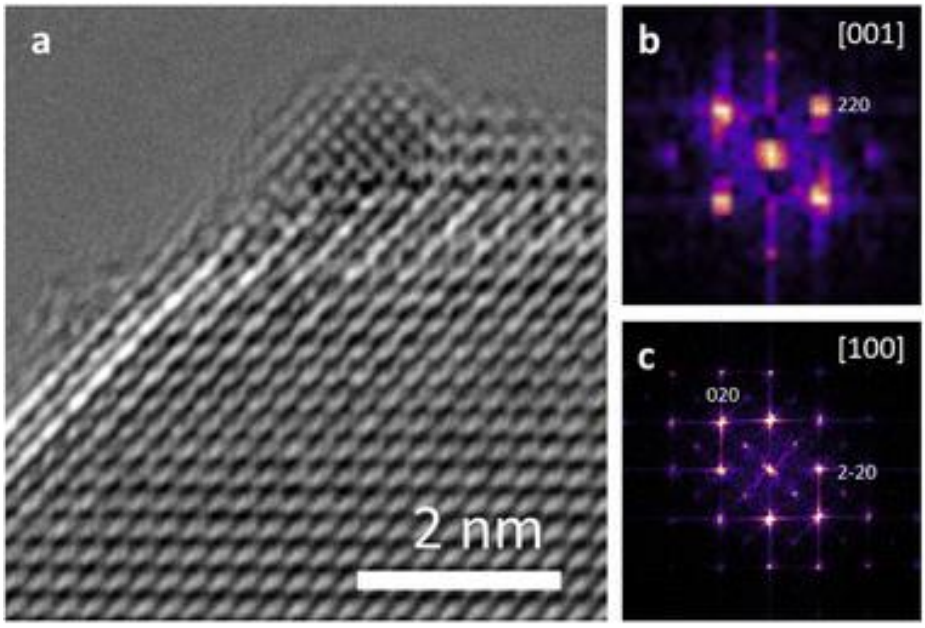

Fig. 5.20 (a) Aberration corrected HRTEM of platinum nanoparticle grafted onto STO. Fast Fourier transform patterns of the (b) platinum nanoparticle and (c) STO indicating the orientation and cube-on-cube epitaxial growth. The purple color in (b) and (c) is the result of both noise and overlapping intensities in the diffraction pattern. The white and yellow points in these sub-figures were used to determine which Pt and STO facets were imaged.

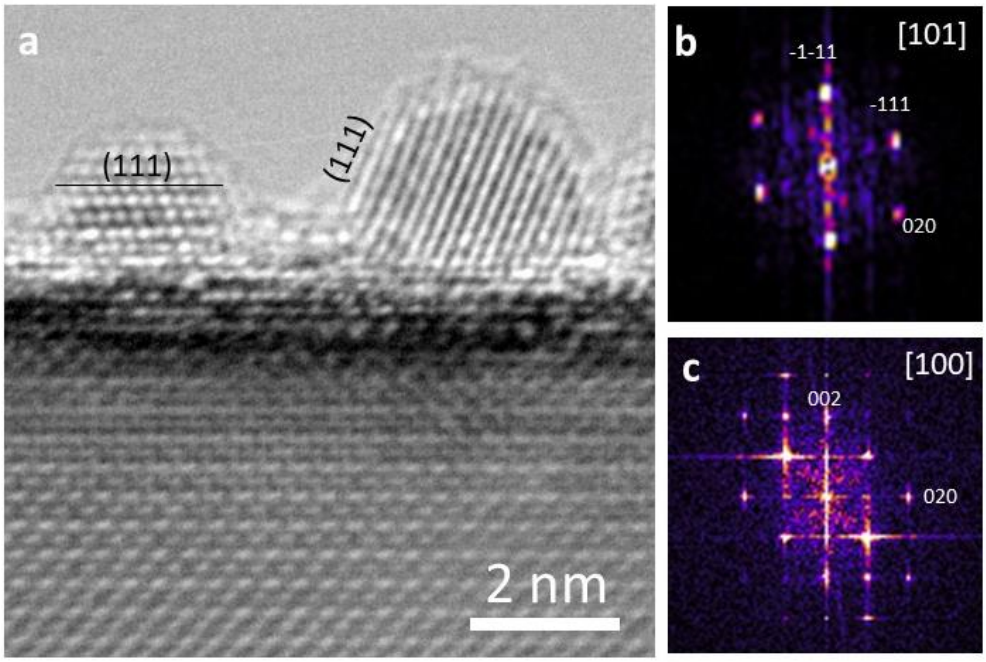

Fig. 5.21 (a) Aberration corrected HAADF of platinum nanoparticles grafted onto STO with two different exposed orientations. Fourier transform of the (b) leftmost platinum nanoparticle and (c) STO indicating the orientation of the nanoparticle on STO.

5.3.8. Catalytic Testing and Recyclability

The 2cPt_red/STO was tested in the hydrogenolysis of i-PP at 300 °C and 180 psi for 24 h. The sample was chosen because its Pt loading and average Pt particle diameter most closely match Pt/STO catalysts synthesized by one cycle of ALD,[7,60] allowing comparison of hydrogenolysis results between physically similar samples. The yield of liquid products was 96.3%. The M_n of the product was ~270 Da with a dispersity ($Đ$) of 1.1 (**Fig. 5.22**). A key feature of the ALD-Pt/STO is its reusability, which is a result of its stability against sintering, as determined by repeated catalytic tests and TEM of the post-reaction catalyst. The 2cPt_red/STO was recovered and used four additional times for a total of five catalytic runs, and full conversion of i-PP was obtained for all runs (no solid product remained). The M_n of the product was obtained from the used 2cPt_red/STO catalyst was identical to the first experiment with fresh catalyst.

There were a few changes in hydrogenolysis experiments over catalyst recycling. First, the molar H_2 consumption, corresponding to the moles of C–C bonds that are hydrogenolyzed, was 3.0 mmol for the first run and approximately 4 mmol for subsequent runs, with less than 10% of the i-PP converted (**Fig. 5.23**). There was a small decrease in the quantity of methane formed after the first two runs, which may be related to changes in the available active sites. After the first catalytic run, the headspace is comprised of around 70 mol% methane. An equivalent mole percent of methane formation was reported by Hackler *et al.*, who used a comparable Pt/STO catalyst for i-PP upcycling under largely equivalent conditions.[46]

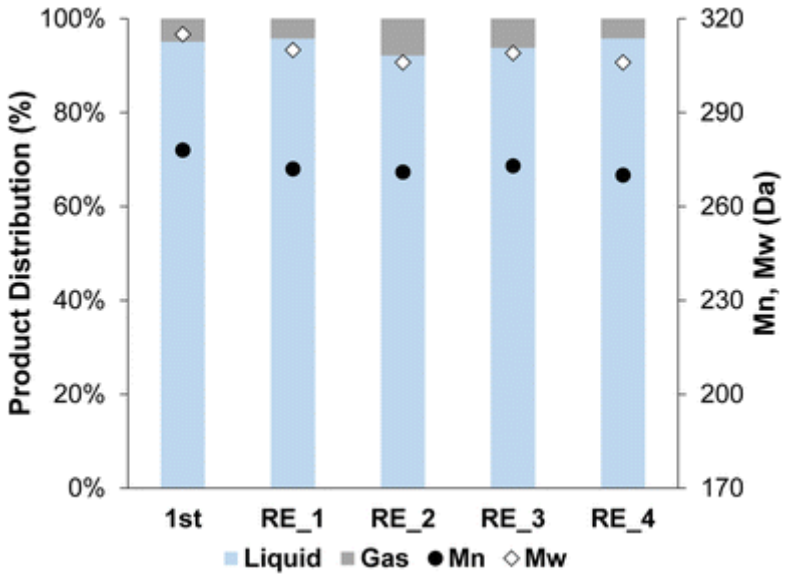

Fig. 5.22 Product distribution (liquid and gas) and M_n and M_w from OL after the first hydrogenolysis and 4 consecutive recycling experiments using 2cPt_red/STO. Conditions: i-PP (3 g), 301.0 mg 2cPt_red/STO catalyst, 300 °C, 180 psi mixed gas, 24 h. For gas distribution, see ESI.† No solid products were observed. $Đ$ = 1.1 for all.

After the 5 consecutive catalytic runs, Pt particle size increased slightly from 1.2 nm to 1.8 nm (**Fig. 5.24**) and the Pt loading increased from 1.082 to 1.204 wt%, likely because of the loss of carbon-rich species from the as-prepared catalyst. However, the Pt/Ti ratio decreased only slightly from 0.0446 to 0.0443, indicating a negligible loss of Pt.

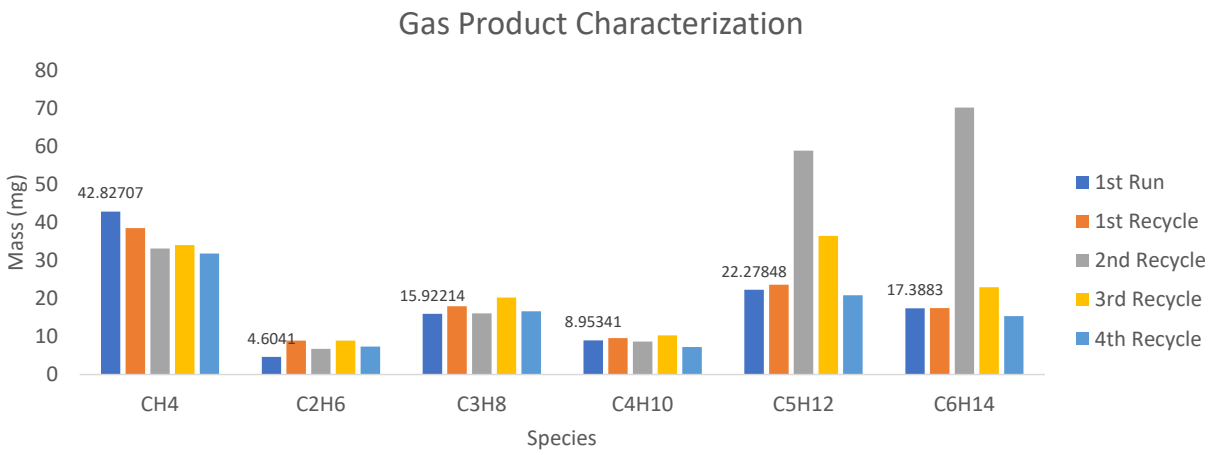

	Gas (%)	H_2 Consumption (%)
1st Run	0.149 g (4.9%)	4.1 mmol (12.2%)
1st Recycle	0.128 g (4.2%)	5.6 mmol (16.9%)
2nd Recycle	0.255 g (8.5%)	5.9 mmol (17.9%)
3rd Recycle	0.185 g (6.2%)	5.6 mmol (16.9%)
4th Recycle	0.129 g (4.2%)	5.9 mmol (17.8%)

Fig. 5.23 Characterization of Gas Products Formed Via iPP Hydrogenolysis of 2cPt/STO_red.

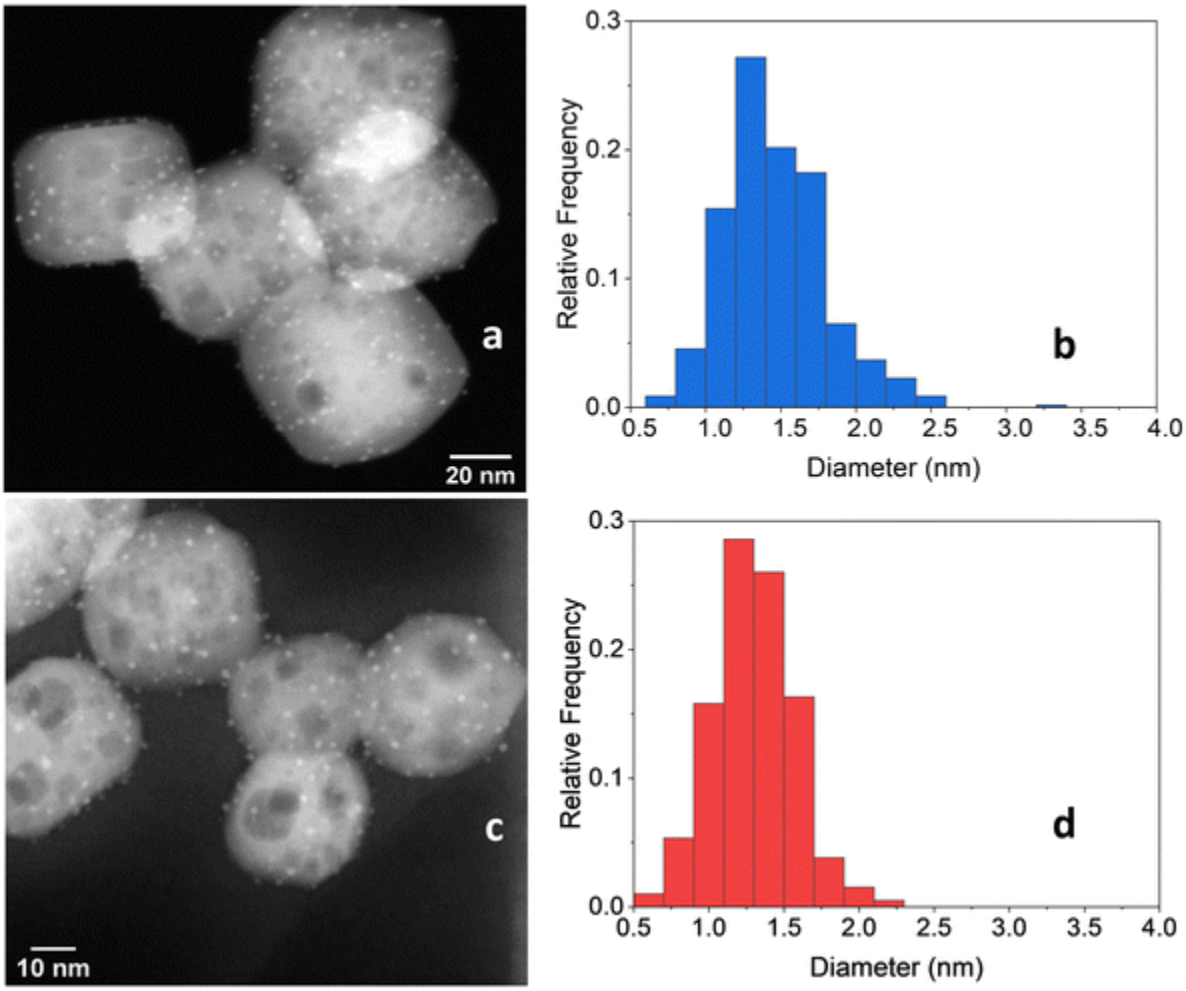

Fig. 5.24 (a) STEM-HAADF image of 2cPt/STO and (b) platinum particle size distributions (1.8 ± 0.89 nm) (right) after 5 catalytic runs. The initial sample is 2cPt_red/STO (**Table 5.3**). (c) STEM-HAADF image of 2cPt/STO and (d) platinum particle size distributions (1.3 ± 0.49 nm) after 5 catalytic runs. The initial sample is 2cPt_cal+red/STO (**Table 5.3**).

The 2cPt_cal+red/STO catalyst, containing smaller nanoparticles, was also tested for stability against sintering by repeated catalytic testing for i-PP hydrogenolysis at 300 °C, 180 psi for 24 h. The M_n of the product was ~200 Da for the first 4 runs and 218 Da after the 4th run (**Fig. 5.25**). More light gases, in

particular methane, and liquid alkanes (C_5H_{12} and C_6H_{14}) were formed after initial runs, although the amounts of gases and liquids formed decreased with successive reactions (**Fig. 5.26**).

It was previously proposed that smaller catalyst nanoparticles produce lower molecular-weight upcycling products due to the availability of more Pt edge sites, which may be active sites for polymer hydrogenolysis, potentially explaining the greater methane production. The particle sizes reported above are consistent with this relative definition of “smaller” particles.[7] Pictures of the initial polymer and final products are presented in Fig. **5.27**.

In general, the SOMC-derived Pt/STO catalyst reported herein hydrogenolyzes polyolefins to upcycled products with similar yields and average molecular weights to those made by comparable catalysts, such as those reported by Hackler.[46,56] A table of comparable catalysts is presented in **Table 5.4**. After the 5 consecutive catalytic runs, Pt particle size increased slightly from 1.0 nm to 1.3 nm (**Fig. 5.24 c** and **d**) and the Pt loading increased from 0.936 to 0.960 wt%. However, the Pt/Ti ratio decreased only slightly from 0.0374 to 0.0214, also indicating a negligible loss of Pt.

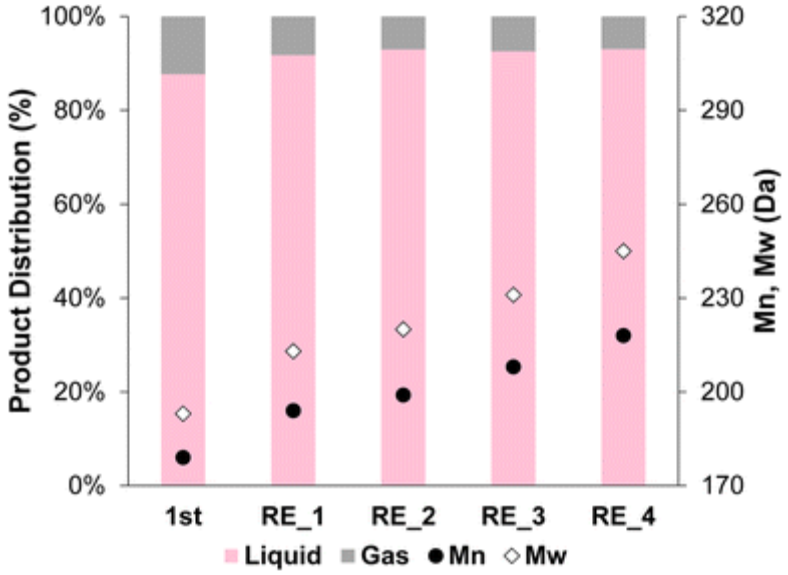

Fig. 5.25. Product distribution (liquid and gas) and M_n and M_w from OL after the first hydrogenolysis and 4 consecutive recycling experiments using 2cPt_cal+red/STO. Conditions: i-PP (3 g), 301.0 mg 2cPt_cal+red/STO catalyst, 300 °C, 180 psi mixed gas, 24 h. For gas distribution, see **Fig. 5.26**. No solid products were observed. $Đ$ = 1.1 for all.

Table 5.4. Upcycling Data for Supported Pt Upcycling Catalysts Comparable to SOMC-derived Catalysts Reported in This Work.

Sample	Starting Sample	$M_{n,i}$ (Da)	Time (h)	$M_{n,f}$ (Da)	Đ	Yield (%)
ALD Pt/STO[46]	iPP	6000	24	250	1.4	83
1c-ALD Pt/STO[7]	HDPE	8150	24	1250	4.7	91
Pt/Al_2O_3[7]	HDPE	8150	18	1850	5.8	-

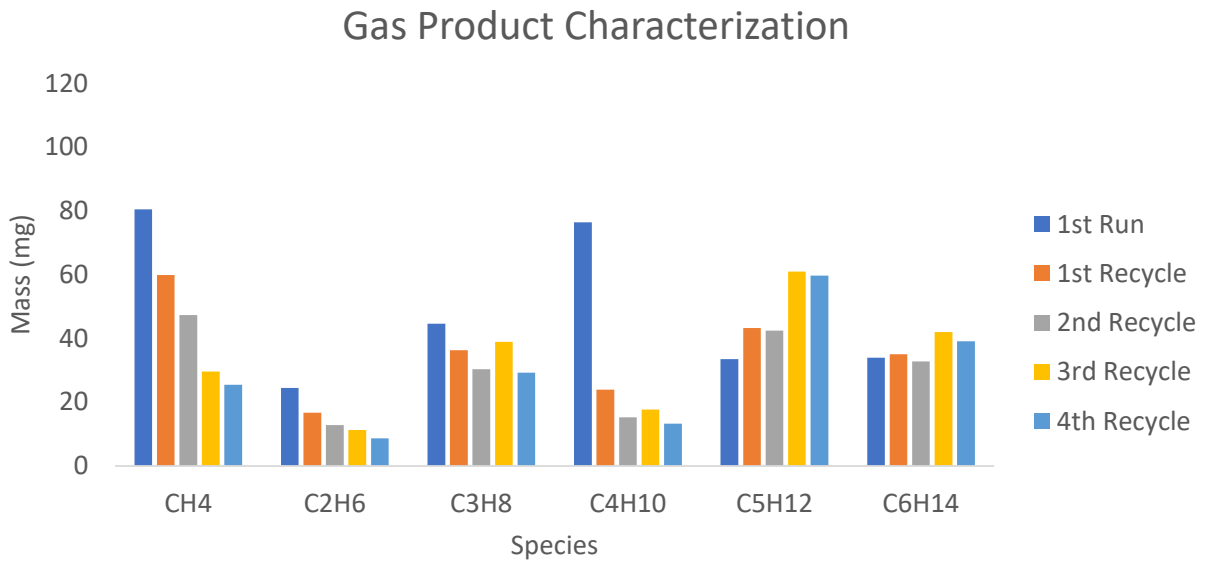

	Gas (%)	H_2 Consumption (%)
1st Run	0.374 g (12.3%)	8.0 mmol (23.9%)
1st Recycle	0.248 g (8.2%)	6.2 mmol (18.6%)
2nd Recycle	0.212 g (7.0%)	5.2 mmol (15.6%)
3rd Recycle	0.224 g (7.4%)	7.3 mmol (22.0%)
4th Recycle	0.207 g (6.9%)	6.8 mmol (20.3%)

Fig. 5.26 Characterization of Gas Products Formed Via iPP Hydrogenolysis of 2cPt/STO_cal+red

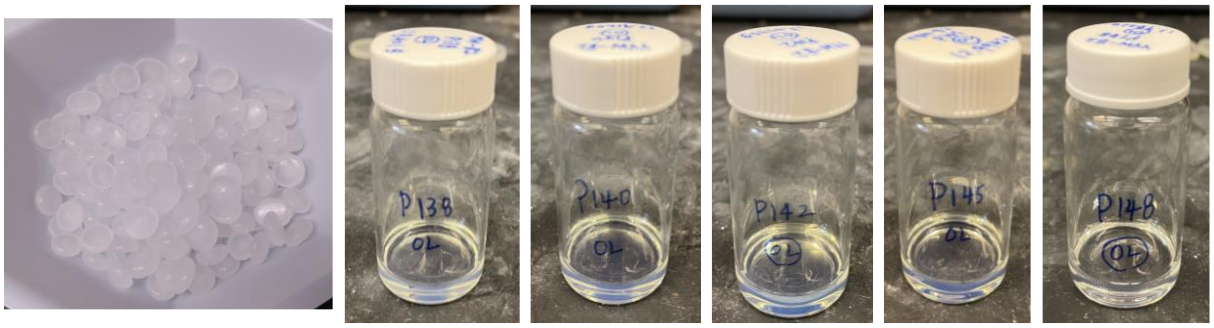

iPP **1st Run** **1st Recycle** **2nd Recycle** **3rd Recycle** **4th Recycle**

Fig. 5.27 Images of the initial polymer and after the 5 successive hydrogenolyses using 2cPt/STO_cal+red.

XAFS was performed on the fresh and spent 2cPt_red/STO and 2cPt_cal+red/STO. According to the Pt L3 XANES, the 2cPt_cal+red/STO was the least reduced sample while the two spent samples were the most reduced (**Fig. 5.28**) by qualitative comparison of the spectra with Pt metal and PtO_2. Linear combination fitting (LCF) with the metal and oxide spectra for the fresh samples indicates a larger fraction of oxidized Pt in 2cPt_cal+red/STO than 2cPt_red (**Table 5.5**), consistent with smaller average particle sizes observed for the former (**Table 5.3**). Spent 2cPt_red and 2cPt_cal+red/STO closely resemble metallic Pt even after air exposure (**Fig. 5.28**), suggesting surface species deposited from the hydrogenolysis experiments may have prevented re-oxidation of surface Pt unlike the fresh materials. After an *in situ* reduction in 3.5% H_2/He at 250 °C for 10 min, all samples were reduced (**Fig. 5.29**). For both samples, there was no significant change in the Pt–Pt coordination number (**Table 5.6**) after reaction, although larger Pt–Pt bond lengths and smaller Debye–Waller factors fit for the spent samples also support an increase in the average Pt particle size following hydrogenolysis for both 2cPt_cal+red/STO and 2cPt_red. The sample that was calcined first had a lower coordination number (8.2 *vs.* 8.5) and Pt–Pt bond length than the sample reduced without calcination which is also in agreement with a smaller particle size observed in TEM and suggested from XANES LCF results (**Table 5.7**).

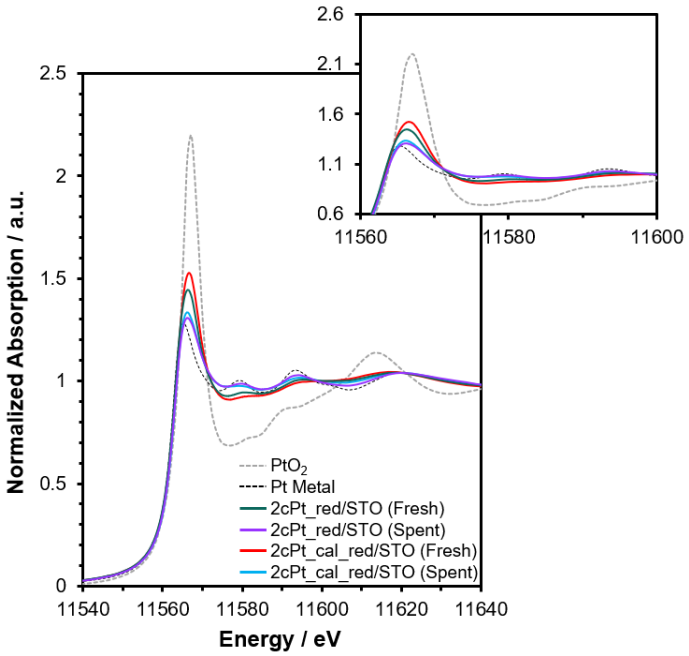

Fig. 5.28 XANES region for 2cPt_red and 2cPt_cal+red before and after reaction. All materials were measured without treatment at room temperature under inert flow.

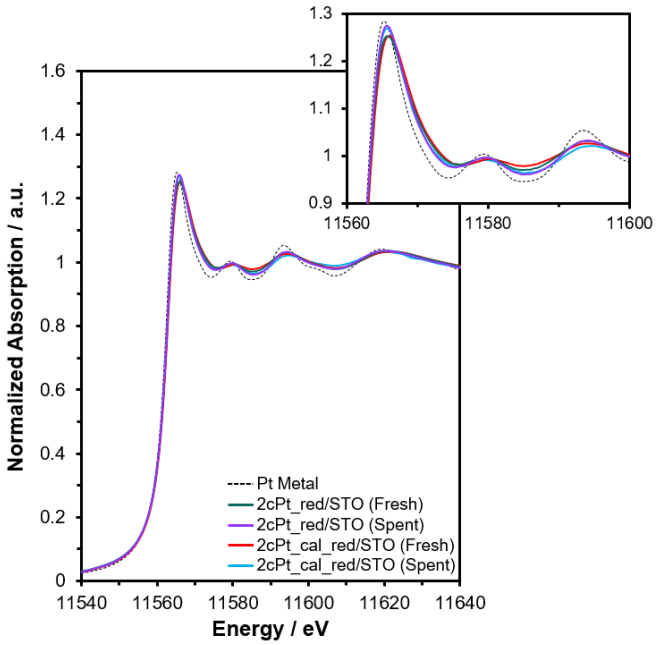

Fig. 5.29 XANES region for 2cPt_red and 2cPt_cal+red before and after reaction. All materials were reduced in-situ at 250 °C, 3.5% H_2 prior to measurement at room temperature under inert flow.

Table 5.6 Pt L3 edge EXAFS fit results for 2cPt/STO samples before and after 5 reactions (k = 3.0–15 Å^{-1}, Δk = 0.5, $k^N N$ = 1, 2, 3, R = 1.9–3.1 Å). S_0^2 set to the value (0.84) fit for the Pt reference foil. Notation: N – coordination number, R – distance to neighboring atom, σ^2 – Debye–Waller factor, ΔE_0 – energy correction

Sample		***N***	***R* (Å)**	**σ^2 (×10^{-3} Å^2)**	**ΔE_0 (eV)**	***R*-Factor**
2cPt_red/STO	Fresh	8.5 ± 0.4	2.727 ± 0.002	7.5 ± 0.3	5.8 ± 0.4	0.004
	Spent	8.6 ± 0.4	2.737 ± 0.002	6.6 ± 0.3	5.6 ± 0.4	0.004
2cPt_cal+red/STO	Fresh	8.2 ± 0.8	2.711 ± 0.006	9.5 ± 0.7	5.0 ± 0.3	0.020
	Spent	7.7 ± 0.4	2.716 ± 0.003	8.2 ± 0.3	4.3 ± 0.4	0.004
Pt metal	—	12	2.765 ± 0.002	4.8 ± 0.2	7.6 ± 0.4	0.008

Table 5.7. Linear combination fitting results for the as-received Pt-STO samples using PtO_2 and Pt as references. Fit in XANES from 11553 to 11603 eV.

Sample	**Condition**	**PtO_2**	**Pt**
2cPt_red/STO	Fresh	0.212 ± 0.009	0.788 ± 0.009
2cPt_cal+red/STO	Fresh	0.299 ± 0.009	0.701 ± 0.009

5.4 CONCLUSIONS

In this work, we have established a multi-cycle, SOMC-derived process by which Pt/STO catalysts can be synthesized from organometallic Pt precursors in a toluene solution. Prior to deposition, the STO support surface is calcined, ozonolysed, and steamed at 200 °C. $MeCpPtMe_3$ and $Pt(acac)_2$ were both grafted onto STO in toluene, and $Pt(acac)_2$ was found to afford a significantly higher Pt loading. Deposition of $Pt(acac)_2$ at 80 °C was found to be optimal because it produced the highest Pt loading and best homogeneity after surface decoration. This afforded samples with average Pt particle sizes of 1.3, 1.2, and 1.5 nm, corresponding to Pt loadings of 0.6 wt%, 1.1 wt%, and 1.6 wt% after 1, 2, and 3 cycles of deposition and reduction in H_2, respectively. These data suggest that SOMC techniques, when applied in successive cycles, favor new particle deposition over increasing the size of existing particles.

Two samples of 2cPt/STO, one which was reduced and another which was both calcined and reduced after synthesis, were tested for hydrogenolysis of isotactic polypropylene (M_n = 5 kDa, M_w = 12 kDa). The Pt/STO samples have average Pt particle sizes of around 1.2 and 1.0 nm, respectively, and afforded final upcycling products (all >95% yield) with molecular weights around 300 and 200 Da, respectively. This suggests that smaller supported Pt nanoparticles are generally more active for polyolefin hydrogenolysis, which is consistent with previous reports of plastic upcycling with the Pt/STO system. Overall, the results suggest that SOMC-derived Pt/STO catalysts meet several proof-of-concept criteria and have the potential to be commercially viable upcycling catalysts.

Chapter 6

Solution-Phase Platinum Deposition by SEA and Related Upcycling

This Chapter was adapted with permission from " M. Meirow, I.L. Peczak, R.M. Kennedy, M. Delferro, K. Poeppelmeier, E. Luijten. **2023**, *In Preparation*."

6.1 ABSTRACT

$Pt/SrTiO_3$ (Pt/STO) selectively hydrogenolyzes plastics into liquid products that have 30 – 200 carbon atom backbones and is therefore an attractive catalyst for use in commercialized plastic upcycling processes. Commercial use of Pt/STO will require, among other things, developing a Pt deposition method that can output larger quantities of catalyst than currently achievable, while still retaining control over the decoration of Pt on the STO support surface. In this work, strong electrostatic adsorption (SEA), a charge-meidated solution-phase deposition technique, was used to synthesize Pt/STO catalysts on 0.3 g and 1 g scales. At the 0.3 g scale, multiple cycles of Pt deposition and reduction in H_2 were employed to increase the amount of Pt nanoparticles on the STO surface in a controlled fashion. The effect of such sequential deposition and reduction on the physical properties (e.g. particle size) of deposited Pt was investigated. The one- (1c) and three-cycle (3c) catalysts were tested for polyethylene hydrogenolysis to determine the effects of properties such as average Pt particle size on final product distribution.

6.2 INTRODUCTION

Catalytic hydrogenolysis is a promising method for the upcycling of single-use plastics into value-added materials.[31] These processes employ catalysts such as platinum nanoparticles (Pt) on $SrTiO_3$ nanocuboid supports (STO; Pt/STO), which have been investigated for their high selectivity in upcycling pristine and spent polyethylene and polypropylene into uniform hydrocarbon oils.[7,41,42,46,56,59] Several features of Pt/STO, such as epitaxial stabilization of Pt on the support surface and the well-defined faceting of the STO nanocuboids, make this material both a state-of-the-art catalyst and a useful model system via which

to study the mechanism of polyolefin hydrogenolysis. These reasons incentivize continued study of Pt/STO synthesis and hydrogenolysis.[42,54,64,70]

Owing to its ability to deposition nanoparticles in a precise fashion, most reported syntheses for Pt/STO catalysts have utilized atomic layer deposition (ALD) to decorate the STO surface with Pt.[7,60,63,64] ALD, however, is not an ideal technique for scale-up because it requires specialized instrumentation and expensive precursors, resulting in a significant capital investment. On the other hand, readily scalable techniques that are widely used in industry, such as incipient wetness impregnation, do not afford the same control over catalyst dispersion on the support surface as does a technique such as ALD.

Overall, it is desirable to substitute ALD for a solution-phase that can deposit Pt in a controlled fashion without requiring expensive instrumentation. Recently, a solution-phase Pt/STO synthesis using surface organometallic chemistry (SOMC) was reported to upcycle isotatic polypropylene into hydrocarbon products with 20 – 30 carbon atom backbones, demonstrating that Pt/STO upcycling catalysts can be synthesized by solution-phase deposition techniques.[41] However, SOMC relies on the chemisorption of an organometallic Pt precursor ($MePtCpMe_3$ or $Pt(acac)_2$) with hydroxyls or existing Pt particles on the STO surface, as is observed by ALD.[63] It remains to be seen whether techniques that do not utilize covalent bonding between catalyst precursors and the STO support surface can deposit Pt in a comparable manner.

Strong electrostatic adsorption (SEA) is a solution-phase deposition method that takes advantage of the charge-dependent nature of a metal oxide support surface.[264] In an SEA process, an ionic catalyst precursor, e.g. $Pt(NH_3)_4^{2+}$, electrostatically binds to surface hydroxyls, which are either protonated or deprotonated through manipulation of solution pH. This ligated catalyst precursor is then introduced in an oxidizing or reducing environment, ultimately affording bare nanoparticles on the support surface.[264,265] This phenomenon has long been understood and has been exploited to synthesize various support catalysts for a suite of industrial applications.[266–274] An SEA-derived synthesis of Pt/STO has also been reported,[42] though the effect of multiple cycles of deposition and reduction on final catalyst properties for this material has not been explored.

In this work, a scalable synthesis for a SEA-derived Pt/STO upcycling catalyst is reported. A series of sequential Pt depositions and reductions (up to 3 cycles), termed a “multi-cycle” approach, was employed

to increase the amount of Pt catalyst loaded onto the STO surface in a controlled fashion. The one-cycle and three-cycle (1c & 3c, respectively) Pt/STO catalysts were tested for high-density polyethylene (HDPE) hydrogenolysis and were found to afford liquid products comparable to those obtained in previous studies using Pt/STO.

6.3 EXPERIMENTAL

6.3.1 Materials and Instrumentation

Electron Microscopy. Nanoparticles were imaged using a Hitachi HD2300 scanning transmission electron microscope operated at 200kV. This instrument was used in coordination with the NU Atomic and Nanoscale Characterization Experimental Center at Northwestern University. In preparation for analysis, solid samples (~20mg) were sonicated in ethanol (10mL) for 30 minutes, at which point the resulting suspension was dropcast onto a lacey carbon TEM grid (Ted Pella, Inc., UC-A on Lacey 400 mesh Cu) and dried for 30 minutes prior to imaging. Pt particle sizes were measured using Fiji-enhanced ImageJ software by circumscribing a circle around each Pt particle so that the diameter of said circle matches the widest width of the particle. [cite] This technique was used to calculate individual Pt particle diameters, and these values were averaged across all Pt particles in each sample.

Inductively Coupled Plasma Optical Emission Spectrometry (ICP-OES). Elemental Pt, Sr, and Ti compositions in Pt/STO were measured by a **Thermo iCAP 7600 Inductively Coupled Plasma Optical Emission Spectroscopy (ICP-OES) system operated through the Quantitative Bio-element Imaging Center at Northwestern University.** Pt/STO samples (15 mg) were digested in aqua regia (15 mL) for 48 hours, after which 0.5 mL of the resulting solution was diluted twenty-fold with a 2 % HNO_3 / HCl solution in water (10 mL total sample volume) and analyzed. Five stock solutions were made by serial dilution from Pt, Sr, and Ti standards to span a range of 1 – 40 ppm for each metal for calibration. A calibration curve was computed internally through the ICP-OES system software. Final concentration data were used to calculate the weight percent of Pt metal relative to total catalyst mass.

6.3.2 Pt Deposition

$Pt(NH_3)_4(NO_3)_2$ (PTA, Sigma-Aldrich, 60 mg) was added to a beaker (100 mL) containing a stir bar and STO nanocuboids (0.4 g, ~60 nm average size). Next, an aqueous NaOH solution (3mL, pH 11) was added to the beaker and the resulting mixture was stirred for 2h. The solid in the mixture was separated

by vacuum filtration, and dried overnight, after which it was reduced in a tube furnace (5% H_2/N_2, 450°C, 12h) to afford the final Pt/STO catalyst.

A multi-cycle (i.e., multiple cycles of deposition and reduction) procedure was employed to increase Pt loading on the STO surface. After one cycle (1c) of deposition and reduction, the resulting Pt/STO catalyst was re-introduced into a new aqueous, pH 11 solution with 60 mg PTA. Afterward, the solid was removed from solution and reduced to afford bare metal Pt nanoparticles on the STO surface. This was defined as a two-cycle (2c) Pt/STO sample. To produce a three-cycle (3c) Pt/STO catalyst, the resulting 2c-Pt/STO catalyst was subjected to another cycle of Pt deposition and treatment in a reducing environment as described above.

6.4 RESULTS & DISCUSSION

Investigations into the SEA-derived synthesis of Pt/STO began with scale-up of the synthesis to a 1 g scale (**Figure 6.1**).

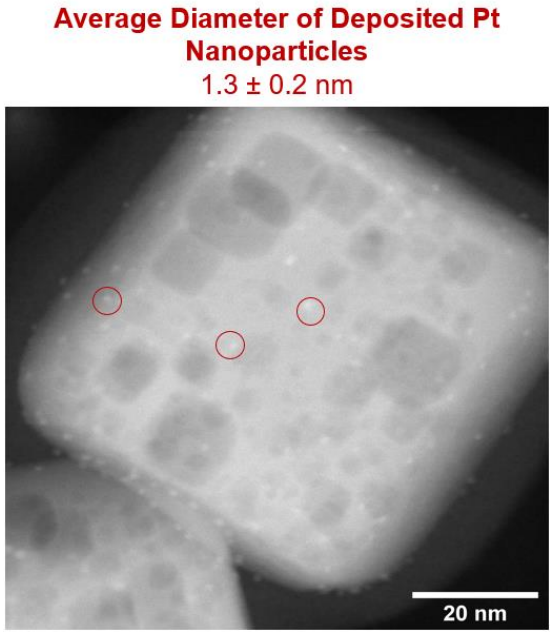

Figure 6.1. SEA-Derived Synthesis of Pt/STO on a 1 g scale. Average Pt particle size was 1.3 ± 0.2 nm, which is consistent with particle sizes observed for samples synthesized on a 300 mg scale. Relevant deposition parameters are presented in **Table 6.1.**

A previously reported procedure was modified to extend stir times from 2 h to 24 h.[42] The mass of STO support, PTA precursor, and water volume were increased proportionally, and solution pH was held constant at 11. The results in **Figure 6.1** demonstrate that SEA techniques can be used to synthesize 1g Pt/STO samples with Pt properties generally equivalent to those seen for samples synthesized on a 300 mg scale.

Table 6.1. Synthetic parameters used for Pt deposition onto STO supports on a 300 mg and 1 g scale. In both cases, the STO support had an average size of around 60 nm, corresponding to a surface area of roughly 20 $m^2 g^{-1}$**.**

Parameters	300 mg Scale	1 g Scale
Stir time (h)	2	2
m_{STO} (g)	0.4	1.3
m_{PTA} (mg)	60	190
Solution pH	11	11
V_{water} (mL)	3	10
Final Mass	~0.3	1.1
(*% Recovered*)	(*75 %*)	(*85 %*)

Next, multiple cycles of deposition and reduction were used in sequence to synthesize Pt/STO catalysts to determine whether such a method can increase overall Pt loading on the STO surface, and how introducing additional Pt metal affects the physical properties of already deposited nanoparticles. After

one cycle of deposition and reduction, the resulting Pt/STO sample was re-introduced into a fresh solution of $Pt(NH_3)_4^{2+}$ at pH 11 and stirred for 24 hours. After separation from the supernatant, the ligated one-cycle (1c-Pt/STO) sample was placed into a reducing environment (5 % H_2, 450 ^oC, 12 h) to afford a "two-cycle" Pt/STO catalyst, designated as "2c-Pt/STO". This process was again repeated with "2c-Pt/STO" sample to obtain a final "3c-Pt/STO" sample. These materials were then analyzed by ICP and electron microscopy to determine the weight loading of Pt and average particle size of each sample (**Figure 6.2**).

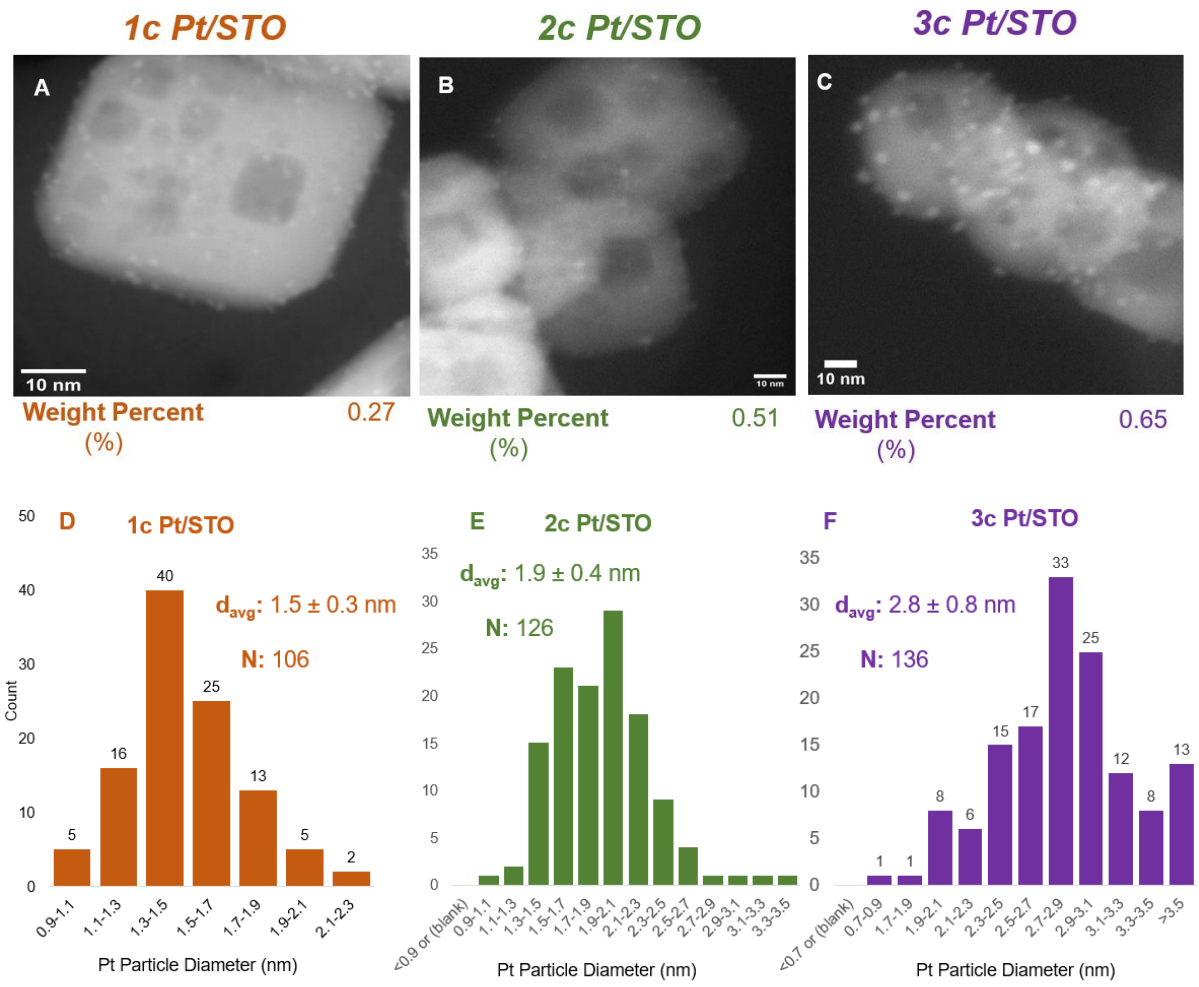

Figure 6.2. Multi-Cycle Synthesis of Pt/STO with Varied Pt Loadings. Samples were analyzed by transmission electron microscopy and ICP-OES. The 1c-Pt/STO sample contained 0.27 % Pt by weight with an average Pt particle size of 1.5 ± 0.3 nm. The 2c-Pt/STO sample contained 0.51 % Pt by weight

and had Pt particles with an average size of 1.9 ± 0.4 nm. 3c-Pt/STO contained 0.65 % Pt by weight and had Pt particles with an average size of 2.8 ± 0.8 nm.

The increase in catalyst loading by mass (weight percent) after additional cycles of deposition and reduction demonstrates that multi-cycle treatments are successful in installing more Pt on the STO surface. There is also a simultaneous increase in average Pt particle size, from 1.5 ± 0.3 nm to 1.9 ± 0.4 nm and 2.8 ± 0.8 nm after one, two, and three cycles of deposition and reduction, respectively. The increase in size variance size with successive deposition and reduction suggests that changes in particle size are less pronounced than would be suggested by changes to the average size alone. Owing to the presence of a limited amount of relatively smaller nanoparticles (< 1.5 nm) in both the 2c- and 3c-Pt/STO samples (**Figure 6.2**) it appears that a multi-cycle deposition treatment favors the growth of already deposited Pt nanoparticles. Further investigation is required to fully understand SEA-derived nucleation and growth and compare it to analogous processes for SOMC- and ALD-based syntheses of Pt/STO.

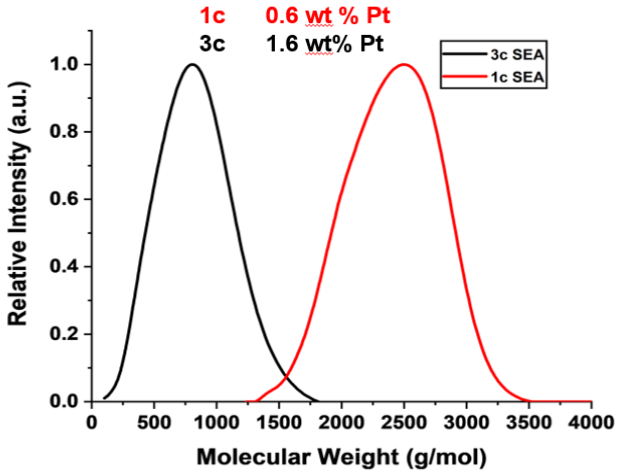

Figure 6.3. HDPE Hydrogenolysis with SEA-Derived Pt/STO. 1c-Pt/STO upcycles HDPE to a final hydrocarbon product with an average mass of 2500 g mol^{-1} (~200 carbon atom backbone), while 3c-Pt/STO upcycles HDPE to a hydrocarbon product with an average mass of ~750 g mol^{-1} (~ 50 – 60 carbon atom backbone). In each case, around 300 mg Pt/STO and 3g HDPE (1:10 catalyst to polymer ratio) was loaded into the reactor.

Separate 1c and 3c Pt/STO samples were tested for the hydrogenolysis of HDPE (M_n ≈ 35,000 Da) to determine how variation in both overall Pt loading and particle size affect the distribution of the final upcycling product (**Figure 6.3**). Average Pt particle size and Pt loading by weight for these samples (green shading) and comparable ALD-derived Pt/STO samples (blue shading), along with final and initial number-averaged polymer molecular weights are presented below in **Table 6.2**. The results demonstrate that HDPE upcycling with the 1c-Pt/STO sample, which has a Pt loading of 0.6 wt % and average particle size of 1.5 ± 0.3 nm, upcycles HDPE to a final product with an average mass of ~2500 g mol^{-1} and ~200 carbon atom backbone. By contrast, 3c-Pt/STO, which has an area loading of 3.8 Pt atoms per nm^2 and an average particle size of 2.0 ± 0.4 nm, upcycles HDPE to a final product with an average mass of ~700 g mol^{-1} and a 50 - 60 carbon atom backbone.

Table 6.2. Relevant Data for Comparison of SEA-Derived and ALD-Derived Pt/STO Upcycling of Polyethylene Samples. **ALD Samples** are colored in **Blue**, and **SEA samples** are colored in **Green**.

d_{avg} (nm)	Pt wt %	SA (m^2/g)	Reaction Time (h)	$M_{n,i}$	$M_{n,f}$
1.2	1.7	~20	2.7	24	8,150
2.0	7.3	~20	12.2	24	8,150
2	10	~20	17.1	24	38,850
1.5	0.6	~20	96	35,000	2500
2.0	1.6	~20	96	35,000	700

In general, the average size of the final polymer product obtained from HDPE upcycling by SEA-derived Pt/STO catalysts appears consistent with that obtained using ALD-derived Pt/STO. Because the amount of catalyst in the reactor was normalized by mass, it is unclear how average Pt particle size and areal

loading affect upcycling product distribution. It has previously been postulated that smaller average Pt particle sizes result in smaller average molecular weights of the upcycled polymer because of a larger number of active sites on the Pt particle surface. Future investigations to definitively confirm or refute this observation will focus on using chemisorption to quantify the dispersion on the 1c, 2c, and 3c SEA-derived Pt/STO samples presented in **Figure 6.2**. This will be used to determine available Pt surface area on each catalyst, and the 1c, 2c, and 3c SEA-derived Pt/STO samples presented in **Figure 6.2** will be tested for HDPE hydrogenolysis while normalizing for this variable. Future synthetic efforts will focus on variation of global deposition parameters to determine the extent to which interparticle spacing and particle size can be controlled in a multi-cycle deposition and reduction regime.

6.5 CONCLUSION

SEA techniques were used to synthesize Pt/STO catalysts on a 1 g scale. It was determined that Pt deposition on the 1 g scale affords a final catalyst with comparable Pt particle sizes and weight loadings to catalysts synthesized on a 300 mg scale. Three sequential cycles of Pt deposition and reduction in H_2 were next used to increase overall catalyst loading on the STO support surface in a controlled fashion. The average amount of Pt by weight increased from 0.27 % to 0.51 % and 0.65 % after one, two, and three cycles, respectively. Average Pt particle size increased from 1.5 +/- 0.3 nm after one cycle of deposition and reduction, to 1.9 ± 0.4 nm and 2.8 ± 0.8 nm after two and three cycles of deposition and reduction, respectively. These results suggest that Pt loading on the STO surface increases with multiple cycles of deposition and reduction. Average particle size appears to increase, though the increase in size variance suggests that this increase may be less pronounced than it appears. Based on these preliminary data, successive deposition and reduction by SEA appears to drive the growth of existing Pt particles on the STO surface. The results of HDPE hydrogenolysis by SEA-derived Pt/STO is generally consistent with upcycling results obtained using catalysts made by ALD.

CHAPTER 7

Future Work and Conclusions

This Chapter was adapted with permission from "I.L. Peczak, R. M. Kennedy, R. A. Hackler, B. Lee, M. Meirow, E. Luijten, M. Delferro, K. R. Poeppelmeier. 'Treasuring Trash: Pt/$SrTiO_3$ Catalysts Process Plastic Waste into High-Value Materials' *Matter*, **2023**, *Submitted*."

7.1 FUTURE WORK

7.1.1 Scale-Up of Catalyst Synthesis and Hydrogenolysis to Pilot Scale

For commercial applications, both catalyst synthesis and hydrogenolysis processes will need to be reconfigured to a pilot-plant flow system to produce lubricant materials on scales sufficient address the plastic waste pollution problem. Process design will require considerations of parameters that may not meaningfully impact catalyst synthesis and testing at the batch scale. For example, new determinations in catalyst stability may affect the catalyst regeneration process, while switching from powder catalysts to extrudates may affect parameters such as yield and process retention time. Moreover, switching from a powder catalyst to an extrudate will invite engineering challenges associated with extrudate formation and its separation in a flow system. First, parameters that influence extrudate composition, such as binder identity and ratio, will need to be evaluated to ensure that there is sufficient contact between the catalyst material and reactant feedstock. Additionally, it will be necessary to evaluate parameters that will affect the interaction of the feedstock and extrudate, such as contact time, flow rate, and feedstock composition. Separation of the extrudate from the reaction process will need to be studied to ensure that the catalyst material can readily be regenerated for successive cycles of conversion. Feedstock optimization will also need to be assessed to properly account for electricity usage.

7.1.2 Feedstocks Containing Mixed Plastics, Additives, and Contaminants

Many products currently sold to consumers comprise mixtures of plastics or contain additives that complicate their recycling. Moreover, a significant fraction of plastics that enter the recycling stream is contaminated because of limited ability to effectively clean these materials prior to processing. This complicates catalytic hydrogenolysis processes, since many catalysts only have a demonstrated ability to convert pure feedstocks into uniform, value-added products. Hydrogenolysis catalysts that can effectively process plastic waste as part of a circular economy will need to be able to selectively convert wide ranges of complex plastic feedstocks with varying degrees of contamination. This applies to both post-consumer waste, e.g., food matter, and non-plastic materials often found in commercial products, such as additives and dyes. Though several attempts have been made to process uncontaminated mixed plastic samples,[46] a more complete treatment of this problem will require an understanding of how variation in contaminant degree and identity impact hydrogenolysis product distributions and how hydrogenolysis processes can be optimized to select for different final products in spite of contaminated feedstocks.

7.1.3 Mechanism and Kinetics Governing Hydrogenolysis

The mechanism behind polyolefin hydrogenolysis is currently not well understood and there is a dearth of thorough investigations into these reactions. Some preliminary insights can be gained from analogous studies of alkane hydrogenolysis, as *n*-alkanes are structurally similar to polyolefins. The kinetics and mechanism governing C_2–C_{10} alkane hydrogenolysis over Pt, Ir, Ru, and Rh nanoparticle catalysts were studied via transition-state theory and statistical-mechanical descriptions of the chemisorbed chains.[32–34] This approach proposed a series of elementary steps to explain observed variations of catalytic performance with temperature, H_2 pressure, degree of polymerization, and branching. These elementary steps involve a sequence of quasi-equilibrated dehydrogenation at a particular carbon–carbon bond, followed by cleavage and hydrogenation of the resulting alkane fragments. Notably, owing to the greater conformational degrees of freedom of a longer chain that yield larger transition state entropies, longer alkanes are predicted to exhibit faster hydrogenolysis turnover rates than shorter alkanes and a

preference for non-terminal C–C bond cleavage. First-principles (i.e., DFT-based) calculations in conjunction with microkinetic modeling are another important tool for predicting reaction pathways and revealing preferential hydrogenolysis products of short alkanes.[33,275,276]

While methods like DFT and transition-state theory provide detailed mechanistic insight, they are limited to descriptions of short, isolated alkanes. In contrast, typical polyolefin hydrogenolysis reactions deconstruct chains comprising 10^2–10^4 CH_2 units and occur in melt conditions. Product distribution trends that depend on reaction conditions or molecule type provide some insight into the polyolefin hydrogenolysis mechanism.[46,277] However, given a large experimental parameter space, computational models that reveal the underlying basis for such trends are an important tool. Recently, a coarse-grained molecular dynamics simulation model of polyethylene hydrogenolysis in a porous core–shell $mSiO_2$/Pt/SiO_2 structure was developed to understand how the diameter of the pores controls the cleavage products.[278] These simulations qualitatively explained the diameter dependence of the product distributions from the dependence of chain conformations and dynamics of exchange between the pore and bulk polymer melt on pore geometry.

For non-porous catalytic systems like Pt/STO, understanding the interfacial structure of an entangled polymer melt interacting with a catalytic metal nanoparticle is a key step toward the rational design of future catalysts. Particle-based molecular dynamics simulations are particularly instructive for this purpose since they resolve ensemble-averaged conformations and dynamics near the interface with atomistic detail. A question particularly relevant for polyolefin hydrogenolysis is whether longer reactant chains or shorter reaction products are preferred near the catalyst surface. Existing polymer theory and population balance modeling indicate that the adsorption preference depends on the chemical details of the polymer–surface interaction as well as entropic effects.[279] For Pt/STO, preliminary simulation work employing a united-atom representation of polyethylene suggests that long chains are preferentially adsorbed, corroborating computational results for polyethylene on a flat platinum facet as well as experimental observations.[7,280] The continued study of such models will be facilitated through continued advancements in supercomputing, such as Aurora at Argonne National Laboratory and the Exascale Computing Project at Oak Ridge National Laboratory,[281] which will enable simulation of larger systems

over the long time periods required to accurately determine conformational characteristics and chain dynamics.[282]

7.1.4 Targeting Epitaxial Stabilization in Rational Catalyst Design

To be effective at waste plastic upcycling and have commercial potential, a catalyst must be (i) active enough to produce products of a target molecular weight; (ii) selective enough to produce uniform final product mixtures that meet target specifications for commercial viability; and (iii) stable enough to be able to process plastics for the extended lifetimes required in a pilot plant or at a larger scale. As mentioned, cube-on-cube epitaxy between Pt and STO is likely largely responsible for the stability of Pt/STO against sintering during hydrogenolysis. To develop other viable upcycling catalysts, it may be useful to target materials where there is lattice match between the support and catalyst particles. Specifically, one can pair nanoparticle catalysts with prospective supports based on crystallographic information to select catalyst–support combinations with desirable lattice matching. Some preliminary examples of this already exist. For example, rare-earth scandates, such as $LaScO_3$, are a series of ternary metal oxides with well-defined crystalline structures and pseudo-cubic morphologies. Importantly, variation of the rare-earth metal cation changes the lattice parameter of the support, suggesting that an array of catalysts can be synthesized to lattice match various noble metal uni- and bimetallic catalyst combinations. Synthetic techniques have been developed to produce rare-earth scandate materials with well-defined morphologies for Au deposition and use in CO oxidation.[283–285] These catalysts and analogous materials could likely be utilized for hydrogenolysis of various polymer feedstocks into value-added products. Advances in the development of these new catalysts may benefit from the implementation of self-driving labs, which will allow for more unified integration of catalyst synthesis, characterization, and testing.[286]

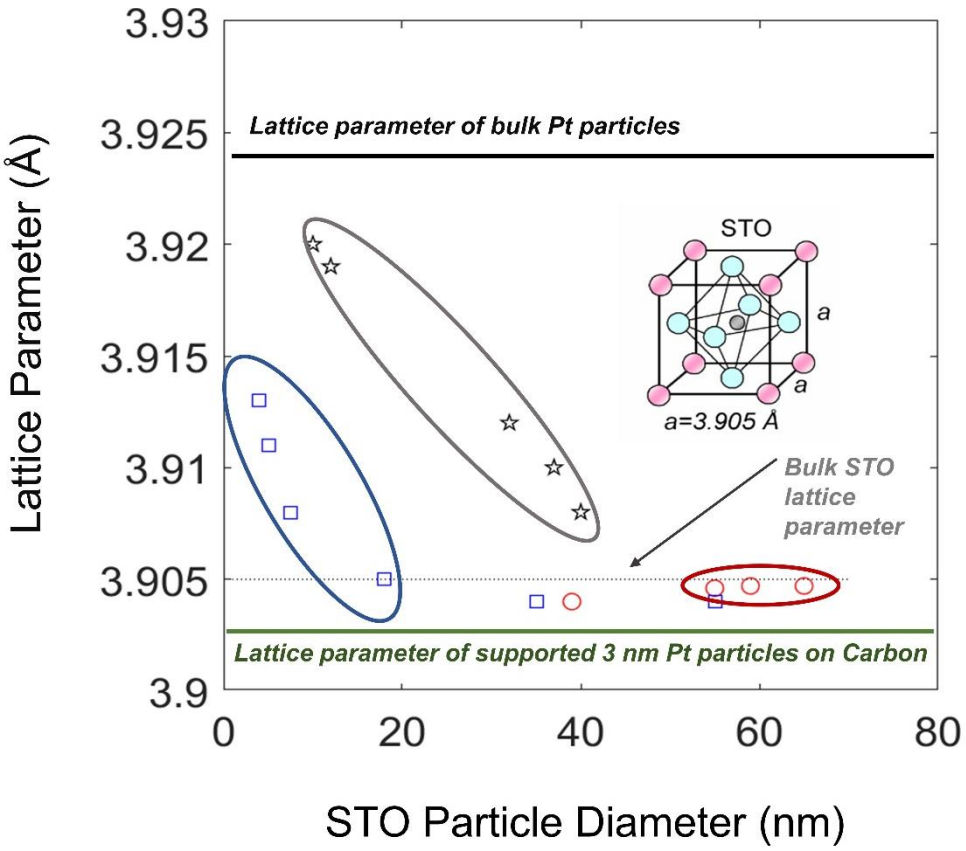

Figure 7.1. Variation in Pt and STO Lattice Parameters As a Result of Reductions in Particle Size. Lattice parameters for cuboidal STO nanoparticles (red circles) are compared with those of irregularly shaped STO nanoparticles in the literature (blue squares[287] and black stars[288]). The measured lattice parameter of ALD Pt on a cubic STO has been compared to those of bulk Pt [60] and 3 nm Pt on a carbon support.[289]

Moreover, it will be important to consider how deposition of a catalyst on a support may impact the lattice parameters of each material. The lattice constant of bulk polycrystalline STO has been shown to expand for nanoparticles below 40 nm in average size,[287,288] while the Pt lattice constant begins to decrease at 5 nm and decreases to ~3.903 Å at 3 nm (**Figure 7.1**).[289] However, wide-angle x-ray scattering data collected at the Advanced Photon Source of Argonne National Laboratory showed that for Pt/STO, the STO lattice constant is 3.9049 ± 0.0001 Å, and the Pt lattice constant is 3.914 ± 0.005 Å. Changes to STO lattice parameters based on variation in particle size are marginal for the nanocuboid particles

(**Figure 7.1**, red circles), and the value of the Pt lattice parameter when deposited on STO is smaller than that of bulk Pt but larger than that of Pt nanoparticles of the same size supported on carbon. This suggests that changes to average Pt particle size cause less pronounced changes to Pt nanoparticle lattice parameters on STO than on carbon. Nevertheless, changes in lattice constants may impact epitaxial matching. For Pt/STO in particular, it will be important to understand how these changes for both Pt and STO impact the degree of epitaxial matching and whether this in turn impacts catalyst stability against sintering. In general, future work in the development of supported catalysts could focus on understanding how catalyst deposition on a support creates stress or strain in a catalyst sample, which in turn may affect the lattice constant and the degree of epitaxial matching.

7.2 CONCLUSION

Single-use plastics are generated at alarming rates, and our current economic system offers limited opportunities through which to recycle them. Most plastics end up in landfills, and current state-of-the-art recycling methods (mechanical recycling and pyrolysis) are not yet able to convert polyolefin materials into value-added products, as would be needed to meaningfully address the plastic waste pollution problem. Catalytic hydrogenolysis is a promising technique for converting polyolefin materials into products with potential commercial use, and several supported Pt and Ru catalysts have demonstrated conversion of various polyethylene and polypropylene into liquid products with yields between 65 % and 99 %. Hydrothermal syntheses have been developed for 20 – 80 nm STO using both microwave heating and convection heating, both with and without titanium (IV) chloride as a Ti^{4+} source. Previous issues with batch-to-batch variability have been resolved, and the underlying causes for this variation have been explained through observations about how mixture pH and phase stability of various Sr- and Ti-containing compounds affect the composition of the STO hydrothermal reaction mixture prior ot heating. The general process by which STO nanocuboids form during heating of an Sr-Ti-OH mixture has also now been described and understood (Chapter 3). The rapid formation of a pH 14 solution is important for the precipitation of STO crystallites in the precursor solution. If solution pH does not rapidly reach pH 14,

other phases, such as $SrCO_3$ and titanium-containing sol-gels, will form, slowly the formation of nanocuboids. The formation of this rapid pH 14 solution can be ensured by selecting an order of operations for the Sr-Ti-OH reaction mixture in which Sr and Ti are added into a basic NaOH solution. Importantly, if a Ti^{4+} source other than $TiCl_4$ is used, STO does not precipitate in any Sr-Ti-OH mixture, and more heating is required to eventually form STO nanocuboids. This is readily achieved with microwave heating but not so with convection heating, explaining why most reported syntheses use $TiCl_4$ as a Ti^{4+} source.

Surface organometallic chemistry and strong electrostatic adsorption were both used to develop solution-phase deposition procedures for introducing Pt nanoparticles (1.3 nm < d_{avg} < 2.1 nm) onto the surface of STO nanocuboids. In both cases, multiple cycles of deposition and reduction were employed to increase Pt loading on the STO surface in a controlled fashion. When this method was employed for SOMC-derived Pt/STO, successive cycles of deposition and reduction appear to favor the formation of new nanoparticles rather than the growth of existing nanoparticles. By contrast, for SEA-derived Pt/STO, additional deposition appears to drive both the formation of new nanoparticles and the growth of existing nanoparticles.

Both SOMC- and SEA-derived Pt/STO can upcycle polyethylene and polypropylene samples to final liquid products with narrow size distributions. The upcycling results confirm previous postulations that smaller Pt particles (e.g., d_{avg} < 1.5 nm) are likely more active for hydrogenolysis than relatively larger Pt nanoparticles but also suggests that the number of Pt particles on the support surface plays an important role in determining the final average molecular weight of the upcycled products.

REFERENCES

(1) Hou, Q.; Zhen, M.; Qian, H.; Nie, Y.; Bai, X.; Xia, T.; Laiq Ur Rehman, M.; Li, Q.; Ju, M. Upcycling and Catalytic Degradation of Plastic Wastes. *Cell Rep. Phys. Sci.* **2021**, *2* (8), 100514. https://doi.org/10.1016/j.xcrp.2021.100514.

(2) Freinkel, S. *A Brief History of Plastic's Conquest of the World*. Scientific American. https://www.scientificamerican.com/article/a-brief-history-of-plastic-world-conquest/ (accessed 2023-03-12).

(3) Geyer, R.; Jambeck, J. R.; Law, K. L. Production, Use, and Fate of All Plastics Ever Made. *Sci. Adv.* **2017**, *3* (7), e1700782. https://doi.org/10.1126/sciadv.1700782.

(4) Britt, P.; Byers, J.; Chen, E.; Coates, G.; Coughlin, B.; Ellison, C.; Garcia, J.; Goldman, A.; Guzman, J.; Hartwig, J. Basic Energy Sciences Roundtable: Chemical Upcycling of Polymers. *Off. Sci. Tech. Inf.* **2019**.

(5) Andrady, A. L. The Plastic in Microplastics: A Review. *Mar. Pollut. Bull.* **2017**, *119* (1), 12–22. https://doi.org/10.1016/j.marpolbul.2017.01.082.

(6) He, P.; Chen, L.; Shao, L.; Zhang, H.; Lü, F. Municipal Solid Waste (MSW) Landfill: A Source of Microplastics? -Evidence of Microplastics in Landfill Leachate. *Water Res.* **2019**, *159*, 38–45. https://doi.org/10.1016/j.watres.2019.04.060.

(7) Celik, G.; Kennedy, R. M.; Hackler, R. A.; Ferrandon, M.; Tennakoon, A.; Patnaik, S.; LaPointe, A. M.; Ammal, S. C.; Heyden, A.; Perras, F. A.; Pruski, M.; Scott, S. L.; Poeppelmeier, K. R.; Sadow, A. D.; Delferro, M. Upcycling Single-Use Polyethylene into High-Quality Liquid Products. *ACS Cent. Sci.* **2019**, *5* (11), 1795–1803. https://doi.org/10.1021/acscentsci.9b00722.

(8) Borrelle, S. B.; Ringma, J.; Law, K. L.; Monnahan, C. C.; Lebreton, L.; McGivern, A.; Murphy, E.; Jambeck, J.; Leonard, G. H.; Hilleary, M. A.; Eriksen, M.; Possingham, H. P.; De Frond, H.; Gerber, L. R.; Polidoro, B.; Tahir, A.; Bernard, M.; Mallos, N.; Barnes, M.; Rochman, C. M. Predicted Growth in Plastic Waste Exceeds Efforts to Mitigate Plastic Pollution. *Science* **2020**, *369* (6510), 1515–1518. https://doi.org/10.1126/science.aba3656.

(9) Lau, W. W. Y.; Shiran, Y.; Bailey, R. M.; Cook, E.; Stuchtey, M. R.; Koskella, J.; Velis, C. A.; Godfrey, L.; Boucher, J.; Murphy, M. B.; Thompson, R. C.; Jankowska, E.; Castillo Castillo, A.; Pilditch, T. D.; Dixon, B.; Koerselman, L.; Kosior, E.; Favoino, E.; Gutberlet, J.; Baulch, S.; Atreya, M. E.; Fischer, D.; He, K. K.; Petit, M. M.; Sumaila, U. R.; Neil, E.; Bernhofen, M. V.; Lawrence, K.; Palardy, J. E. Evaluating Scenarios toward Zero Plastic Pollution. *Science* **2020**, *369* (6510), 1455–1461. https://doi.org/10.1126/science.aba9475.

(10) IMPACT Report: Reducing Embodied Energy and Decreasing Emissions, 2022. https://static1.squarespace.com/static/59678de486e6c0c5f27e2a3c/t/6351867dab3f4e74544dd3ac/1666287232349/REMADE-Impact+Report-2021-Spreads.pdf (accessed 2023-03-27).

(11) Geng, Y.; Sarkis, J.; Bleischwitz, R. How to Globalize the Circular Economy. *Nature* **2019**, *565* (7738), 153–155. https://doi.org/10.1038/d41586-019-00017-z.

(12) Jehanno, C.; Alty, J. W.; Roosen, M.; De Meester, S.; Dove, A. P.; Chen, E. Y.-X.; Leibfarth, F. A.; Sardon, H. Critical Advances and Future Opportunities in Upcycling Commodity Polymers. *Nature* **2022**, *603* (7903), 803–814.

(13) Al-Salem, S. M.; Lettieri, P.; Baeyens, J. Recycling and Recovery Routes of Plastic Solid Waste (PSW): A Review. *Waste Manag.* **2009**, *29* (10), 2625–2643. https://doi.org/10.1016/j.wasman.2009.06.004.

(14) Ragaert, K.; Delva, L.; Van Geem, K. Mechanical and Chemical Recycling of Solid Plastic Waste. *Waste Manag.* **2017**, *69*, 24–58. https://doi.org/10.1016/j.wasman.2017.07.044.

(15) Kazemi, M.; Faisal Kabir, S.; Fini, E. H. State of the Art in Recycling Waste Thermoplastics and Thermosets and Their Applications in Construction. *Resour. Conserv. Recycl.* **2021**, *174*, 105776. https://doi.org/10.1016/j.resconrec.2021.105776.

(16) Pascault, J.-P.; Williams, R. J. J. Thermosetting Polymers. In *Handbook of Polymer Synthesis, Characterization, and Processing*; John Wiley & Sons, Ltd, 2013; pp 519–533. https://doi.org/10.1002/9781118480793.ch28.

(17) Singh, N.; Hui, D.; Singh, R.; Ahuja, I. P. S.; Feo, L.; Fraternali, F. Recycling of Plastic Solid Waste: A State of Art Review and Future Applications. *Compos. Part B Eng.* **2017**, *115*, 409–422. https://doi.org/10.1016/j.compositesb.2016.09.013.

(18) Ravve, A. *Principles of Polymer Chemistry*; Springer Science & Business Media, 2013.
(19) Beyler, C. L.; Hirschler, M. M. Thermal Decomposition of Polymers. *SFPE Handb. Fire Prot. Eng.* **2002**, *2* (7), 111–131.
(20) Ahmad, I.; Khan, M. I.; Khan, H.; Ishaq, M.; Tariq, R.; Gul, K.; Ahmad, W. Pyrolysis Study of Polypropylene and Polyethylene Into Premium Oil Products. *Int. J. Green Energy* **2015**, *12* (7), 663–671. https://doi.org/10.1080/15435075.2014.880146.
(21) Palos, R.; Gutiérrez, A.; Vela, F. J.; Maña, J. A.; Hita, I.; Asueta, A.; Arnaiz, S.; Arandes, J. M.; Bilbao, J. Assessing the Potential of the Recycled Plastic Slow Pyrolysis for the Production of Streams Attractive for Refineries. *J. Anal. Appl. Pyrolysis* **2019**, *142*, 104668. https://doi.org/10.1016/j.jaap.2019.104668.
(22) Miskolczi, N.; Angyal, A.; Bartha, L.; Valkai, I. Fuels by Pyrolysis of Waste Plastics from Agricultural and Packaging Sectors in a Pilot Scale Reactor. *Fuel Process. Technol.* **2009**, *90* (7), 1032–1040. https://doi.org/10.1016/j.fuproc.2009.04.019.
(23) Butler, E.; Devlin, G.; McDonnell, K. Waste Polyolefins to Liquid Fuels via Pyrolysis: Review of Commercial State-of-the-Art and Recent Laboratory Research. *Waste Biomass Valorization* **2011**, *2* (3), 227–255. https://doi.org/10.1007/s12649-011-9067-5.
(24) Mark, L. O.; Cendejas, M. C.; Hermans, I. The Use of Heterogeneous Catalysis in the Chemical Valorization of Plastic Waste. *ChemSusChem* **2020**, *13* (22), 5808–5836. https://doi.org/10.1002/cssc.202001905.
(25) Sperber, R. J.; Rosen, S. L. Recycling of Thermoplastic Waste: Phase Equilibrium in Polystyrene-PVC-Polyolefin Solvent Systems. *Polym. Eng. Sci.* **1976**, *16* (4), 246–251. https://doi.org/10.1002/pen.760160405.
(26) Sherwood, J. Closed-Loop Recycling of Polymers Using Solvents : Remaking Plastics for a Circular Economy. *Johns. Matthey Technol. Rev.* **2020**, *64* (1), 4–15. https://doi.org/10.1595/205651319X15574756736831.
(27) Pappa, G.; Boukouvalas, C.; Giannaris, C.; Ntaras, N.; Zografos, V.; Magoulas, K.; Lygeros, A.; Tassios, D. The Selective Dissolution/Precipitation Technique for Polymer Recycling: A Pilot Unit Application. *Resour. Conserv. Recycl.* **2001**, *34* (1), 33–44. https://doi.org/10.1016/S0921-3449(01)00092-1.
(28) Achilias, D. S.; Roupakias, C.; Megalokonomos, P.; Lappas, A. A.; Antonakou, E. V. Chemical Recycling of Plastic Wastes Made from Polyethylene (LDPE and HDPE) and Polypropylene (PP). *J. Hazard. Mater.* **2007**, *149* (3), 536–542. https://doi.org/10.1016/j.jhazmat.2007.06.076.
(29) *Solvent-Based Recycling of Waste Plastics - 199H | S&P Global*. https://www.spglobal.com/commodityinsights/en/ci/products/solvent-based-recycling-of-waste-plastics-199h.html (accessed 2023-03-21).
(30) Connor, R.; Adkins, H. HYDROGENOLYSIS OF OXYGENATED ORGANIC COMPOUNDS. *J. Am. Chem. Soc.* **1932**, *54* (12), 4678–4690. https://doi.org/10.1021/ja01351a026.
(31) A. Kots, P.; C. Vance, B.; G. Vlachos, D. Polyolefin Plastic Waste Hydroconversion to Fuels, Lubricants, and Waxes: A Comparative Study. *React. Chem. Eng.* **2022**, *7* (1), 41–54. https://doi.org/10.1039/D1RE00447F.
(32) Flaherty, D. W.; Iglesia, E. Transition-State Enthalpy and Entropy Effects on Reactivity and Selectivity in Hydrogenolysis of n-Alkanes. *J. Am. Chem. Soc.* **2013**, *135* (49), 18586–18599.
(33) Flaherty, D. W.; Hibbitts, D. D.; Gürbüz, E. I.; Iglesia, E. Theoretical and Kinetic Assessment of the Mechanism of Ethane Hydrogenolysis on Metal Surfaces Saturated with Chemisorbed Hydrogen. *J. Catal.* **2014**, *311*, 350–356.
(34) Hibbitts, D. D.; Flaherty, D. W.; Iglesia, E. Effects of Chain Length on the Mechanism and Rates of Metal-Catalyzed Hydrogenolysis of n-Alkanes. *J. Phys. Chem. C* **2016**, *120* (15), 8125–8138.
(35) Martín, A. J.; Mitchell, S.; Mondelli, C.; Jaydev, S.; Pérez-Ramírez, J. Unifying Views on Catalyst Deactivation. *Nat. Catal.* **2022**, *5* (10), 854–866. https://doi.org/10.1038/s41929-022-00842-y.
(36) Kots, P. A.; Liu, S.; Vance, B. C.; Wang, C.; Sheehan, J. D.; Vlachos, D. G. Polypropylene Plastic Waste Conversion to Lubricants over Ru/TiO2 Catalysts. *ACS Catal.* **2021**, *11* (13), 8104–8115. https://doi.org/10.1021/acscatal.1c00874.
(37) Vance, B. C.; Kots, P. A.; Wang, C.; Granite, J. E.; Vlachos, D. G. Ni/SiO2 Catalysts for Polyolefin Deconstruction via the Divergent Hydrogenolysis Mechanism. *Appl. Catal. B Environ.* **2023**, *322*, 122138. https://doi.org/10.1016/j.apcatb.2022.122138.

(38) Rorrer, J. E.; Ebrahim, A. M.; Questell-Santiago, Y.; Zhu, J.; Troyano-Valls, C.; Asundi, A. S.; Brenner, A. E.; Bare, S. R.; Tassone, C. J.; Beckham, G. T.; Román-Leshkov, Y. Role of Bifunctional Ru/Acid Catalysts in the Selective Hydrocracking of Polyethylene and Polypropylene Waste to Liquid Hydrocarbons. *ACS Catal.* **2022**, *12* (22), 13969–13979. https://doi.org/10.1021/acscatal.2c03596.

(39) Vance, B. C.; Kots, P. A.; Wang, C.; Hinton, Z. R.; Quinn, C. M.; Epps, T. H.; Korley, L. T. J.; Vlachos, D. G. Single Pot Catalyst Strategy to Branched Products via Adhesive Isomerization and Hydrocracking of Polyethylene over Platinum Tungstated Zirconia. *Appl. Catal. B Environ.* **2021**, *299*, 120483. https://doi.org/10.1016/j.apcatb.2021.120483.

(40) Wang, C.; Xie, T.; Kots, P. A.; Vance, B. C.; Yu, K.; Kumar, P.; Fu, J.; Liu, S.; Tsilomelekis, G.; Stach, E. A.; Zheng, W.; Vlachos, D. G. Polyethylene Hydrogenolysis at Mild Conditions over Ruthenium on Tungstated Zirconia. *JACS Au* **2021**, *1* (9), 1422–1434. https://doi.org/10.1021/jacsau.1c00200.

(41) E. McCullough, K.; L. Peczak, I.; M. Kennedy, R.; Wang, Y.-Y.; Lin, J.; Wu, X.; L. Paterson, A.; A. Perras, F.; Hall, J.; Jeremy Kropf, A.; A. Hackler, R.; Shin, Y.; Niklas, J.; G. Poluektov, O.; Wen, J.; Huang, W.; D. Sadow, A.; R. Poeppelmeier, K.; Delferro, M.; S. Ferrandon, M. Synthesis of Platinum Nanoparticles on Strontium Titanate Nanocuboids via Surface Organometallic Grafting for the Catalytic Hydrogenolysis of Plastic Waste. *J. Mater. Chem. A* **2023**. https://doi.org/10.1039/D2TA08133D.

(42) Peczak, I. L.; Kennedy, R. M.; Hackler, R. A.; Wang, R.; Shin, Y.; Delferro, M.; Poeppelmeier, K. R. Scalable Synthesis of Pt/SrTiO3 Hydrogenolysis Catalysts in Pursuit of Manufacturing-Relevant Waste Plastic Solutions. *ACS Appl. Mater. Interfaces* **2021**, *13* (49), 58691–58700. https://doi.org/10.1021/acsami.1c18687.

(43) Rorrer, J. E.; Troyano-Valls, C.; Beckham, G. T.; Román-Leshkov, Y. Hydrogenolysis of Polypropylene and Mixed Polyolefin Plastic Waste over Ru/C to Produce Liquid Alkanes. *ACS Sustain. Chem. Eng.* **2021**, *9* (35), 11661–11666. https://doi.org/10.1021/acssuschemeng.1c03786.

(44) Rorrer, J. E.; Beckham, G. T.; Román-Leshkov, Y. Conversion of Polyolefin Waste to Liquid Alkanes with Ru-Based Catalysts under Mild Conditions. *JACS Au* **2021**, *1* (1), 8–12. https://doi.org/10.1021/jacsau.0c00041.

(45) Nakaji, Y.; Tamura, M.; Miyaoka, S.; Kumagai, S.; Tanji, M.; Nakagawa, Y.; Yoshioka, T.; Tomishige, K. Low-Temperature Catalytic Upgrading of Waste Polyolefinic Plastics into Liquid Fuels and Waxes. *Appl. Catal. B Environ.* **2021**, *285* (119805). https://doi.org/10.1016/j.apcatb.2020.119805.

(46) Hackler, R. A.; Lamb, J. V.; Peczak, I. L.; Kennedy, R. M.; Kanbur, U.; LaPointe, A. M.; Poeppelmeier, K. R.; Sadow, A. D.; Delferro, M. Effect of Macro- and Microstructures on Catalytic Hydrogenolysis of Polyolefins. *Macromolecules* **2022**, *55* (15), 6801–6810. https://doi.org/10.1021/acs.macromol.2c00805.

(47) Zichittella, G.; Ebrahim, A. M.; Zhu, J.; Brenner, A. E.; Drake, G.; Beckham, G. T.; Bare, S. R.; Rorrer, J. E.; Román-Leshkov, Y. Hydrogenolysis of Polyethylene and Polypropylene into Propane over Cobalt-Based Catalysts. *JACS Au* **2022**, *2* (10), 2259–2268. https://doi.org/10.1021/jacsau.2c00402.

(48) Mason, A. H.; Motta, A.; Das, A.; Ma, Q.; Bedzyk, M. J.; Kratish, Y.; Marks, T. J. Rapid Atom-Efficient Polyolefin Plastics Hydrogenolysis Mediated by a Well-Defined Single-Site Electrophilic/Cationic Organo-Zirconium Catalyst. *Nat. Commun.* **2022**, *13* (1), 7187. https://doi.org/10.1038/s41467-022-34707-6.

(49) *Ultrasmall amorphous zirconia nanoparticles catalyse polyolefin hydrogenolysis | Nature Catalysis*. https://www.nature.com/articles/s41929-023-00910-x (accessed 2023-03-13).

(50) Gao, J.; Zhu, L.; Conley, M. P. Cationic Tantalum Hydrides Catalyze Hydrogenolysis and Alkane Metathesis Reactions of Paraffins and Polyethylene. *J. Am. Chem. Soc.* **2023**, *145* (9), 4964–4968. https://doi.org/10.1021/jacs.2c13610.

(51) Liu, S.; Kots, P. A.; Vance, B. C.; Danielson, A.; Vlachos, D. G. Plastic Waste to Fuels by Hydrocracking at Mild Conditions. *Sci. Adv.* **2021**, *7* (17), eabf8283. https://doi.org/10.1126/sciadv.abf8283.

(52) Ellis, L. D.; Orski, S. V.; Kenlaw, G. A.; Norman, A. G.; Beers, K. L.; Román-Leshkov, Y.; Beckham, G. T. Tandem Heterogeneous Catalysis for Polyethylene Depolymerization via an Olefin-Intermediate Process. *ACS Sustain. Chem. Eng.* **2021**, *9* (2), 623–628. https://doi.org/10.1021/acssuschemeng.0c07612.

(53) Chen, B.-R.; George, C.; Lin, Y.; Hu, L.; Crosby, L.; Hu, X.; Stair, P. C.; Marks, L. D.; Poeppelmeier, K. R.; Van Duyne, R. P.; Bedzyk, M. J. Morphology and Oxidation State of ALD-Grown Pd Nanoparticles on TiO2- and SrO-Terminated SrTiO3 Nanocuboids. *Surf. Sci.* **2016**, *648*, 291–298. https://doi.org/10.1016/j.susc.2015.10.057.

(54) Enterkin, J. A.; Poeppelmeier, K. R.; Marks, L. D. Oriented Catalytic Platinum Nanoparticles on High Surface Area Strontium Titanate Nanocuboids. *Nano Lett.* **2011**, *11* (3), 993–997. https://doi.org/10.1021/nl104263j.

(55) Kennedy, R. M.; Crosby, L. A.; Ding, K.; Canlas, C. P.; Gulec, A.; Marks, L. D.; Elam, J. W.; Marshall, C. L.; Poeppelmeier, K. R.; Stair, P. C. Replication of SMSI via ALD: TiO2 Overcoats Increase Pt-Catalyzed Acrolein Hydrogenation Selectivity. *Catal. Lett.* **2018**, *148* (8), 2223–2232. https://doi.org/10.1007/s10562-018-2458-5.

(56) *Synthetic Lubricants Derived from Plastic Waste and their Tribological Performance - Hackler - 2021 - ChemSusChem - Wiley Online Library*. https://chemistry-europe.onlinelibrary.wiley.com/doi/full/10.1002/cssc.202100912 (accessed 2022-12-29).

(57) Base Fluids. In *Lubricants*; John Wiley & Sons, Ltd, 2014; pp 45–61. https://doi.org/10.1002/9781118799734.ch3.

(58) Rahimi, A.; García, J. M. Chemical Recycling of Waste Plastics for New Materials Production. *Nat. Rev. Chem.* **2017**, *1* (6), 1–11. https://doi.org/10.1038/s41570-017-0046.

(59) Cappello, V.; Sun, P.; Zang, G.; Kumar, S.; Hackler, R.; Delgado, H. E.; Elgowainy, A.; Delferro, M.; Krause, T. Conversion of Plastic Waste into High-Value Lubricants: Techno-Economic Analysis and Life Cycle Assessment. *Green Chem.* **2022**, *24* (16), 6306–6318. https://doi.org/10.1039/D2GC01840C.

(60) Christensen, S. T.; Elam, J. W.; Rabuffetti, F. A.; Ma, Q.; Weigand, S. J.; Lee, B.; Seifert, S.; Stair, P. C.; Poeppelmeier, K. R.; Hersam, M. C.; Bedzyk, M. J. Controlled Growth of Platinum Nanoparticles on Strontium Titanate Nanocubes by Atomic Layer Deposition. *Small* **2009**, *5* (6), 750–757. https://doi.org/10.1002/smll.200801920.

(61) Wang, C.; Hu, L.; Lin, Y.; Poeppelmeier, K.; Stair, P.; Marks, L. Controllable ALD Synthesis of Platinum Nanoparticles by Tuning Different Synthesis Parameters. *J. Phys. Appl. Phys.* **2017**, *50* (41), 415301. https://doi.org/10.1088/1361-6463/aa8709.

(62) Enterkin, J. A.; Kennedy, R. M.; Lu, J.; Elam, J. W.; Cook, R. E.; Marks, L. D.; Stair, P. C.; Marshall, C. L.; Poeppelmeier, K. R. Epitaxial Stabilization of Face Selective Catalysts. *Top. Catal.* **2013**, *56* (18), 1829–1834. https://doi.org/10.1007/s11244-013-0118-y.

(63) Setthapun, W.; Williams, W. D.; Kim, S. M.; Feng, H.; Elam, J. W.; Rabuffetti, F. A.; Poeppelmeier, K. R.; Stair, P. C.; Stach, E. A.; Ribeiro, F. H.; Miller, J. T.; Marshall, C. L. Genesis and Evolution of Surface Species during Pt Atomic Layer Deposition on Oxide Supports Characterized by in Situ XAFS Analysis and Water−Gas Shift Reaction. *J. Phys. Chem. C* **2010**, *114* (21), 9758–9771. https://doi.org/10.1021/jp911178m.

(64) Enterkin, J. A.; Setthapun, W.; Elam, J. W.; Christensen, S. T.; Rabuffetti, F. A.; Marks, L. D.; Stair, P. C.; Poeppelmeier, K. R.; Marshall, C. L. *Propane Oxidation over Pt/SrTiO3 Nanocuboids*. ACS Publications. https://doi.org/10.1021/cs200092c.

(65) *Forge Nano*. Forge Nano. https://www.forgenano.com/ (accessed 2023-03-26).

(66) Ferrandon, M. S.; Byron, C.; Celik, G.; Zhang, Y.; Ni, C.; Sloppy, J.; McCormick, R. A.; Booksh, K.; Teplyakov, A. V.; Delferro, M. Grafted Nickel-Promoter Catalysts for Dry Reforming of Methane Identified through High-Throughput Experimentation. *Appl. Catal. Gen.* **2022**, *629*, 118379. https://doi.org/10.1016/j.apcata.2021.118379.

(67) Munnik, P.; de Jongh, P. E.; de Jong, K. P. Recent Developments in the Synthesis of Supported Catalysts. *Chem. Rev.* **2015**, *115* (14), 6687–6718. https://doi.org/10.1021/cr500486u.

(68) Mehrabadi, B. A. T.; Eskandari, S.; Khan, U.; White, R. D.; Regalbuto, J. R. Chapter One - A Review of Preparation Methods for Supported Metal Catalysts. In *Advances in Catalysis*; Song, C., Ed.; Academic Press, 2017; Vol. 61, pp 1–35. https://doi.org/10.1016/bs.acat.2017.10.001.

(69) *Strong Electrostatic Adsorption of Metals onto Catalyst Supports | 20*. https://www.taylorfrancis.com/chapters/edit/10.1201/9781420006506-20/strong-electrostatic-adsorption-metals-onto-catalyst-supports-john-regalbuto (accessed 2022-12-29).

(70) Peczak, I.; Kennedy, R. M.; Simpson, A.; Delferro, M.; Poeppelmeier, K. Microwave-Assisted Synthesis of SrTiO3 Nanocuboids without TiCl4. *Small Sci.* https://doi.org/10.1002/smsc.202200107.

(71) Crosby, L. A.; Kennedy, R. M.; Chen, B.-R.; Wen, J.; Poeppelmeier, K. R.; Bedzyk, M. J.; Marks, L. D. Complex Surface Structure of (110) Terminated Strontium Titanate Nanododecahedra. *Nanoscale* **2016**, *8* (37), 16606–16611.

(72) Erdman, N.; Marks, L. D. SrTiO3(001) Surface Structures under Oxidizing Conditions. *Surf. Sci.* **2003**, *526* (1), 107–114. https://doi.org/10.1016/S0039-6028(02)02573-6.

(73) Erdman, N.; Poeppelmeier, K. R.; Asta, M.; Warschkow, O.; Ellis, D. E.; Marks, L. D. The Structure and Chemistry of the TiO2-Rich Surface of SrTiO3 (001). *Nature* **2002**, *419* (6902), 55–58. https://doi.org/10.1038/nature01010.

(74) Erdman, N.; Warschkow, O.; Asta, M.; Poeppelmeier, K. R.; Ellis, D. E.; Marks, L. D. Surface Structures of SrTiO3 (001): A TiO2-Rich Reconstruction with a c(4 × 2) Unit Cell. *J. Am. Chem. Soc.* **2003**, *125* (33), 10050–10056. https://doi.org/10.1021/ja034933h.

(75) Andersen, T. K.; Wang, S.; Castell, M. R.; Fong, D. D.; Marks, L. D. Single-Layer TiOx Reconstructions on SrTiO3 (111): ($\sqrt{7}$ × $\sqrt{7}$)R19.1°, ($\sqrt{13}$ × $\sqrt{13}$)R13.9°, and Related Structures. *Surf. Sci.* **2018**, *675*, 36–41. https://doi.org/10.1016/j.susc.2018.04.011.

(76) Andersen, T. K.; Fong, D. D.; Marks, L. D. Pauling's Rules for Oxide Surfaces. *Surf. Sci. Rep.* **2018**, *73* (5), 213–232. https://doi.org/10.1016/j.surfrep.2018.08.001.

(77) Lanier, C.; Van de Walle, A.; Erdman, N.; Landree, E.; Warschkow, O.; Kazimirov, A.; Poeppelmeier, K.; Zegenhagen, J.; Asta, M.; Marks, L. Atomic-Scale Structure of the Sr Ti O 3 (001)− c (6× 2) Reconstruction: Experiments and First-Principles Calculations. *Phys. Rev. B* **2007**, *76* (4), 045421.

(78) Crosby, L. A.; Chen, B.-R.; Kennedy, R. M.; Wen, J.; Poeppelmeier, K. R.; Bedzyk, M. J.; Marks, L. D. All Roads Lead to TiO2: TiO2-Rich Surfaces of Barium and Strontium Titanate Prepared by Hydrothermal Synthesis. *Chem. Mater.* **2018**, *30* (3), 841–846.

(79) Hu, L.; Wang, C.; Lee, S.; Winans, R. E.; Marks, L. D.; Poeppelmeier, K. R. SrTiO3 Nanocuboids from a Lamellar Microemulsion. *Chem. Mater.* **2013**, *25* (3), 378–384. https://doi.org/10.1021/cm303303x.

(80) Lin, Y.; Wen, J.; Hu, L.; Kennedy, R. M.; Stair, P. C.; Poeppelmeier, K. R.; Marks, L. D. Synthesis-Dependent Atomic Surface Structures of Oxide Nanoparticles. *Phys. Rev. Lett.* **2013**, *111* (15), 156101. https://doi.org/10.1103/PhysRevLett.111.156101.

(81) Bai, L.; Polo-Garzon, F.; Bao, Z.; Luo, S.; Moskowitz, B. M.; Tian, H.; Wu, Z. Impact of Surface Composition of SrTiO3 Catalysts for Oxidative Coupling of Methane. *ChemCatChem* **2019**, *11* (8), 2107–2117.

(82) Bao, Z.; Fung, V.; Polo-Garzon, F.; Hood, Z. D.; Cao, S.; Chi, M.; Bai, L.; Jiang, D.; Wu, Z. The Interplay between Surface Facet and Reconstruction on Isopropanol Conversion over SrTiO3 Nanocrystals. *J. Catal.* **2020**, *384*, 49–60.

(83) Foo, G. S.; Hood, Z. D.; Wu, Z. Shape Effect Undermined by Surface Reconstruction: Ethanol Dehydrogenation over Shape-Controlled SrTiO3 Nanocrystals. *Acs Catal.* **2018**, *8* (1), 555–565.

(84) Polo-Garzon, F.; Fung, V.; Liu, X.; Hood, Z. D.; Bickel, E. E.; Bai, L.; Tian, H.; Foo, G. S.; Chi, M.; Jiang, D. Understanding the Impact of Surface Reconstruction of Perovskite Catalysts on CH4 Activation and Combustion. *ACS Catal.* **2018**, *8* (11), 10306–10315.

(85) Canu, G.; Buscaglia, V. Hydrothermal Synthesis of Strontium Titanate: Thermodynamic Considerations, Morphology Control and Crystallisation Mechanisms. *CrystEngComm* **2017**, *19* (28), 3867–3891. https://doi.org/10.1039/C7CE00834A.

(86) Phoon, B. L.; Lai, C. W.; Juan, J. C.; Show, P.-L.; Chen, W.-H. A Review of Synthesis and Morphology of SrTiO3 for Energy and Other Applications. *Int. J. Energy Res.* **2019**, *43* (10), 5151–5174. https://doi.org/10.1002/er.4505.

(87) Xu, H.; Wei, S.; Wang, H.; Zhu, M.; Yu, R.; Yan, H. Preparation of Shape Controlled SrTiO3 Crystallites by Sol–Gel-Hydrothermal Method. *J. Cryst. Growth* **2006**, *1* (292), 159–164. https://doi.org/10.1016/j.jcrysgro.2006.04.089.

(88) Calderone, V. R.; Testino, A.; Buscaglia, M. T.; Bassoli, M.; Bottino, C.; Viviani, M.; Buscaglia, V.; Nanni, P. Size and Shape Control of SrTiO3 Particles Grown by Epitaxial Self-Assembly. *Chem. Mater.* **2006**, *18* (6), 1627–1633. https://doi.org/10.1021/cm0525961.
(89) Rabuffetti, F. A.; Stair, P. C.; Poeppelmeier, K. R. Synthesis-Dependent Surface Acidity and Structure of SrTiO3 Nanoparticles. *J. Phys. Chem. C* **2010**, *114* (25), 11056–11067.
(90) Dong, L.; Shi, H.; Cheng, K.; Wang, Q.; Weng, W.; Han, W. Shape-Controlled Growth of SrTiO3 Polyhedral Submicro/Nanocrystals. *Nano Res.* **2014**, *7* (9), 1311–1318. https://doi.org/10.1007/s12274-014-0495-y.
(91) Hao, Y.; Wang, X.; Li, L. Highly Dispersed SrTiO3 Nanocubes from a Rapid Sol-Precipitation Method. *Nanoscale* **2014**, *6* (14), 7940–7946. https://doi.org/10.1039/C4NR00171K.
(92) Dang, F.; Mimura, K.; Kato, K.; Imai, H.; Wada, S.; Haneda, H.; Kuwabara, M. Growth of Monodispersed SrTiO3 Nanocubes by Thermohydrolysis Method. *CrystEngComm* **2011**, *13* (11), 3878–3883. https://doi.org/10.1039/C1CE05296A.
(93) Rajamathi, M.; Seshadri, R. Oxide and Chalcogenide Nanoparticles from Hydrothermal/Solvothermal Reactions. *Curr. Opin. Solid State Mater. Sci.* **2002**, *6* (4), 337–345. https://doi.org/10.1016/S1359-0286(02)00029-3.
(94) Kappe, C. O. Controlled Microwave Heating in Modern Organic Synthesis. *Angew. Chem. Int. Ed.* **2004**, *43* (46), 6250–6284. https://doi.org/10.1002/anie.200400655.
(95) Rao, K. J.; Vaidhyanathan, B.; Ganguli, M.; Ramakrishnan, P. A. Synthesis of Inorganic Solids Using Microwaves. *Chem. Mater.* **1999**, *11* (4), 882–895. https://doi.org/10.1021/cm9803859.
(96) Tompsett, G. A.; Conner, W. C.; Yngvesson, K. S. Microwave Synthesis of Nanoporous Materials. *ChemPhysChem* **2006**, *7* (2), 296–319. https://doi.org/10.1002/cphc.200500449.
(97) Polshettiwar, V.; Nadagouda, M. N.; Varma, R. S. Microwave-Assisted Chemistry: A Rapid and Sustainable Route to Synthesis of Organics and Nanomaterials. *Aust. J. Chem.* **2009**, *62* (1), 16. https://doi.org/10.1071/CH08404.
(98) Bowman, M. D.; Holcomb, J. L.; Kormos, C. M.; Leadbeater, N. E.; Williams, V. A. Approaches for Scale-Up of Microwave-Promoted Reactions. *Org. Process Res. Dev.* **2008**, *12* (1), 41–57. https://doi.org/10.1021/op700187w.
(99) Leonelli, C.; Lojkowski, W. Main Development Directions in the Application of Microwave Irradiation to the Synthesis of Nanopowders. *Chim. Oggi* **2007**, *25*.
(100) Bilecka, I.; Niederberger, M. Microwave Chemistry for Inorganic Nanomaterials Synthesis. *Nanoscale* **2010**, *2* (8), 1358–1374. https://doi.org/10.1039/B9NR00377K.
(101) Reverón, H.; Aymonier, C.; Loppinet-Serani, A.; Elissalde, C.; Maglione, M.; Cansell, F. Single-Step Synthesis of Well-Crystallized and Pure Barium Titanate Nanoparticles in Supercritical Fluids. *Nanotechnology* **2005**, *16* (8), 1137. https://doi.org/10.1088/0957-4484/16/8/026.
(102) Helen, R.; Cyril, A.; Anne, L.-S.; Mario, M.; Catherine, E.; François, C. Synthesis of Barium Titanate Powders Using a Continuous-Flow Tubular Reactor.
(103) Cansell, F.; Reverón, H.; Aymonier, C.; Loppinet-Serani, A.; Maglione, M.; Elissalde, C. Synthesis of Barium Titanate Powders Using a Continuous-Flow Tubular Reactor. *Asian Pac. Confed. Chem. Eng. Congr. Program Abstr.* **2004**, *2004*, 574–574. https://doi.org/10.11491/apcche.2004.0.574.0.
(104) Philippot, G.; Elissalde, C.; Maglione, M.; Aymonier, C. Supercritical Fluid Technology: A Reliable Process for High Quality BaTiO3 Based Nanomaterials. *Adv. Powder Technol.* **2014**, *25* (5), 1415–1429. https://doi.org/10.1016/j.apt.2014.02.016.
(105) Dunne, P. W.; Starkey, C. L.; Munn, A. S.; Tang, S. V.; Luebben, O.; Shvets, I.; Ryder, A. G.; Casamayou-Boucau, Y.; Morrison, L.; Lester, E. H. Bench-and Pilot-Scale Continuous-Flow Hydrothermal Production of Barium Strontium Titanate Nanopowders. *Chem. Eng. J.* **2016**, *289*, 433–441.
(106) Foley, R. Role of the Chloride Ion in Iron Corrosion. *Corrosion* **1970**, *26* (2), 58–70.
(107) Song, Y.; Jiang, G.; Chen, Y.; Zhao, P.; Tian, Y. Effects of Chloride Ions on Corrosion of Ductile Iron and Carbon Steel in Soil Environments. *Sci. Rep.* **2017**, *7* (1), 6865. https://doi.org/10.1038/s41598-017-07245-1.
(108) Schwarz, J. A.; Contescu, C.; Contescu, A. Methods for Preparation of Catalytic Materials. *Chem. Rev.* **1995**, *95* (3), 477–510.
(109) Wieckowski, A.; Savinova, E. R.; Vayenas, C. G. *Catalysis and Electrocatalysis at Nanoparticle Surfaces*; CRC Press, 2003.

(110) Taylor, W.; Yates, D.; Sinfelt, J. Catalysis over Supported Metals. II. The Effect of the Support on the Catalytic Activity of Nickel for Ethane Hydrogenolysis. *J. Phys. Chem.* **1964**, *68* (10), 2962–2966.
(111) Taylor, W.; Sinfelt, J.; Yates, D. Catalysis over Supported Metals. IV. Ethane Hydrogenolysis over Dilute Nickel Catalysts. *J. Phys. Chem.* **1965**, *69* (11), 3857–3863.
(112) Sinfelt, J. Hydrogenolysis of Ethane over Supported Platinum. *J. Phys. Chem.* **1964**, *68* (2), 344–346.
(113) Kanbur, U.; Zang, G.; Paterson, A. L.; Chatterjee, P.; Hackler, R. A.; Delferro, M.; Slowing, I. I.; Perras, F. A.; Sun, P.; Sadow, A. D. Catalytic Carbon-Carbon Bond Cleavage and Carbon-Element Bond Formation Give New Life for Polyolefins as Biodegradable Surfactants. *Chem* **2021**, *7* (5), 1347–1362.
(114) Zhang, F.; Zeng, M.; Yappert, R. D.; Sun, J.; Lee, Y.-H.; LaPointe, A. M.; Peters, B.; Abu-Omar, M. M.; Scott, S. L. Polyethylene Upcycling to Long-Chain Alkylaromatics by Tandem Hydrogenolysis/Aromatization. *Science* **2020**, *370* (6515), 437–441. https://doi.org/10.1126/science.abc5441.
(115) Heller, M. C.; Mazor, M. H.; Keoleian, G. A. Plastics in the US: Toward a Material Flow Characterization of Production, Markets and End of Life. *Environ. Res. Lett.* **2020**, *15* (9), 094034.
(116) Hopewell, J.; Dvorak, R.; Kosior, E. Plastics Recycling: Challenges and Opportunities. *Philos. Trans. R. Soc. B Biol. Sci.* **2009**, *364* (1526), 2115–2126. https://doi.org/10.1098/rstb.2008.0311.
(117) Sánchez-Rivera, K. L.; Huber, G. W. Catalytic Hydrogenolysis of Polyolefins into Alkanes. *ACS Cent. Sci.* **2021**, *7* (1), 17–19. https://doi.org/10.1021/acscentsci.0c01637.
(118) Jia, C.; Xie, S.; Zhang, W.; Intan, N. N.; Sampath, J.; Pfaendtner, J.; Lin, H. Deconstruction of High-Density Polyethylene into Liquid Hydrocarbon Fuels and Lubricants by Hydrogenolysis over Ru Catalyst. *Chem Catal.* **2021**, *1* (2), 437–455.
(119) Lee, W.-T.; Bobbink, F. D.; van Muyden, A. P.; Lin, K.-H.; Corminboeuf, C.; Zamani, R. R.; Dyson, P. J. Catalytic Hydrocracking of Synthetic Polymers into Grid-Compatible Gas Streams. *Cell Rep. Phys. Sci.* **2021**, *2* (2), 100332.
(120) Deak, D. Strontium Titanate Surfaces. *Mater. Sci. Technol.* **2007**, *23* (2), 127–136.
(121) Goodenough, J. B. Electronic and Ionic Transport Properties and Other Physical Aspects of Perovskites. *Rep. Prog. Phys.* **2004**, *67* (11), 1915.
(122) Zhang, Z.; Li, L.; Yang, J. C. Adhesion of Pt Nanoparticles Supported on γ-Al2O3 Single Crystal. *J. Phys. Chem. C* **2013**, *117* (41), 21407–21412. https://doi.org/10.1021/jp407798b.
(123) Rabuffetti, F. A.; Kim, H.-S.; Enterkin, J. A.; Wang, Y.; Lanier, C. H.; Marks, L. D.; Poeppelmeier, K. R.; Stair, P. C. Synthesis-Dependent First-Order Raman Scattering in SrTiO3 Nanocubes at Room Temperature. *Chem. Mater.* **2008**, *20* (17), 5628–5635. https://doi.org/10.1021/cm801192t.
(124) Huang, K.; Yuan, L.; Feng, S. Crystal Facet Tailoring Arts in Perovskite Oxides. *Inorg. Chem. Front.* **2015**, *2* (11), 965–981.
(125) Plastics for a Circular Economy Workshop: Summary Report.
(126) Schreier, M.; Regalbuto, J. R. A Fundamental Study of Pt Tetraammine Impregnation of Silica: 1. The Electrostatic Nature of Platinum Adsorption. *J. Catal.* **2004**, *225* (1), 190–202.
(127) Miller, J. T.; Schreier, M.; Kropf, A. J.; Regalbuto, J. R. A Fundamental Study of Platinum Tetraammine Impregnation of Silica: 2. The Effect of Method of Preparation, Loading, and Calcination Temperature on (Reduced) Particle Size. *J. Catal.* **2004**, *225* (1), 203–212.
(128) Schneider, C. A.; Rasband, W. S.; Eliceiri, K. W. NIH Image to ImageJ: 25 Years of Image Analysis. *Nat. Methods* **2012**, *9* (7), 671–675.
(129) Alpay, D.; Peng, L.; Marks, L. D. Are Nanoparticle Corners Round? *J. Phys. Chem. C* **2015**, *119* (36), 21018–21023.
(130) Rabenau, A. The Role of Hydrothermal Synthesis in Preparative Chemistry. *Angew. Chem. Int. Ed. Engl.* **1985**, *24* (12), 1026–1040.
(131) Laudise, R. A. Hydrothermal Synthesis of Crystals. *50 Years Prog. Cryst. Growth* **2004**, 185.
(132) Lencka, M. M.; Riman, R. E. Thermodynamic Modeling of Hydrothermal Synthesis of Ceramic Powders. *Chem. Mater.* **1993**, *5* (1), 61–70.
(133) Lencka, M. M.; Riman, R. E. Thermodynamics of the Hydrothermal Synthesis of Calcium Titanate with Reference to Other Alkaline-Earth Titanates. *Chem. Mater.* **1995**, *7* (1), 18–25.

(134) Lencka, M. M.; Riman, R. E. Hydrothermal Synthesis of Perovskite Materials: Thermodynamic Modeling and Experimental Verification. *Ferroelectrics* **1994**, *151* (1), 159–164.
(135) Sugimoto, T.; Zhou, X.; Muramatsu, A. Synthesis of Uniform Anatase TiO2 Nanoparticles by Gel–Sol Method: 1. Solution Chemistry of Ti(OH)n(4−n)+ Complexes. *J. Colloid Interface Sci.* **2002**, *252* (2), 339–346. https://doi.org/10.1006/jcis.2002.8454.
(136) Makiura, R. Influence of Solution PH and Reaction Atmosphere on the Morphology of SrTiO 3 Nanocubes Synthesized by Thermohydrolysis. *Res. Chem. Intermed.* **2018**, *44*, 4775–4782.
(137) Hagen, J. *Industrial Catalysis: A Practical Approach*; John Wiley & Sons, 2015.
(138) Kent, J. A. *Handbook of Industrial Chemistry and Biotechnology*; Springer Science & Business Media, 2013.
(139) Tauster, S. J.; Steger, J. J. Molecular Die Catalysis: Hexane Aromatization over Pt/KL. *J. Catal.* **1990**, *125* (2), 387–389. https://doi.org/10.1016/0021-9517(90)90311-7.
(140) Mielczarski, E.; Hong, S. B.; Davis, R. J.; Davis, M. E. Aromatization of N-Hexane by Platinum-Containing Molecular Sieves II. n-Hexane Reactivity. *J. Catal.* **1992**, *134* (1), 359–369. https://doi.org/10.1016/0021-9517(92)90235-A.
(141) Catlow, C. R.; Davidson, M.; Hardacre, C.; Hutchings, G. J. Catalysis Making the World a Better Place. *Philos. Trans. R. Soc. Math. Phys. Eng. Sci.* **2016**, *374* (2061), 20150089.
(142) Eerkes-Medrano, D.; Thompson, R. C.; Aldridge, D. C. Microplastics in Freshwater Systems: A Review of the Emerging Threats, Identification of Knowledge Gaps and Prioritisation of Research Needs. *Water Res.* **2015**, *75*, 63–82.
(143) Lebreton, L.; Andrady, A. Future Scenarios of Global Plastic Waste Generation and Disposal. *Palgrave Commun.* **2019**, *5* (1), 1–11.
(144) Garcia, J. M.; Robertson, M. L. The Future of Plastics Recycling. *Science* **2017**, *358* (6365), 870–872.
(145) Lopez, G.; Artetxe, M.; Amutio, M.; Bilbao, J.; Olazar, M. Thermochemical Routes for the Valorization of Waste Polyolefinic Plastics to Produce Fuels and Chemicals. A Review. *Renew. Sustain. Energy Rev.* **2017**, *73*, 346–368.
(146) Rorrer, J. E.; Beckham, G. T.; Román-Leshkov, Y. Conversion of Polyolefin Waste to Liquid Alkanes with Ru-Based Catalysts under Mild Conditions. *JACS Au* **2021**, *1* (1), 8–12. https://doi.org/10.1021/jacsau.0c00041.
(147) Tennakoon, A.; Wu, X.; Paterson, A. L.; Patnaik, S.; Pei, Y.; LaPointe, A. M.; Ammal, S. C.; Hackler, R. A.; Heyden, A.; Slowing, I. I.; Coates, G. W.; Delferro, M.; Peters, B.; Huang, W.; Sadow, A. D.; Perras, F. A. Catalytic Upcycling of High-Density Polyethylene via a Processive Mechanism. *Nat. Catal.* **2020**, *3* (11), 893–901. https://doi.org/10.1038/s41929-020-00519-4.
(148) Xuewen, W.; Zhiyong, Z.; Shuixian, Z. Preparation of Nano-Crystalline SrTiO3 Powder in Sol-Gel Process. *Mater. Sci. Eng. B* **2001**, *86* (1), 29–33.
(149) Hutchings, G. J.; King, F.; Okoye, I. P.; Rochester, C. H. Influence of Chlorine Poisoning of Copper/Alumina Catalyst on the Selective Hydrogenation of Crotonaldehyde. *Catal. Lett.* **1994**, *23*, 127–133.
(150) Mendyka, B.; Musialik-Piotrowska, A.; Syczewska, K. Effect of Chlorine Compounds on the Deactivation of Platinum Catalysts. *Catal. Today* **1992**, *11* (4), 597–610.
(151) Steinbach, F.; Krall, R. The Influence of Chlorine on the Catalytic Decomposition of Methanol on Nickel Foil: Transition from Poison to Promoter upon Modification of Deposit. *J. Catal.* **1985**, *94* (1), 142–147.
(152) Aboul-Fotouh, S. M.; Aboul-Gheit, A. K. Hydroconversion of Cyclohexene Using Platinum-Containing Catalysts Promoted with Other Noble Metals and Chlorine or Fluorine. *Appl. Catal. Gen.* **2001**, *208* (1–2), 55–61.
(153) Bartholomew, C. H. Mechanisms of Catalyst Deactivation. *Appl. Catal. Gen.* **2001**, *212* (1–2), 17–60. https://doi.org/10.1016/S0926-860X(00)00843-7.
(154) Llados, F.; Murray, H. E. Toxicological Profile for Titanium Tetrachloride. **1997**.
(155) Wang, Z.; Benavides, P. T.; Dunn, J. B.; Cronauer, D. C. *Development of GREET Catalyst Module*; Argonne National Lab.(ANL), Argonne, IL (United States), 2015.
(156) Nakashima, K.; Kera, M.; Fujii, I.; Wada, S. A New Approach for the Preparation of SrTiO3 Nanocubes. *Ceram. Int.* **2013**, *39* (3), 3231–3234.

(157) Yang, G.; Park, S.-J. Conventional and Microwave Hydrothermal Synthesis and Application of Functional Materials: A Review. *Materials* **2019**, *12* (7), 1177.
(158) Guo, L.; Luo, H.; Gao, J.; Guo, L.; Yang, J. Microwave Hydrothermal Synthesis of Barium Titanate Powders. *Mater. Lett.* **2006**, *60* (24), 3011–3014.
(159) Lin, H.; Cian, L.-T. Microwave-Assisted Hydrothermal Synthesis of SrTiO3:Rh for Photocatalytic Z-Scheme Overall Water Splitting. *Appl. Sci.* **2019**, *9* (1), 55. https://doi.org/10.3390/app9010055.
(160) Moreira, M. L.; Longo, V. M.; Avansi Jr, W.; Ferrer, M. M.; Andres, J.; Mastelaro, V. R.; Varela, J. A.; Longo, E. Quantum Mechanics Insight into the Microwave Nucleation of SrTiO3 Nanospheres. *J. Phys. Chem. C* **2012**, *116* (46), 24792–24808.
(161) Patterson, A. The Scherrer Formula for X-Ray Particle Size Determination. *Phys. Rev.* **1939**, *56* (10), 978.
(162) Walton, R. I.; Millange, F.; Smith, R. I.; Hansen, T. C.; O'Hare, D. Real Time Observation of the Hydrothermal Crystallization of Barium Titanate Using in Situ Neutron Powder Diffraction. *J. Am. Chem. Soc.* **2001**, *123* (50), 12547–12555.
(163) Isley, S. L.; Penn, R. L. Titanium Dioxide Nanoparticles: Effect of Sol− Gel PH on Phase Composition, Particle Size, and Particle Growth Mechanism. *J. Phys. Chem. C* **2008**, *112* (12), 4469–4474.
(164) Knauss, K. G.; Dibley, M. J.; Bourcier, W. L.; Shaw, H. F. Ti (IV) Hydrolysis Constants Derived from Rutile Solubility Measurements Made from 100 to 300 C. *Appl. Geochem.* **2001**, *16* (9–10), 1115–1128.
(165) Hasenkox, U.; Hoffmann, S.; Waser, R. Influence of Precursor Chemistry on the Formation of MTiO3 (M= Ba, Sr) Ceramic Thin Films. *J. Sol-Gel Sci. Technol.* **1998**, *12*, 67–79.
(166) Livage, J.; Sanchez, C. Sol-Gel Chemistry. *J. Non-Cryst. Solids* **1992**, *145*, 11–19.
(167) Dorosheva, I.; Valeeva, A.; Rempel, A. Sol-Gel Synthesis of Nanosized Titanium Dioxide at Various PH of the Initial Solution; AIP Publishing LLC, 2017; Vol. 1886, p 020006.
(168) Gao, M.; Zhang, L.; Zhang, J. Acid-Controlled Synthesis of Carboxylate-Stabilized Ti44-Oxo Clusters: Scaling up Preparation, Exchangeable Protecting Ligands, and Photophysical Properties. *Chem. Eur. J.* **2019**, *25* (44), 10450–10455.
(169) Lopez, T.; Gomez, R.; Pecci, G.; Reyes, P.; Bokhimi, X.; Novaro, O. Effect of PH on the Incorporation of Platinum into the Lattice of Sol–Gel Titania Phases. *Mater. Lett.* **1999**, *40* (2), 59–65.
(170) Doeuff, S.; Henry, M.; Sanchez, C.; Livage, J. Hydrolysis of Titanium Alkoxides: Modification of the Molecular Precursor by Acetic Acid. *J. Non-Cryst. Solids* **1987**, *89* (1–2), 206–216.
(171) Leaustic, A.; Babonneau, F.; Livage, J. Structural Investigation of the Hydrolysis-Condensation Process of Titanium Alkoxides Ti (OR) 4 (OR= OPr-Iso, OEt) Modified by Acetylacetone. 2. From the Modified Precursor to the Colloids. *Chem. Mater.* **1989**, *1* (2), 248–252.
(172) Blanchard, J.; Ribot, F.; Sanchez, C.; Bellot, P.-V.; Trokiner, A. Structural Characterization of Titanium-Oxo-Polymers Synthesized in the Presence of Protons or Complexing Ligands as Inhibitors. *J. Non-Cryst. Solids* **2000**, *265* (1–2), 83–97.
(173) Sanchez, C.; Livage, J.; Henry, M.; Babonneau, F. Chemical Modification of Alkoxide Precursors. *J. Non-Cryst. Solids* **1988**, *100* (1–3), 65–76.
(174) Schubert, U. Chemical Modification of Titanium Alkoxides for Sol–Gel Processing. *J. Mater. Chem.* **2005**, *15* (35–36), 3701–3715.
(175) Mehrotra, R. Synthesis and Reactions of Metal Alkoxides. *J. Non-Cryst. Solids* **1988**, *100* (1–3), 1–15.
(176) Mehrotra, R. C. Chemistry of Alkoxide Precursors. *J. Non-Cryst. Solids* **1990**, *121* (1–3), 1–6.
(177) Stawski, T. M.; Veldhuis, S. A.; Besselink, R.; Castricum, H. L.; Portale, G.; Blank, D. H.; ten Elshof, J. E. Nanoscale Structure Evolution in Alkoxide–Carboxylate Sol–Gel Precursor Solutions of Barium Titanate. *J. Phys. Chem. C* **2011**, *115* (42), 20449–20459.
(178) Simonsen, M. E.; Søgaard, E. G. Sol–Gel Reactions of Titanium Alkoxides and Water: Influence of PH and Alkoxy Group on Cluster Formation and Properties of the Resulting Products. *J. Sol-Gel Sci. Technol.* **2010**, *53*, 485–497.
(179) Soloviev, A.; Søgaard, E. G. Application of Electro-Spray Ionization Mass Spectrometry for Characterization of Titanium Polyoxoalkoxides in Sol-Gel Processes. *J. Mater. Sci.* **2006**, *41*, 6159–6161.

(180) Soloviev, A.; Jensen, H.; Søgaard, E. G.; Kanaev, A. Aggregation Kinetics of Sol-Gel Process Based on Titanium Tetraisopropoxide. *J. Mater. Sci.* **2003**, *38*, 3315–3318.
(181) Soloviev, A.; Tufeu, R.; Sanchez, C.; Kanaev, A. Nucleation Stage in the Ti (OPr i) 4 Sol− Gel Process. *J. Phys. Chem. B* **2001**, *105* (19), 4175–4180.
(182) Sugimoto, T.; Zhou, X. Synthesis of Uniform Anatase TiO2 Nanoparticles by the Gel–Sol Method: 2. Adsorption of OH− Ions to Ti (OH) 4 Gel and TiO2 Particles. *J. Colloid Interface Sci.* **2002**, *252* (2), 347–353.
(183) Sugimoto, T.; Zhou, X.; Muramatsu, A. Synthesis of Uniform Anatase TiO2 Nanoparticles by Gel–Sol Method: 3. Formation Process and Size Control. *J. Colloid Interface Sci.* **2003**, *259* (1), 43–52.
(184) Sugimoto, T.; Zhou, X.; Muramatsu, A. Synthesis of Uniform Anatase TiO2 Nanoparticles by Gel–Sol Method: 4. Shape Control. *J. Colloid Interface Sci.* **2003**, *259* (1), 53–61.
(185) Wulff, G. Xxv. Zur Frage Der Geschwindigkeit Des Wachsthums Und Der Auflösung Der Krystallflächen. *Z. Für Krist.-Cryst. Mater.* **1901**, *34* (1–6), 449–530.
(186) Marks, L.; Peng, L. Nanoparticle Shape, Thermodynamics and Kinetics. *J. Phys. Condens. Matter* **2016**, *28* (5), 053001.
(187) Crosby, L.; Enterkin, J.; Rabuffetti, F.; Poeppelmeier, K.; Marks, L. Wulff Shape of Strontium Titanate Nanocuboids. *Surf. Sci.* **2015**, *632*, L22–L25.
(188) Ruddlesden, S.; Popper, P. The Compound Sr3Ti2O7 and Its Structure. *Acta Crystallogr.* **1958**, *11* (1), 54–55.
(189) Sorensen, E. M.; Barry, S. J.; Jung, H.-K.; Rondinelli, J. M.; Vaughey, J. T.; Poeppelmeier, K. R. Three-Dimensionally Ordered Macroporous Li4Ti5O12: Effect of Wall Structure on Electrochemical Properties. *Chem. Mater.* **2006**, *18* (2), 482–489.
(190) Kirillov, S.; Romanova, I.; Lisnycha, T.; Potapenko, A. High-Rate Electrochemical Performance of Li4Ti5O12 Obtained from TiCl4 by Means of a Citric Acid Aided Route. *Electrochimica Acta* **2018**, *286*, 163–171.
(191) Li, Y.; Fu, Z.; Su, B. Hierarchically Structured Porous Materials for Energy Conversion and Storage. *Adv. Funct. Mater.* **2012**, *22* (22), 4634–4667.
(192) Law, K. L.; Starr, N.; Siegler, T. R.; Jambeck, J. R.; Mallos, N. J.; Leonard, G. H. The United States' Contribution of Plastic Waste to Land and Ocean. *Sci. Adv.* **2020**, *6* (44), eabd0288. https://doi.org/10.1126/sciadv.abd0288.
(193) Jambeck, J. R.; Geyer, R.; Wilcox, C.; Siegler, T. R.; Perryman, M.; Andrady, A.; Narayan, R.; Law, K. L. Plastic Waste Inputs from Land into the Ocean. *Science* **2015**, *347* (6223), 768–771.
(194) Ertem, S. P.; Onuoha, C. E.; Wang, H.; Hillmyer, M. A.; Reineke, T. M.; Lodge, T. P.; Bates, F. S. Hydrogenolysis of Linear Low-Density Polyethylene during Heterogeneous Catalytic Hydrogen–Deuterium Exchange. *Macromolecules* **2020**, *53* (14), 6043–6055. https://doi.org/10.1021/acs.macromol.0c00696.
(195) Jaydev, S. D.; Martín, A. J.; Pérez-Ramírez, J. Direct Conversion of Polypropylene into Liquid Hydrocarbons on Carbon-supported Platinum Catalysts. *ChemSusChem* **2021**, *14* (23), 5179–5185.
(196) Miandad, R.; Barakat, M.; Rehan, M.; Aburiazaiza, A.; Ismail, I.; Nizami, A. Plastic Waste to Liquid Oil through Catalytic Pyrolysis Using Natural and Synthetic Zeolite Catalysts. *Waste Manag.* **2017**, *69*, 66–78.
(197) Aboulkas, A.; El Bouadili, A. Thermal Degradation Behaviors of Polyethylene and Polypropylene. Part I: Pyrolysis Kinetics and Mechanisms. *Energy Convers. Manag.* **2010**, *51* (7), 1363–1369.
(198) *Chevron Phillips Chemical successfully completes first U.S. commercial scale production of circular polyethylene from recycled mixed-waste plastics | Chevron Phillips Chemical*. https://www.cpchem.com/media-events/news/press-release/chevron-phillips-chemical-successfully-completes-first-us (accessed 2023-04-02).
(199) *Car parts made from post-consumer plastic waste • Plastics Europe*. https://plasticseurope.org/case-studies/car-parts-made-from-post-consumer-plastic-waste/ (accessed 2023-04-02).
(200) *ExxonMobil to Build its First Large-Scale Plastic Waste Advanced Recycling Facility*. https://www.ptonline.com/news/exxonmobil-to-build-its-first-large-scale-plastic-waste-advanced-recycling-facility (accessed 2023-04-02).

(201) Sharuddin, S. D. A.; Abnisa, F.; Daud, W. M. A. W.; Aroua, M. K. A Review on Pyrolysis of Plastic Wastes. *Energy Convers. Manag.* **2016**, *115*, 308–326.
(202) Delferro, M.; McInnis, J. P.; Marks, T. J. Ethylene Polymerization Characteristics of an Electron-Deficient Nickel (II) Phenoxyiminato Catalyst Modulated by Non-Innocent Intramolecular Hydrogen Bonding. *Organometallics* **2010**, *29* (21), 5040–5049.
(203) Shu, D.; Mouat, A. R.; Stephenson, C. J.; Invergo, A. M.; Delferro, M.; Marks, T. J. Ligand-Unsymmetrical Phenoxyiminato Dinickel Catalyst for High Molecular Weight Long-Chain Branched Polyethylenes. *ACS Macro Lett.* **2015**, *4* (11), 1297–1301.
(204) Kudchadker, A.; Zwolinski, B. Vapor Pressure and Boiling Points of Normal Alkanes, C21 to C100. *J. Chem. Eng. Data* **1966**, *11* (2), 253–255.
(205) Tzounis, P.-N.; Argyropoulou, D. V.; Anogiannakis, S. D.; Theodorou, D. N. Tacticity Effect on the Conformational Properties of Polypropylene and Poly (Ethylene–Propylene) Copolymers. *Macromolecules* **2018**, *51* (17), 6878–6891.
(206) Pinijmontree, T.; Vao-soongnern, V. Dynamics of Polypropylene Chains in Their Binary Blends of Different Stereochemical Sequences Studied by Monte Carlo Simulations. *Chin. J. Polym. Sci.* **2014**, *32* (5), 640–649.
(207) Foo, G. S.; Polo-Garzon, F.; Fung, V.; Jiang, D.; Overbury, S. H.; Wu, Z. Acid–Base Reactivity of Perovskite Catalysts Probed via Conversion of 2-Propanol over Titanates and Zirconates. *ACS Catal.* **2017**, *7* (7), 4423–4434. https://doi.org/10.1021/acscatal.7b00783.
(208) Chen, Z.; Liu, S.; Zhang, H.; He, P.; Ren, J.; Wen, X.; Li, Y.-W. Selective Regulation of n -Dodecane Isomerization and Cracking Performance in Pt/Beta Catalysts via Orientation Control of Brønsted Acid Site Distribution. *Catal. Sci. Technol.* **2021**, *11* (6), 2094–2102. https://doi.org/10.1039/D0CY02088E.
(209) Davis, S.; Gillespie, W.; Somorjai, G. Deuterium Isotope Effects for Hydrocarbon Reactions Catalyzed over Platinum Single Crystal Surfaces. *J. Catal.* **1983**, *83* (1), 131–140.
(210) Oliver, J.; Kemball, C. Hydrogenolysis and Related Reactions of Hydrocarbons (C3 to C5) on Silica-Supported Rh-Pt Bimetallic Catalysts. *Proc. R. Soc. Lond. Math. Phys. Sci.* **1990**, *429* (1876), 17–43.
(211) *Vistamaxx™ Product Data Sheets | ExxonMobil Product Solutions*. https://www.exxonmobilchemical.com/en/resources/product-data-sheets/polymer-modifiers/vistamaxx-performance-polymers (accessed 2023-04-02).
(212) Popov, K. V.; Knyazev, V. D. Initial Stages of the Pyrolysis of Polyethylene. *J. Phys. Chem. A* **2015**, *119* (49), 11737–11760. https://doi.org/10.1021/acs.jpca.5b07440.
(213) Levine, S. E.; Broadbelt, L. J. Detailed Mechanistic Modeling of High-Density Polyethylene Pyrolysis: Low Molecular Weight Product Evolution. *Polym. Degrad. Stab.* **2009**, *94* (5), 810–822. https://doi.org/10.1016/j.polymdegradstab.2009.01.031.
(214) Yang, Y.; Zhang, D.; Ji, W.; Bi, F.; Song, L.; Zhang, X. Uniform Platinum Nanoparticles Loaded on Universitetet i Oslo-66 (UiO-66): Active and Stable Catalysts for Gas Toluene Combustion. *J. Colloid Interface Sci.* **2022**, *606*, 1811–1822. https://doi.org/10.1016/j.jcis.2021.08.127.
(215) Koch, V. M.; Barr, M. K. S.; Büttner, P.; Mínguez-Bacho, I.; Döhler, D.; Winzer, B.; Reinhardt, E.; Segets, D.; Bachmann, J. A Solution-Based ALD Route towards (CH3NH3)(PbI3) Perovskite via Lead Sulfide Films. *J. Mater. Chem. A* **2019**, *7* (43), 25112–25119. https://doi.org/10.1039/C9TA09715E.
(216) Le Monnier, B. P.; Wells, F.; Talebkeikhah, F.; Luterbacher, J. S. Atomic Layer Deposition on Dispersed Materials in Liquid Phase by Stoichiometrically Limited Injections. *Adv. Mater.* **2019**, *31* (52), 1904276. https://doi.org/10.1002/adma.201904276.
(217) Fichtner, J.; Wu, Y.; Hitzenberger, J.; Drewello, T.; Bachmann, J. Molecular Layer Deposition from Dissolved Precursors. *ECS J. Solid State Sci. Technol.* **2017**, *6* (9), N171. https://doi.org/10.1149/2.0291709jss.
(218) Zankowski, S. P.; van Hoecke, L.; Mattelaer, F.; de Raedt, M.; Richard, O.; Detavernier, C.; Vereecken, P. M. Redox Layer Deposition of Thin Films of MnO_2 on Nanostructured Substrates from Aqueous Solutions. *Chem. Mater.* **2019**, *31* (13), 4805–4816. https://doi.org/10.1021/acs.chemmater.9b01219.

(219) Wu, Y.; Döhler, D.; Barr, M.; Oks, E.; Wolf, M.; Santinacci, L.; Bachmann, J. Atomic Layer Deposition from Dissolved Precursors. *Nano Lett.* **2015**, *15* (10), 6379–6385. https://doi.org/10.1021/acs.nanolett.5b01424.
(220) Witzke, R. J.; Chapovetsky, A.; Conley, M. P.; Kaphan, D. M.; Delferro, M. Nontraditional Catalyst Supports in Surface Organometallic Chemistry. *ACS Catal.* **2020**, *10* (20), 11822–11840. https://doi.org/10.1021/acscatal.0c03350.
(221) Stalzer, M. M.; Delferro, M.; Marks, T. J. Supported Single-Site Organometallic Catalysts for the Synthesis of High-Performance Polyolefins. *Catal. Lett.* **2015**, *145* (1), 3–14. https://doi.org/10.1007/s10562-014-1427-x.
(222) Copéret, C.; Comas-Vives, A.; Conley, M. P.; Estes, D. P.; Fedorov, A.; Mougel, V.; Nagae, H.; Núñez-Zarur, F.; Zhizhko, P. A. Surface Organometallic and Coordination Chemistry toward Single-Site Heterogeneous Catalysts: Strategies, Methods, Structures, and Activities. *Chem. Rev.* **2016**, *116* (2), 323–421. https://doi.org/10.1021/acs.chemrev.5b00373.
(223) Pelletier, J. D. A.; Basset, J.-M. Catalysis by Design: Well-Defined Single-Site Heterogeneous Catalysts. *Acc. Chem. Res.* **2016**, *49* (4), 664–677. https://doi.org/10.1021/acs.accounts.5b00518.
(224) Copéret, C.; Allouche, F.; Chan, K. W.; Conley, M. P.; Delley, M. F.; Fedorov, A.; Moroz, I. B.; Mougel, V.; Pucino, M.; Searles, K.; Yamamoto, K.; Zhizhko, P. A. Bridging the Gap between Industrial and Well-Defined Supported Catalysts. *Angew. Chem. Int. Ed.* **2018**, *57* (22), 6398–6440. https://doi.org/10.1002/anie.201702387.
(225) Copéret, C.; Fedorov, A.; Zhizhko, P. A. Surface Organometallic Chemistry: Paving the Way Beyond Well-Defined Supported Organometallics and Single-Site Catalysis. *Catal. Lett.* **2017**, *147* (9), 2247–2259. https://doi.org/10.1007/s10562-017-2107-4.
(226) Poeppelmeier, K. R.; Trowbridge, T. D.; Kao, J.-L. Process for Loading Platinum into Zeolite-L. US4568656A, February 4, 1986. https://patents.google.com/patent/US4568656A/en?oq=US+pat+4568656 (accessed 2023-04-02).
(227) Tauster, S. J.; Montagna, A. A.; Steger, J. J.; Fung, S. C.; Cross, V. R. Zeolite Catalyst and Process for Using Said Catalyst (C-1591). US4634517A, January 6, 1987. https://patents.google.com/patent/US4634517A/en?oq=US+pat+4634517 (accessed 2023-04-02).
(228) Marques, J. P.; Gener, I.; Ayrault, P.; Bordado, J. C.; Lopes, J. M.; Ramôa Ribeiro, F.; Guisnet, M. Infrared Spectroscopic Study of the Acid Properties of Dealuminated BEA Zeolites. *Microporous Mesoporous Mater.* **2003**, *60* (1), 251–262. https://doi.org/10.1016/S1387-1811(03)00382-2.
(229) Batonneau-gener, I.; Yonli, A.; Hazael-pascal, S.; Pedro Marques, J.; Madeira Lopes, J.; Guisnet, M.; Ramôa Ribeiro, F.; Mignard, S. Influence of Steaming and Acid-Leaching Treatments on the Hydrophobicity of HBEA Zeolite Determined under Static Conditions. *Microporous Mesoporous Mater.* **2008**, *110* (2), 480–487. https://doi.org/10.1016/j.micromeso.2007.06.037.
(230) Son, I. H.; Lee, S. J.; Soon, A.; Roh, H.-S.; Lee, H. Steam Treatment on Ni/γ-Al2O3 for Enhanced Carbon Resistance in Combined Steam and Carbon Dioxide Reforming of Methane. *Appl. Catal. B Environ.* **2013**, *134–135*, 103–109. https://doi.org/10.1016/j.apcatb.2013.01.001.
(231) Schrock, R. R. Preparation and Characterization of M(CH3)5 (M = Nb or Ta) and Ta(CH2C6H5)5 and Evidence for Decomposition by α-Hydrogen Atom Abstraction. *J. Organomet. Chem.* **1976**, *122* (2), 209–225. https://doi.org/10.1016/S0022-328X(00)80612-9.
(232) Zagdoun, A.; Casano, G.; Ouari, O.; Schwarzwälder, M.; Rossini, A. J.; Aussenac, F.; Yulikov, M.; Jeschke, G.; Copéret, C.; Lesage, A.; Tordo, P.; Emsley, L. Large Molecular Weight Nitroxide Biradicals Providing Efficient Dynamic Nuclear Polarization at Temperatures up to 200 K. *J. Am. Chem. Soc.* **2013**, *135* (34), 12790–12797. https://doi.org/10.1021/ja405813t.
(233) Perras, F. A.; Kobayashi, T.; Pruski, M. Natural Abundance 17O DNP Two-Dimensional and Surface-Enhanced NMR Spectroscopy. *J. Am. Chem. Soc.* **2015**, *137* (26), 8336–8339. https://doi.org/10.1021/jacs.5b03905.
(234) Zhao, X.; Hoffbauer, W.; Schmedt auf der Günne, J.; Levitt, M. H. Heteronuclear Polarization Transfer by Symmetry-Based Recoupling Sequences in Solid-State NMR. *Solid State Nucl. Magn. Reson.* **2004**, *26* (2), 57–64. https://doi.org/10.1016/j.ssnmr.2003.11.001.
(235) Nagashima, H.; Trébosc, J.; Kon, Y.; Sato, K.; Lafon, O.; Amoureux, J.-P. Observation of Low-γ Quadrupolar Nuclei by Surface-Enhanced NMR Spectroscopy. *J. Am. Chem. Soc.* **2020**, *142* (24), 10659–10672. https://doi.org/10.1021/jacs.9b13838.

(236) A. Perras, F.; C. Boteju, K.; I. Slowing, I.; D. Sadow, A.; Pruski, M. Direct 17 O Dynamic Nuclear Polarization of Single-Site Heterogeneous Catalysts. *Chem. Commun.* **2018**, *54* (28), 3472–3475. https://doi.org/10.1039/C8CC00293B.
(237) Larsen, F. H.; Skibsted, J.; Jakobsen, H. J.; Nielsen, N. Chr. Solid-State QCPMG NMR of Low-γ Quadrupolar Metal Nuclei in Natural Abundance. *J. Am. Chem. Soc.* **2000**, *122* (29), 7080–7086. https://doi.org/10.1021/ja0003526.
(238) Bielecki, A.; Kolbert, A. C.; Levitt, M. H. Frequency-Switched Pulse Sequences: Homonuclear Decoupling and Dilute Spin NMR in Solids. *Chem. Phys. Lett.* **1989**, *155* (4), 341–346. https://doi.org/10.1016/0009-2614(89)87166-0.
(239) Venkatesh, A.; Gioffrè, D.; Atterberry, B. A.; Rochlitz, L.; Carnahan, S. L.; Wang, Z.; Menzildjian, G.; Lesage, A.; Copéret, C.; Rossini, A. J. Molecular and Electronic Structure of Isolated Platinum Sites Enabled by the Expedient Measurement of 195Pt Chemical Shift Anisotropy. *J. Am. Chem. Soc.* **2022**, *144* (30), 13511–13525. https://doi.org/10.1021/jacs.2c02300.
(240) Clark, S. J.; Segall, M. D.; Pickard, C. J.; Hasnip, P. J.; Probert, M. I. J.; Refson, K.; Payne, M. C. First Principles Methods Using CASTEP: *Z. Für Krist. - Cryst. Mater.* **2005**, *220* (5–6), 567–570. https://doi.org/10.1524/zkri.220.5.567.65075.
(241) Vanderbilt, D. Soft Self-Consistent Pseudopotentials in a Generalized Eigenvalue Formalism. *Phys. Rev. B* **1990**, *41* (11), 7892–7895. https://doi.org/10.1103/PhysRevB.41.7892.
(242) Perdew, J. P.; Burke, K.; Ernzerhof, M. Generalized Gradient Approximation Made Simple. *Phys. Rev. Lett.* **1996**, *77* (18), 3865–3868. https://doi.org/10.1103/PhysRevLett.77.3865.
(243) Grimme, S. Semiempirical GGA-type density functional constructed with a long-range dispersion correction. *J. Comput. Chem.* **2006**, *27* (15), 1787–1799. https://doi.org/10.1002/jcc.20495.
(244) Pickard, C. J.; Mauri, F. All-Electron Magnetic Response with Pseudopotentials: NMR Chemical Shifts. *Phys. Rev. B* **2001**, *63* (24), 245101. https://doi.org/10.1103/PhysRevB.63.245101.
(245) Yates, J. R.; Pickard, C. J.; Mauri, F. Calculation of NMR Chemical Shifts for Extended Systems Using Ultrasoft Pseudopotentials. *Phys. Rev. B* **2007**, *76* (2), 024401. https://doi.org/10.1103/PhysRevB.76.024401.
(246) Ravel, B.; Newville, M. ATHENA, ARTEMIS, HEPHAESTUS: Data Analysis for X-Ray Absorption Spectroscopy Using IFEFFIT. *J. Synchrotron Radiat.* **2005**, *12* (4), 537–541. https://doi.org/10.1107/S0909049505012719.
(247) Bolin, T. B.; Wu, T.; Schweitzer, N.; Lobo-Lapidus, R.; Kropf, A. J.; Wang, H.; Hu, Y.; Miller, J. T.; Heald, S. M. In Situ Intermediate-Energy X-Ray Catalysis Research at the Advanced Photon Source Beamline 9-BM. *Catal. Today* **2013**, *205*, 141–147. https://doi.org/10.1016/j.cattod.2012.09.034.
(248) M. Kienzle, D.; D. Marks, L. Surface Transmission Electron Diffraction for SrTiO 3 Surfaces. *CrystEngComm* **2012**, *14* (23), 7833–7839. https://doi.org/10.1039/C2CE25204J.
(249) Grillo, F.; Van Bui, H.; La Zara, D.; Aarnink, A. A. I.; Kovalgin, A. Y.; Kooyman, P.; Kreutzer, M. T.; van Ommen, J. R. From Single Atoms to Nanoparticles: Autocatalysis and Metal Aggregation in Atomic Layer Deposition of Pt on TiO2 Nanopowder. *Small* **2018**, *14* (23), 1800765. https://doi.org/10.1002/smll.201800765.
(250) Crespin, M.; Hall, W. K. The Surface Chemistry of Some Perovskite Oxides. *J. Catal.* **1981**, *69* (2), 359–370. https://doi.org/10.1016/0021-9517(81)90171-8.
(251) Domingo, N.; Pach, E.; Cordero-Edwards, K.; Pérez-Dieste, V.; Escudero, C.; Verdaguer, A. Water Adsorption, Dissociation and Oxidation on SrTiO 3 and Ferroelectric Surfaces Revealed by Ambient Pressure X-Ray Photoelectron Spectroscopy. *Phys. Chem. Chem. Phys.* **2019**, *21* (9), 4920–4930. https://doi.org/10.1039/C8CP07632D.
(252) Becerra-Toledo, A. E.; Enterkin, J. A.; Kienzle, D. M.; Marks, L. D. Water Adsorption on SrTiO3(001): II. Water, Water, Everywhere. *Surf. Sci.* **2012**, *606* (9), 791–802. https://doi.org/10.1016/j.susc.2012.01.010.
(253) Becerra-Toledo, A. E.; Castell, M. R.; Marks, L. D. Water Adsorption on SrTiO3(001): I. Experimental and Simulated STM. *Surf. Sci.* **2012**, *606* (7), 762–765. https://doi.org/10.1016/j.susc.2012.01.008.
(254) Kienzle, D. M.; Becerra-Toledo, A. E.; Marks, L. D. Vacant-Site Octahedral Tilings on ${\mathrm{SrTiO}}_{3}$ (001), the $(\sqrt{13}\ifmmode\times\else\texttimes\fi{}\sqrt{13})R33.7\ifmmode^\circ\else\textdegree\fi{}$

Surface, and Related Structures. *Phys. Rev. Lett.* **2011**, *106* (17), 176102. https://doi.org/10.1103/PhysRevLett.106.176102.
(255) Astruc, D. *Nanoparticles and Catalysis*; John Wiley & Sons, 2008.
(256) Hodnett, B. K. Heterogeneous Catalytic Oxidation : Fundamental and Technolgical Aspects of the Selective and Total Oxidation of Organic Compounds. *No Title*.
(257) Dossi, C.; Psaro, R.; Bartsch, A.; Brivio, E.; Galasco, A.; Losi, P. Organometallics-Chemical Vapor Deposition: A New Technique for the Preparation of Non-Acidic, Zeolitesupported Pd and Pt Catalysts. *Catal. Today* **1993**, *17* (3), 527–535. https://doi.org/10.1016/0920-5861(93)80055-6.
(258) Miura, H. Preparation of Supported Bimetallic Catalysts by Means of Selective Deposition Using Mobile Metal Compounds as Precursors. *Catal. Today* **1996**, *28* (3), 215–221.
(259) Camacho-Bunquin, J.; Ferrandon, M.; Sohn, H.; Yang, D.; Liu, C.; Ignacio-de Leon, P. A.; Perras, F. A.; Pruski, M.; Stair, P. C.; Delferro, M. Chemoselective Hydrogenation with Supported Organoplatinum(IV) Catalyst on Zn(II)-Modified Silica. *J. Am. Chem. Soc.* **2018**, *140* (11), 3940–3951. https://doi.org/10.1021/jacs.7b11981.
(260) Martín González, M. S.; Aguirre, M. H.; Morán, E.; Alario-Franco, M. Á.; Perez-Dieste, V.; Avila, J.; Asensio, M. C. In Situ Reduction of (100) SrTiO3. *Solid State Sci.* **2000**, *2* (5), 519–524. https://doi.org/10.1016/S1293-2558(00)01068-2.
(261) Jentys, A. Estimation of Mean Size and Shape of Small Metal Particles by EXAFS. *Phys. Chem. Chem. Phys.* **1999**, *1* (17), 4059–4063. https://doi.org/10.1039/A904654B.
(262) Second, C. R.; Edition, E.; Ertl, G.; Knözinger, H.; Schüth, F.; Weitkamp, J.; KGaA, W.-V. V. G. C. Handbook of Heterogeneous Catalysis. **2008**.
(263) Gallagher, J. R.; Li, T.; Zhao, H.; Liu, J.; Lei, Y.; Zhang, X.; Ren, Y.; Elam, J. W.; Meyer, R. J.; Winans, R. E.; Miller, J. T. In Situ Diffraction of Highly Dispersed Supported Platinum Nanoparticles. *Catal Sci Technol* **2014**, *4* (9), 3053–3063. https://doi.org/10.1039/C4CY00414K.
(264) Regalbuto, J. R. Strong Electrostatic Adsorption of Metals onto Catalyst Supports. In *Catalyst preparation*; CRC press, 2016; pp 311–332.
(265) Hao, X.; Spieker, W. A.; Regalbuto, J. R. A Further Simplification of the Revised Physical Adsorption (RPA) Model. *J. Colloid Interface Sci.* **2003**, *267* (2), 259–264. https://doi.org/10.1016/s0021-9797(03)00644-1.
(266) Ma, Y.; Kuhn, A. N.; Gao, W.; Al-Zoubi, T.; Du, H.; Pan, X.; Yang, H. Strong Electrostatic Adsorption Approach to the Synthesis of Sub-Three Nanometer Intermetallic Platinum–Cobalt Oxygen Reduction Catalysts. *Nano Energy* **2021**, *79*, 105465. https://doi.org/10.1016/j.nanoen.2020.105465.
(267) Riyapan, S.; Zhang, Y.; Wongkaew, A.; Pongthawornsakun, B.; Monnier, J. R.; Panpranot, J. Preparation of Improved Ag–Pd/TiO2 Catalysts Using the Combined Strong Electrostatic Adsorption and Electroless Deposition Methods for the Selective Hydrogenation of Acetylene. *Catal. Sci. Technol.* **2016**, *6* (14), 5608–5617. https://doi.org/10.1039/C6CY00121A.
(268) Wong, A.; Liu, Q.; Griffin, S.; Nicholls, A.; Regalbuto, J. R. Synthesis of Ultrasmall, Homogeneously Alloyed, Bimetallic Nanoparticles on Silica Supports. *Science* **2017**, *358* (6369), 1427–1430. https://doi.org/10.1126/science.aao6538.
(269) Lambert, S.; Job, N.; D'Souza, L.; Pereira, M. F. R.; Pirard, R.; Heinrichs, B.; Figueiredo, J. L.; Pirard, J.-P.; Regalbuto, J. R. Synthesis of Very Highly Dispersed Platinum Catalysts Supported on Carbon Xerogels by the Strong Electrostatic Adsorption Method. *J. Catal.* **2009**, *261* (1), 23–33. https://doi.org/10.1016/j.jcat.2008.10.014.
(270) Zhang, L.; Wen, G.; Liu, H.; Wang, N.; Su, D. S. Preparation of Palladium Catalysts Supported on Carbon Nanotubes by an Electrostatic Adsorption Method. *ChemCatChem* **2014**, *6* (9), 2600–2606. https://doi.org/10.1002/cctc.201402175.
(271) Hasse, B.; Gläsel, J.; Kern, A. M.; Murzin, D. Yu.; Etzold, B. J. M. Preparation of Carbide-Derived Carbon Supported Platinum Catalysts. *Catal. Today* **2015**, *249*, 30–37. https://doi.org/10.1016/j.cattod.2014.10.049.
(272) Feltes, T. E.; Espinosa-Alonso, L.; Smit, E. de; D'Souza, L.; Meyer, R. J.; Weckhuysen, B. M.; Regalbuto, J. R. Selective Adsorption of Manganese onto Cobalt for Optimized Mn/Co/TiO2 Fischer–Tropsch Catalysts. *J. Catal.* **2010**, *270* (1), 95–102. https://doi.org/10.1016/j.jcat.2009.12.012.

(273) Cho, H.-R.; Regalbuto, J. R. The Rational Synthesis of Pt-Pd Bimetallic Catalysts by Electrostatic Adsorption. *Catal. Today* **2015**, *246*, 143–153. https://doi.org/10.1016/j.cattod.2014.09.029.
(274) D'Souza, L.; Regalbuto, J. R. Strong Electrostatic Adsorption for the Preparation of Pt/Co/C and Pd/Co/C Bimetallic Electrocatalysts. In *Studies in Surface Science and Catalysis*; Gaigneaux, E. M., Devillers, M., Hermans, S., Jacobs, P. A., Martens, J. A., Ruiz, P., Eds.; Scientific Bases for the Preparation of Heterogeneous Catalysts; Elsevier, 2010; Vol. 175, pp 715–718. https://doi.org/10.1016/S0167-2991(10)75143-0.
(275) Almithn, A.; Hibbitts, D. Comparing Rate and Mechanism of Ethane Hydrogenolysis on Transition-Metal Catalysts. *J. Phys. Chem. C* **2019**, *123* (9), 5421–5432. https://doi.org/10.1021/acs.jpcc.8b11070.
(276) Xie, T.; Wittreich, G. R.; Vlachos, D. G. Multiscale Modeling of Hydrogenolysis of Ethane and Propane on Ru(0001): Implications for Plastics Recycling. *Appl. Catal. B Environ.* **2022**, *316*, 121597. https://doi.org/10.1016/j.apcatb.2022.121597.
(277) Chen, L.; Zhu, Y.; Meyer, L. C.; Hale, L. V.; Le, T. T.; Karkamkar, A.; Lercher, J. A.; Gutiérrez, O. Y.; Szanyi, J. Effect of Reaction Conditions on the Hydrogenolysis of Polypropylene and Polyethylene into Gas and Liquid Alkanes. *React. Chem. Eng.* **2022**, *7* (4), 844–854. https://doi.org/10.1039/D1RE00431J.
(278) Meirow, M.; Luijten, E. Coarse-Grained Modeling of Polymer Cleavage within a Porous Catalytic Support. *ACS Macro Lett.* **2023**, *12*, 189–194.
(279) Yappert, R.; Peters, B. Population Balance Models for Polymer Upcycling: Signatures of the Mechanism in the Molecular Weight Evolution. *J. Mater. Chem. A* **2022**, *10* (45), 24084–24095. https://doi.org/10.1039/D2TA04628H.
(280) Zare, M.; Kots, P. A.; Caratzoulas, S.; Vlachos, D. G. Conformations of Polyolefins on Platinum Catalysts Control Product Distribution in Plastics Recycling. *Chem. Sci.* **2023**, *14* (8), 1966–1977. https://doi.org/10.1039/D2SC04772A.
(281) *Exascale Computing Project* | *ORNL*. https://www.ornl.gov/exascale (accessed 2023-03-26).
(282) *What exascale computing could mean for chemistry*. Chemical & Engineering News. https://cen.acs.org/physical-chemistry/computational-chemistry/exascale-computing-mean-chemistry/100/i31 (accessed 2023-03-12).
(283) Paull, R. J.; Mansley, Z. R.; Ly, T.; Marks, L. D.; Poeppelmeier, K. R. Synthesis of Gadolinium Scandate from a Hydroxide Hydrogel. *Inorg. Chem.* **2018**, *57* (7), 4104–4108.
(284) Paull, R. J.; Ly, T.; Mansley, Z. R.; Poeppelmeier, K. R.; Marks, L. D. Controlled Two-Step Formation of Faceted Perovskite Rare-Earth Scandate Nanoparticles. *Crystals* **2019**, *9* (4), 218.
(285) Mansley, Z.; Paull, R.; Greenstein, E.; Wen, J.; Poeppelmeier, K.; Marks, L. ScO x Rich Surface Terminations on Lanthanide Scandate Nanoparticles. *Phys. Rev. Mater.* **2021**, *5* (12), 125002.
(286) Abolhasani, M.; Kumacheva, E. The Rise of Self-Driving Labs in Chemical and Materials Sciences. *Nat. Synth.* **2023**, 1–10. https://doi.org/10.1038/s44160-022-00231-0.
(287) Makarova, M.; Drahokoupil, J.; Bykov, P.; Dejneka, A.; Dlabacek, Z.; Jastrabik, L.; Trepakov, V.; Sazama, P.; Franc, J.; Okawa, Y.; Aono, M. Size Effect on the Structure and Optical Properties in Nanocrystalline $SrTiO_3$. *E-J. Surf. Sci. Nanotechnol.* **2012**, *10* (0), 406–410. https://doi.org/10.1380/ejssnt.2012.406.
(288) Wu, X.; Liu, X. Negative Pressure Effects in Strontium Titanate Nanoparticles. *J. Lumin.* **2007**, *122*, 869–872.
(289) Leontyev, I. N.; Kuriganova, A. B.; Leontyev, N. G.; Hennet, L.; Rakhmatullin, A.; Smirnova, N. V.; Dmitriev, V. Size Dependence of the Lattice Parameters of Carbon Supported Platinum Nanoparticles: X-Ray Diffraction Analysis and Theoretical Considerations. *RSC Adv.* **2014**, *4* (68), 35959–35965. https://doi.org/10.1039/C4RA04809A.